Nanocharacterization of Materials for Biomagnetic Sensing using TEM

Dissertation

zur Erlangung des akademischen Grades

Doktor der Ingenieurwissenschaften

(Dr.-Ing.)

der Technischen Fakultät

der Christian-Albrechts-Universität zu Kiel

Viktor Hrkac

Kiel

2013

Referent: Prof. Dr. Lorenz Kienle
1. Koreferent: Prof. Dr. Rainer Adelung
2. Koreferent: Prof. Dr. Oliver Eibl
Datum der mündlichen Prüfung: 06.02.2013
Zum Druck genehmigt: 06.02.2013

There are places I remember
All my life, though some have changed
Some forever not for better
Some have gone and some remain
All these places have their moments
With lovers and friends I still can recall
Some are dead and some are living
In my life I've loved them all

But of all these friends and lovers
There is no one compares with you
And these memories lose their meaning
When I think of love as something new
Though I know I'll never lose affection
For people and things that went before
I know I'll often stop and think about them
In my life I love you more

- *The Beatles*

Abstract

The collaborative research center (SFB 855 "Magnetoelectric Composites - Future Biomagnetic Interfaces") aims to develop biomagnetic sensors with the capability of a precise detection of signals in the Femtotesla regime. Novel ME composites are the material of choice and include strain mediated 2-2, 0-3, and 1-1 designs. Such composites are accompanied in many instances with complex structural features. As functionality and property optimization of the materials are based on the minute understanding of such phenomena, structural characterization becomes indispensable particularly at the nanoscale. Within the scope of this work methods of transmission electron microscopy (TEM) were applied to obtain detailed information of the real structure from SFB relevant (magnetostrictive and piezoelectric) materials and ME composites provided by other cooperation parterns. The emphasize is placed on the uncovering of the chemical and structural details of the materials, e. g. their morphology, defects and interfaces.

Defects strongly affect the physical properties of materials, e. g. twin boundaries in piezoelectric materials. Quantitative structural models can be designed allowing the interpretation and simulation of high resolution contrast and the dynamic simulation of electron diffraction patterns for any zone axis. These models were created for SnO_2 with the coherent twin boundary $\{1\,0\,1\}$, AlN with a stacking mismatch boundary caused by total displacement vector of $1/2\,[1\,0\,\bar{1}\,1]$, ZnO showing a superposition twinning supported by a nanospike texture along the $[2\,\bar{1}\,\bar{1}\,3]$ zone axis, and $(Ba_{0.7}Ca_{0.3}TiO_3)0.5$ - $[Ba(Zr_{0.2}Ti_{0.8})O_3]0.5$ (BCZT) exhibiting a superposition contrast, which can be related to twinning with the twin plane $\{1\,1\,1\}$. Further, investigations on the ferroelectric BCZT exhibited a considerable difference between bulk and thin film samples. Only for the latter a considerable appearance of twin defects and modulations were observable. With a modulation vector of $1/7<1\,1\,1>$ a first interpretation as 7L polytype was provided.

The growth behavior on different substrates and an $[0\,0\,0\,1]$ (c-axis) oriented texture was investigated for piezoelectric AlN thin films by applying advanced TEM methods. Measurements with the automated crystal orientation mapping (ACOM) system enabled a direct correlation with piezoelectric property measurements.

In the progress of developing 0-3 nanocomposites, Co nanoparticles were incorporated into such AlN thin films. Electron diffraction methods showed a significant perturbance of the c-axis oriented growth of AlN. This pivotal result supports the statement of 0-3 nanocomposite for being unsuitable as base for highly sensitive ME materials.

A magentostrictive multilayer system composed of repetitive sequences of Ta/ Cu/ $Mn_{70}Ir_{30}$/ ferromagnet (F) ($Fe_{50}Co_{50}$ or FeCoSiB) exhibits epitaxial growth between the seed bilayer (Ta, Cu) and the antiferromagnetic (AF) $Mn_{70}Ir_{30}$ layer on the $(1\,1\,1)$ planes. Due to the direct interface of the AF and the F layers, an exchanged bias coupling can be established. In the case of $Fe_{50}Co_{50}$, the F layers are polycrystalline with a textured growth along the $[1\,1\,1]$ direction. This texture characteristic for the F layers decreases from the multilayer-substrate interface to the surface of the spec-

imen. A 2-2 demonstrator was created by depositing the multilayer on the rough surface of an AlN thin film. Electron tomography was applied to investigate the roughness propagation and evolution within the multilayer. Using FeCoSiB, these amorphous F layers contain crystalline filaments. Ex- and in-situ annealing processes were applied for this sample at different temperatures (250 °C and 350 °C). At the lower temperature, no substantial change in the real structure was detected. At 350 °C crystallization processes were present. The soft magnetic properties of the system were not significantly affected by the second annealing step.

Zusammenfassung

Der Sonderforschungsbereich (SFB 855 "Magnetoelektrische Verbundwerkstoffe - biomagnetische Schnittstellen der Zukunft") verfolgt das ambitionierte Ziel biomagnetische Sensoren zu entwicklen, die eine Detektion von neurologischen Signalen bis in einen Femtoteslabereich ermöglichen. Grundbaustein für solche Sensoren sollen ME Komposite darstellen, welche ihrerseits ein hohes Maß an Gestaltung erlauben; darunter fallen 2-2, 0-3 sowie 1-1 Konzeptionierungen. In vielen Fällen zeigten sich komplexe Strukurphänomene in diesen Materialien. Um eine Optimierung der Funktionalität und der Materialeigenschaften zu erreichen, ist ein präzises Verständnis der Charakteristika jener Phänomene unabdingbar, welches sich im Besonderen auf die nanoskaligen Strukturmerkmale bezieht. Im Rahmen dieser Arbeit werden Methoden der Transmissionselektronenmikroskopie angewandt, um relevante Erkenntnise der Mikro- und Nanostruktur SFB spezifischer Materialien zu sammeln und quantitativ zu interpretieren. Einen besonderen Akzent wird auf die Analyse folgender Materialdetails gelegt: Morphologie sowie die atomare Struktur von Defekten und Grenzflächen.

Defekte innerhalb von kristallographischen Strukturen können zu einer Beeinflussung und Modifizierung von physikalischen Eigenschaften führen, ein Beispiel in diesem Zusammenhang stellen Zwillingsgrenzen innerhalb von Piezoelektrika dar. Basierend auf hochauflösenden Abbildung und Elektronenbeugungsbildern, können Strukturmodelle erstellt werden, die ihrerseits eine Interpretation sowie eine Simulation der experimentellen Resultate, ebenfalls unter Einbeziehung der dynamischen Theorie, erlauben. Solche Strukturmodelle wurden für eine kohärente Zwillingsgrenze $\{1\,0\,1\}$ innerhalb des Materials SnO_2, einer *stacking mismatch boundary* mit dem Verschiebungsvektor $1/2<1\,0\,\bar{1}\,1>$ für AlN, einem Überlagerungszwilling mit der Zwillingsgrenze $[2\,\bar{1}\,\bar{1}\,3]$ für ZnO sowie für einen Überlagerungskontrast innherlab von $(Ba_{0.7}Ca_{0.3}TiO_3)0\ 5$ - $[Ba(Zr_{0.2}Ti_{0.8})O_3]0.5$ (BCZT), welches einer Verzwillingung gemäß der Zwillingsebene $\{1\,1\,1\}$ zuzuschreiben ist, erstellt. Weiterführende Untersuchungen am BCZT offenbarten erheblich Unterschiede zwischen *Bulk*- und Dünnschichtproben. Ausschließlich im letzteren Fall wurde das Vorhandensein von Zwillingsdefekten und Modulationseffekten, die einen Modulationsvektor von $1/7<1\,1\,1>$ aufwiesen und in Form einer Erstinterpretation als 7L Polytyp identifiziert worden sind, beobachtet.

Das Wachstumsverhalten und die Texturierung von AlN Körnern entlang der $[0\,0\,0\,1]$ Richtung (c-Achse) wurde für die, im Rahmen des SFB hergestellten, Dünnfilmschichten mittels moderner TEM Methoden analysiert. Durch Messungen mit dem *automated crystal orientation mapping* (ACOM) System konnte eine Korrelation zwischen Realstruktur und den piezoelektrischen Eigenschaften aufgezeigt werden.

Im Entwicklungsprozess von 0-3 ME Kompositen sind Co Nanopartikel in AlN Dünnfilme hineingebracht worden. Entsprechende Daten, die durch Methoden der Elektronenbeugen erhoben worden sind, zeigten eine signifikante Verschlechterung des geforderten Wachstumsverhaltens des AlNs, welches wiederum keine nennenswerte Funktionalität erlaubt. Dieses Strukturresultat ist ein wesentlicher Faktor für eine

negative Bewertung von 0-3 Kompositen als geeignete Kandidaten für hochsensitive ME Materialien.
Ein magnetostriktives Vielschichtsystem, bestehend aus einer repetitiven Schichtsequenz von Ta/ Cu/ Mn_{70} Ir_{30}/ Ferrogmaneten (F) (($Fe_{50}Co_{50}$ oder FeCoSiB)), zeigt eine epitaktische Beziehung von der Startschicht (Ta, Cu) und der antiferromagnetischen (AF) $Mn_{70}Ir_{30}$ Schicht entlang der (1 1 1) Ebenen. Aufgrund der direkten Grenzfläche der AF und der F Schichten, kann sich eine *exchange bias* Kopplung einstellen. Wird $Fe_{50}Co_{50}$ als F Schicht genutzt, so beobachtet man ein polykristallines Verhalten jener Schichten mit einer Texturierung entlang der [1 1 1] Richtung. Die Ausprägung dieser Textur verringert sich von der Grenzfläche des Substrat-Vielschichtssystems hin zur Oberfläche der magnetostriktiven Phase. Ein 2-2 Demonstrator wurde durch die Abscheidung des Vielschichtsystems auf einen AlN Dünnfilm hergestellt. Aufgrund der rauen Beschaffenheit der AlN Oberfläche, ergaben sich zusätzliche Rauigkeitseffekte innerhalb des Vielschichtsystems. Die Ausbreitung und die Entwicklung jener wurde mittels Elektronentomographie studiert. Bei der Verwendung von FeCoSiB als armorphe F-Schicht, wurden innerhalb dieser Schicht kristalline Filamente endteckt. Ex und in situ Heizexperimente wurden für dieses Material bei verschiedenen Temperaturen (250°C und 350°C) vollzogen. Für die niedrigere Temperatur wurden keine substantiellen Änderungen der Realstruktur beobachtet. Bei 350 °C wurden Kristallisationprozesse festgestellt. Weichmagnetische Eigenschaften dieses Systems wurden durch die unterschiedlichen Temperaturbehandlungen nicht entscheidend beeinflußt.

Contents

1 Introduction

1.1 Magnetoelectric Composites - Future Biomagnetic Interfaces

Modern therapies of cortical diseases and dysfunctions demand a precise localization of activation signals in brain regions during external stimulation [1, 2, 3, 4, 5]. A non-inverse method for the detection of such signals is the magnetoencephalography (MEG) [6], which measures the magnetic fields created by ion currents in the brain tissue. The order of magnitude for these fields is in the range of Femtotesla. State-of-the-art sensors are capable of reaching the desired sensitivity using superconducting quantum interference devices (SQUIDs). The technology contains still a number of drawbacks. For the operation process a cooling system is required using liquid helium. The consequence is a relative large instrumental setup and high operating costs. Thus, MEG is considered more as a diagnostic tool for special purposes instead for general clinical use [7].
To improve the status of MEG another approach is pursued on magnetoelectric (ME) nanocomposites in the frame of the collaborative research center (*SFB 855: Magnetoelectric Composites - Future Biomagnetic Interfaces*). These ME materials consist of a strain-mediated combination of magnetostrictive and piezoelectric phases. The physical quantity connecting magnetostriction and piezoelectricity is given by the ME voltage coefficient α_{ME} [8, 9]. With ME coefficients exceeding those of direct multiferroics substantially, these materials attracted considerable attention for fundamental research as well as for technical applications [10, 8, 11, 12, 13]. In particular, promising results in the progress of magnetic field sensors based on the ME effect raised expectations in approaching sensitivities of low-temperature SQUID sensors [14, 15, 16, 17, 18]. The ME sensors have a passive nature and are envisaged for experimental measurements at room temperature [7]. Due to the obsolete cooling, additional options are offered for a more effectively arrangement of single ME sensors within interconnected arrays. Thus, an enhancement in spatial resolution and data collection could be achieved, particular by considering vector field measurements [7, 19]. Moreover, a significant cost reduction would be yielded for the operation process.
Encouraged by preliminary studies [20, 8, 21] different designs for ME nanocomposites are considered for research and development processes in the beginning of the SFB, as demonstrated in Figure 1.1. Apart from these nanoengineering aspects and associated property characterization including experimental and theoretical works [19, 22], novel sensors concepts must be elaborated [23]. Micro-electro-

mechanical systems (MEMS) with integrated ME composites seem to be excellent candidates for biomagnetic interfaces [24, 13]. Additional medical oriented studies emphasize further the multidisciplinary approach of the SFB 855 [7].

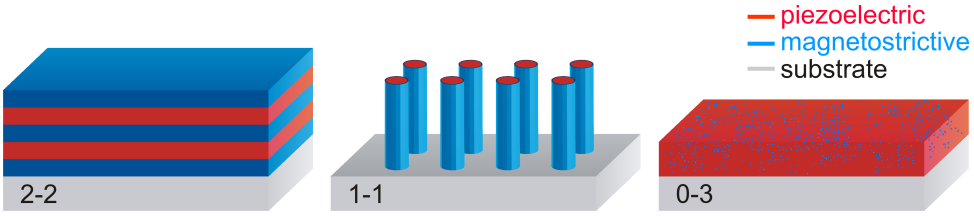

Figure 1.1: Different designs of ME nanocomposites investigated in the SFB 855.

1.2 Scope of this work

For nanoengineering, in particular for sensor systems for highly precise measurement capabilities, the comprehensive understanding of real structure-property relationships is of paramount significant. As known for a variety of examples, e. g. spontaneous polarization due to local atom displacements in ferroelectric lead zirconate titanate [25, 26, 27, 28, 29], the structural condition and features at the nanoscale predetermine macroscopic properties. Transmission electron microscopy (TEM) proofed its exceptional value for the characterization of such features and its analyses techniques belong to the generally accepted standard methods in the field of nanoscience. As direct crystallographic and compositional information are achievable with atomic resolution (and in many instances also in real-time), in-situ observations belong also to the repertoire of TEM.
The subject of this work covers the structural analysis of relevant components for ME devices, demonstrators including 2-2, 0-3, 1-1 composites, and functional materials, as part of innovative syntheses processes developed for bio-magnetic sensing. The aim is to provide an enhanced understanding of a certain material and, thus, creating starting points for future development and optimized processing procedures as well as for fundamental research. By choosing an adequate set of TEM techniques, tailor-made investigations are provided, which accounts for the specific peculiarities of each material, e. g. morphology, crystallographic habitus, or structural ordering. Further, experimental data are compared with computational obtained simulations enabling quantitative interpretation of the structure.
The discussed results substantiate, as a supplement, other (SFB 855) studies, which focus exclusively on synthesis procedures and experimentally or theoretically determined properties of ME based sensors. Key aspects from those works are included in the respective discussions of this thesis to provide a comprehensive scientific context. The work is structured in the following sections:

- Chapter 2: A brief introduction of the most important TEM techniques for this work is provided. The complete experimental setup is given for the discussed investigations.

- Chapter 3: Materials resulting from the flame transport synthesis are investigated. As the structures of those materials are strongly affect by defects, i. e. twin boundaries, a supercell approach is also introduced. Further, investigations on a 1-1 ME demonstrator device is given.
- Chapter 4: Piezoelectric materials are investigated, which were synthesized in the framework of SFB 855 and are suitable for the ME sensors. Advanced TEM methods are applied on AlN thin films to work out crystallographic information on different length scales. A critical evaluation is performed on 0-3 nanocomposites. For the perovskite $0.5Ba(Zr_{0.2}Ti_{0.8})O_3$ - $0.5Ba_{0.7}Ca_{0.3}TiO_3$, structural variations between bulk and thin film systems are compared and elaborated.
- Chapter 5: A magnetostrictive multilayer based on the exchange biased coupling between $Mn_{70}Ir_{30}$ and a ferromagnet ($Fe_{50}Co_{50}$ or $Fe_{70.2}Co_{7.8}Si_{12}B_{10}$) is introduced. In situ annealing studies are carried out to investigate the structure-property relation for different multilayers. The interface studies and the influence of surface roughness are investigated on a 2-2 demonstrator by electron tomography.

2 Methodology

This chapter deals with the basic experimental equipment which is mandatory for the nanostructure characterizations discussed in the following studies. In the first part the capabilities of the applied analysis methods are briefly explained. The fundamental principles of transmission electron microscopy will not be discussed here. For an enhanced insight into this field the reader is referred to the textbook of Williams and Carter [30]. In the second part the used TEM instruments and their respective specifications are listed.

2.1 Analysis Techniques

The two major aspects for structure characterization in this thesis are electron diffraction (ED) and high resolution transmission electron microscopy (HRTEM). In the following, the aim is to present the capabilities as well as the advantages and drawbacks of the respective methods. Chemical investigations were performed by energy-dispersive X-ray (EDX) spectroscopy. A description of EDX working procedures will not be provided.

2.1.1 Electron Diffraction

In general, the key for understanding the nature of a structure and their own characteristic features is placed in the feasibility of finding and producing crystallographic information from the respective specimen. One of the most valuable and versatile TEM discipline, providing the desired information, is electron diffraction.

Basic Description

Electron diffraction [30] is based on the interaction of electrons with atoms of a certain specimen by elastic scattering. For the interpretation of the interaction the wave character of the electrons is assumed. Using the quantum mechanical approach of the wave-particle-dualism a (de-Broglie) wavelength can be determined for the electrons and according to the applied kinetic energy of these electrons a resolution in the sub-angstrom regime is achievable.

Constructive interference (will be named as diffraction reflections) within an electron diffraction pattern is obtained when the Laue condition

$$\vec{k} - \vec{k'} = \vec{G}$$

is fulfilled: i. e. the difference of the wave vectors of an incident beam $\vec{k}$ and of a corresponding scattered beam $\vec{k'}$ equals a reciprocal lattice vector $\vec{G}$. Considering the equivalent concept of Ewalds construction, an extension of the radius of the Ewald's sphere is obtained for electrons with respect to X-rays, which is a direct result from the respective wavelengths. As a consequence of the size of Ewald's sphere (can approximated as plane) and low specimen thicknesses ($\ll 500\,\mathrm{nm}$), a gain in information is achieved for the diffraction patterns represented by an increased number of reflections corresponding to lattice planes of the investigated material with respect to other methods as XRD. Moreover, under the validity of the kinematic theory the intensity of the reflections can be directly correlated with the atoms in the unit cell in a certain structure via the structure factor (e. g. expressed by extinction rules). The strong interaction of the electron with the specimen can result in multiple scattering. In such a case the kinematic model fails and a change in the intensity ratios must be explained by a dynamical approach, see Figure 2.1a and b. However, a structural interpretation of the intensities is significantly influenced and can be more complicated.

Methods

A manipulation of the electron beam, by magnetic electron lenses, allows the use of different experimental methods in electron diffraction, which in turn provide detailed crystallographic information:

- **Selected Area Electron Diffraction (SAED)** [30, 31]:
  A parallel electron beam (beam diameter: 1 - 10 μm) is placed on an electron transparent specimen. The term *selected area* refers to the possibility of the operator to limit and to choose the illuminated area of a specimen by applying a diffraction aperture (diameter of the restricted illuminated area on the specimen: $>$100 nm). Due to the size of the investigated area in SAED, the patterns can contain additional undesirable effects and specimen features, including thickness gradients, multiple numbers of grains, and change in orientation.
  SAED is used for the fundamental characterization and identification of chemical phases, defect structures or growing directions on larger scales. The data set can vary from spot patterns representing single crystals with Bragg reflections to complete ring patterns indicating polycrystalline structures.

- **Convergent Beam Electron Diffraction (CBED)** [32, 33]:
  A convergent electron beam (beam diameter: 1 - 100 nm, convergence angle $\geq$ 10 mrad) is placed on an electron transparent specimen. This leads to the

formation of disc shapes for the intensities within diffraction patterns. Those discs include structures revealing additional information about high-order Laue zones (HOLZ) and are caused by dynamical effects. Due to the dimensions of the irradiated area orientation and thickness variations are of no particular relevance.
CBED allows obtaining three dimensional informations of the symmetry of a structure (point group), specimen thickness, strain, etc..

- **Precession Electron Diffraction (PED)** [34, 35]:
  In a PED mode the electron beam is tilted away from its initial position along the optical axis by a certain angle (≤3°) and is precessed on a cone surface. For any beam position a respective diffraction pattern in off-axis condition is generated. By averaging over all those a resulting pattern in zone-axis condition is obtained[1]. This averaging effect leads to a reduction of multiple scattering phenomena (cf. Figure 2.1b and c) and simultaneously to a general resolution enhancement as reflections originating from HOLZ are excited in the off-axis patterns, compare Figure 2.1b with a and c.
  The PED mode can be operated with a parallel or convergent incident electron beam. In general, the PED is coupled with SAED. With the enhanced kinematic character of the PED patterns (cf. Figure 2.2) a reliably determination of the Laue-symmetry and space groups is enabled. The reflections from HOLZ provide three dimensional structure information, which is particularly valuable for defect investigations. As stated by Schürmann et al. [35] this feature is unique among all methods based on structure projection.

- **Automated Crystal Orientation Mapping (ACOM)** [37, 38, 39]:
  Automated crystal orientation mapping enables orientation measurements for a large number of grains. The obtained orientation map gives results which are similar to electron backscattering diffraction (EBSD) in scanning electron microscopy (SEM); however the spatial resolution is enhanced by at least one order of magnitude.
  The ACOM method is based on the high speed recording of ED patterns during the scanning of a region of interest with the electron beam of the TEM. With a template matching system the recorded experimental patterns are compared with simulations for all phases and orientations of preset structures. The quality of the experiment/simulation accordance is determined by the cross-correlation index Q_i

$$Q_i = \frac{\sum_{j=1}^{m} P(x_j, y_j) T_i(x_i, y_i)}{\sqrt{\sum_{j=1}^{m} P^2(x_j, y_j)} \sqrt{\sum_{j=1}^{m} T^2(x_j, y_j)}}$$

  with $P(x, y)$ as the experimental spot diffraction pattern, $T(x, y)$ as the simulated diffraction pattern from a template, and the relibility index R

[1] A complementary descan of all diffracted beams is required to superimpose the respective same reflections on identical positions in the final diffraction pattern [36].

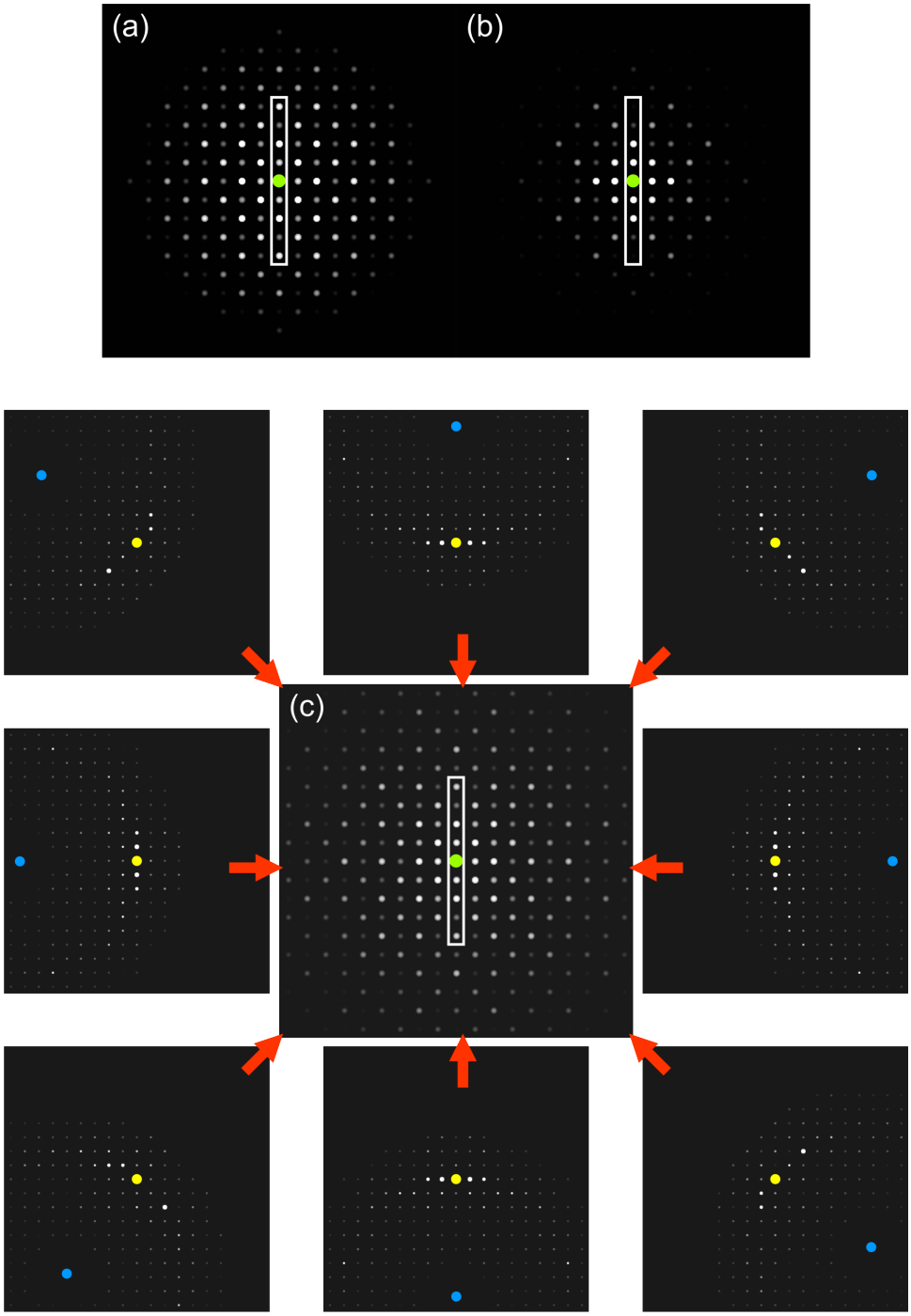

Figure 2.1: The influence of the specimen thickness to electron diffraction demonstrated for calculations of $BaTiO_3$ along [1 0 0]: (a) kinematic SAED pattern (nominal specimen thickness 0 nm) vs. (b) SAED pattern (specimen thickness 48 nm). A reduction of multiple scattering phenomena can be achieved by PED. (c) PED pattern (specimen thickness 48 nm). Marks in the image: yellow - center of the pattern; blue - position of the beam; green - congruence of yellow and blue. White boxes mark the position of intensity investigations shown in Figure 2.2.

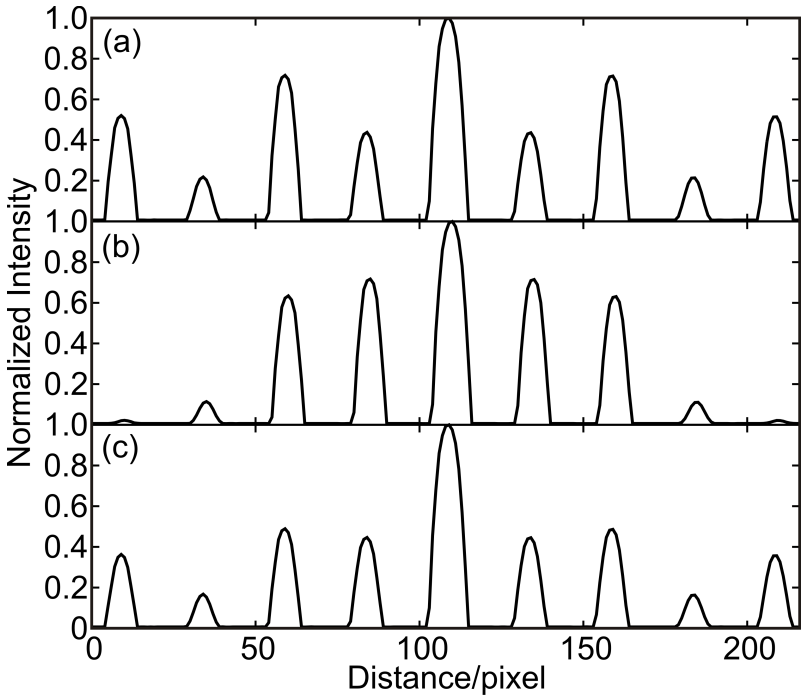

Figure 2.2: Intensity distributions of the marked positions in Figure 2.1. (a) kinematic SAED (specimen thickness 0 nm), (b) SAED (48 nm), (c) PED (48 nm).

$$R = 100(1 - (Q_2/Q_1))$$

with Q_1 as the cross-correlation index of the best coincidence and Q_2 as the cross-correlation index of the second best coincidence [37]. Further, the ED patterns can provide reliable data also for plastically deformed material in contrast to Kikuchi patterns used in EBSD as stated by [39].

2.1.2 High Resolution Analysis

High resolution investigations allow the indirect observation of real structure and the influence of potential crystallographic or stoichiometric features to it on a nanoscale. In the following key parameters for the interpretation and simulation of high resolution transmission electron microscopy (HRTEM) micrographs will be addressed. Further a theoretical introduction to the advanced method of geometric phase analysis will be given.

Structural Investigations and Interpretation using High Resolution TEM

The HRTEM represents the centerpiece of every real structure investigation as it is a two-dimensional imaging technique providing information at the atomic scale.

By comparing experimental with simulated data this method enables a direct correlation between the high resolution contrast within a (HR)TEM micrograph and the atomic configuration of a model system. Despite instrumental parameters of the microscope (e. g. spherical aberration), two parameters must be emphasized for the interpretation of a HRTEM micrograph: the specimen thickness and the objective-lens defocus (Δf). To illustrate the influence of these parameters a defocus and a thickness series are presented in Figure 2.3, respectively. In both cases, slight variations lead to strong alterations in the HRTEM contrast.

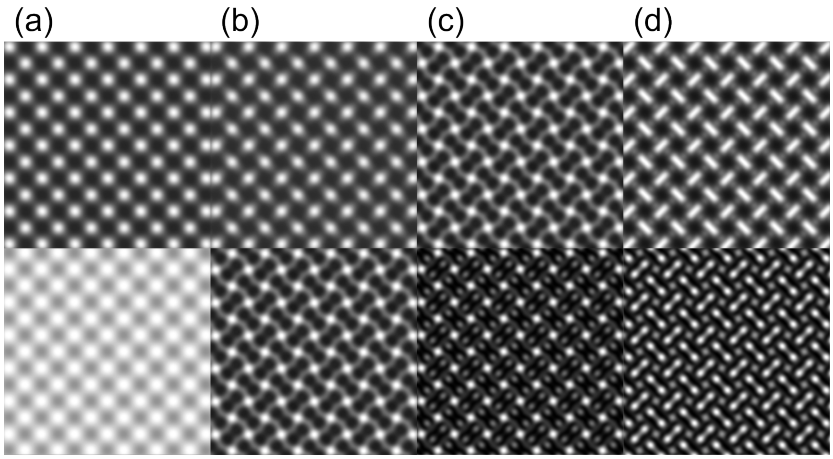

Figure 2.3: Series of simulated HRTEM micrographs along the zone axis $[0\,0\,0\,1]^r$ for SnO_2: (top) Defocus series: the specimen thickness was set to 5.73 nm, the respective Δf are (a) 0 nm, (b) -5 nm, (c) -60 nm, (d) -95 nm. (bottom) Thickness series: Δf was set to -60 nm, the respective specimen thickness (a) 0.32 nm, (b) 5.73 nm, (c) 9.87 nm, (d) 13.05 nm.

Geometrical Phase Analysis

Geometrical phase analysis (GPA) [40, 41] has developed into a standard technique for the analysis of strain distribution at the nanoscale. It is based on the Fourier anaylsis of HRTEM micrographs, locally expressing a selected set of lattice fringes in terms of amplitude A_g and phase P_g for a certain set of lattice fringes $\mathbf{g}$. Following the mathematical treatment provided by Hÿtch et al. [40], these selected set of fringes (Bragg filtered image B_g depending on the position $\mathbf{r}$) can be expressed by

$$B_g(\mathbf{r}) = 2A_g(\mathbf{r})\cos\{2\pi\mathbf{g}\cdot\mathbf{r} + P_g(\mathbf{r})\}$$

when a mask is positioned around a specific Brag intensities $\pm\mathbf{g}$ in the Fourier transform corresponding to a set of lattice fringes. To relate the phase information with a displacement field, a shifted reciprocal lattice vector with respect to a reference area shall be assumed (reference vector: $\mathbf{g} \rightarrow$ shifted vector: $\mathbf{g} + \Delta\mathbf{g}$, with $\Delta\mathbf{g}$ as shift). The resulting Bragg filtered image can be derived as:

$$B_g(\mathbf{r}) = 2A_g\cos\{2\pi\mathbf{g}\cdot\mathbf{r} + 2\pi\Delta\mathbf{g}\cdot\mathbf{r} + P_g\}$$

with P_g as arbitary constant phase term [40] With the argument for the displacement field $\mathbf{u}$ ($\mathbf{r} \rightarrow \mathbf{r} - \mathbf{u}$) as introduced by Hirsch et al. [42], the Bragg filtered image can be also written as

$$B_g(\mathbf{r}) = 2A_g\cos\{2\pi\mathbf{g}\cdot\mathbf{r} - 2\pi\mathbf{g}\cdot\mathbf{u} + P_g\}.$$

Comparing the last three equations, the phase in dependence of the position $\mathbf{r}$ can be related with the displacment field by

$$P_g(r) = 2\pi\Delta\mathbf{g}\cdot\mathbf{r} = -2\pi\mathbf{g}\cdot\mathbf{u}$$

the constant phase term was neglected. For the calculation of a vectorial displacement field in two dimensions, two independent sets of lattice fringes are required. The phase $P_g(r)$ corresponds to a respective $\mathbf{g}$ vector, the following linear equations system is required for the calculation of the displacement field components:

$$\begin{pmatrix} u_x \\ u_y \end{pmatrix} = -(2\pi)^{-1} \begin{pmatrix} g_{1x} & g_{1y} \\ g_{2x} & g_{2y} \end{pmatrix}^{-1} \begin{pmatrix} P_{g1} \\ P_{g1} \end{pmatrix} = -(2\pi)^{-1} \begin{pmatrix} a_{1x} & a_{1y} \\ a_{2x} & a_{2y} \end{pmatrix} \begin{pmatrix} P_{g1} \\ P_{g1} \end{pmatrix}$$

with a_{ii} as the components of the real space vectors. From the first derivative of the displacement field components the local distortion in term of a matrix e can be calculated.

$$e = \begin{pmatrix} e_{xx} & e_{xy} \\ e_{yx} & e_{yy} \end{pmatrix} = \begin{pmatrix} \frac{\partial u_x}{\partial x} & \frac{\partial u_x}{\partial y} \\ \frac{\partial u_y}{\partial x} & \frac{\partial u_y}{\partial y} \end{pmatrix}$$

The in-plane strain tensor components, ϵ_{ij}, and the in-plane rigid body rotation, ω_{ij}, are generally expressed by [40, 43, 44]

$$\epsilon = \frac{1}{2}\{e + e^T\} \quad \text{and} \quad \omega = \frac{1}{2}\{e - e^T\},$$

with T for transpose of the matrix e. Note, that the strain measured by GPA is always expressed relative to a reference lattice within a HRTEM micrograph, which is supposed to be unstrained [45]. This provides a good qualitative idea of the stress distribution in an area of interest, but a quantitative interpretation is further limited by stress-relaxation in the thin film during sample preparation. Further, using spherical aberration corrected microscopes delocalization effects can be avoided, which increases the spatial resolution of the GPA measurement.

2.2 Instrumentation: Applied Transmission Electron Microscopes

The structural analysis was carried out using four different TEMs:

- **FEI Tecnai F30 G^2 STwin**
  operated at 300 kV (field emission gun (FEG), spherical aberration coefficient $C_S = 1.2$ mm) (measurements were performed in the University of Kiel (TEM center of the technical faculty)).
- **Philips CM 30 ST microscope**
  (LaB_6 cathode, 300 kV, $C_S = 1.15$ mm) (measurements performed at the Max-Planck-Institute for solid state research by V. Duppel).
- **FEI Tecnai F20 G^2 STwin**
  with FEG operated at 200 kV and equipped with a NanoMegas ASTAR system for ACOM data acquisition (ACOM measurements were performed at the Karlsruhe Institute of Technology by V. S. K. Chakravadhanula).
- **FEI Titan 80-300**
  operated at 300 kV for aberration corrected HRTEM imaging (measurements were performed at the Karlsruhe Institute for Technology by V. S. K. Chakravadhanula and in the Ernst Ruska-Centre Jülich by Dr M. Luysberg).

SAED was performed by using apertures limiting the illuminated area of a specimen to diameters up to 250 nm (Tecnai F30) and 100 nm (Philips). PED was enabled by a spinning star device attached to the microscope (Philips)[2] . Scanning (S)TEM images which display atomic number dependent (Z)-contrast were recorded via a high angle annular dark field (HAADF) detector (Tecnai F30). Energy-dispersive X-ray (EDX) nanoprobe analysis were conducted using a Si/Li detector (EDAX System (Tecnai F30)/ Thermo Fisher, Noran System Seven (Philips)).
The evaluation of all high resolution (HR)TEM micrographs, Fast Fourier Transforms (FFTs) and ED patterns was performed with the program Digital Micrograph 3.6.1 (Gatan, Inc.) (DM). For the calculation of the GPA a FRWRtools plugin for DM (http://elim.physik.uni-ulm.de) was applied.
Simulations of HRTEM micrographs, FFT, SAED, and PED patterns were performed with the following software: JEMS program package [46], xHREM image simulation [47] program, Calidris CRISP, Analitex eMap. Preferences for HRTEM: multislice formalism, spread of defocus: 70 Å, illumination semiangle: 1.2 mrad. A contrast enhancement for HRTEM micrographs was achieved by applying the HRTEM filter plug-in for DM was applied [48]. Another method was the Bragg filter, which was an implemented feature in DM.
For TEM preparation using focused ion beam (FIB) milling a lift-out method with a FEI Helios Nanolab system was applied. The prepared specimens are thin lamellae

[2] During the progress of this thesis a PED system was installed and configured in Kiel. First preliminary works were performed with the setup.

offering a cross-sectional view. To obtain specimens with a basal view, a conventional preparation (sandwich method) was performed: two face-to-face bonded films are polished, dimple-grinded, and subsequently ion milled by a Gatan Precision Ion Polishing System (PIPS). Another preparation method was the mechanical grinding and dispersion in n-butanol. A drop of this suspension was transferred to holey carbon/Cu grid.
In situ heating experiments were performed using a Gatan 652 Tantalum heating holder. For heating experiments specimens were prepared or placed on Mo grids otherwise on Cu grids. Cooling experiments were performed with Gatan Be double tilt LN2 cooling holder.
Electron tomography was performed using a Fischione tomography holder enabling a tilting range of (±70°). The presented data in this thesis was recorded with 1° intervals between the images using an acquisition package from FEI. For data processing the programs Inspect 3D and Amira were used. The tomography data was recorded in the STEM Z-contrast mode.

Applied Preparation Methods for the Investigated Specimens

All specimens investigated in chapter 3 were prepared by the grinding method. The ZnO rod in the push-to-pull device was not prepared for TEM. In chapter 4, the cross-sectional view of the AlN thin films were prepared by FIB technique, the sandwich method was applied to obtain the basel view. The BCZT bulk specimens were grinded and cross-sectional FIB lamellae were cut out the BCZT thin films. All specimens in chapter 5 were prepared as FIB lamellae.

3 Structural Investigations on Complex Functional Nanomaterials Produced by the Flame Transport Synthesis

The recently established flame transport synthesis (FTS) showed promising capabilities for developing functional nanomaterials with relevance for fundamental research and bio-magnetic sensing in terms of 1-1 ME nanocomposites. The materials produced by FTS are of high complexity, since single building elements of such structures are connected by defect phenomena. In this chapter the main focus is placed on an analytical process allowing a full three-dimensional (3D) analysis of defect structures particularly for TEM.
The chapter is subdivided into three parts. In the first part of the chapter the main aspects for FTS are addressed with a particular focus on structural characteristics, for information regarding the synthesis and macroscopic properties the reader is referred to [49, 50, 51]. In the second part a supercell approach is introduced as quantitative investigation method and applied explicitly on defects in SnO_2. The third part of the chapter provides investigations on ZnO with studies on complex defect structures and preliminary investigations on a 1-1 ME demonstrator system with an outlook for in situ measurments on 1D ZnO structures.[1]

3.1 Flame Transport Synthesis

The flame transport synthesis[2] is a rapid method for the production of macroscopic amounts of oxide semiconductor or ceramic materials with tuneable properties for an efficient application adaptation and can be considered as modified vapour liquid solid (VLS) process. As reported by Mishra et al. [50] three distinct synthesis types were firmly established[3]:

1. Hierarchical 3D network and array structures: Metal oxide networks created by interconnecting of various structures.

[1] The sections dealing with structural investigations are based on studies from [52, 53, 54].
[2] The synthesis method was developed in the frame of the SFB 855 by the working group of Rainer Adelung, *Functional Nanomaterials*.
[3] The nomenclature was directly adopted from [50].

2. Sea-urchin type structures: Metal oxide materials consisting of core-spike structures. 3D networks are established by interconnection of the spikes from neighboring particles.

3. 1D micro/nanostructures using the so-called burner approach: The capability of producing a large variety of single domain structures with a variable coating rate up to the m^2 regime.

The principle of generating 3D systems is based on the combination of building blocks via (defect) interconnections. A structural understanding of these single components can help in process developments for a deliberate control of these defects and, thus, a tailoring of the material properties. The advantages of the FTS approach are represented in its simplicity, low cost, mass scale production and versatility of free-standing structures [49, 50].

3.2 Defect Description by the Supercell Approach

The key for the understanding of structural defect phenomena observed in TEM lies in the possibility of their computational simulation and, thus, in their quantitative description. In this process, the main challenge is the combination of comparatively uncomplicated simulations of periodic structures with those of non-periodic objects, i.e. defects (twin boundary, planar defect, antiphase domain, etc.). In order to resolve this problem the well proven supercell approach [55, 56, 57] can be applied. Thereby, the respective defect is converted into a pseudo periodic feature by embedding it into a suitable supercell. The generation of a supercell can be subdivided into three general steps [57]:

1. Initially, a transformation of the ideal structure into a triclinic (P1) structure must be performed (Figure 3.1). Due to the reduction to a P1 space group symmetry restrictions are avoided and all symmetry elements of the ideal structure are preserved as pseudo-symmetry elements. Particularly for the presented defect models in this thesis, an optimized metric of the model (all angles within the cell are restricted to 90°) is required for the implementation of the corresponding defect. It should be pointed out, that the necessary information for the model design, including the orientation and the type of the defect, must be obtained from experimental observations. The mathematical formulation for a unit-cell transformation into an unconventional description of a crystal structure is provided by Arnold [58]:

$$(\mathbf{a'},\mathbf{b'},\mathbf{c'})=(\mathbf{a},\mathbf{b},\mathbf{c})\mathbf{P}$$

$$\begin{pmatrix} u' \\ v' \\ w' \end{pmatrix} = \mathbf{Q} \begin{pmatrix} u \\ v \\ w \end{pmatrix}$$

$$\mathbf{Q}=\mathbf{P}^{-1}$$

with (**a**,**b**,**c**) as basis vectors of the direct space; (u,v,w) as indices of a direction in direct space; (') mark the parameters for the P1 cell; **P** and **Q** are (3x3) square matrices, linear parts of an affine transformation.

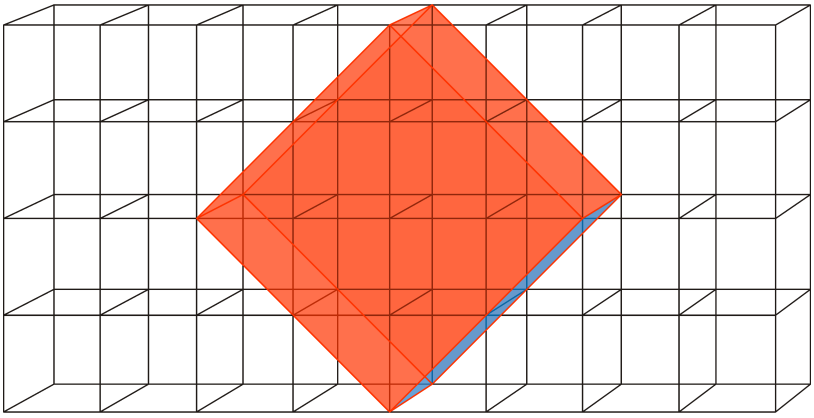

Figure 3.1: Supercell approach, transformation: Stylized representation of periodic crystal (black bordered cubes represent unit cells). The supercell (cross-hatched red cuboid) is extracted from the perodic crystal. Blue hatched plane indicates the position of the defect.

2. As all atoms within the obtained supercell are crystallographically independent, a straightforward manipulation of the atom positions is enabled. Particularly, the characteristic symmetry element of the defect determines the number and the construction manner of modified supercells. An exemplary case of a twin plane is depicted in Figure 3.2a. The blue colored side surface represents the twin plan separating the two individual twin domains. By superimposing the supercell of step 1 with its modified counterparts a so-called superposition structure (SPS) can be constructed. Only by following the angle restriction, mentioned in step 1, an artifact-free SPS model can be deliberately created, see Figure 3.2b.
   Although the SPS represents actually only an intermediate step, it serves as an adequate basis for the simulations of electron diffraction patterns. This is attributable to the translational invariance of the reciprocal lattice. Thus, superposition of defect introduced scattering phenomena are always present. The proportion by volume of the domain individuals and single atoms can be adjusted by varying the occupancy factor.

3. In the final step a segregation of domain individuals within the SPS is performed, generating further a domain boundary within the new established supercell, see Figure 3.2c. Especially, at the domain boundary non-scientific interatomic spacings may occur. In such a case, an additional correction vector must be applied which shifts the respective atomic positions of a individual domain with respect to a certain reference domain.

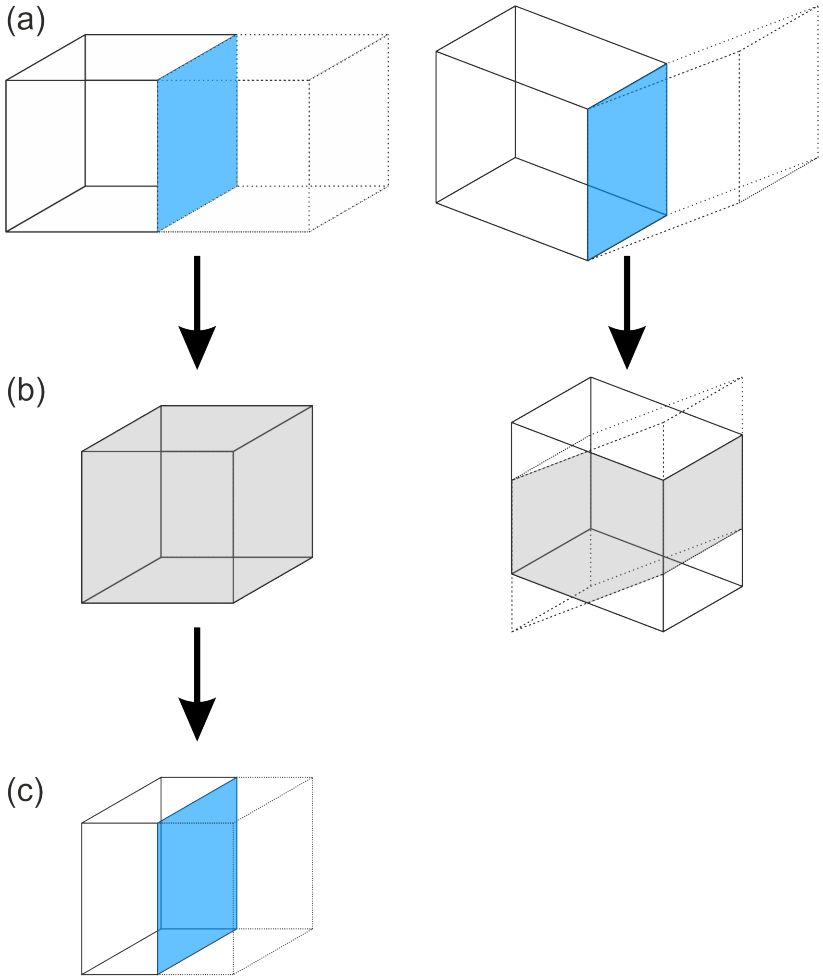

Figure 3.2: Supercell approach, superposition and separation: (a, left side) The supercell (black bordered cube) is mirrored or inversed (dashed bordered cube) with respect to the defect plane (blue). (b, left), SPS: Superposition of the supercells is performed (grey colored cube). (a, right side) Misaligned supercells leading to a (b, right side) deformed SPS. (c) Separated SPS including the domain boundary (blue).

Defect Analysis on SnO_2 Array Structures

The superior capability of FTS is demonstrated in the production of complex three dimensional (3D) networks of SnO_2 occupying macroscopic volumes [54, 59]. Such a network is built up by defect-introduced interconnections of anisotropic nano- and microstructures, as demonstrated in the SEM micrograph[4] in Figure 3.3. As discussed in other studies [60, 54, 59] these free-standing large scale structures are promising candidates in fields of Lithium-ion batteries and biological applications.

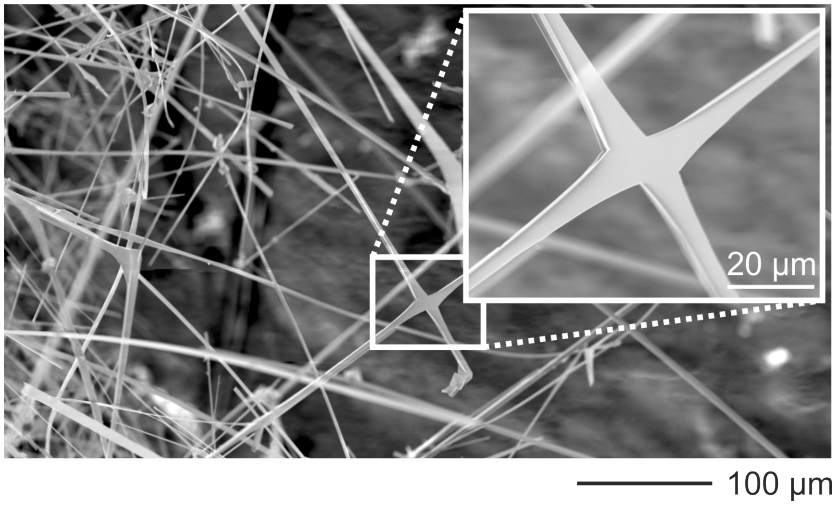

Figure 3.3: SEM micrograph of a SnO_2 three dimensional network. Inset: Magnified view of a twinned SnO_2 branch.

Further property improvements of the 3D networks, including the functionality and the possibility of a precise growth control of the network, demand an in-depth crystallographic knowledge of the interconnections. In the following a quantitative TEM study is presented on the observed defect structures.

Nanoscale Morphology

A detailed characterization of SnO_2 was performed on representative grains of a grinded specimen. According to the experimentally obtained PED patterns, a rutile-type structure (index label: r) with the tetragonal space group $P4_2mnm$ was identified. The appearance of twinning defects was a frequently observed feature. To exclude structural variations due to chemical changes, EDX was performed showing only composition of SnO_2 without any significant impurities. In Figure 3.4a a representative HRTEM micrograph is depicted containing such a defect structure for the viewing directions $[0\,1\,0]^r$. Arrows highlight the position of the twin boundary in the HRTEM micrograph. Analyzing the FFTs (Figure 3.4b) of the marked areas the twin plane was identified to be $\{1\,0\,1\}^r$. The mirroring of the two domains corresponds to a rotation of 68.5° for the domains to each other.

[4]Scanning electron microscopy observations were performed by Yogendra Kumar Mishra and Ingo Paulowicz

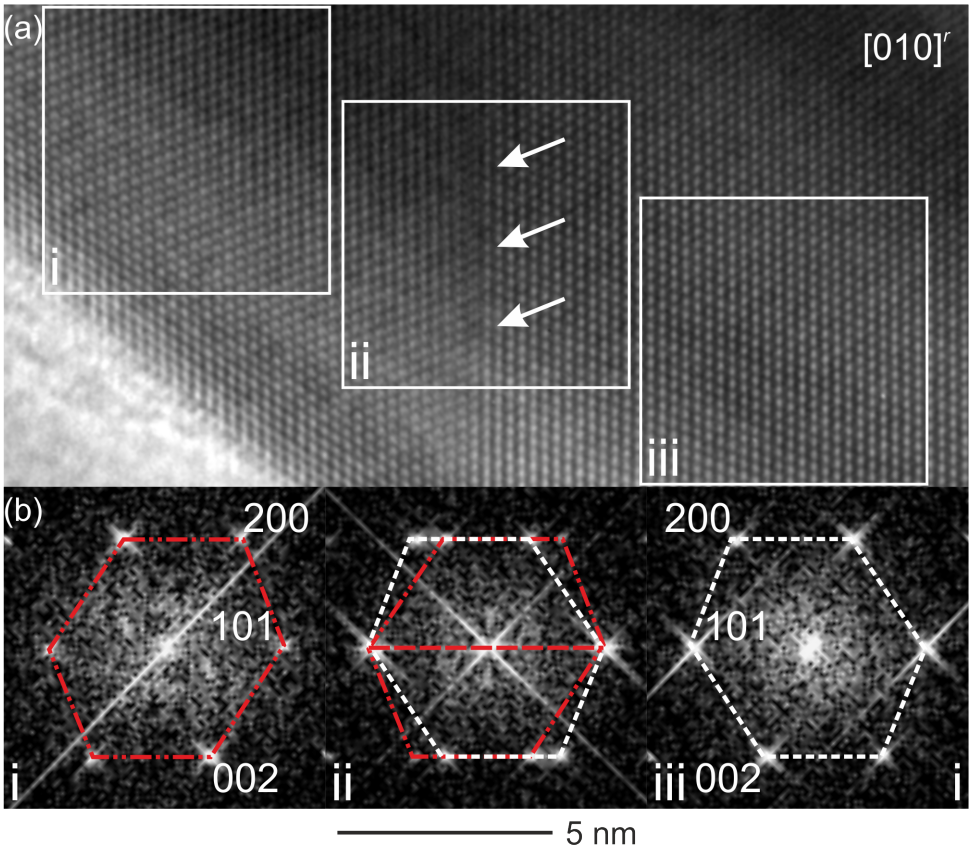

Figure 3.4: (a) Experimentally obtained HRTEM micrograph of the SnO_2 twin interface with the $(1\,0\,1)^r$ coherent twin boundary for the $[0\,1\,0]^r$ direction. (b) Fast Fourier Transformation patterns of the respective single (i, iii) and twin structure (ii).

As described by Zheng et al. [61] the present twin is a growth twin consisting of a coherent twin boundary (CTB) as no misfit[5] between the two domains was experimentally detectable for all examined viewing directions. Further, a tendency of intertwining was reported for the CTB leading. The considerable influence of such defects was investigated for optoelectronical and electrical properties in particular for SnO_2 thin films [62, 63]. Although, high quality models were already described [61, 64, 65], a substantial improvement can still be achieved especially considering the simulation of the high resolution contrast by applying a supercell approach.

[5] In Figure 3.4 the high resoultion contrast seems to show a splitting close to the twin boundary (see white marks in box (ii)). This feature was only observed for this particular grain and in this direction. Also no significant contribution was found within the FFT pattern of area (ii) stemming from this feature. Therefore, it appears to be an additional and individual structural effect, which will not be considered for the following supercell approach.

Model Design by the Supercell Approach

For a quantitative interpretation of the experimental observations a supercell approach was applied. The principle construction of this model follows the procedure introduced in section 3.2 - *Defect Description by the Supercell Approach*. An illustration of the single steps of the supercell construction is depicted in Figure 3.5.

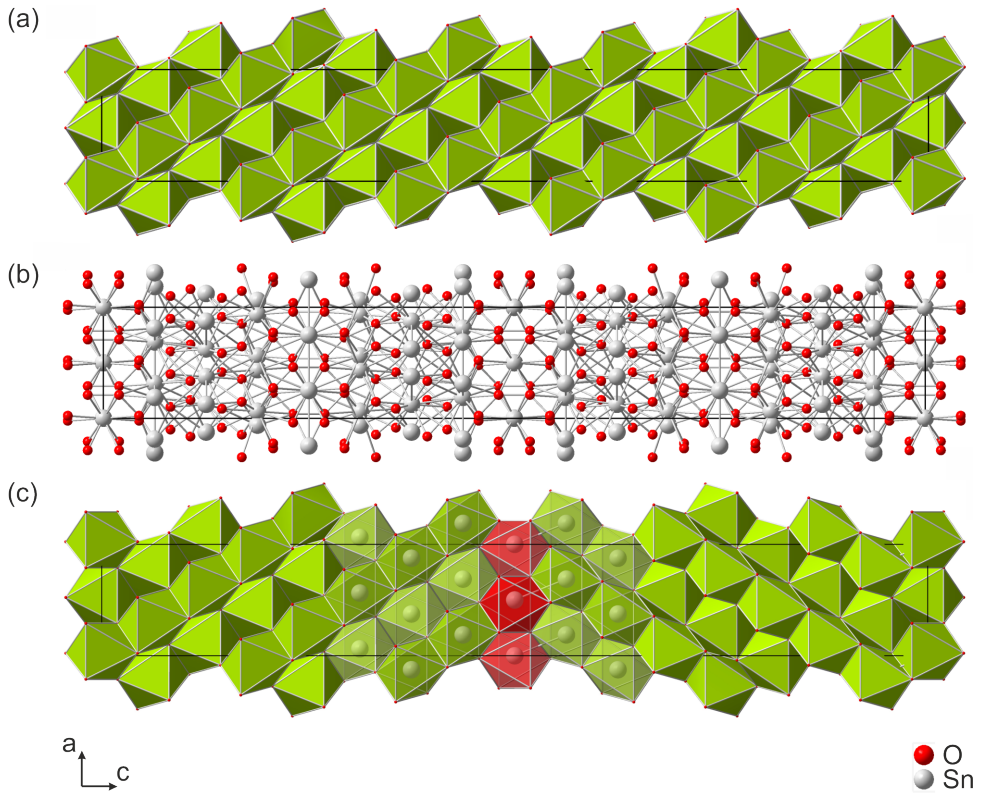

Figure 3.5: 3D model design for the $(1\,0\,1)^r$ CTB along $[0\,1\,0]^r$ direction. (a) Supercell model of the rutile-type SnO_2 structure. (b) SPS model (c) Separated twin model with the CTB indicated by the red octahedra.

1. **Transformation of the ideal SnO_2 structure**
   The tetragonal $P4_2/mnm$ structure of the ideal rutile-type SnO_2 is transformed to a rectangular supercell with a triclinic ($P1$) symmetry, see Figure 3.5a. The transformation [58] is performed by applying the matrices P and Q to the basis vectors (a, b, c) and the indices of the direction in direct space [u, v, w], resulting in the new coordinates (a', b', c') and [u', v', w']:

$$\mathrm{P} = \begin{pmatrix} 1 & 0 & 1 \\ 0 & 1 & 0 \\ -5 & 0 & 11 \end{pmatrix}, \mathrm{Q} = \begin{pmatrix} 11/16 & 0 & 5/16 \\ 0 & 1 & 0 \\ -1/16 & 0 & 1/16 \end{pmatrix}$$

   The new cell parameters are a' = 0.5706 nm, b' = 0.4735 nm, c' = 4.2272 nm, $\alpha' = 90°$, $\beta' = 90.14°$, $\gamma' = 90°$. For the following steps the angle β' is set to 90°. This approximation is legitimate as the slight deviation of the angle from

the intended 90° results in a negligible error. Note, all following transformed indices are labeled with a t, otherwise the tetragonal defect free structure still refers to a r.

2. **Creating the SPS**
   For the supercell, the position of the twin boundary is now perpendicular to the $[5\,0\,1]^t$ direction (corresponding to $[0\,0\,1]^r$). A second supercell is created and inverted with respect to the twin boundary. A subsequent superimposition of the supercell with its inverse supercell leads to the formation of a SPS, cf. Figure 3.5b.

3. **Separation and Shift**
   The number of atoms of the SPS has been reduced in order to achieve a unit cell containing two distinct single domain structures separated by a line of distorted octahedra, cf. Figure 3.5c. The latter can be assigned to the CTB of SnO_2. The atomic distances of the boundary octahedra was adapted by shifting one of the single domain structures along the $[0\,1\,0]^r$ direction for 0.5 Å with respect to the other domain. These octahedra are connected by common edges.

As the twin boundary became an incorporated feature of the newly established unit cell, this also enables the simulation of multiple twinning. By combining slightly modified cells from step 1 and 3 a large variety of three dimensional defect structures can be produced straightforward. Moreover, the presented unit cells and the corresponding transformation matrices can also be used as base for other rutile-type structures which contain the same $\{1\,0\,1\}^r$ twin plane.

Defect Structure: Edge-On View

For the verification of the defect model experimentally obtained TEM data and corresponding simulations were compared. First, experimental PED patterns for two distinct viewing directions $[0\,1\,0]^r$ and $[1\,1\,1]^r$ were analyzed. In both cases, twin related superposition effects were observed, cf. marks in the left sided pattern of Figure 3.6. The white marked reflections correspond to the $\{1\,0\,1\}^r$ planes and denote the mirror plane within both PED patterns. These reflections can be determined as common anchor points of the mirrored single domain structures (blue, red marks in Figure 3.6). In order to obtain simulated ED patterns along these zone axes, the SPS (see Figure 3.5b) was used. The corresponding zone axis for the simulation can be found by multiplying the transformation matrix Q (see step 1) to the column vector of the desired zone axis, i. e. $[0\,1\,0]^r$ is transferred into $[0\,1\,0]^t$ and $[1\,1\,1]^r$ into $[1\,1\,0]^t$. An initial comparison of the correlated experimental and simulated PED showed a convincing agreement. For a more substantial and critical assessment detailed investigations of the reflections rows parallel to the $[0\,1\text{-}1]^{*r}$ were carried out. In Figure 3.7 profile measurements of these respective rows are depicted for both viewing directions.

The straight red lines represent the experiment and the dashed black lines the simulated data. According to the high coincidence of associated peaks within the diagrams, the symmetry of the experiment can be expressed convincingly by the defect model. Further appearing reflections in the experimental PED pattern of Figure 3.6a can be considered as artifacts, which represent contributions from other grain or debris. A seemingly contradiction arises from the comparison of the intensities as slight deviations of experiment and simulation are present. This difference can be explained by considering the investigated volumes of the twin domains. For the simulation a kinematic model was applied where the occupancy factor for all atoms were set to the same value. Thus, the unit cell from step 3 includes a twin domain ratio of 1:1. The experimental observation of such an idealized case may be highly improbable, in particular, considering the grinding TEM preparation. Nevertheless, a better matching of the intensities can be achieved by varying the occupancy factor for the atoms within the defect model. An in-depth discussion of this topic is given in section 3.3.1 - *Interpretation of the High Resolution Texture*.

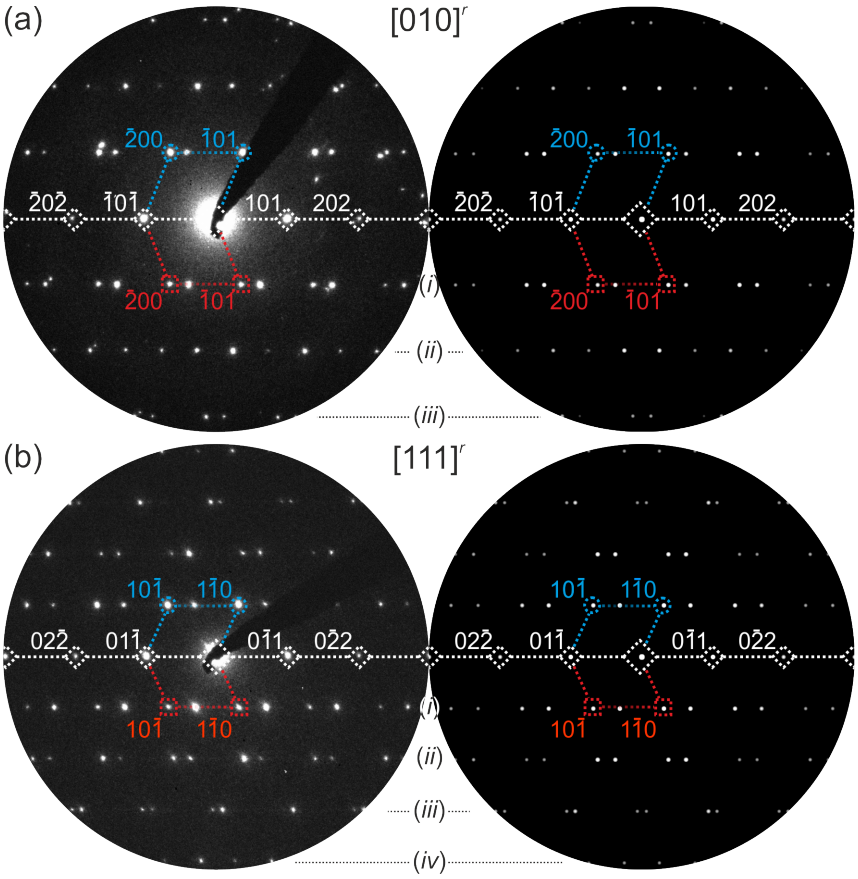

Figure 3.6: Comparision of (left) experimentally obtained PED patterns with (right) simulated PED patterns of SnO_2 with a CTB containing area. Zone axes: (a) $[0\,1\,0]^r$, (b)$[1\,1\,1]^r$. Dashed white line: mirror plane introduced from the defect structure. White squares: common reflections of the rutile single domains. Blue, red marks: respective rutile single domain patterns.

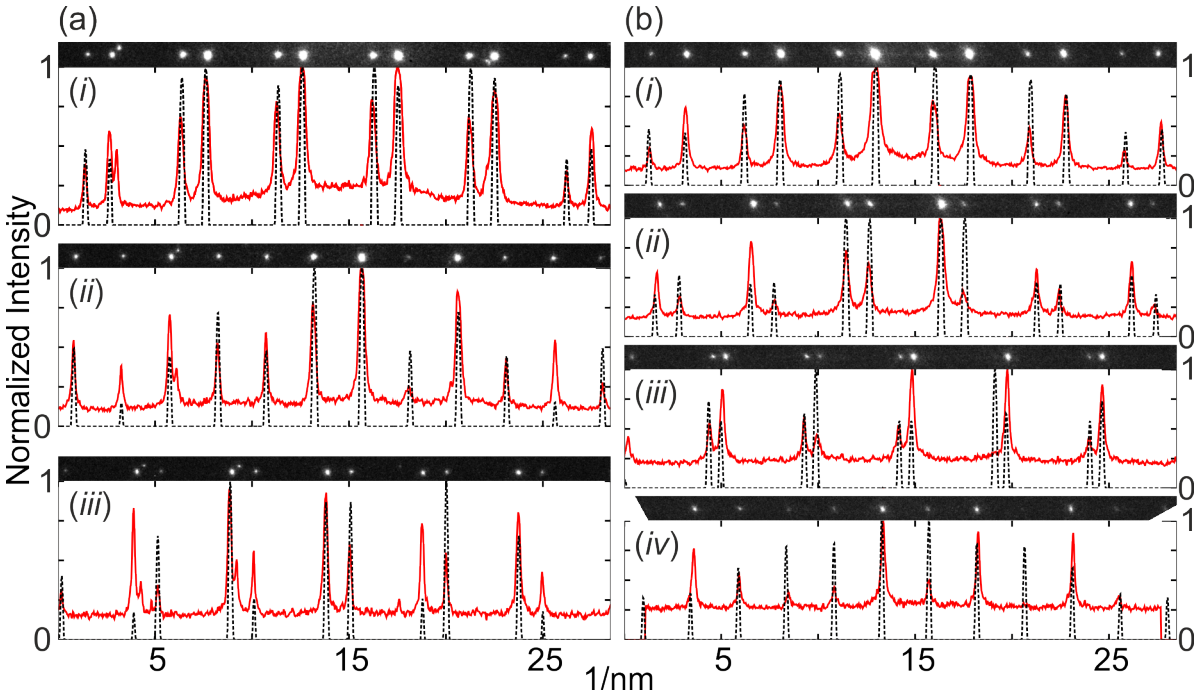

Figure 3.7: Enlarged view and profile measurements of the reflections rows parallel to the [0 1 -1]* direction from Figure 3.6. (a) $[0\,1\,0]^r$, (b) $[1\,1\,1]^r$. The redline represent the experimental data, and the black dashed line simulated data.

The analysis of the HRTEM contrast of the CTB was performed by applying a multi-slice formalism to the separation model from step 3. With this unit cell simulations were prepared for the viewing directions along $[0\,1\,0]^r$ and $[1\,1\,1]^r$ in accordance with the experimentally recorded micrographs. The latter were additionally filtered leading to an improvement of the present contrast and compared with simulations which were placed as insets, see Figure 3.8.

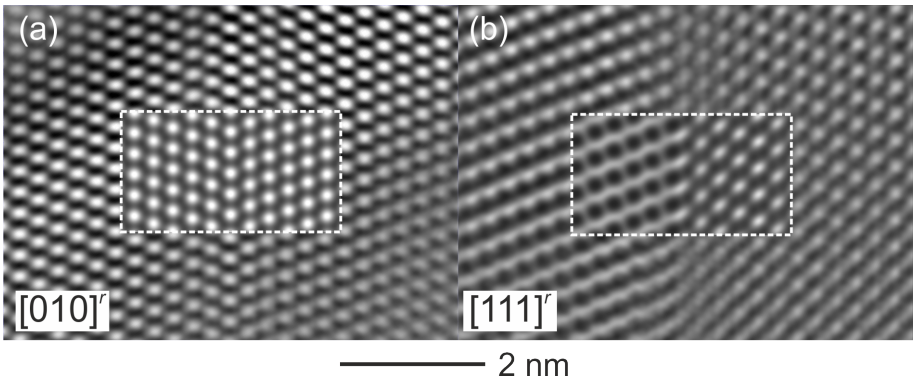

Figure 3.8: Experimentally obtained and filtered HRTEM micrographs of the CTB along (a) $[0\,1\,0]^r$ and (b) $[1\,1\,1]^r$. Insets: simulated micrographs of the defect structure with the parameters (a) $\Delta f = 0$ nm, t = 4.73 nm and (b) Δf = -52 nm, t = 4.45 nm.

In this case, an excellent agreement between experiment and simulation was achieved by using the parameters for the objective lens defocus $\Delta f = 0$ nm and specimen thickness t = 4.73 nm (Figure 3.8a) and Δf = -52 nm and t = 4.45 nm for (Figure 3.8b), respectively. Particularly, the strong change in contrast at the twin interface in Figure 3.8b is noticeable. This variation originates from an oblique viewing direction to the CTB.

Defect Structure: Superposition View

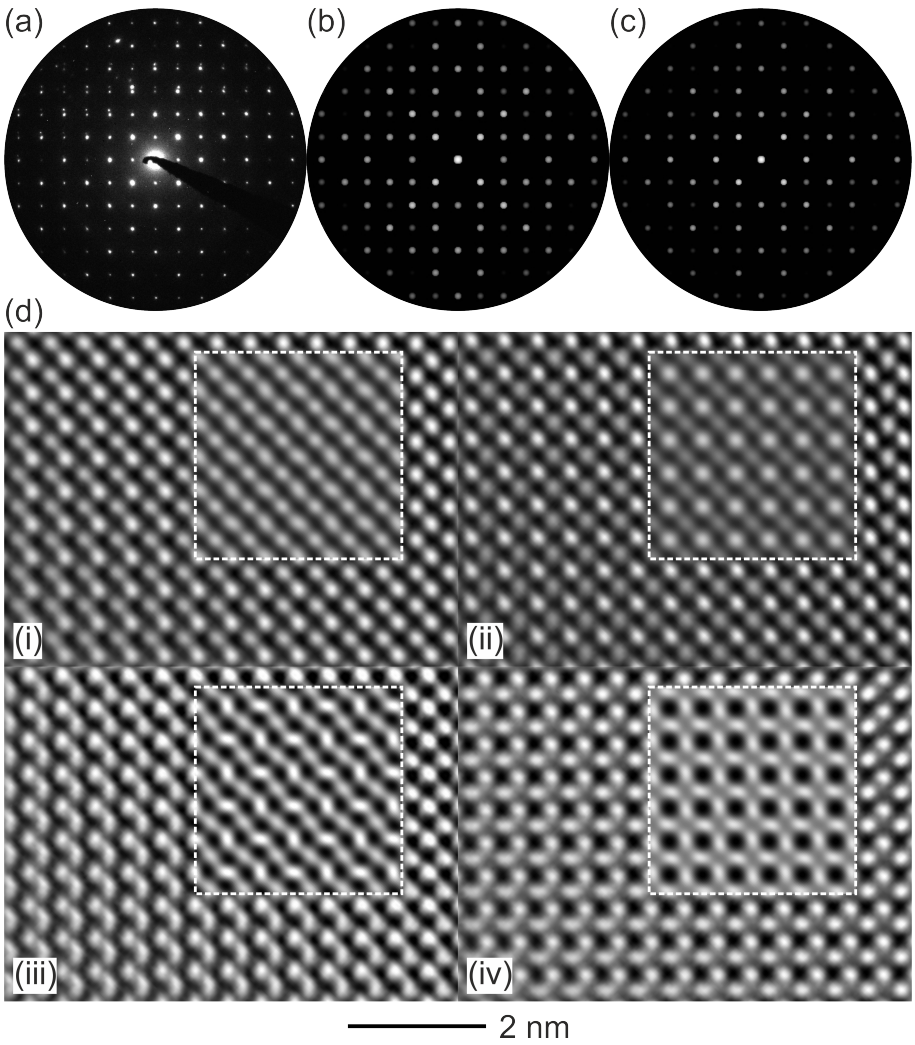

Figure 3.9: Electron diffraction patterns of SnO_2 along the $[0\,0\,1]^r$ zone axis. (a) Experimentally obtained PED pattern, (b) simulated pattern based on the rutile-type structure, (c) simulated pattern based on the defect structure of step 2. (d) HRTEM defocus series of a superposition structure caused by the CTB along the $[0\,0\,1]^r$ direction. Insets: Simulations based on the defect model of step 3. The specimen thickness for all simulated micrographs was set to t = 5.73 nm, the objective lens defocus Δf is for (i) 0 nm, (ii) −5 nm, (iii) −60 nm, (iv) −95 nm.

An experimentally obtained PED pattern was recorded along the $[0\,0\,1]^r$ viewing direction as depicted in Figure 3.9a. According to simulated patterns based on a rutile type (Figure 3.9b) and the defect model (Figure 3.9c), a clear distinction between single domain and defect structure is not possible. A defocus series performed within the HRTEM studies exhibited only convincing agreement with the high resolution contrast simulations of the defect model as demonstrated in Figure 3.9d. A comparison of simulated defocus series for both models is provided in Figure 3.10 demonstrating the considerable differences in the high resolution contrast of the rutile model to the defect model and thus to the experimental findings.

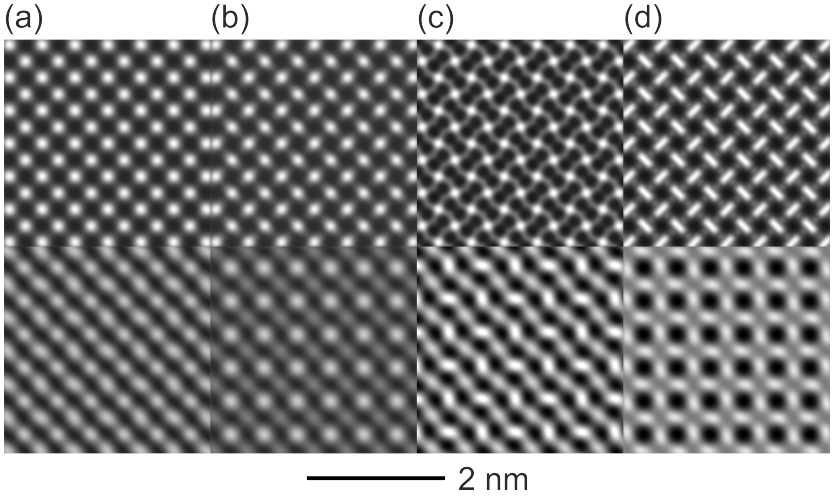

Figure 3.10: Simulated high resolution defocus series along the zone axis $[0\,0\,1]^r$ for the rutile-type structure (top) and the defect model (bottom). The specimen thickness t = 5.73 nm, the objective lens defocus Δf is for (a) −0 nm, (b) −5 nm, (c) −60 nm, (d) −95 nm.

Evaluation of the Distorted Octahedrons

Due to these results, a superposition of two single domains was found confirming the quality and reliability of the applied separation model from step 3. Therefore, this model becomes feasible for the determination of the degree of distortion within the rutile-type octahedrons directly at the CTB. Following from a comparison of defect-free octahedron with a distored one (see Figure 3.11) an distortion is present for the atomic distances up to ca. 15%. It must be noted, that the limited resolution of the used experimental methods prevents are more detailed study. Aberration corrected TEM would enable more precise information of the structural nature at the CTB and support a possible adjustment of the separation model. However, simulations with different shift vectors indicated already that only small variations to the used vector lead also to reasonable structures and atomic distances. Hence, such an additional experimentally effort seemed not to be justified.

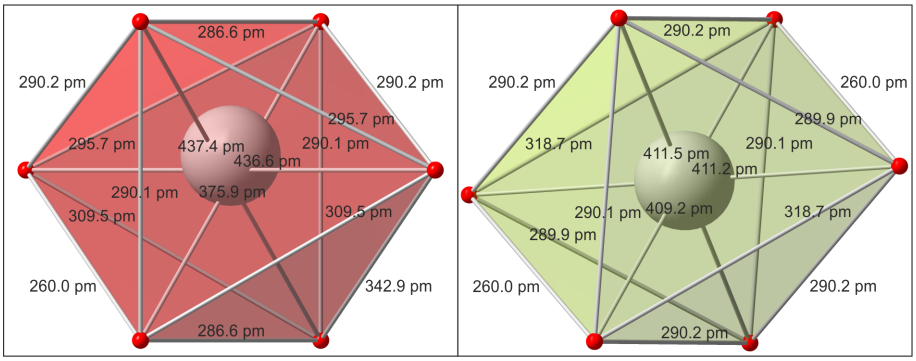

Figure 3.11: (a) Distorted octahedron at the CTB vs. (b) distortion-free octahedron from the bulk of SnO_2. The atom label follow Figure 3.5.

3.3 Zinc Oxide

In the framework of the FTS zinc oxide (ZnO) was produced in different morphologies. By introducing first the basic characteristics for ZnO, the main features for two distinct 1D-FTS structures will be discussed for this material.

The Polar Axis of Zinc Oxide

The semiconductor ZnO (space group: $P6_3mc$) shows useful piezoelectric properties when comparing the respective piezoelectric tensors and tensor components of different wurtzite-type (for the rest of the section labelled by 'w') structures [66, 67, 68, 69, 70]. The latter is a non-centrosymmetric polar structure and it is set up by coordination tetrahedrons stacked along the $[0\,0\,0\,1]^w$ polar axis. Depending on the central atom (in this case Zn or O) the respective tetrahedrons are oriented inversely. Provoking a displacement of the center atom by an external stress along the polar axis, a dipole moment is created. The sum over all dipole moments within the system leads to a macroscopic piezoelectric effect. For ME composites the growth of anisotropic one-dimensional (1D) nanostructures seems to be very promising [53, 51], as single crystalline columns grown along the $[0\,0\,0\,1]^w$ direction exhibit the highest piezoelectric voltages under plastic deformation for such systems [71]. Investigations on conventional VLS processes proved the capability of precise and well defined crystal-growth control of 1D structures [72, 73, 74]. A discussion on the VLS procedure and the FTS is provided in section 3.3.2 - *Investigations on a 1-1 ME Demonstrator System* in the scope of ZnO nanostructures relevant for 1-1 ME sensors.

Twin Boundaries in ZnO

A considerable influence to the properties of a material is provided by induced defects such as twin boundaries. The latter can lead to a short-circuit of the piezoelectric effect (e. g. in sputter-deposited ZnO [75]), demanding an ideal growth for ME sensor applications. However, in many instances the presence of defects and their deliberate control creates new capabilities for applications, such as gas sensors. In this particular case the absence of piezoelectric voltages is a necessary prerequisite [76, 77, 78]. With close structure-property relations, systematic approaches for nanoscale characterization serves as first step of optimization and understanding of the material. Several studies on ZnO and related wurtzite-type structures already demonstraded this requirement [79, 80, 81, 82]. For instances, in 1D structures the twin boundaries of $(0\,1\,\bar{1}\,\mathrm{n})$ (n = 1-4) and $(\bar{2}\,1\,1\,2)$ were a commonly observed feature and theoretically descriped.

3.3.1 Sea-Urchin Type Structures: Superposition Twinning Supported by Texture in ZnO Nanospikes

Nanostructures similar to the ZnO sea-urchin nanospikes were first characterized by Huang et al. [83, 84] demonstrating twin boundaries at $(2\,\bar{1}\,\bar{1}\,1)^w$. In the next section investigations on scattering and contrast effects produced by such superposition twinning were performed using a quantitative crystal design which includes all relevant morphology and real structural features.

Nanospike Morphology and Resulting TEM Features

The morphology of an as-prepared ZnO sea-urchin structure can be seen in the SEM micrograph[6] of Figure 3.12a. The structure consists of a sphere-like center particle covered with nanospikes. The latter exhibit an anisotropic shape as triangular flat rods with a marginal thickness and a decreasing width with typically dimensions along the nanospike from below 1 μm at the bottom to several nanometers at the tip. Chemical impurities within the ZnO nanospikes were excluded by performing EDX in SEM and TEM mode.

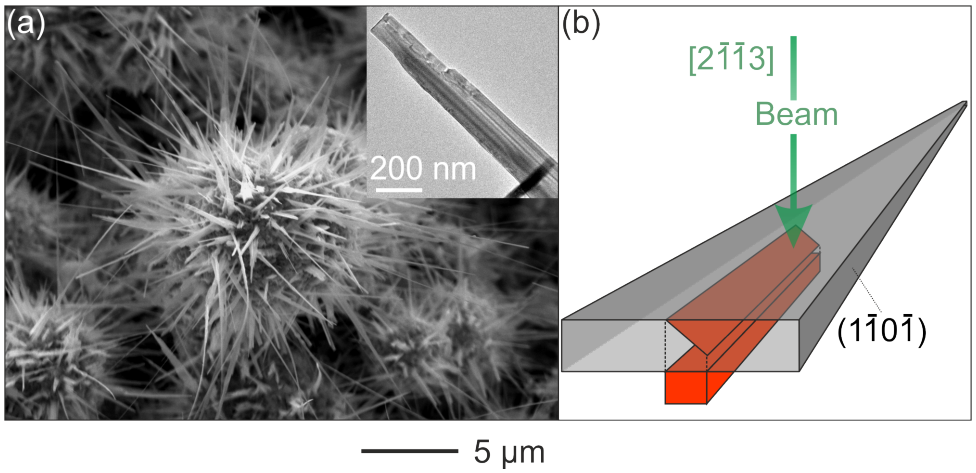

Figure 3.12: (a) SEM micrograph of a ZnO sea-urchin shape with sphere-spike structure. Inset: TEM bright-field image of nanospike tip. (b) Schematic representation of the geometry and the key features of single nanospike. A nanospike consists of separated majority and minority (red) domains connected via the twin boundary $(2\,\bar{1}\,\bar{1}\,1)^w$ (shown as red plane in a schematically manner).

Subsequent TEM investigations revealed that the edges of the nanospikes‘ long axes were always parallel to $(1\,\bar{1}\,0\,\bar{1})^w$ planes. As a consequence of the anisotropic crystal morphology, a preferred viewing direction was found for all investigated nanospikes along the $[2\,\bar{1}\,\bar{1}\,3]^w$ zone axis when dispersed on TEM grids [83, 52], see sketch Figure 3.12b (further explanation of the sketch see below in section 3.3.1).
A representative TEM bright field image of the nanospike is shown in Figure 3.13a.

[6]SEM was performed by Yogendra Kumar Mishra

As common observation for all examined nanospikes, the crystals seems to be subdivided into two major parts with a sharp boundary parallel to the long axis of the nanospike, as marked by white arrows in Figure 3.13a. A HRTEM micrograph was recorded next to the the transition of the two areas, exhibiting a highly crystalline structure for the entire tip region, cf. 3.13b. Two types of contrast phenomena are observable on both sides of the boundary: region (i) shows a periodic arrangement of bright spots. This contrast can be assigned to a single domain wurtzite-type structure of ZnO as simulated micrographs for the zone axis $[2\,\bar{1}\,\bar{1}\,3]^w$, Δf$\approx$-70 nm and a specimen thickness of 6.75 nm confirmed. In region (ii), a spot pattern is visible with additionally fringes propagating parallel to the boundary and the $(1\,\bar{1}\,0\,\bar{1})^w$ planes. A fringe spacing of ca. 1 nm was determined. To provide a better understanding of the both contrast features, FFT patterns were calculated for the respective regions. While the FFT pattern of region (i) verifies the expected wurtzite-type ZnO structure, additional reflections appear in the FFT of region (ii). These reflections are consistent with the assumption of a superposition of two single domains with a mirror plane parallel or perpendicular to $(1\,\bar{1}\,0\,\bar{1})^w$, cf. marks in Figure 3.13c-i and c-ii. A similar description of the assumed superposition was given by [83], where two single domain patterns are rotated around the common zone axis $[2\,\bar{1}\,\bar{1}\,3]^w$ by an angle of 52.188°.

In the FFT pattern of region (ii) a third group of intensities can be seen, which cannot be assigned to the fundamental intensities of the wurtzite-type domains. Such phenomena originate from superposition related multiple scattering and appear in FFT and electron diffraction patterns as high intensity reflections close to the fundamental ones. In the following this type of reflections is labeled by 'satellite reflections'. The influence of the satellites to the real structure contrast can be emphasized by applying Bragg filtering on the FFT of a respective selected area and recalculate the HRTEM contrast. A series of differently filtered micrographs is demonstrated in Figure 3.14 for region (ii) of Figure 3.13. As reference the unfiltered region is depicted in Figure 3.14a with the combined features of bright spots and fringes. The Bragg filter was applied separately on the fundamental (Figure 3.14b) and satellites reflections (Figure 3.14c). The filtered micrograph of Figure 3.14b exhibit a considerable suppression of the fringes, while in the micrograph of Figure 3.14c the reversed effect is pronounced with dominant fringes. Apparently, the satellites contribute to the real structure contrast as lamellar fringes.

Rationalization of the TEM Contrast by a Simplified Model

The scheme in Figure 3.15 illustrated the connection of the morphology from the ZnO nanospike tip with the superposition contrast of a typical HRTEM micrograph. As the experimental data validated, the preferred viewing direction for the model and therefore for each twin component is given by $[2\,\bar{1}\,\bar{1}\,3]^w$. Two single domain wurtzite micrographs, systematically rotated by 52.188°, represent the layers perpendicular to the preferred viewing direction. A domain boundary exists at $(2\,\bar{1}\,\bar{1}\,1)^w$ [84] and propagates nearly parallel to the growth direction of the nanospike, cf. red plane in

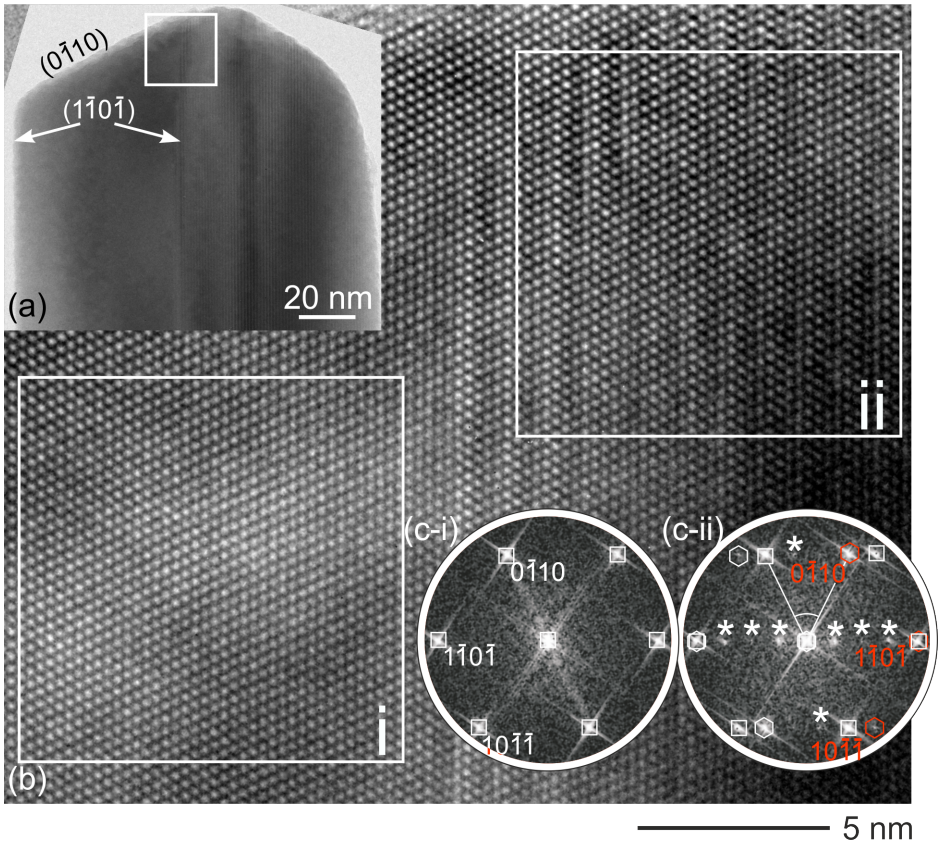

Figure 3.13: TEM observations of a ZnO nanospike tip with two separated regions: simple spot pattern (region (i)) and additionally lamellar fringes (region (ii)). (a) Bright field image, (b) HRTEM micrograph recorded from the marked area of (a). (c) Comparison of the calculated FFT patterns from region (i) ad (ii). The marked intensities can be subdivided into three groups: two wurtzite-type single domains (squares, hexagons) with the square marked intensities as part of the majority component. The intensities marked with asterisks are induced by multiple scattering resulting from superpositioning and will be called 'satellite' reflections. The indexing is performed comparing experimental with literature values [85] for the interplanar spacings [nm]: $1\,\bar{1}\,0\,\bar{1}$ (0.248/0.24755), $1\,0\,\bar{1}\,\bar{1}$ (0.248/0.24755), $0\,1\,\bar{1}\,0$ (0.286/0.2814).

Figure 3.15. Using the calculation rules for hexagonal lattice systems given by Otte and Crocker [86], the angle of opening between the viewing direction ($[2\,\bar{1}\,\bar{1}\,3]^w$) and the plane normal of the domain boundary results in 47.5°. This angle serves as the origin for the superposition of the domains along the preferred viewing direction and, thus, for the characteristic fringe contrast, see the lamellar fringes in Figure 3.15 [83, 84, 87].

This specific morphology leads also to the presence of fringes at least in selected areas of the recorded HRTEM micrographs. However, in the model of Figure 3.15 two equivalent domains are assumed. According to such a domain structure, three distinct (two mirrored single domain and the fringe) contrasts must be present for an ideal nanospike. Experimental observations never showed mirrored orientations

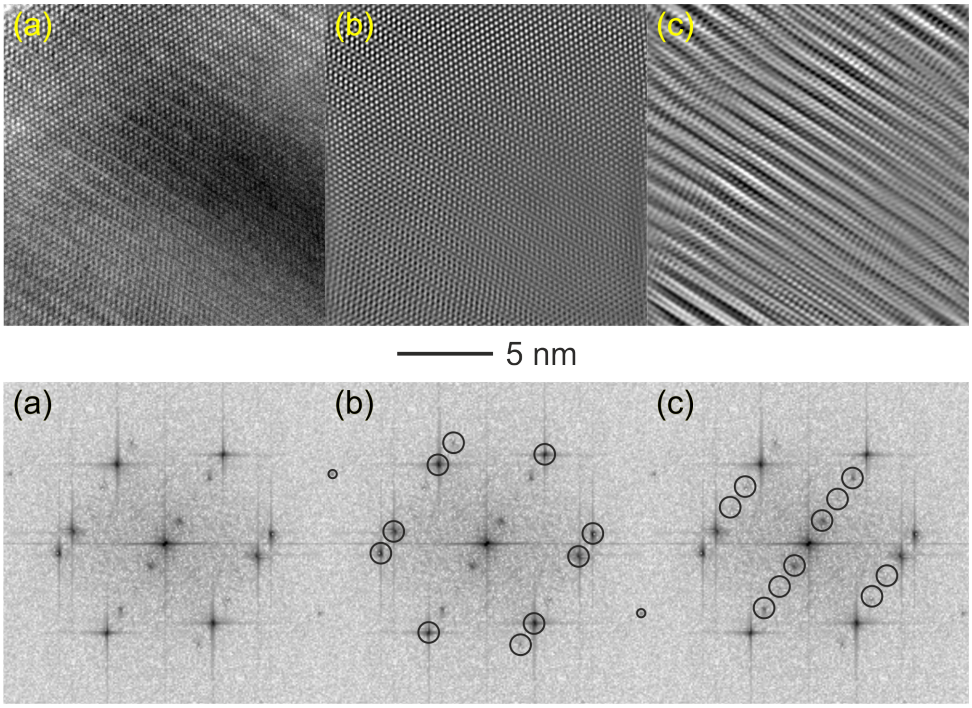

Figure 3.14: Influence of superposition to the high resolution contrast shown for an experimentally obtained HRTEM micrograph with associated FFT pattern of the twinned region (ii). (a) Unprocessed micrograph. Bragg filter applied on (b) the fundamental intensities of the two wurtzite-type domains and (c) on the satellite intensities, respectively.

of the single domains in a plane-view of the same nanospike. In all findings only one single domain was seen in accompany with a superposition contrast. This reproduced result indicates that the model of Figure 3.15 is strongly idealized and that one of the domains form a majority component with an attached minority component at the top/bottom surface having marginal volume fraction and irregular shape, cf. sketch in Figure 3.12b. Otherwise, two domains, similar in size and volume, must show mirrored contrasts according to the single domains at the opposite edges of the same nanospike.
The fringe contrast is a pure projection effect of the combination of superposition and viewing direction. With wide angle tilting experiments an edge-on view onto the domain boundary and thus the twin boundary (cross-section view) would lead to an absence of the fringes. However, such tilting experiments become complicated due to a significant thickness increase of the specimen in the course of tilting. Another problem arises from the applied microscope. The tilt angle of 47.5° exceeded the maximum of 30° for the used TEM as the limiting factor is the confined space between specimen holder and pole pieces. Possible solutions would be given by:

- Using a microscope and a specimen holder allowing a wide angle tilt.
- Different TEM cross section preparation techniques, e.g. by FIB or other dedicated techniques following [88, 89, 90, 91].

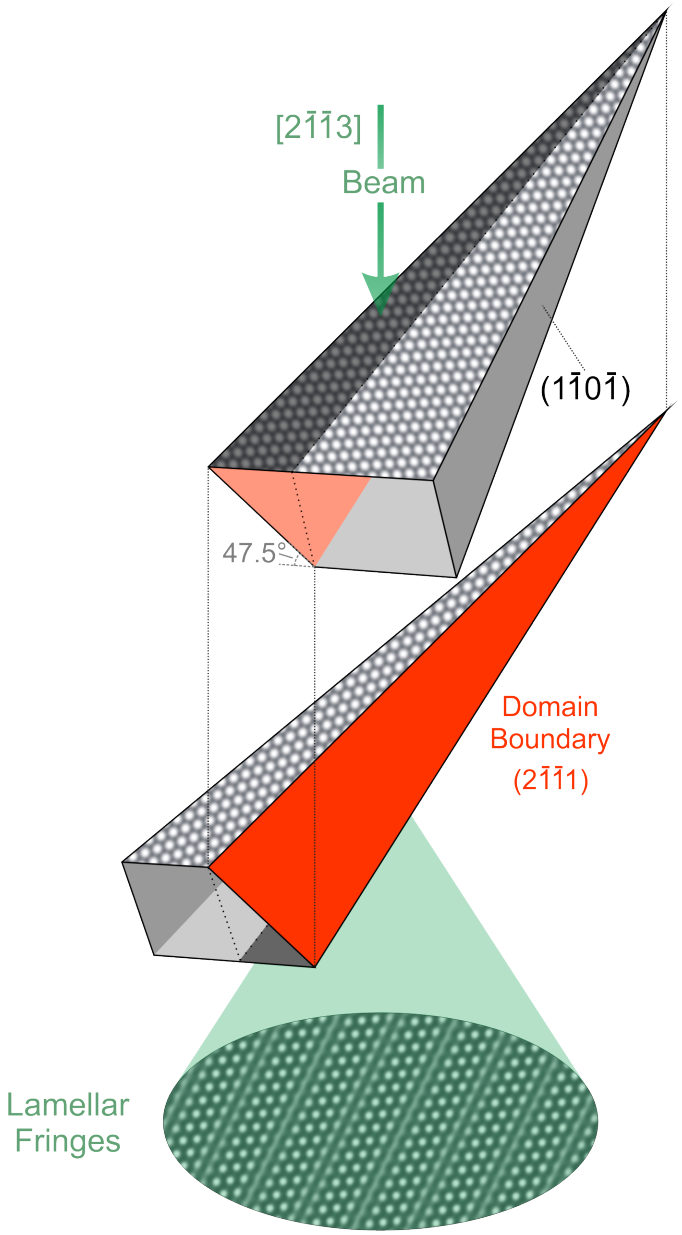

Figure 3.15: An idealized schematic model for the creation of fringe contrast by the superposition of twinned nanospikes (simulated micrographs for zone axis $[2\,\bar{1}\,\bar{1}\,3]^w$, thickness 3.68 nm, Δf = -70 nm). The domain boundary $(2\,\bar{1}\,\bar{1}\,1)^w$ is nearly parallel to the growth direction and is tilted with respect to the viewing direction by 47.5°, resulting in lamellar fringe contrast due to superposition. (Taken from Hrkac et al. [52])

Possible drawbacks for those solutions are that typically the TEM equipment cannot be replaced easily. Moreover, trials with FIB point to considerable experimental problems interrelated with charging and therefore bending and damaging of the nanospikes. It is worth to remind that TEM specimen preparation can be a time consuming issue, which increases the attractiveness of additional solutions for interpretation of already available data. In the subsequent discussion an adapted

supercell/SPS approach shall be discussed in order to rationalize quantitatively the lamellar fringes seen in HRTEM micrographs.

Setup of a SPS Model for an Indirect View to a Defect System

The following construction scheme of the supercell and the SPS differs from the more conventional edge-on view presented in section 3.2 for SnO_2. As the scope of the simulation is the computational visualization of the HRTEM texture and multiple scattering in electron diffraction, a separation step for the SPS becomes obsolete. Note, that this SPS is also a three dimensional model and could be used for the exposition of any arbitrary zone axis, where the separation may be considered.
Further, the complexity of finding the transformation conditions for the supercell increases (e. g. with respect to the SnO_2 model) according to the special specimen geometry and viewing direction. These factors determine decisively the model design, and in particular the metrics of the supercell. The construction of the supercell starts with the hexagonal unit cell of the wurtzite-type, but the metrics must be optimized for the implementation of the defect structure. As demand from the experiments, the preferred zone axis $[2\,\bar{1}\,\bar{1}\,3]^w$ must establish one principle axis. Following the supercell procedure, see section 3.2, the twin individuals are implemented in one common rectangular cell, which is again set into a triclinic ($P1$) space group, see section 3.2. For a successful HRTEM simulation all symmetry elements of the single domains have to be included as well as the experimentally identified twin element, i. e., the mirror plane $(1\,\bar{1}\,0\,\bar{1})^w$.
Despite the absent separation step, the supercell/SPS approach can still be divided into three steps. Thereby, the complex nanospike morphology necessitates an extensive setting procedure for the supercell, where two steps are distinct. The third step describes a common SPS generation. The description of the respective steps is excerpted from Hrkac et al. [52]:

1. "[**Presetting of a Suitable Starting Cell**
   The coincidence of main viewing direction $[2\,\bar{1}\,\bar{1}\,3]^w$ and a principle axis of the supercell is required. Therefore, the symmetry of the wurtzite-type structure is reduced in two steps from $P6_3mc$ to the t-subgroups $Cmc2_1$ (a, a+2b, c) and subsequently to Cc (a, b, c, $\beta = 90°$). This transformations adopt exactly the zone axis $[2\,\bar{1}\,\bar{1}\,3]^w$ as principle axis.

2. **Intermediate Cell and Supercell**
   By rotation of the Cc structure around $[2\,\bar{1}\,\bar{1}\,3]^w$, one of the principle faces of the supercell is aligned parallel to plane $(1\,\bar{1}\,0\,\bar{1})^w$. In this step a rectangular supercell is required for the realization of the third step. The larger the distortions from rectangularity, the larger will be the error in the atomic positions of the superposition structure. Thus, only slightest deviations (<<1°) are acceptable for the respective angles. In order to meet these criteria, a two-step transformation of the Cc structure was applied. Firstly, to an intermediate triclinic model (lattice parameters: a = 3.249 Å, b = 5.627 Å, c = 6.138 Å; $\alpha = 90°$,

$\beta = 121.96°$, $\gamma = 90°$) by applying the matrices P and Q, respectively (transformation conventions refer to Hahn, 2002),

$$\mathbf{P} = \begin{pmatrix} 25 & 0 & 7 \\ 0 & 1 & 0 \\ 0 & 0 & 1 \end{pmatrix}, \mathbf{P}^T = \begin{pmatrix} 25 & 0 & 1 \\ 0 & 1 & 0 \\ 7 & 0 & 1 \end{pmatrix}, \mathbf{Q}^T = \begin{pmatrix} 1/25 & 0 & 1 \\ 0 & 1 & 0 \\ -7/25 & 0 & 1 \end{pmatrix}$$

and secondly to the final triclinic and rectangular $P1$ supercell, cf. Figure 3.16a (lattice parameters: a = 76.74 Å, b = 156.7 Å, c = 6.138 Å; $\alpha = 90.01°$, $\beta = 90.02°$, $\gamma = 90°$) via

$$\mathrm{P} = \begin{pmatrix} 1 & 6 & 0 \\ 1 & -25 & 0 \\ 0 & 0 & 1 \end{pmatrix}, \mathrm{P}^T = \begin{pmatrix} 1 & 1 & 0 \\ 6 & -25 & 0 \\ 7 & 0 & 1 \end{pmatrix}, \mathrm{Q}^T = \begin{pmatrix} 25/31 & 1/31 & 0 \\ 6/31 & -1/31 & 0 \\ 0 & 0 & 1 \end{pmatrix}$$

3. **Creating the SPS**
   Maintaining rectangularity, the twinning can be introduced easily. The SPS is generated by adding the atomic coordinates of two structures, namely the one obtained in step 2 and the mirrored one by inversion of the y-parameter (i.e. applying a mirror plane at $(0\,1\,0)^{\mathrm{SPS}}$ as illustrated in Figure 3.16b). Thus, the number of atoms with respect to the triclinic supercell of Figure 3.16a is doubled resulting in a total number of 12000 atoms.]"

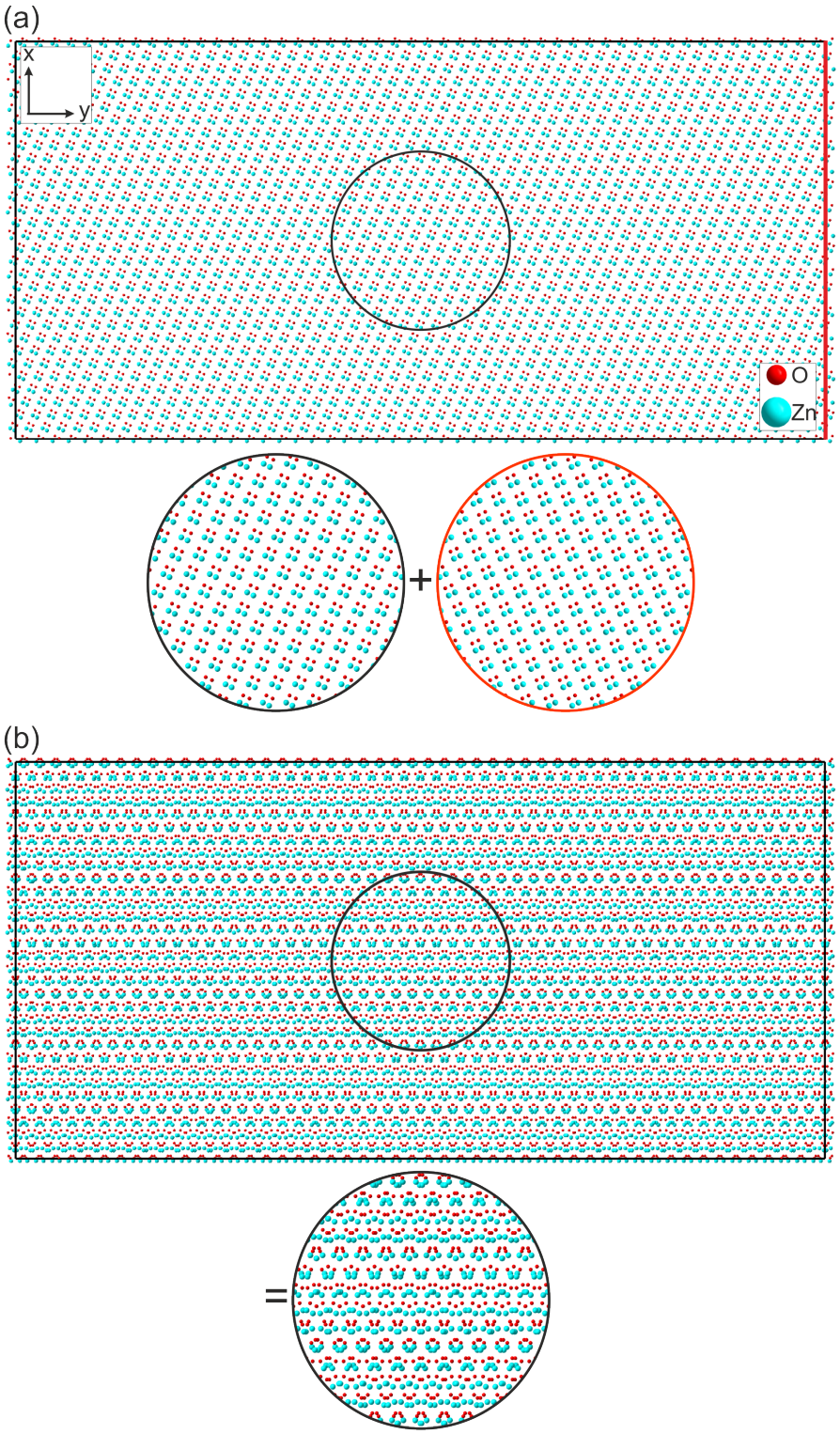

Figure 3.16: Supercell approach for the wurtzite-type ZnO nanospike along $[2\,\bar{1}\,\bar{1}\,3]^{w}$. (a) Supercell generated after transformation step (2). Red line marks the alignment of the $\{0\,1\,0\}^{\text{Supercell}}$ plane. (Bottom) Enlarged view on the supercell structure (black) and a correlated mirrored structure (red). (b) SPS generated after transformation step (3). (Bottom) Enlarged view of the atomic structure.

Identification of Dynamical Scattering in Diffraction Patterns

The modeled SPS allows not only the calculation of kinematic intensities for electron diffraction patterns but also the inclusion of multiple scattering phenomena. Thus, the direct interpretation of experimental PED patterns is improved. For this purpose, a series of simulated diffraction patterns with increasing specimen thickness is illustrated in Figure 3.17a, c, d and compared with an experimental PED pattern (Figure 3.17b).

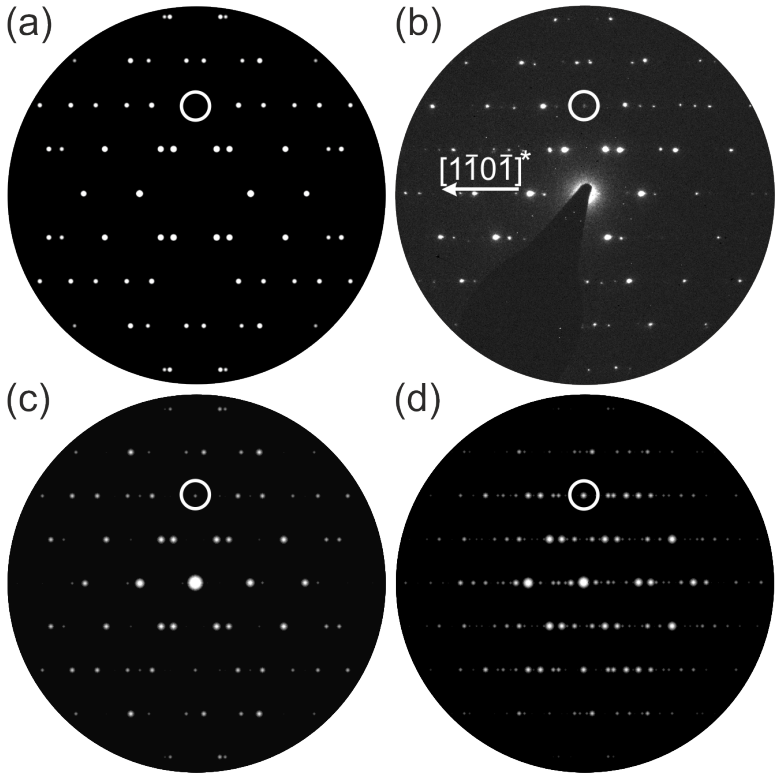

Figure 3.17: Experimental and simulated PED patterns for twinned ZnO along zone axis $[2\,\bar{1}\,\bar{1}\,3]^w$, using a twin component ratio of 1:1 for the simulations. (a) Kinematic simulation versus (b) experimental pattern. (c) and (d) Simulated PED patterns based on specimen thicknesses of (c) 2.46 nm and (d) 6.14 nm, illustrating multiple scattering effects by the occurrence of satellite reflections. (Taken from Hrkac et al. [52])

The specimen thickness in Figure 3.17a was reduced to a virtual value of 0 nm, which means a complete exclusion for multiple scattering phenomena. The resulting Bragg reflections and their corresponding intensities stem from a purely kinematical procedure. Consequently, the differences of the patterns from Figure 3.17a and 3.17b exhibit dynamical contributions in terms of additional reflections in the experimental data. In order to prove further this first identification a multi-slice algorithm was applied for a more explicit demonstration of the multiple scattering. Thereby, slight thickness increases of the specimen by 2.46 nm (Figure 3.17c) and 6.14 nm (Figure 3.17d) lead to an immediate appearance of the satellite reflections. This simulated excitation of dynamical intensities showed their strongest expression for

the marked satellite. Especially, the latter seems to be in good agreement with the experiment. However, the pattern of Figure 3.17d shows a remarkable number of additional reflections, particularly high order satellites, which are not present in the experiment. The best agreement with the experimental PED pattern is achieved with the simulated pattern of Figure 3.17c. Hence, the specimen thickness can be considered as low for the investigated area. This assumption is supported by the strong intensity of the primary beam (cf. 3.17b), which can only result from a high transmission of the electron beam through the specimen without large interaction of electrons with the matter.
It must be noted, that the recording of diffraction patterns at thicker areas did not exhibit a substantial number of high order satellites. Apparently, for the simulations another parameter was neglected. The second decisive parameter, despite the specimen thickness, is the twin component ratio and its variation. The influence of this parameter will be demonstrated and discussed in the next two sections. Also, the Bragg reflections exhibit a slightly incommensurability in some instances within the experimentally obtained PED pattern. This feature seems to be a result of the special morphology and the usage of PED (see section 3.3.1 - *Influence of a Tilted Domain Boundary to PED*). The simulations of the SPS are not showing this effect.

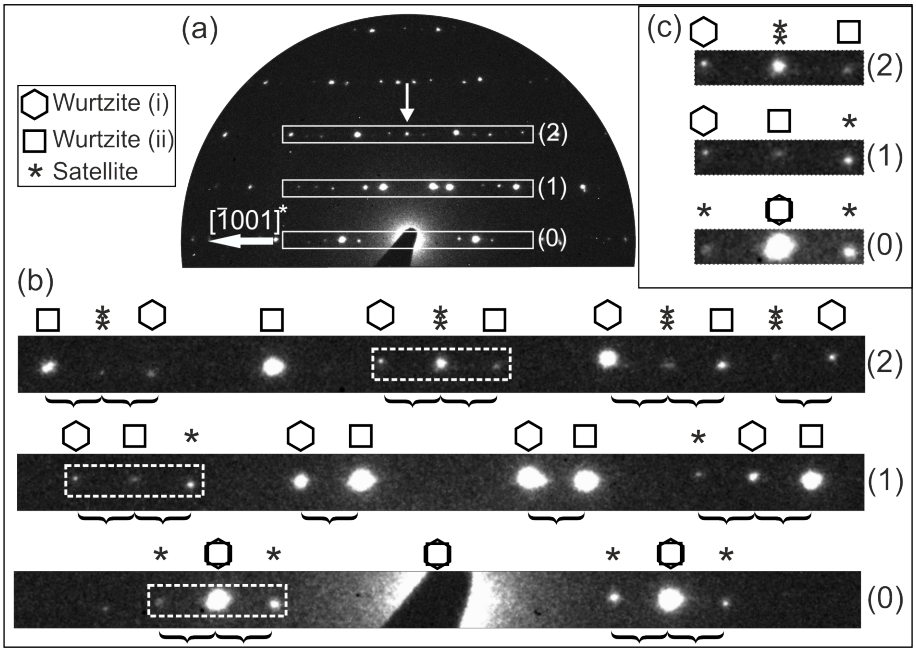

Figure 3.18: Experimental PED pattern of the twinned ZnO structure along the $[2\,\bar{1}\,\bar{1}\,3]^w$ zone axis. (b) Enlarged view of rows of reflections (0, 1 and 2) parallel to the $[1\,\bar{1}\,0\,\bar{1}]^*$ direction. Hexagons and squares denote reflections of each wurtzite domain, and asterisks denote the first-order satellites of the twin pattern. The repeat distance between reflections is marked with downward pointing brackets. (c) Reflection triplets (dashed boxes) of the respective rows, with variable origin. Satellites labelled with two asterisks are excited by two adjacent fundamental Bragg reflections. (Taken from Hrkac et al. [52])

Benefiting from the diffraction simulations, particularly from the included dynamical theory, a detailed classification of the reflections within the diffraction patterns is enabled. The experimental PED pattern from Figure 3.17b is chosen and "three systematic rows of reflections (0, 1, 2) parallel to $[1\,\bar{1}\,0\,\bar{1}]^*$ were investigated" [52], see Figure 3.18. Reflections marked with squares and hexagons (cf. Figure 3.18b) belong to two separated single domain ZnO structures and are respectively assembled in the pattern of zone axis $[2\,\bar{1}\,\bar{1}\,3]^w$. All those reflections can be regarded as kinematic contributions of the individual wurtzite components and are thus designated as main structure intensities. The peak-to-peak distance of those intensities show a repeating distance of ca. $4.12\,\mathrm{nm}^{-1}$ (see downward pointing brackets) for each domain. Additionally, the presence of first order satellite reflections (marked with asterisks) within all systematic rows can be confirmed. These satellites appear at distance of 1 $(\pm 0.1)\,\mathrm{nm}^{-1}$ with respect to main structure intensities. As noticeable feature, resulting from the superposition, reflections triplets are formed in each row, as illustrated in the enlarged sections in Figure 3.18c. The rows show a varying origin for the reflections. While in row 0 main structure intensities are coinciding, an increasing separation of such intensities is observed for row 1 and row 2. Also in this row coinciding first order satellites can be seen. In particular, the marked triplet in row 2 is a remarkable feature. On the one side the first order satellite reflection (marked with an arrow Figure 3.18a and top in Figure 3.18b) exhibit strong intensity, on the other side the adjacent main structure intensities are kinematical forbidden in their respective single domain structures. These reflections can be assigned to the $((1\,1\,\bar{2}\,\bar{1})^w$ and $(\bar{1}\,2\,\bar{1}\,1)^w)$ planes and violate the zonal reflection condition hh$2\bar{\mathrm{h}}$l: l = 2n according to the wurtzite-type structure. This in turn, can be the reason for the strong intensity of the satellite reflection as a dynamical contribution is provided from both main structure intensities to the same extent, see Figure 3.18c.

Interpretation of the High Resolution Texture

The variable 3D shape of the nanospike leads to different volume fractions of the superimposed single domains. Consequently, the resulting twin component ratio must follow an equivalent local variation. To investigate these ratios, a manipulation of the occupancy factors of each atom could be implemented in the SPS. All atoms of a respective individual domain have the same occupancy factor and the sum of the values for both domains is restricted to one.
How does this additional parameter influence the high resolution contrast? The twin component ratio can be considered as measure for the superposition texture. More precisely, all associated features, i. e., the characteristic stripe contrast, can be directly controlled by this parameter within the simulation. The variation of the twin component ratio and its influence to a HRTEM micrograph is exemplified in Figure 3.19 for a magnified area of the SPS (see sketch illustrated in Figure 3.19) along the zone axis $[2\,\bar{1}\,\bar{1}\,3]^w$). For the simulations two ratios were applied: A majority/minority case, which accounts the experimental observations with a ratio of 1:4, and a uniform 1:1 case for both domains. The simulations are presented in Figure

3.19b and 3.19c, respectively. "Assuming Scherzer focus conditions and the weak phase object approximation, the projected potential [(Figure 3.19b)] correlates with the HRTEM contrast, [cf. simulated micrographs depicted in Figure 3.19c]" [52]. Due to the use of the non-aberration corrected microscope (Philips CM 30 ST microscope) closely spaced atoms condense to one respective dark sport as a result of the resolution limitations ($d_{Scherzer}$ = 0.19 nm).
Focusing on the marked regions the strongest deviation between the two cases is explicitly accentuated, when the arrangement of dark spots switch from a rhomboidal to a rectangular shape. In order to understand this phenomenon, the projected potentials needs to be analyzed. For the 1:4 ratio, the majority component contributes much stronger to the potential (Figure 3.19b, top). Thus, the difference to a wurtzite single domain structure is marginal and the rhomboidal arrangement of dark spots from a single domain is preserved within the HRTEM contrast despite the superposition. Note, the main feature of the majority/minority HRTEM simulation is a repetitive slight variation of the intensities of the dark spots (Figure 3.19c, top), which forms the delimitation to the single domain HRTEM contrast. Changing the ratio to 1:1 (Figure 3.19b, bottom) the contrast exhibits a square arrangement for the dark spots, which can be related to the equalized contributions from both twin components to the projected potential (Figure 3.19c, bottom), see the marks in Figure 3.19.

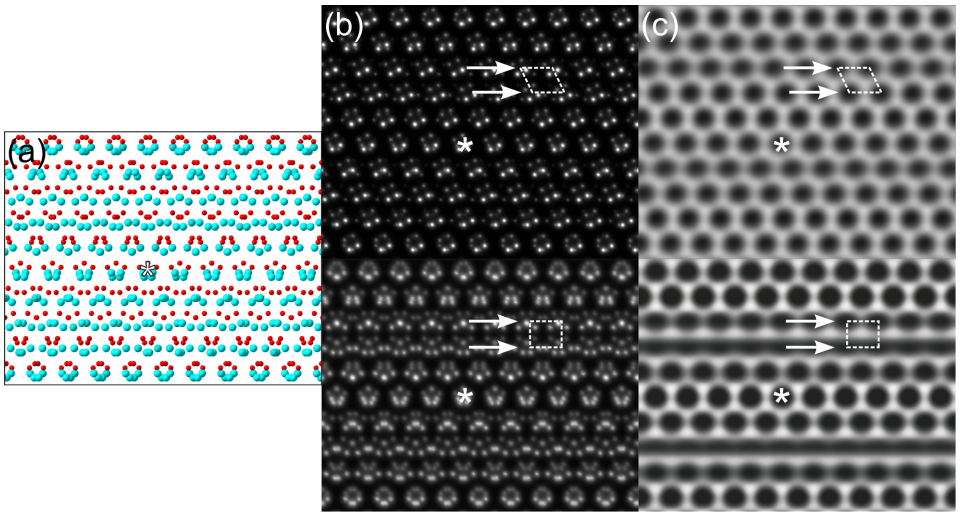

Figure 3.19: Simulation study on the influence of the twin component ratio to the high resolution contrast. (a) Cut-out of the atomic configuration of the SPS. (b and c) (Top) A 1:4 and (bottom) 1:1 ratio for the twin components compared for (b) the projected potential and (c) the resulting high-resolution contrast close to the Scherzer focus (Δf = -56 nm) for a thickness of 3.65 nm. The asterisks mark the same position within the respective images. (Partially excerpted from Hrkac et al. [52].

As descriped in the section 3.2, an additional shift of the two twin individuals relative to each other may cause additional contrast features [80, 92, 57, 54]. Nevertheless, a shift along the viewing direction (namely along z-direction) is irrelevant

as a projection of superpositioning is under investigation. An in-plane shift can be a reasonable parameter for changing HRTEM contrast. This kind of shift becomes negligible for the electron diffraction according to the translation invariance of the Fourier transform. The in-plane shift was investigated by changing separately "the x- and y-coordinates of one twin individual within the SPS" [52] and simulating the respective HRTEM contrast. Selected results are compared in Figure 3.20.

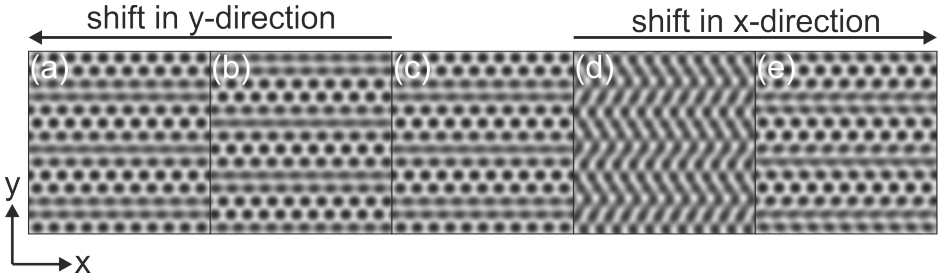

Figure 3.20: Series of simulated high resolution contrast for differently modified SPSs for Scherzer focus (Δf = -56 nm) and specimen thickness of 3.65 nm. In each case an additional shift vector was applied to one of the twin components with respect to other. Applied values to the atomic site fraction (a) y/b+0.1, (b) y/b+0.05, (c) unmodified structure, (d) x/a+0.05, (e) x/a+0.1.

In the course of changing the y-coordinates (i. e. shift parallel to the fringes), a shift of highly related HRTEM contrasts (Figure 3.20a, b, c) is observable along the y-direction. Possible slight structural changes can only be produced on such low atomic scale, that the spatial resolution limit ,given by the used microscope parameters, cannot discern these arrangements. Contrary to this findings, the influence of changed x-coordinates to the simulated HRTEM micrographs are significant, see Figure 3.20c, d, e. Finally, simulated and experimental HRTEM contrasts were compared with each other, as depicted in Figure 3.21.

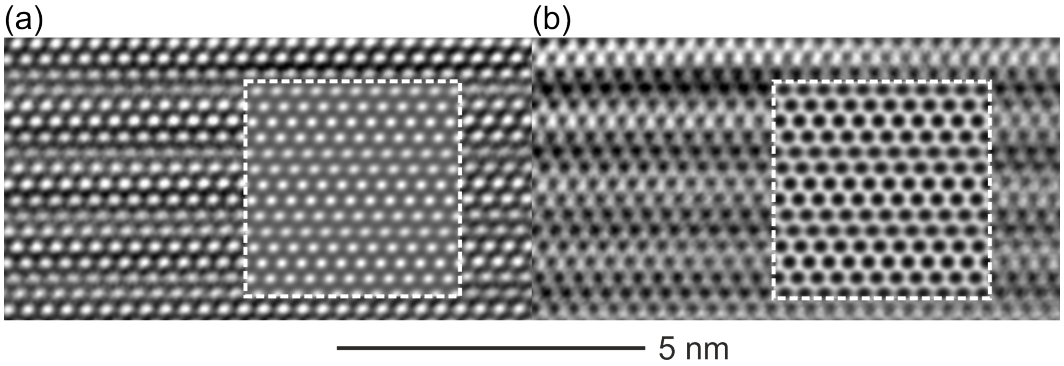

Figure 3.21: Experimentally obtained defocus series of a superposition region with (Bragg filtered) HRTEM micrographs recorded at (a) Δf = -80 nm and (b) Δf = -56 nm for a specimen thickness of 3.65 nm along the zone axis $[2\,\bar{1}\,\bar{1}\,3]^w$. Insets: Simulated HRTM micrographs.

The presented experimental micrographs were recorded at underfocus imaging conditions: Δf = -80 nm (Figure 3.21a) and Δf = -56 nm (close to Scherzer focus, Figure

8b). The different focus values cause a complementary black and white contrast during defocusing. By applying the Bragg filter an enhanced image and contrast quality is achieved simplifying the direct comparison with the simulations. A convincing agreement was obtained by excluding any (x/y)-shift and setting the twin component ratio to 1:4 for the demonstrated HRTEM micrographs, cf. insets in Figure 3.21. The results from the HRTEM contrast served as basis for a further investigation of the twin component ratio via FFTs. The experimentally obtained FFT pattern of region (ii) from Figure 3.13 was compared with FFT patterns calculated from circular areas of simulated HRTEM micrographs with respective twin ratios of 1:4 and 1:1, see (Figure 3.22). Apparently, the most prominent feature for the experimental pattern is reflected in the high asymmetry of the peak intensities. However, the symmetry of the peak intensities and thus a *mm*-symmetry for the pattern are mandatory for a 1:1 ratio, cf. Figure 3.22b. Introducing a considerable mismatch within the ratio (1:4), a comparable behavior within the structure of the simulations is generated and an increase in the quality of the experiment/simulation - consistency is obtained.

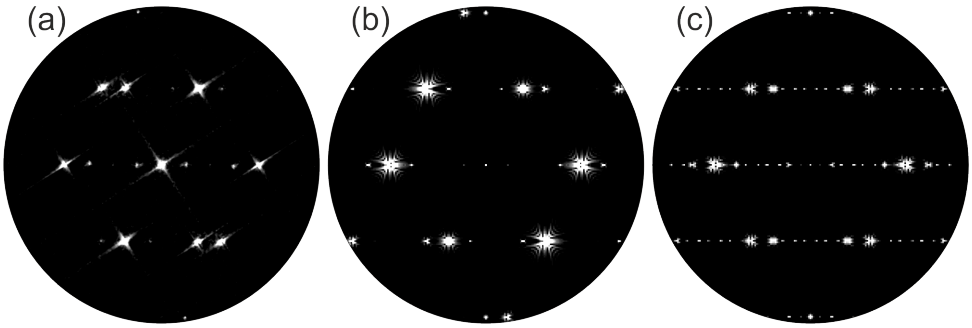

Figure 3.22: Comparison of an (a) experimentally obtained FFT pattern recorded on a superposition region (HRTEM micrograph: $\Delta f = -70$ nm | thickness: 6.75 nm) vs. simulated FFT pattern with a twin component ratio of (b) 1:4 and (c) 1:1 for the $[2\,\bar{1}\,\bar{1}\,3]^w$. (Partially excerpted from Hrkac et al. [52].

Influence of a Tilted Domain Boundary to PED

The special morphology of the ZnO nanospike is reflected in a remarkable effect for electron diffraction. A comparative study of PED and SAED was performed on the same boundary area, which shows a single domain and a superposition area of the twin individuals. The different methods exhibit dramatic intensity variations for multiple equivalent reflections, as demonstrated in Figure 3.23a and b. According to the intensity ratios of the simulated diffraction patterns (see Figure 3.23c and d), the SAED pattern can be assigned to a twin component ratio of 1:4 and the PED pattern to ratio of 1:1. Moreover, additionally satellite reflections with enhanced intensity are also displayed for the PED, confirming the agreement with the simulated pattern of Figure 3.23d.

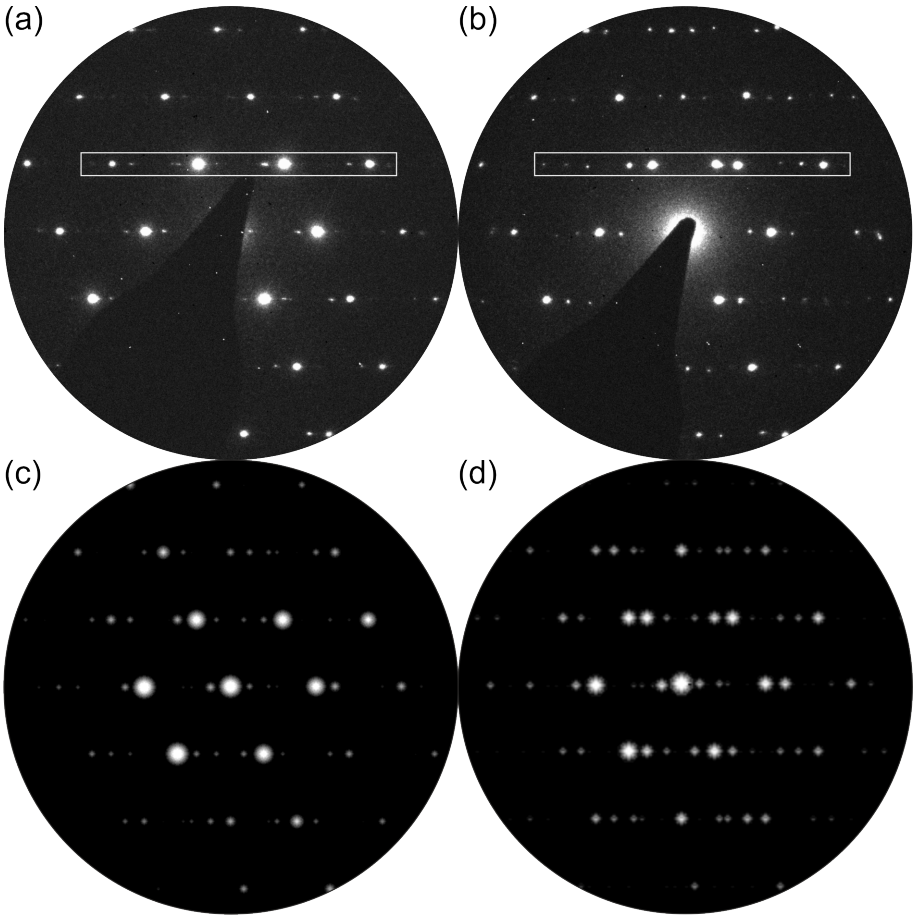

Figure 3.23: Influence of the nanospike geometry to the precession electron diffraction. Comparison of experimentally obtained (a) SAED vs. (b) PED pattern of the same area along $[2\,\bar{1}\,\bar{1}\,3]^w$. (c, d) Dynamical simulations of electron diffraction patterns for a twin component ratio of (c) 1:4 and (d) 1:1. A matching between the patterns of (a) and (c), as well as between (b) and (d) is observable. White boxes in (a) and (b) mark areas of further investigations depicted in Figure 3.24.

The difference in both investigations must originate from the increased kinematic contributions of the second twin component in the PED pattern. In a conventional case, a reduction of multiple scattering effects particular by superposition is expected in PED compared to the SAED mode, as described in section 2.1.1. Thus, only different transmitted crystal volumes can explain the two results.
In PED mode, the precession movement leads to an enhanced transmitted volume. Considering the observation direction ($[2\,\bar{1}\,\bar{1}\,3]^w$) and the position of the twin boundary the minor twin individual is consequently emphasized. Further, in the PED pattern incommensurable Bragg reflections can be detected as demonstraded in Figure 3.24. In the latter, marked rows of the experimentally obtained SAED and PED patterns of Figure 3.23 were extracted and compared with each other. Drawing a straight line, all Bragg reflections are intersected through the respective center in the case of the SAED pattern (Figure 3.24a). This behavior changes after applying the PED mode (Figure 3.24b). Apparently, the incommensurable Bragg reflections are an artifact produced due to the usage of PED.

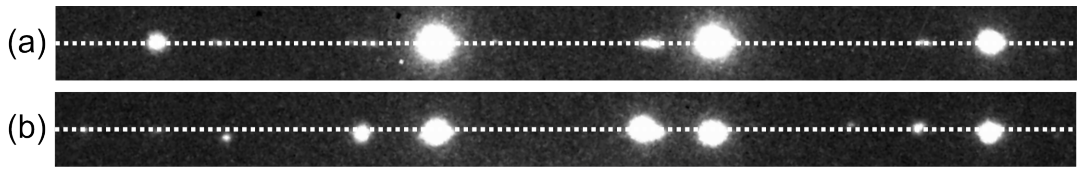

Figure 3.24: Comparison of the marked rows from the experimentally obtained diffraction patterns of Figure 3.23: (a) SAED, (b) PED. The white dashed lines emphasize the presence of incommensurable Bragg reflections after applying the PED mode.

3.3.2 Investigations on a 1-1 ME Demonstrator System

The motivation for 1-1 ME composites manifests in the possibility of producing bio-magnetic sensors without a clamping to a substrate as necessary for thin film technology. In this manner, an elastic deformation of the magnetostrictive phase is used exclusively for the deformation of the piezoelectric phase mediated by a strain interaction. Thus, an undesired reduction of the ME effect can be prevented. In order to constitute a 1-1 sensor setup, vertically free standing ZnO structures are grown anisotropically along $[0\,0\,0\,1]^w$ by VLS methods. Subsequently, isolated ZnO structures are coated with the magnetostrictive $Fe_{70.2}Co_{7.8}Si_{12}B_{10}$ (FeCoSiB). As discussed by Kaps et al. [53, 51] 1-1 composites are subject to several length restrictions in order to achieve an optimum in performance for biomagnetic sensing. Only mesoscale sensors provide sufficient electrical currents for highly accurate measurements and simultaneously avoiding disturbance by shear losses of mechanical coupling.

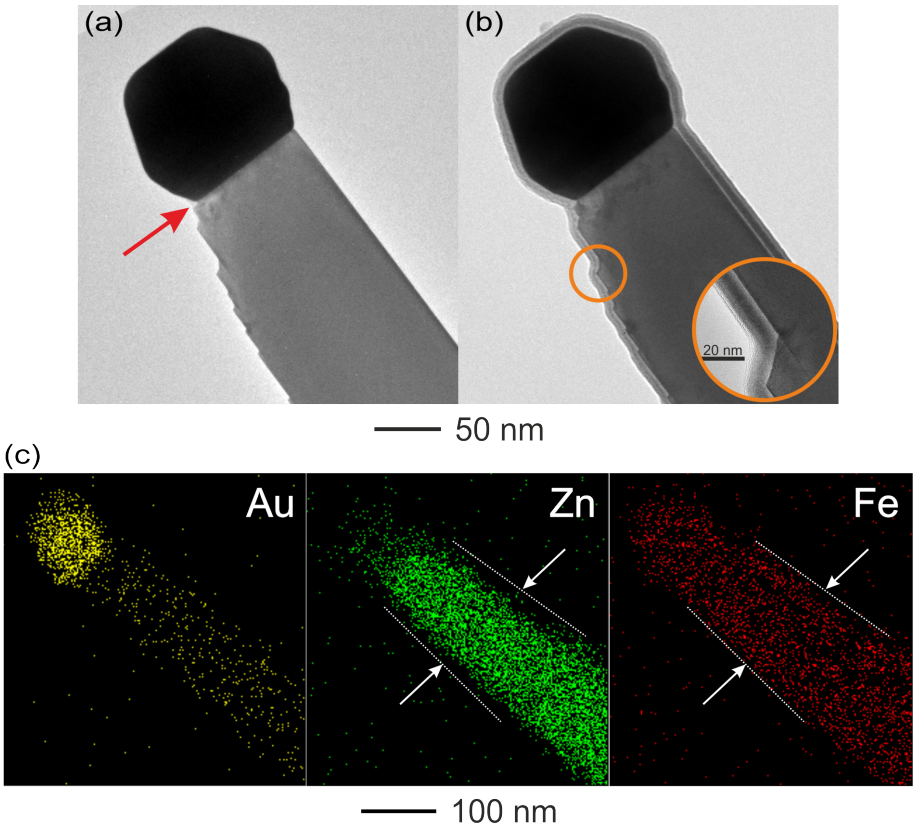

Figure 3.25: ZnO nanosail tip grown by conventional VLS with Au as growth catalyst: TEM bright field image (a) before and (b) after the deposition of FeCoSiB. The red arrow marks the position of a HRTEM observation (presented in Figure 3.26). Inset in (b): magnified view of the additional FeCoSiB layer. (c) Chemical investigations (EDX) after the deposition. The nanosail is uniformly covered by the FeCoSiB layer, represented by Fe. The white arrows show the spatial dimensions of the FeCoSiB layers.

Another factor for a high ME effect is the crytallinity of ZnO and the consistency of the common interface with amorphous FeCoSiB. To study these structural aspects a demonstrator system was fabricated using a conventional VLS process. The latter requires gold (Au) nanoparticles as catalyst for a sufficient growth of 1D ZnO nanostructures [93], see Figure 3.25a.

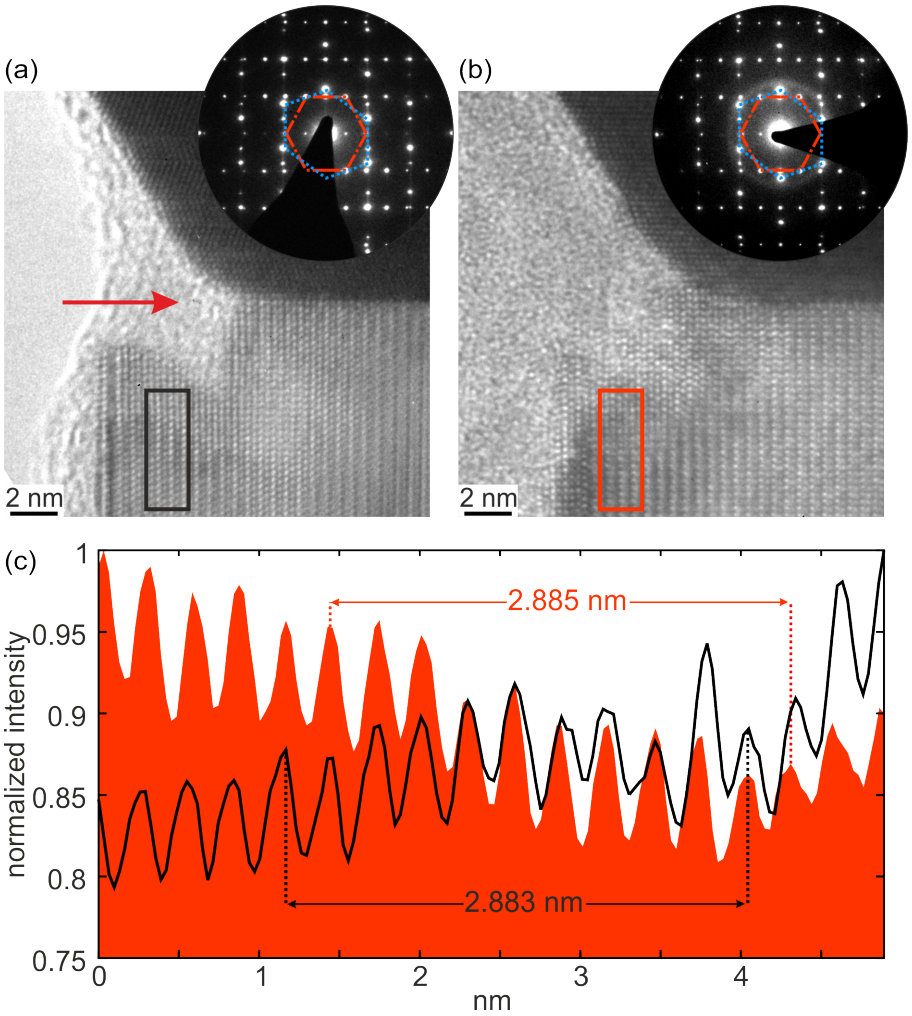

Figure 3.26: HRTEM micrographs and correlated PED patterns (a) before and (b) after deposition of FeCoSiB. The red arrow emphasizes the same area as shown in Figure 3.25.PED: red marks ZnO along the zone axis $[2\,\bar{1}\,\bar{1}\,0]^w$, blue marks Au along the zone axis [1 1 0]. A profile measurement of the HRTEM contrast was performed (black, red marks). (c) Normalized intensity profile of the HRTEM contrast before (black) and after (red) deposition. The averaged peak-to-peak distances are 0.2883 and 0.2885 nm, respectively.

By coating[7] the nanosail with ca. 10 nm thick FeCoSiB layer (Figure 3.25b) high resolution investigations of the interface were ensured, as the region of interest remained electron transparent. By chemical investigations a complete and homogenous covering of the piezoelectric material by FeCoSiB was confirmed, see representative

[7] The nanosails were placed and investigated on a Cu-grid. Afterwards the entire grid was coated with FeCoSiB and studied again.

elemental maps in Figure 3.25b. Moreover, the separation of the intensities from Au and Zn in the elemental maps proves the growth mechanism by conventional VLS. HRTEM investigations showed a polysynthetical twinning (twin interface parallel to (1 1 1)) within the Au particle in agreement with former studies [94]. Before the deposition with FeCoSiB all investigated areas of the ZnO nanosail exhibited a defect-free crystalline structure, see Figure 3.26a. In this micrograph a thin amorphous layer is visible at the edge of the nanosail. It results from carbon contamination during the observation of the specimen by the electron beam and is negligible for the further discussion. After deposition no significant change of the respective Au and ZnO structures was traced, as demonstrated by the comparison of the HRTEM micrographs and associated PED patterns from Figure 3.26. The diffuse ring within the PED pattern of Figure 3.26b demonstrates the contribution of a complete amorphous FeCoSiB layer. An evaluation of the inter-atomic distances of ZnO was performed close to the common interface with FeCoBSi before and after deposition, see marks corresponding plot of Figure 3.26. Within the limits of accuracy of the measurements, the average distance remained constant. Consequently, significant interdiffusion at the interface can be excluded [53]. These TEM findings can be considered as important preliminary work for FTS 1D nanostructues, as the shown results maintaine their validity also for the SFB relevant ME composites.
Investigations of the field-induced strain at the magnetoelectric interface were intensively performed on prototype 1-1 ME composites using grazing incidence and nanofocus X-ray diffraction [95, 71]. These studies revealed the high quality of single crystalline character of the ZnO structures confirming the presented TEM results. Key results were a saturation strain along $[1\,\bar{1}\,0]$ of about $3{\cdot}10^{-5}$ at room temperature for coated ZnO single crystals (Crystec GmbH) [95] and the determination of magnetization and strain changes in the order of 10^{-5} for 1-1 ME microcomposites [71].

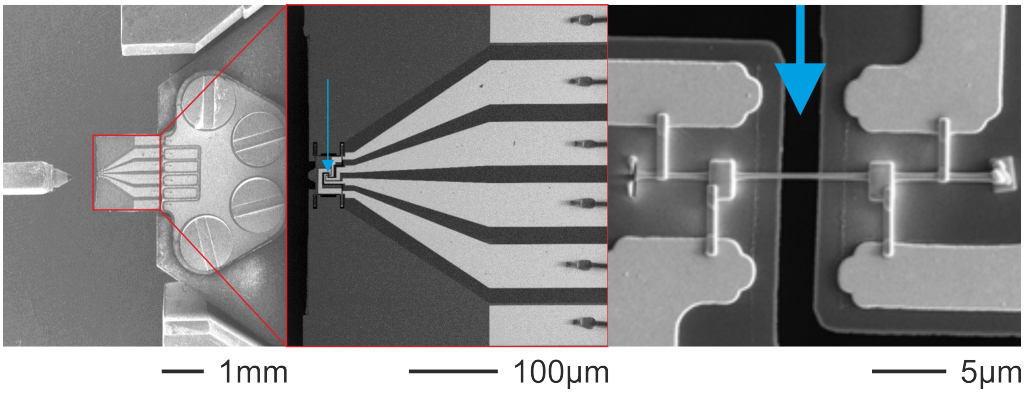

Figure 3.27: SEM micrographs of a push-to-pull device for the combined mechanical and electrical characterization of nanostructures and in particular for a FTS ZnO nanorod. (Left) Overivew of the device with a movable tip, (center) magnified view of the red marked area, arrows shows the position of (right) the mounted ZnO nanorod.

For investigations on the electromechanical characteristics of the FTS-ZnO rods first preliminary studies were carried out using a TEM/SEM electrical push-to-pull

(E-PTP) device[8] (Figure 3.27). The latter enables strain-rate controlled tensile measurements of mesoscale rods (dimensions: diameter 300 - 400 nm, length ca. 20 μm) with the possibility of high resolution analysis of selected areas. By monitoring the external introduced variations of the real structure, e. g. elongation or tapering of the rod, so-called true stress and strain values can be obtained and related to mechanical or electrical response. According to the E-PTP measurements, an elastic modulus of the ZnO rods was calculated to be ca. 88 GPa [51, 96]. Further, experiments with an alternating stress supply generated by a periodic square-wave voltage, indicated a strong relation between tensile elongations with electrical transport properties.
As future outlook, the E-PTP measurements must be combined with analytical TEM methods (aberration corrected HRTEM, GPA) and grazing incidence X-ray diffraction to provide first a substantial understanding on the rod properties. In the same manner, subsequent measurements on 1-1 composites can provided an enhanced understanding on the coupling mechanisms at the ME interfaces.

3.4 Summary: Complex Functional Nanomaterials Produced by Flame Transport Synthesis

The flame transport synthesis (FTS) is a newly established process for the production of functional nanomaterials also capable in fields of bio-magnetic sensing. The produced structures can be categorized in three main morphology types: 3D networks and array structures, sea-urchin type structures, and 1D micro-/ nanostructures. For each category a particular material was analyzed using TEM. For quantitative data interpretation the supercell approach was introduced allowing a full 3D analysis with a single model.
The investigated 3D networks are based on the defect-introduced interconnection of 1D SnO_2 structures. The defect type was identified as twinning with the $\{1\,0\,1\}$ planes as coherent twin boundary. Experimental edge-on views were obtained for the directions along the $[0\,1\,0]$ and $[1\,1\,1]$ zone axes, respectively. According to the experimental observations supercells were computationally generated, including the coherent twin boundary as intrinsic feature. Thus, the simulation of electron diffraction patterns and high resolution contrasts were enabled showing a convincing agreement with the corresponding experiments. The exceptional quality of the supercell approach was emphasized by the capability of precisely simulating the superposition contrasts of $\{1\,0\,1\}$ twinned domains created along the zone axis $[0\,0\,1]$.
The studied sea-urchin type structures consisted of ZnO and the focus of structural characterization was placed on the nanospikes. The latter exhibited an intrinsic twinning defect propagating through the entire 1D structure. For all investigations the predetermined viewing direction was $[2\,\bar{1}\,\bar{1}\,3]$, due to the specific nanospike morphology. As a direct consequence, only a superposition contrast of the twin

[8] The E-PTP device is fabricated by the Hysitron. The discussed investigations were performed by Sanjit Bhowmick, Douglas Stauffer and Oden L. Warren as members of Hysitron

domains was observable via TEM. Experimentally, the superposition was expressed by additional fringes in the high resolution contrast as well as multiple scattering phenomena in terms of satellite reflections in electron diffraction patterns. Using a calculated superposition structure, excellent quantitative simulations were provided for the HRTEM experimental data. For the experimentally obtained ED and FFT patterns, the simulations showed a good agreement and allowed an identification of dynamical scattering. The volume ratio of the differently transmitted twin domains plays a decisive role, as it varies considerable the fringe contrast and the intensities within diffraction patterns. The evaluation of the experimental data showed for all cases the presence of a majority domain with an attached minority domain.
As preliminary work, first investigations for an 1-1 ME demonstrator were performed on ZnO structures, which were produced by conventional vapor-liquid-solid synthesis. High resolution measurements on ZnO nanosail structures, before and after the deposition with a FeCoSiB layer, demonstrated that the magnetostrictive material homogeneously covers the entire surface of the nanosail. This result confirms the possibility of using such nanocomposites for bio-magnetic sensing from a structural point of view.
The electrical push-to-pull device was introduced, which enables in-situ measurements of electromechanical characteristics for FTS-ZnO rods as part of future studies.

4 Piezoelectric Thinfilms

In this chapter the focus is placed on piezoelectric materials suitable for thin film applications such as ME sensors[1]. Two materials, Aluminum nitride (AlN) and $(Ba_{0.7}Ca_{0.3}TiO_3)0.5$ - (Ba $Zr_{0.2}Ti_{0.8}$)0.5 (BCZT) were of particular interest according to their promising properties [97, 102]. The first part of the chapter presents a comprehensive structural study of AlN with respect to 2-2 and 0-3 composites. In the second part of the chapter analyses of the ferroelectric BCZT are discussed for bulk and layer specimens.

4.1 Aluminum Nitride

4.1.1 Role and Relevance of the Polar Axis for Development of Magnetoelectric Nanocomposites

The non-toxic III-V semiconductor AlN is of special interest as it exhibits remarkable thermal, mechanical and chemical properties [103, 104, 105, 106, 107]. According to the non-centrosymmetric polar wurtzite-type structure (space group: $P6_3mc$), these properties are, in many instances, directly associated with the crystal axis ([0 0 0 1] direction), especially accentuated for piezoelectricity (comparable to ZnO see section 3.3). Hence, a suitable high net piezoelectric polarization demands a highly textured system, e. g. a large volume fraction of uniformly oriented grains within a polycrystalline thin film. The optimum case of a perfect single crystalline material can hardly be achieved since the synthesis is complex and therefore not straightforward feasible [108]. Also bulk ceramics, like compacted powders, are not suitable as they contain randomly distributed crystal orientations. On the contrary, textured polycrystalline thin films meet these requirements. In the past, a tremendous scientific effort was invested in the fabrication and optimization of high quality textured films (for the [0 0 0 1] direction) [109, 110, 111, 112]. In addition to the sputtering conditions, the selection of the substrate represents the determining factor in controlling the growth and morphology of such a film. As pointed out by Dubois and Muralt [113] the best results are achieved with a nucleation surface showing a well-defined hexagonal symmetry and a chemical inertness against nitrogen, which is obtainable for instance by {1 1 1} textured Pt or polycrystalline Mo[2]

[1] The chapter is based on the studies from [97, 98, 99, 12, 100, 101].

[2] The production of the samples were performed by Stephan Marauska (on Pt and Mo) and by Björn Gojdka (on Pt).

(cf. Figure 4.1). In this manner thin films can be obtained with a piezoelectric coefficient of 5.25/5.70 pm/V for $d_{33,f}$[3] and -1.3 C/m^2 for the transverse coefficient $e_{31,f}$[4] [108, 116, 117, 118].

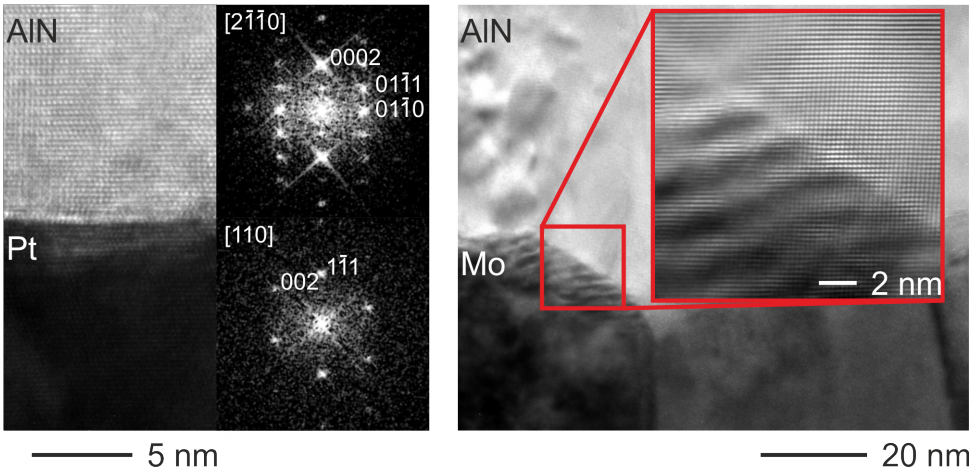

Figure 4.1: (a) HRTEM micrographs of AlN/Pt interface with corresponding FFT patterns. (b) Bright field image of AlN/ Mo interface with (filtered) HRTEM micrograph as inset. In both cases a [0 0 0 1] growth directly starting at the interface can be observed.

4.1.2 Structural Investigations of Columnar Grown AlN

The AlN thin films were studied by preparing samples with a cross-sectional and basal views, respectively. The combined data set provides a comprehensiv understanding for this piezoelectric component.

Cross-Sectional View: Microstructure Analysis via Electron Diffraction

The microstructural characteristics of the AlN thin film were investigated using a cross-section specimen, as depicted in the bright field image of Figure 4.2a. The diffraction contrast reveals columnar shaped grains growing along the [0 0 0 1] direction. In order to substantiate the geometrical features and to monitor the quality of the columnar growth series of electron diffraction patterns were recorded perpendicular and parallel to the [0 0 0 1] direction. For the latter investigations SAED was applied to 250 nm restricted circular areas along a representative set of adjacent columns, cf. white circles in Figure 4.2a. All SAED patterns (insets in Figure 4.2a) showed (0 0 0 2) texture (solid boxes in Figure 1a) corresponding to the reciprocal [0 0 0 1]* direction. This confirms an orientational integrity along the entire size of

[3]Comparative $d_{33,f}$ values are: 5.9 pm/V for ZnO, PZT (1 – 3 μm) 60 - 130 pm/V [114] [115].
[4]Comparative $e_{31,f}$ values are: -1.0 C·m^{-2} for ZnO, PZT (1 – 3 μm) -8 to 12 C·m^{-2} [114] [115].

the columns. Another prominent feature of these patterns is indicated by the presence of intensity alternating reflection couples in rows parallel to [0 0 0 1]*, (dotted and dashed boxes in Figure 4.2b).

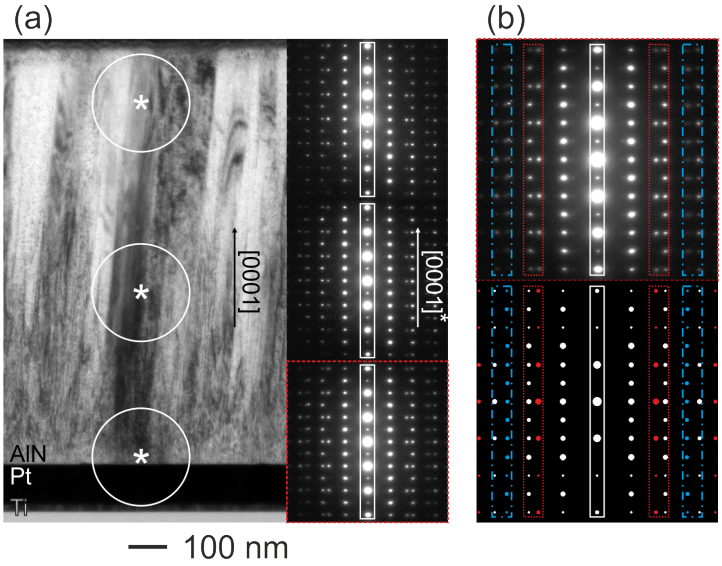

Figure 4.2: (a) TEM bright field images of the cross-sectional view for the columnar grown AlN. Electron diffraction was applied parallel to the growing direction; the circles mark the positions of the SAED aperture. The corresponding diffraction patterns are depicted on the right. A texture of the {0 0 0 1} planes (solid box) is preserved throughout the entire investigated area. (b) Comparison of the SAED pattern (Figure 4.2 a, right bottom, scaled for (b), top) with superimposed kinematical simulated SAED patterns. Color code for the simulated reflections: white: zone axis $[2\,\bar{1}\,\bar{1}\,0]$, red: $[1\,0\,\bar{1}\,0]$, blue: $[5\,\bar{1}\,\bar{4}\,0]$. See text for details.

Comparing the experimental data with kinematic ED simulations, these reflection couples signify a superposition of three rotated single crystalline AlN domains along the beam direction. The zone axes of the domains $[u\ v\ t\ 0]$ ($[2\,\bar{1}\,\bar{1}\,0]$, $[1\,0\,\bar{1}\,0]$, and, $[5\,\bar{1}\,\bar{4}\,0]$, cf. Figure 4.2b, proof the presence of a joined rotation axis of [0 0 0 1]. As all identified directions are perpendicular to [0 0 0 1], consequently, the azimuthal rotation of the columns around the [0 0 0 1] direction is not subject to any restriction, while the [0 0 0 1] texture of AlN is predetermined by the {1 1 1} texture of Pt [113, 119], see Figure 4.1a. Further, the comparison of experiment and simulation allows the identification of multiple scattering phenomena, e. g. the presence of forbidden 0 0 0 l ($l = 2n + 1$) reflections and satellites[5] which are strongly excited in thicker selected areas. As evidence for a high specimen thickness serves the low intensity of the primary beam with respect to the surrounding reflections, which originates from a high interaction of the electron beam with the specimen.
PED was used to record diffraction patterns parallel to the AlN-substrate interface (perpendicular to the growth direction). Despite the common {0 0 0 2} texture,

[5] In some instances refelctions with fainting intensities were observed close to high intensity Bragg reflections and were labelled as satellites. A further consideration of this multiple scattering phenomenon is not provided.

the respective patterns, depicted in Figure 4.3a, exhibited strong variation to each other. In pattern *i* (Figure 4.3) a high specimen thickness with various different column orientations are observable. As a result, kinematically forbidden reflections, i.e. 0 0 0 *l*, were still present. The excitation of the forbidden reflections is strongly reduced with increasing reciprocal distance to the primary beam, which is a typical behavior in multiple scattering. Evaluating and comparing the characteristics of rows parallel to the [0 0 0 1]* direction a contribution of reflections from the [1 0 $\bar{1}$ 0] zone axis can be excluded for pattern i, see dotted boxes of Figure 4.3b. Instead this PED pattern contains information mainly from [2 $\bar{1}$ $\bar{1}$ 0], [5 $\bar{1}$ $\bar{4}$ 0], (dashed boxes Figure 4.3b) and also from non-principle directions such as [7 $\bar{2}$ $\bar{5}$ 0], [3 $\bar{1}$ $\bar{2}$ 0] (not marked). Pattern *ii* includes fewer orientations, which may originate from a lower specimen thickness. The suppression of the the multiple scattering is more successfully. In this pattern a strong contribution of reflections from the zone axis [1 0 $\bar{1}$ 0] was determined. Pattern *iii* seems to be almost exclusively single crystalline oriented along [1 0 $\bar{1}$ 0]. This region shows the lowest specimen thickness of all three patterns and is less dynamical excited. These PED studies confirmed the arbitrary rotations of columns with a [0 0 0 1] texture to each other. A more quanitative appraoch of the investigation on the rotate columns is provided in section 4.1.2 - *Basal View: Microstructure Analysis*.

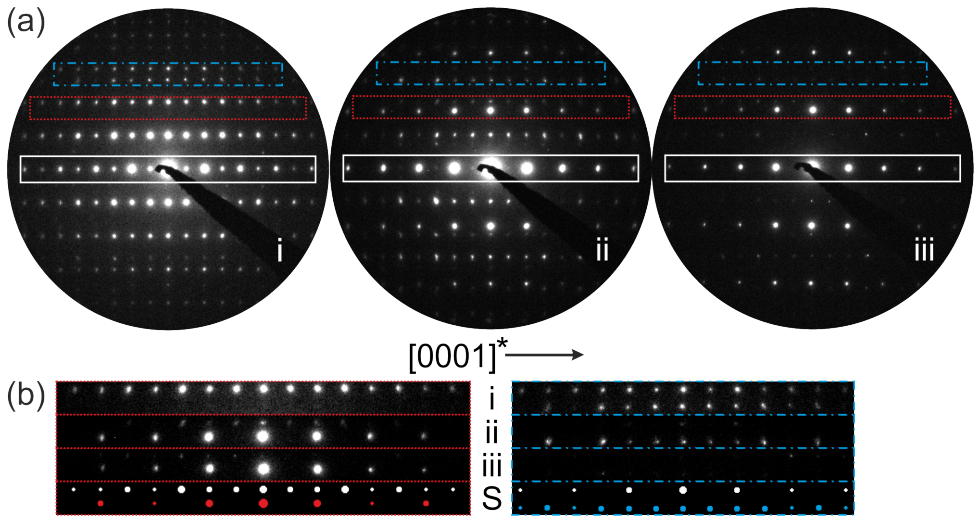

Figure 4.3: PED performed perpendicular to the growth direction for cross-section specimen shows the superimposition of variously oriented columns with zone axes [u v t 0] including the 0 0 0 2 planes (solid box) as common feature. (a) PED patterns with different degree of superposition. (b) Comparison between rows of experimentally obtained reflections parallel to the [0 0 0 1]* direction (i, ii, iii) with kinematically simulated reflections (S). Color code for the simulated reflections in (b): white: zone axis [2 $\bar{1}$ $\bar{1}$ 0], red: [1 0 $\bar{1}$ 0], blue: [5 $\bar{1}$ $\bar{4}$ 0].

Interpretation of High Resolution Contrasts in AlN

In this section, the structural origin for several high resolution contrasts will be discussed.

Superposition:
A direct evidence for superimposition of rotated columns is provided by HRTEM as depicted in Figure 4.4. As a reference, a quantitative analysis for pure single domain HRTEM contrast is depicted for the zone axes $[2\,\bar{1}\,\bar{1}\,0]$ and $[1\,0\,\bar{1}\,0]$ in Figure 4.4a. The series of HRTEM micrographs in Figure 4.4b demonstrates superposition of the the zone axes $[2\,\bar{1}\,\bar{1}\,0]$ and $[1\,0\,\bar{1}\,0]$ with a decreasing influence of the latter from area (i) to (iii). Indeed, in the FFT pattern of area (i) the superposition results in the presence of strongly pronounced satellite reflections, while the calculated FFTs of the areas (ii) and (iii) show only a marginal or vanishing contribution of the Bragg intensities from the zone axis $[1\,0\,\bar{1}\,0]$. As discussed in section 3.3.1, the formation and variation of a superimposed high resolution contrast is significantly influenced by the transmitted volume-ratio of the respective contributing grains.

Defects:
An indication for a planar defect can be seen in area (D) of Figure 4.4b. It propagates perpendicular to the $\{0\,0\,0\,2\}$ planes in the micrograph and is producing diffuse streaks in the associated FFT, cf. arrows. As reported in former studies [120, 121, 122] for thin films with a wurtzite type structure, planar defects are common features and mainly observed at the $\{0\,0\,0\,1\}$, $\{0\,1\,\bar{1}\,0\}$, $\{0\,1\,\bar{1}\,1\}$ and $\{2\,\bar{1}\,\bar{1}\,0\}$ planes. According to the character of a defect two main groups can be separated: inversion and translation domain boundaries (IDB and TDB) subdividing into more specified types such as stacking faults or stacking mismatch boundaries (SMB) [122]. A detailed study on defect structures were performed along the basal view ($[0\,0\,0\,1]$ zone axis). As depicted in the HRTEM micrograph of Figure 4.5a, domain boundaries appeared as periodic zip-like contrast along the $\{2\,\bar{1}\,\bar{1}\,0\}$ planes. From the experimental data a displacement vector of $1/2\langle 1\,0\,\bar{1}\,0\rangle$ perpendicular to the $\langle 2\,\bar{1}\,\bar{1}\,0\rangle$ direction was obtain. A resulting shift of the $\{\bar{1}\,1\,0\,0\}$ planes is reflected in the correlated FFT of Figure 4.5a by diffuse intensities streaks. Information about an additional shift along the viewing direction is inhibited according to the two dimensional limitation of the observed high resolution projection. However, similar findings on textured GaN thin-films performed by Xin et al. [123] showed the presence of such a shift by a vector of $1/2[0\,0\,0\,1]$.
For a quantitative analysis of the high resolution contrast and to evaluate the structure at the domain boundary a supercell approach (introcuded in section 3.2) was carried out. The used tranformation matrices are

$$\mathbf{P} = \begin{pmatrix} 4 & 2 & 0 \\ 0 & 4 & 0 \\ 0 & 0 & 1 \end{pmatrix}, \qquad \mathbf{Q} = \begin{pmatrix} 1/4 & -1/8 & 1 \\ 0 & 1/4 & 0 \\ 0 & 0 & 1 \end{pmatrix}$$

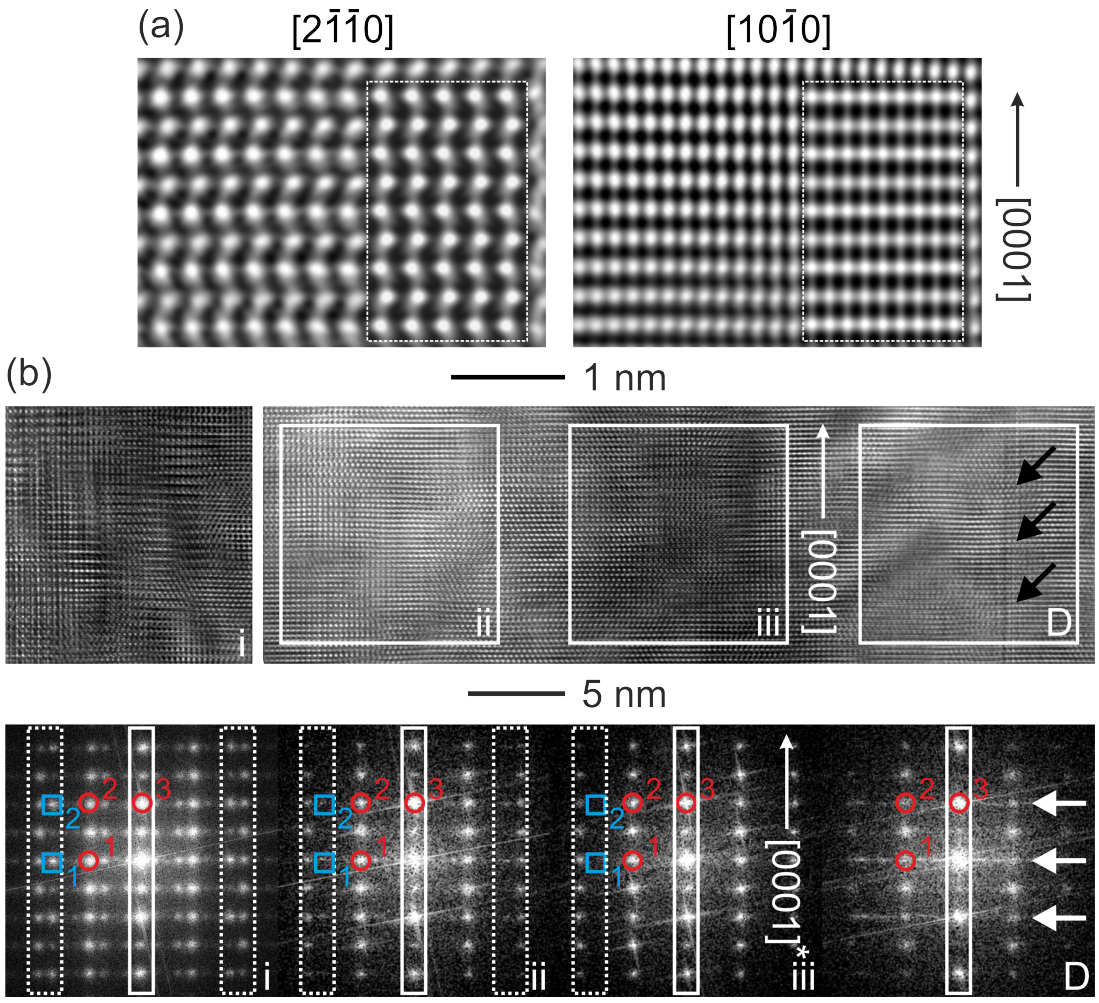

Figure 4.4: Nanostructure investigations of AlN for a cross-section specimen: (a) HRTEM micrographs of single crystalline regions along the zone axes [2 $\bar{1}$ $\bar{1}$ 0] and [1 0 $\bar{1}$ 0]. Insets: simulations with the parameters (objective lens defocus | specimen thickness) of (-15 nm | ca. 19 nm) left and (-180 nm | ca. 13 nm) right. (b) Aberration corrected HRTEM micrographs and associated FFTs of: Area (i - iii) characteristics of superpositioning of the zone axes [2 $\bar{1}$ $\bar{1}$ 0] and [1 0 $\bar{1}$ 0], (i) strongly pronounced leading to the presence of satellite intensities in the FFT, (ii) marginal contribution and (iii) vanishing contribution of a domain with the zone axis [1 0 $\bar{1}$ 0]. Area (D), structure along the zone axis [2 $\bar{1}$ $\bar{1}$ 0] with diffuse intensities perpendicular to the {0 0 0 2} planes indicating the presence of planar defects. The solid box indicates the common growth direction along [0 0 0 1]. Indexing the patterns: along [2 $\bar{1}$ $\bar{1}$ 0] (circles): (1) 0 $\bar{1}$ 1 0, (2) 0 $\bar{1}$ 1 2; along [1 0 $\bar{1}$ 0] (squares): (1) $\bar{1}$ 2 $\bar{1}$ 0, (2) $\bar{1}$ 2 $\bar{1}$ $\bar{2}$; common intensity (circle): (3) 0 0 0 2.

with parameters a' = 12.4920 Å, b' = 10.8184 Å, c' = 4.9880 Å, and α, β, γ = 90° for the new P1 supercell. As obtained by the experimental data a displacement of 1/2<1 0 $\bar{1}$ 0> was implemented. The [1 0 $\bar{1}$ 0] direction for the wurzite-type structure is parallel to b' of the supercell. Thus, the y' coordinates of all atoms must be shifted by $b'/4$ in a reasonable x'-range. Simulations based on a cell with this shift

vector allows the calculation of convincing high resolution simulations. However, the atomic model showed nonsensical interatomic distances directly at the defect boundary demanding a further shift vector. Applying a second shift $b'/2$ to the z' coordinates of all already shifted atoms the total displacement vector of $1/2[1\,0\,\bar{1}\,1]$ is generated.

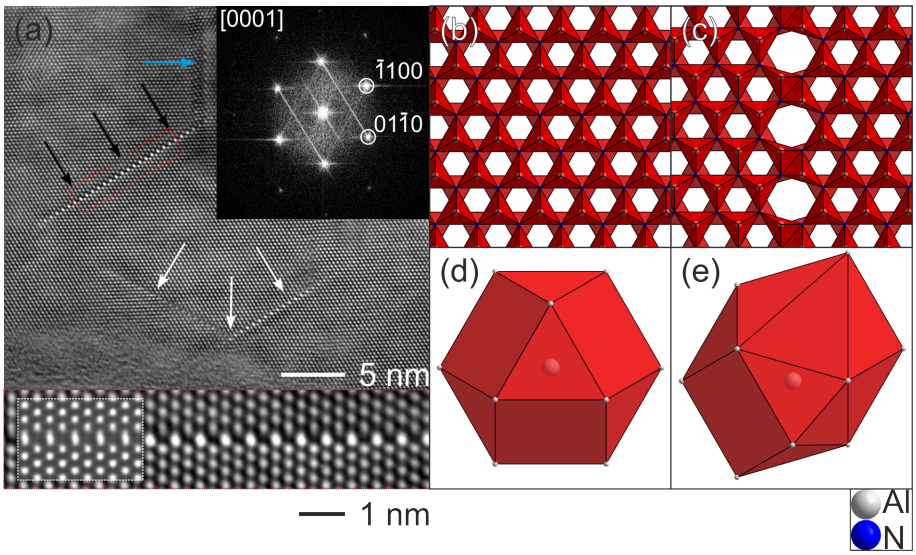

Figure 4.5: (a) HRTEM micrograph along the [0 0 0 1] zone axis with correlated FFT. Arrows mark the symmetry equivalent stacking mismatch boundaries. The defects are reflected by diffuse intensities in the FFT pattern. The enlarged panel shows a stacking mismatch boundary with a simulation as inset (objective lens defocus | specimen thickness) of (-45 nm | ca. 5.5 nm). Calculated view of the tetrahedrons with Al as center atom and N atoms as ligand atoms for (b) the defect-free bulk and (c) the interface structure along [0 0 0 1]. Single cuboctahedron for (d) the bulk and (e) the defect structure set up by Al-Al distances.

The enlarged view of the domain boundary in Figure 4.5a shows the convincing agreement between experimentally obtained and simulated high resolution contrast. In Figure 4.5b and 4.5c the Al-N tetrahedral structures are compared for the defect-free and the domain boundary case. In the wurtzite type structure the Al-N tetrahedrons are linked by common corners. At the interface of the domain boundary the tetrahedrons share one common edge. One Al-N bond is thereby distorted by ca. 12.1 %[6] and shows a distances of ca. 1.67 Å (normal Al-N distance ca. 1.90 Å). To visualize the distortion more clearly cuboctahedrons set up by the Al-Al distances are compared with each other, see Figure 4.5d and 4.5e. A complete set of parameters for the tetrahedrons and the cuboctahedrons are provided in Table 4.1 and 4.2.

[6]The defect simulation represents an idealized case, relaxation process were neglected. Further on, the data were recorded without aberration correction, thus, a detailed strain calculation by GPA was not performed.

Table 4.1: Comparison of the Al-N distances for the bulk (defect-free) and interface tetrahedrons.

Bulk			Interface		
Atom 1	Atom 2	Distance 1,2 Å	Atom 1	Atom 2	Distance 1,2 Å
Al	N	1.8962	Al	N	1.6684
	N	1.8962		N	1.8962
	N	1.8967		N	1.8967
	N	1.9064		N	1.9064

Table 4.2: Comparison of the Al (centre) – Al (ligand) distances for the bulk (defect-free) and interface cuboctahedrons.

Bulk				Interface			
Center	Ligand	Count	Distance 1,2 Å	Center	Ligand	Count	Distance 1,2 Å
Al	Al	2x	3.0774	Al	Al	2x	2.9425
	Al	2x	3.0774		Al	2x	3.0774
	Al	2x	3.0774		Al	2x	3.0777
	Al	1x	3.1230		Al	1x	2.3773
	Al	1x	3.1230		Al	1x	3.1230
	Al	1x	3.1230		Al	1x	3.1230
	Al	1x	3.1230		Al	1x	3.1230
	Al	1x	3.1230		Al	1x	3.2531
	Al	1x	3.1230		Al	1x	3.9390

With the used model the domain boundary can be considered as SMB, corresponding also to a TDB. This means that a reversal in the polarity is not accompanied crossing the domain boundary [122, 123]. Such a defect has no influence to the piezoelectric properties and, thus, to the performance of bio-magnetic sensors. The origin of SMBs was related to the island growth of AlN and a subsequent coalescence of two grains causing the $\{2\,\bar{1}\,\bar{1}\,0\}$ boundaries [124, 125]. Numerical studies by Northrup [126] suggested a model for the existence of closed inversion domains for III-nitrides and the $\{2\,\bar{1}\,\bar{1}\,0\}$ boundaries. However, in a multitude of experimental works IDBs were found normally at the $\{0\,1\,\bar{1}\,0\}$ planes. A procedure for the minute localization of IDBs and TDBs is provided by [122, 127, 128]. Also prismatic stacking faults were observed for the same set of planes showing the same displacement $1/2<1\,0\,\bar{1}\,1>$. A detailed description for these stacking faults are given in [125, 129, 130].

Basal View: Microstructure Analysis

A basal view of the AlN thin film can be seen in the virtual bright field (VBF) image in Figure 4.6a. The term virtual specifies that this image is reconstructed from local variations in the primary beam intensity while applying the ACOM system (Figure 4.6b and 4.7) and, therefore, can be considered as STEM-type bright field image [131, 37]. Based on the contrast variation in Figure 4.6a a heterogeneous size and shape distribution was detected with a mosaic-like morphology of the AlN columns. The orientation map along the growth (out-of-plane) direction (Figure 4.6b) mainly exhibits uniform intensity and color representing a [0 0 0 1] column alignment. On the contrary, as the color code (Figure 4.6b) and the FFTs of the mark areas demonstrate, distinct columns reveal a considerable tilting apart from the [0 0 0 1] texture. These grains are difficult to detect reliably in cross-sectional analysis of the sample, but as ACOM is providing large area crystal orientation information, it is particularly suitable to detect the distribution of this type of grains.

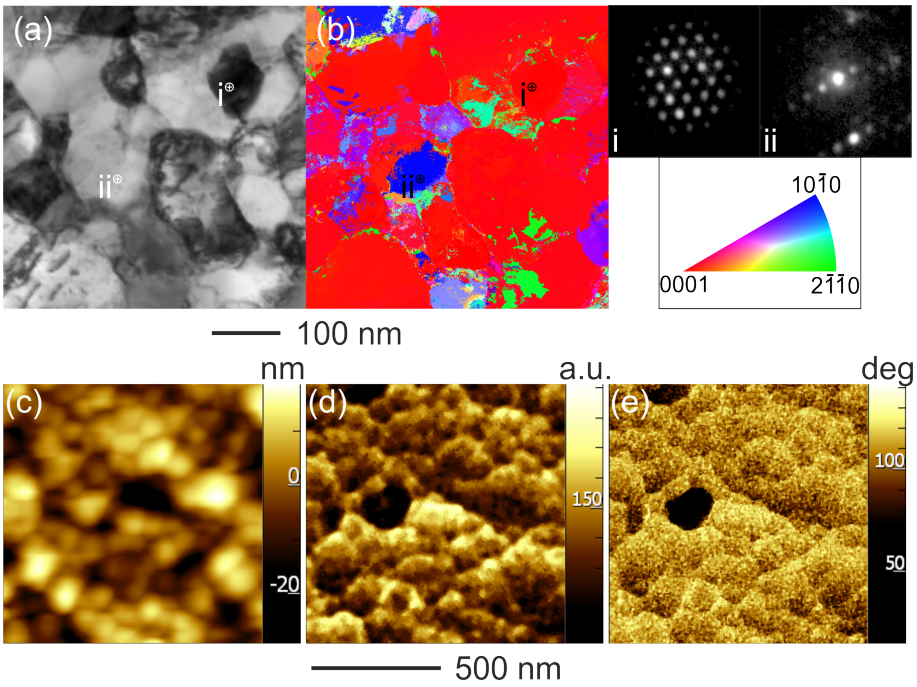

Figure 4.6: Real structure-property relation for AlN thin films along the basal view. (a, b) Automated crystal orientation mapping of AlN (a) Virtual bright field image. Orientation map along out-of-plane direction (b) z-direction. (Right, top) Diffraction patterns of area i) and ii). (Right, bottom) Color code of the stereographic triangle (hexagonal point group: 6mm). (c, d, e) PFM of an AlN thin film: (a) topographic image (b) magnitude signal (vertical) and (c) phase signal (vertical). The comparison indicats that tilteted domains (e. g. blue in orientation map) correlate with dark areas (region of low response) in the magnitude and phase signal.

The influence of the tilted domains on the properties of the AlN film could be directly shown for a comparable region using the piezoresponse force microscopy (PFM) technique[7], cf. Figure 4.6c, d, e. The topological view in Figure 4.6c reveals only minor differences in altitude for the observed structure. Nevertheless, the magnitude (Figure 4.6d) and phase (Figure 4.6e) signals contain both equivalent low signals for the same dark areas. As the piezoresponse signal strongly correlates with the [0 0 0 1] oriented growth of AlN [108, 113, 97] dark areas consequently must stem from misaligned regions similar to those shown in Figure 4.6b. Further, columns can be observed which exhibit strong contrast and orientation variations indicating subgrain structures, see the azimuthal (in-plane) orientation map in 4.7a[8]. The azimuth rotation in the ACOM map confirms the previous PED/HRTEM studies on the cross-sectional specimens. The formation of subgrains can be related to an initial three-dimensional nucleation and partial coalescence of the AlN islands during the growth of the thin film [124]. As stated in former studies the subgrain boundaries are delinated by threading dislocations [123, 133].
A statistical appraoch[9] for evaluating the in-plane rotation and misorientation of the columnar grains is quantitativly achievable by following the data processing developed by Kobler et al. [39]. Important for this purpose is a precise indexing of the grains, which is rated after the cross-correlation between experimental and a template data set by a resultant reliability index, see section 2.1.1. A superposition of orientation and corresponding reliability map exhibits the variation of sufficient data recognition as depicted in Figure 4.7. The areas with darker shading have a low reliability, while intense colouring express high relibilty.
An increase in the quality -here equivalent to noise reduction- of the raw data is obtained by using a so-called grading median filter. Three Euler angles are calculated for each pixel and a certain set of pixels is subsequently graded regarding a respective median. The size of a reliable set depends on parameters as the grain size and defects such as narrow twin planes [39]. With absence of the latter defects and simultaneously large grains containing respectively high pixel numbers, the median calculations can be expanded to larger pixel sets, without corrupting the resulting data. The information of the index and reliability map was also included in the processing of the median filter. Furthermore, limiting boundary conditions were introduced to extract unreliable grains: The segmentation between two grains must exceed an angle of 5°, otherwise it will be considered as one. Grains with a size below 75 pixel = 9.77 nm diameter were removed. The resulting map is presented in Figure 4.7b for the first recognition. However, in this map the presence of voids

[7] PFM measurements were executed by Adrian Petraru using a SmartSPM 1000 Scanning Probe Microscope from AIST-NT was used. A sinusoidal modulation voltage of 5 V peak-to peak at a frequency of 200 kHz was applied between the conductive tip and the bottom electrode. The scan was performed in contact mode and the topographic image together with the vertical piezoelectric response and phase were acquired simultaneously. With this configuration the lateral resolution is in the order of about 20 nm [132].

[8] In this Figure the orientation map for the x-direction is presented. Investigations on the other in-plane direction, namely the y-direction, revealed analogues results. Hence, the following discussion focus on the former case.

[9] The statistical evaluation of the orientation map was performed by Aaron Kobler and Venkata Sai Kiran Chakravadhanula from the Karlsruhr Institute of Technology.

(white areas) can be seen. In a second recognition (Figure 4.7c) the procedure is repeated and these voids are filled with the most probable color configuration (orientation)[10].

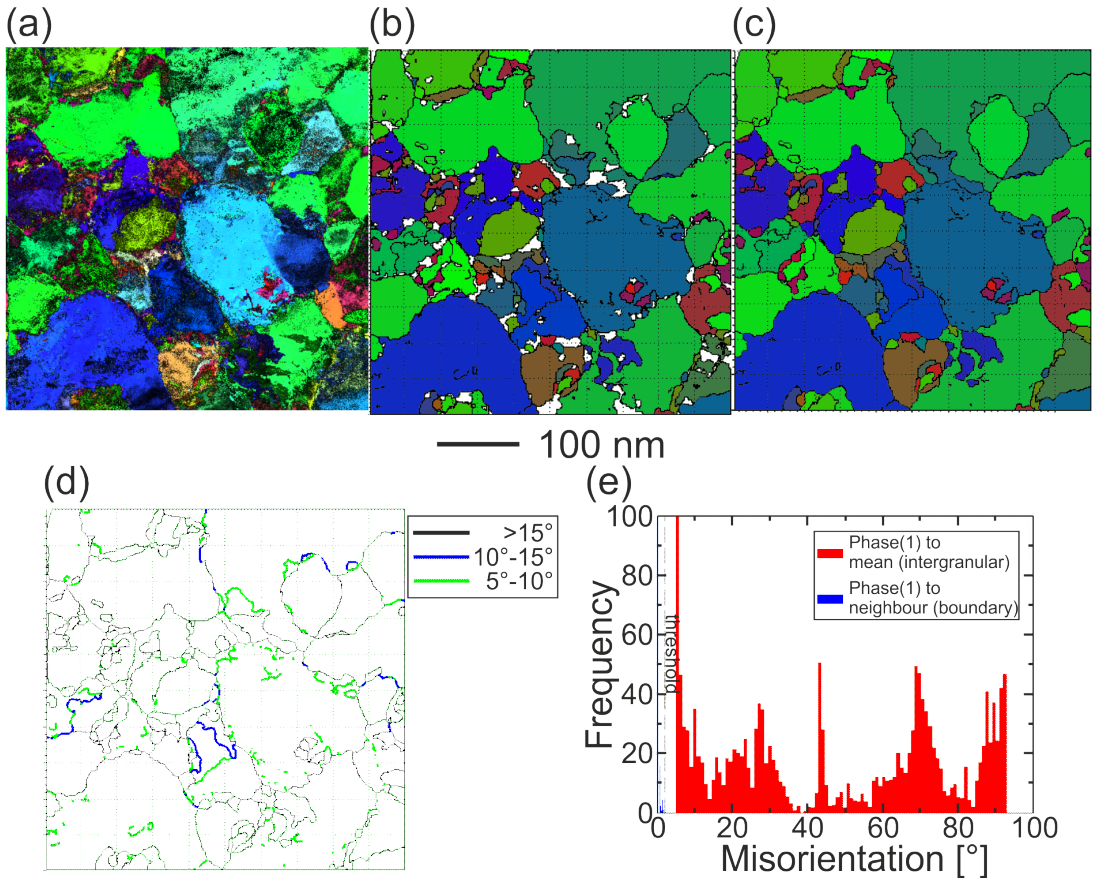

Figure 4.7: Data processing and quantitative evaluation of the orientation map along the in-plane direction (x-direction), which was calculated from region depicted in 4.6a.(a) Raw data: Orientation map overlayed with the corresponding reliability map, colour code is equivalent to Figure 4.6. Processed data: (b) first recognition, (c) second recognition. Statistical evaluation of the columns: intergranular and boundary misorientation, (d) graphical and (e) diagram presentation.

The processed data enables a visualization of the rotation and orientation of the grains to each other, as emphasized by the respective colors of the grain boundries in Figure 4.7d. A correlated statistical evaluation is depicted in Figure 4.7e. A total number of 129 grains was determinded showing a wide range of misorientation angles. The blue bars represent disorientation within the grains, while the red bars stand for the inter-granular disorientations. Separating the plotted data into low-angle and high-angle grain boundries (demarcation criterion: 15° [134]) two tendencies are observable: In the former case, misorientations with lower angle values were dominating, and, for the latter, local maxima in the frequencies were detected

[10]The computational obtained results must be evaluated critically as no direct experimental evidence can be provided for the void areas.

for specific angular values. Some of these maxima can be rationalized using the coincidence-site lattice (CSL) model. In the next paragraph a brief introduction of this model is provided, followed by a comparison of the experimental data with literature values.
First proposed by Kronberg and Wilson [135] two (in a well-defined manner) misoriented and superimposing grains can be assumed which exhibit coinciding atom sites for certain rotation angles. A resulting superlattice is generated with a periodicity of the coincidence-sites. As stated by Lejcek [134] a high number of coinciding lattice positions roughly correlate with lower grain boundary energies. To measure this relation the quantity Σ is introduced, representing the ratio of the CSL and the crystal unit cell volumes [136]. A low Σ value is accompanied with a high number of coincidence points.For hexagonal structures the lowest value is $\Sigma = 7$[11] and even numbers for Σ can also be found [137].
The AlN data can be compared with literature values of CSL parameters, which were determined for metallic hexagonal systems [137, 136, 138, 139]. In this context, Bleris et al. [138] pointed out the pivotal role of the axial c/a ratio for non-cubic materials regarding the presence of possible CSL's[12]. In the case of AlN, the c/a ratio is ca. 1.6 which can be approximately expressed as the fraction number $\sqrt{18/7}$. The angular misorientations, which exhibit local maxima in Figure 4.7e and can be assigned with Σ values, are found at ca. 20.5° (Σ7, theoretical angle = 21.79°, rotation axis (in $u\ v\ w$) = [0 0 1]), ca. 27° (Σ13a, 27.80°, [0 0 1]), ca. 64° (Σ25, 63.90°, [2 1 0]), ca. 87° (Σ13b, 85.59°, [2 1 0]). The experimental misorientation show a more or less pronounced deviation from the ideal CSL orientation relationship. The specific properties of a CSL domain boundary are maintained only in a certain deviation range. To calculate this boundary condition the Brandon criteria [140] can be used for the maximum allowed angular deviation $\Delta\Theta_{max}$:

$$\Delta\Theta_{max} = \Theta_0 \cdot \Sigma^{-m}$$

The paramters Θ_0 and m are constants and are set to 15° and 1/2 in the Brandon criteria. The experimental obtained values fullfill the criteria.
The grain boundaries with the Σ values of 7 and 13a were observed experimentally via SAED and are depicted with associated simulations in Figure 4.8. Individual wurtzite domains were emphasized with different marks in the simulation. For $\Sigma = 7$ the coinciding Bragg reflections can be assigned to the $\{2\,1\,\bar{3}\,0\}$ and the $\{1\,2\,\bar{3}\,0\}$ planes of the respective domains (see arrows in Figure 4.8a) and for $\Sigma = 13a$ the coinciding Bragg reflections correspond to the $\{1\,3\,\bar{4}\,0\}$ and the $\{\bar{1}\,4\,\bar{3}\,0\}$ planes (arrows Figure 4.8b).

It is worth to note, that the pronounced misorientations with angles of ca. 44° and ca. 69° can be related to the literature when assuimg an axial ratio of $\sqrt{8/3}$ (= 1.63) with (Σ14, 44.42°, [2 1 0]) and (Σ18, 70.53°, [1 0 0]). The quotient of the ideal

[11] Naturally $\Sigma = 1$ is the lowest value. It is not part of the discussion as the misorientation angle is 0° for any rotation axis.
[12] CSL's with the rotation axis [0 0 1] are independent from the c/a ratio.

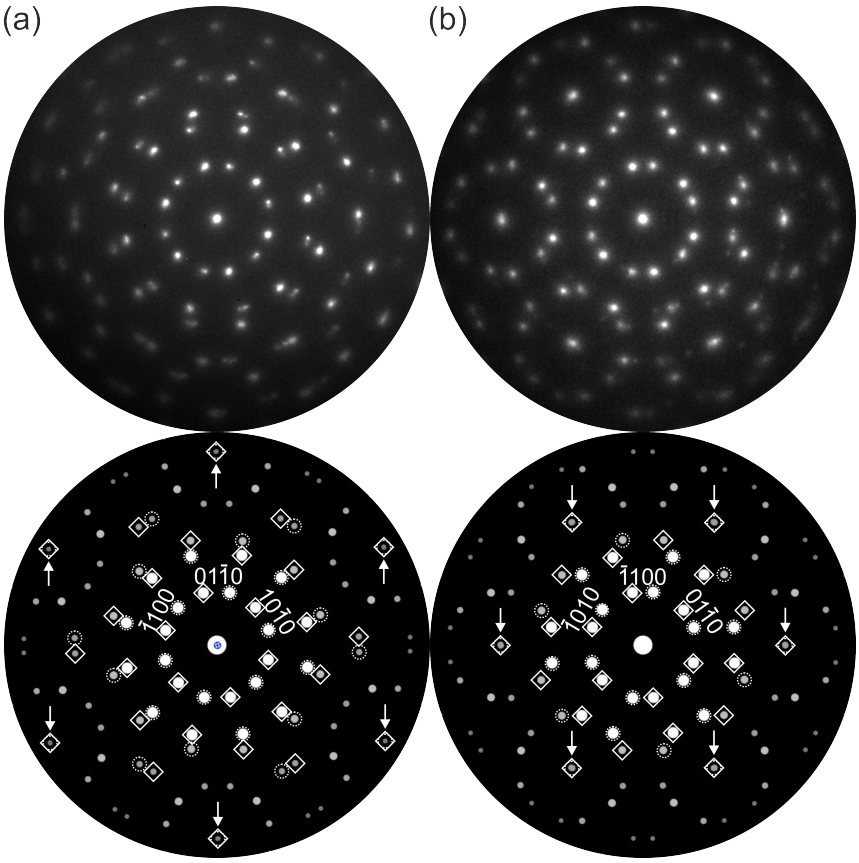

Figure 4.8: SAED patterns at AlN grain boundaries along the [0 0 0 1] zone axis with misorientation angles of (a) ca. 22° (corresponding to a Σ = 7)and (b) ca. 28° (Σ = 13a), (top) experimental and (bottom) simulated data. Squares and circles mark the wurtzite-type single domains, respectively. The arrows emphasize conciding reflections of both single domain patterns.

AlN ratio, 1.60, and 1.63 is ca. 1.8%. A potential strain within the specimen may influence the formation of specific CSL grains. First strain analyses were performed on the basal view and discussed in the next section.

Domain Boundary Study

Using the geometric phase analysis (GPA, theoretical description provided in section 2.1.2) the presence of strain can be determined at the grain boundaries. Note, that the strain measured by GPA is always expressed relative to a reference lattice within a high resolution TEM micrograph, which is supposed to be unstrained [45]. This provides a good qualitative idea of the strain (and stress) distribution in an area of interest, but a quantitative interpretation is further limited by stress-relaxation in the thin film during sample preparation. Using spherical aberration corrected microscopes delocalization effects can be avoided which increase the achievable spatial resolution.

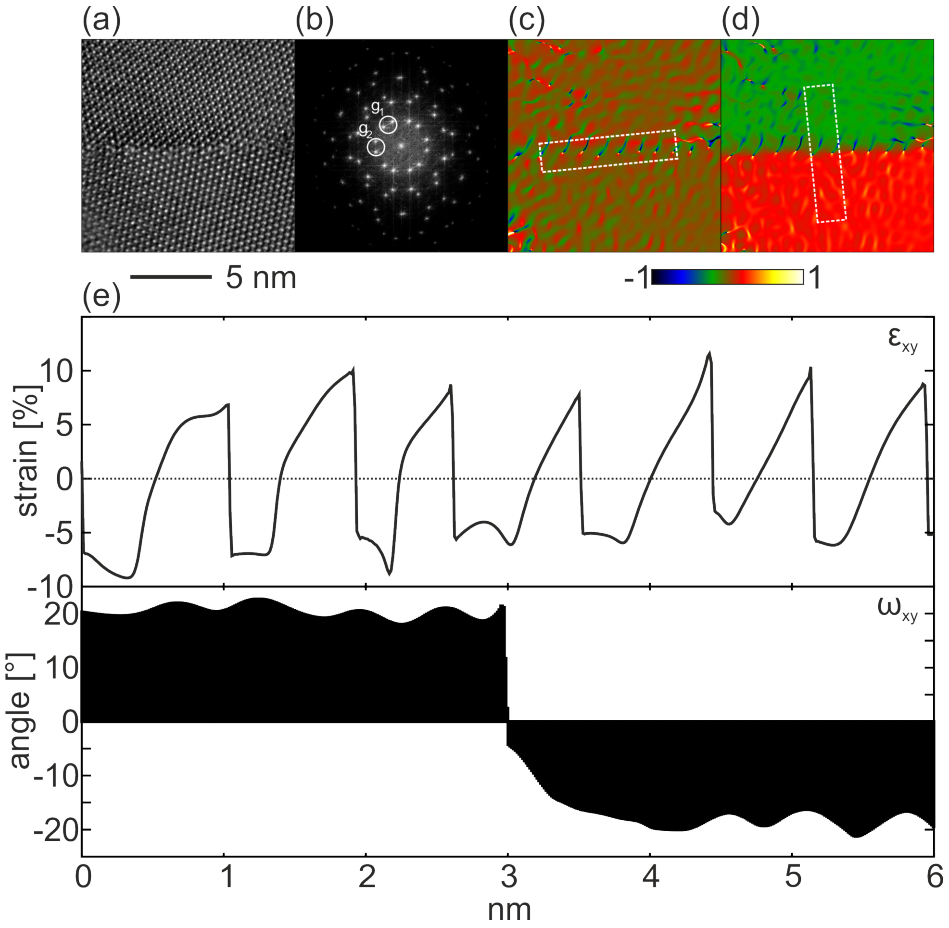

Figure 4.9: Aberration corrected HRTEM micrograph of a well-projected grain boundary separating two adjacent AlN grains along the [0 0 0 1]. (b) Corresponding FFT of (a) showing a rotation angle of ca. 24°. The two marked g-vectors are used for calculating the GPA maps. (c) Shear strain (ϵ_{xy}) map and (d) in-plane rigid-body rotation (ω_{xy}) for (a). The color bar is valid for (c, d) and gives the strain in percent and the rigid body rotation in degrees, respectrively. (e) Plotted strain and rigidy body rotation for the respective marked areas.

An exemplary strain investigation at the grain boundaries is carried out in Figure 4.9. As basis for GPA serves the aberration corrected HRTEM micrograph depicted in Figure 4.9a. To calculate the strain, an internal lattice must be defined within the associated FFT (Figure 4.9b), which is set up by two reciprocal lattice vectors, $g_{1,2}$ [40, 41, 141]. The FFT shows two superimposed single domain patterns which are rotated to each other by an angle of ca. 24°. The assignment of one g-vector was performed by including two intensities with same index. Thus, g_1 is pointing to reflections corresponding to the $(\bar{1}\,0\,1\,0)$ lattice planes and g_2 to the $(\bar{1}\,1\,0\,0)$ planes, cf. marks in Figure 4.9b. The spatial resolution for the GPA maps is defined by Lorentzian masks for the g-vectors in the FFT and was set to 0.7 nm. In Figure 4.9c, d the shear strain ϵ_{xy} and the rigid body rotation ω_{xy} are visualized. The strongest strain was found directly at the grain boundaries. Thereby, a periodic sequence of so-called hot spots were observed (Figure 4.9e), which can be assigned to dislocation

cores [142]. Additionally, the rigid body rotation provides a map emphasizing the shift of the adjacent grains by a delimited color separation at the hot spots.

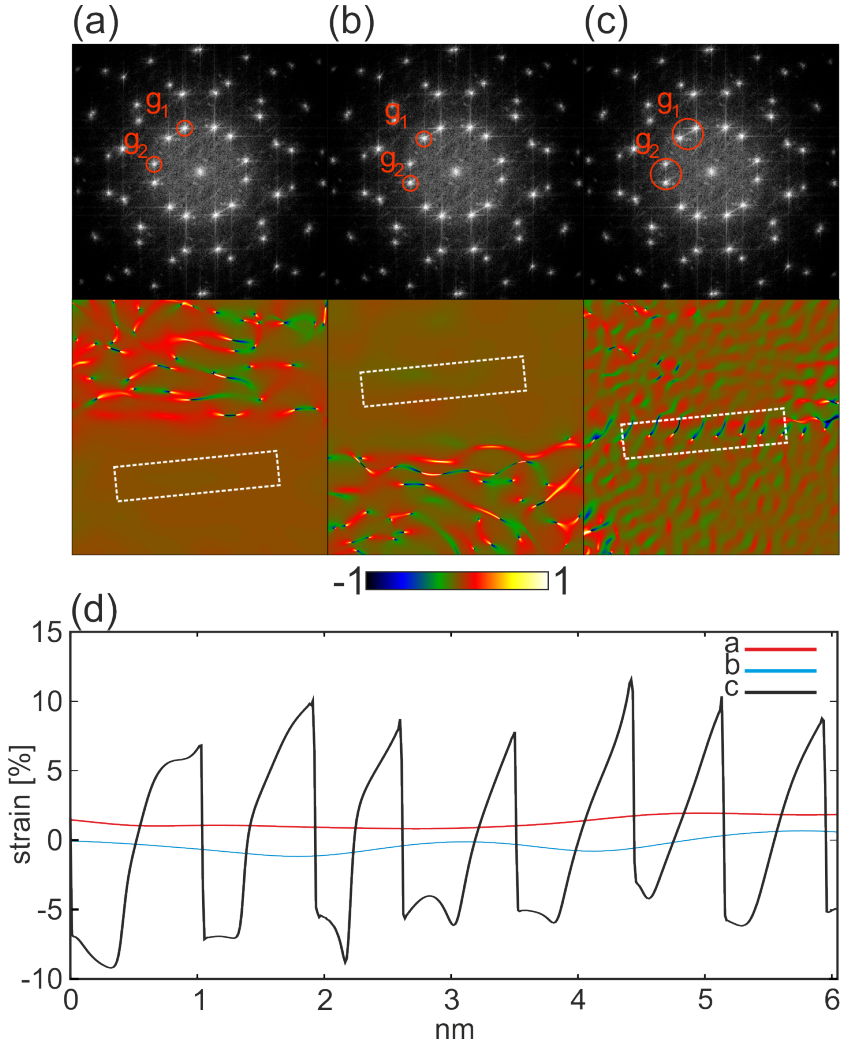

Figure 4.10: Series of shear strain maps (ϵ_{xy}) from the region of Figure 4.9a. (a, b) Respective single grain investigations vs. (c) grain boundary investigation (same as Figure 4.9c). (top) FFT pattern with selected g-vectors, (bottom) corresponding GPA maps. (d) Plotted strain for the marked regions in the strain maps.

A wavy colour gradient can be observed in both GPA maps. This behavior is a direct conseqeunce from the selection of the Lorentzian mask for g-vectors and can be considered as artifical signal. To illustrate the effect, shear strain maps were calculated for the respective single domains and compared with the map from Figure 4.9c, see the selection of g-vectors and the correlate maps in Figure 4.10. In both single domain investigations, the respective matrix exhibits an almost homogenous colour distribution, verifying a strong presence of strain only at the grain boundaries. Note, these maps fail to provide information of the direct grain boundary characteristics, stressing the necessity of the combined structural information of the grains for this region in GPA.

4.1.3 0-3 Magneto-Electric Nanocomposites with Metallic Nanoparticles

An approach for the fabrication of 0-3 nanogranular ME thin films focused on the combination of a dielectric matrix of AlN with magnetic cobalt (Co) nanoparticles. By developing a new concept of a gas aggregation cluster source (GAS) a precise tailoring was enabled for Co nanoparticles in terms of their size distribution and further to embed them by co-sputtering in the AlN matrix. In-depth information for the conceptualization, commissioning of GAS as well as the synthesis procedure for 0-3 nanogranular thin films are provided by Gojdka [117]. In the following section the structural investigations on a 0-3 ME demonstrator are discussed and evaluated particularly with regard to the macroscopic functionality.

Morphology and properties of Co nanoparticles

In a preliminary study the size distribution for different parameters of the GAS was investigated by TEM showing a virtually constant average of a cluster diameter between 4.6 - 5.4 nm and a standard deviation of $\sigma = 0.6$ - 0.8 nm, see Gojdka et al. [98]. At higher coverage of clusters on the substrate a tendency for agglomeration was observable. Both chemical and structural investigations, in terms of energy filtered - and HR-TEM, revealed a core-shell behavior for these agglomerates with metallic Co sourranded by an oxide layer of CoO resulting as passivation phenomenon at room temperature [143][13]. Further, for a thin film of the Co nanoparticles a ferromagnetic behavior with an increased coercivity was found at room temperature. This ferromagnetism stems from interparticle coupling, as explained in detail in [98].

0-3 Demonstrator System and AlN Texture

The 0-3 ME demonstrator is based on a quasi-co-sputtered AlN (matrix)/Co (nanoparticle) composite. For the structural investigations a cross-sectional specimen was prepared with the functional layer sequence of AlN (i) (300 nm) - AlN/Co (ii) (450 nm) - AlN (iii) (150 nm) as depicted in Figure 4.11.
A problem stated in former studies [144, 145] was the formation of CoN during the co-sputtering of AlN/Co inhibiting ferromagnetism. Chemical analysis using STEM nanoprobe EDX excluded the presence of CoN, as exemplary demonstrated in Figure 4.11 by the recording of elemental maps for a nanoscale area at the interface between region (i) and (ii). Further, the attached oxygen map shows only a noise signal, which makes an extensive oxidization of the Co nanoparticles within the AlN matrix highly unlikely. These structural results were confirmed by measurements of the ferromagnetic behavior as provided in [99].

[13] During the transfer from the GAS to the TEM the specimens were exposed to ambient atmosphere

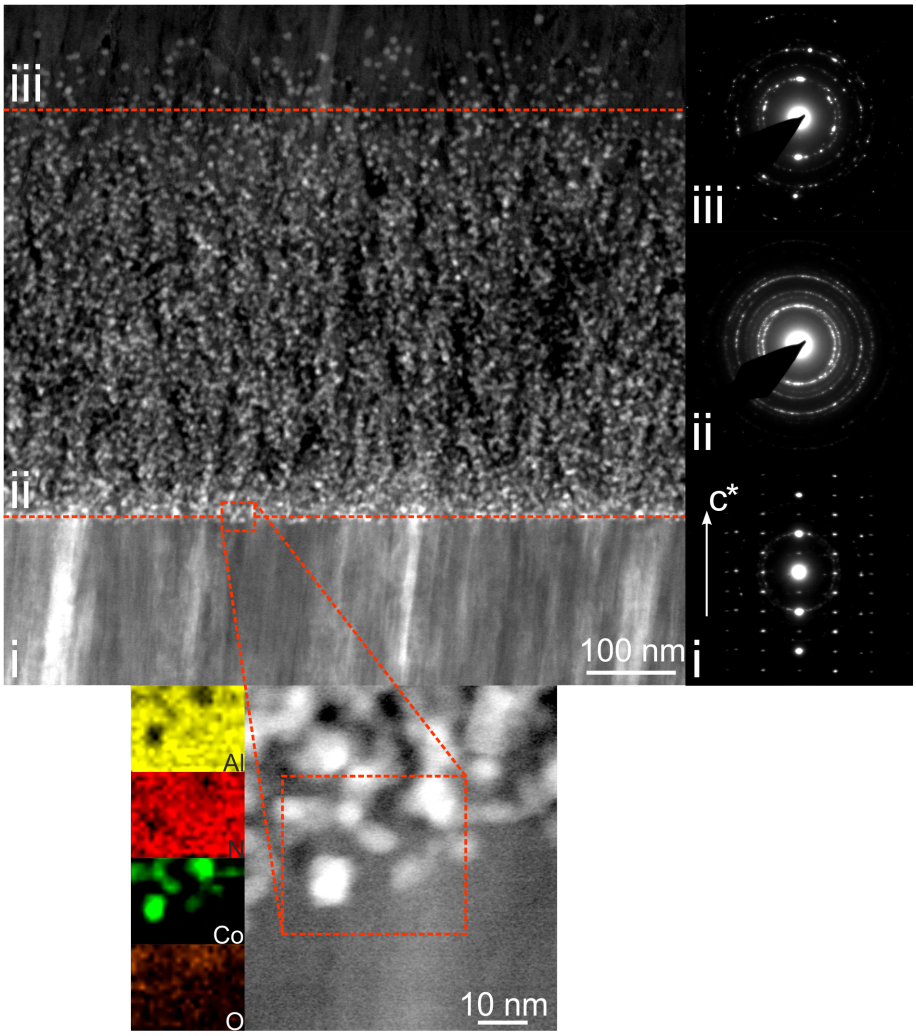

Figure 4.11: STEM Z-contrast image of a cross-section from a granular layer system consisting of 300 nm AlN (i)/ 450 nm AlN/Co (ii)/ 150 nm AlN (iii) deposited on Pt(1 1 1). Insets: associated SAED patterns, the arrow marks the growing direction of AlN along the [0 0 0 1] direction. (Bottom) Magnified view of the interface of region (i)/(ii) with chemical analysis using STEM EDX nanoprobe. See text for details.

As described in section 4.1.2 for determination of the piezoelectric capabilities of the nanogranular thin film, the [0 0 0 1] textured growth of AlN is the decisive parameter. The method of choice for investigating the AlN texture remains electron diffraction. A series of SAED patterns were recorded on circular areas restricted to 250 nm parallel to the growth direction for three distinct positions. Due to the dimensions of the layers and the positioning of the aperture, slight contributions from region (ii) can be found also in the other diffraction patterns. Neglecting this artifact, at first, region (i) reveals a strong [0 0 0 1] texture along the growing direction of the columnar AlN, as presented in the corresponding SAED pattern of Figure 4.11. The description of the features in this SAED pattern is analogues to the interpretation of Figure 4.1. Evaluating the radial intensity distribution for the

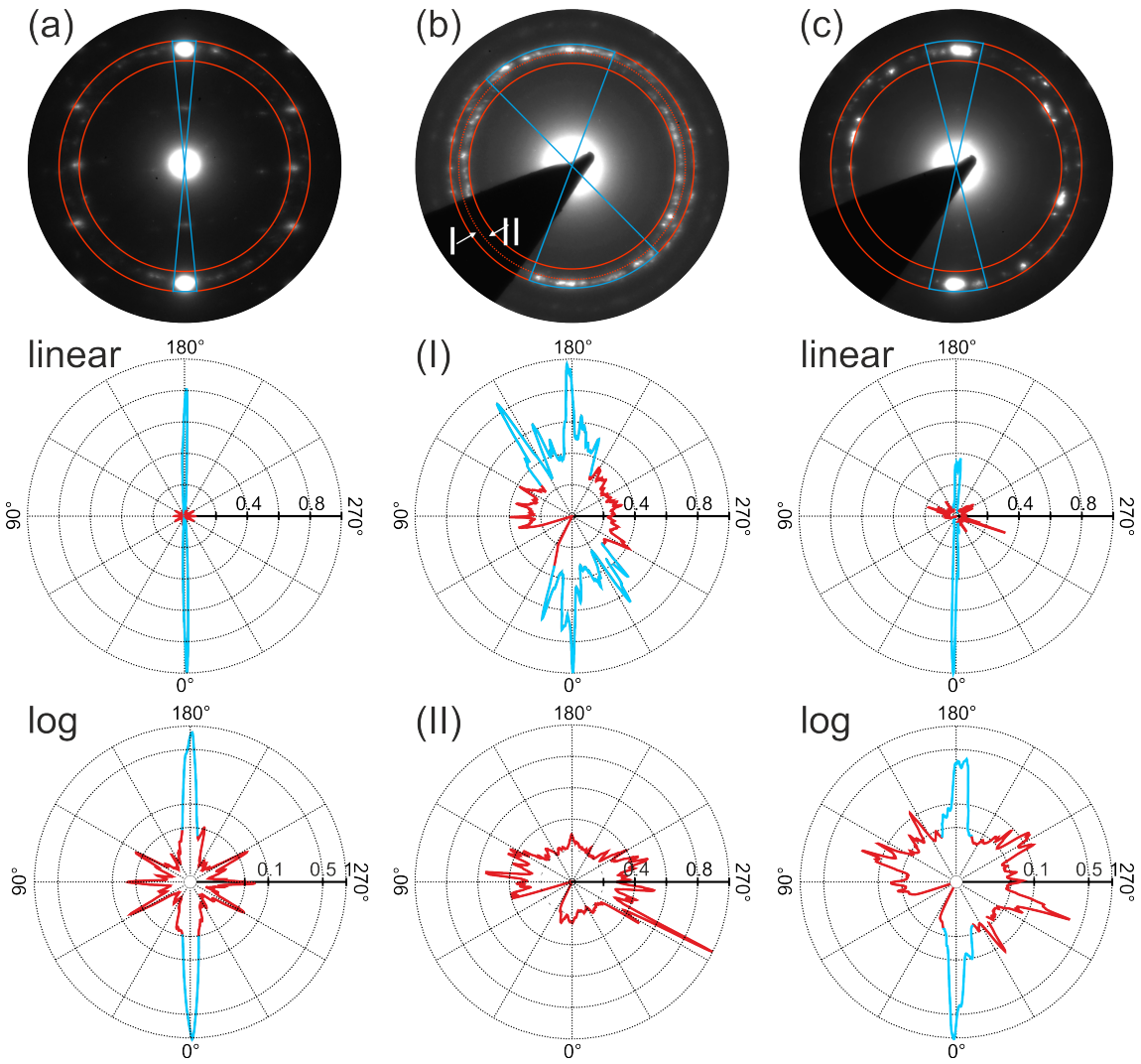

Figure 4.12: (Top row) Magnified view of the SAED patterns of Figure 4.11. (Middle, bottom rows) Quantitative analysis of the $\{0\,0\,0\,2\}$ texture. The intensity within a single pattern was radial integrated from smaller to larger red ring. The blue colour marks the radial spread of the $(0\,0\,0\,2)$ - Bragg intensities. (a) Region (i): radial plot with linear scale emphasising the $\{0\,0\,0\,2\}$ texture/ with logarithmic scale exhibiting contribiutions from region (ii) (see accentuated shoulder for the peak at 180°) and from $\{1\,0\,\bar{1}\,0\}$ Bragg intensities. (b) Region (ii): (I) radial plot with linear scale for the $\{0\,0\,0\,2\}$ planes/ (II) for the $\{1\,0\,\bar{1}\,0\}$ planes. (c) Region (iii): radial plot with linear and logarithmic scale.

$\{0\,0\,0\,2\}$ a quantitative view of the Bragg reflections is achieveable. Two pronounced peaks represent the texture of the layer and reveal a full width at half maximum (FWHM) for the peak at 0° of ca. 10%. However, the influence of multiple scattering phenonema and contributions from region (ii) must be taken into account, causing a broadening of these peaks. Thus, XRD studies were carried out exhibiting a rocking curve for continuous and pulsed sputtered AlN films with a FHWM of 2° [12]. The combination of XRD and SAED can be considered both as fingerprint for a

dominant c-axis oriented growth. In region (ii) Co nanoparticles were incorporated into the AlN matrix. The resulting structure shows a polycrystalline character with an almost vanished texture, cf. the correlated SAED pattern of Figure 4.11. From a magnified view of the SAED pattern depicted in Figure 4.12b, a concentration of the diffracted intensity on circle segments becomes perceivable with a radial spread of ca. 64° for Bragg reflections corresponding to the {0 0 0 2} planes. The third layer, again pure AlN, regains a strong {0 0 0 2} texture, cf. the SAED pattern for region (iii) of Figure 4.11 and the corresponding quantitative analysis of the Bragg intensities in the Figure 4.12c. From these data a less extented texture is observable in region (iii) with respect to region (i). The imperfect growth of the AlN columns can be attributed by the (ii)/(iii) interface, since the AlN/Co layer is not meeting the requirements of an adequate AlN substrate as the initial Pt {1 1 1} substrate. The filling factor of the Co nanoparticles in the into the AlN matrix was set to a relatively low value ($f = 0.02$) [12], causing already a considerable perturbation of the {0 0 0 2}. However, theorectally calculations demand a filling factor of ($f \approx 0.6$) as optimum for nanogranular ME nanocomposites [12]. From a structural point of view, the 0-3 approach based on a AlN/Co system seems not suitable for the production of thin films with a large ME effect. Further experimental and computational obtained results confirmed this prognosis for the properties of 0-3 nanocomposites [12].

4.2 Investigations on $(Ba_{0.7}Ca_{0.3}TiO_3)0.5$-$[Ba(Zr_{0.2}Ti_{0.8})O_3]0.5$

For the use of ferroelectric ceramics in piezoelectric applications, lead based perovskites were the materials of choice due to their remarkable properties [146, 147, 148]. One of the most important and, therefore, extensively investigated materials is $PbZr_{1-x}Ti_xO_3$ (PZT) exhibiting piezoelectric coefficients up to 600 pm/V [149, 150, 151, 152, 153]. To explain the origin of such high values, the complex structural nature must be regarded within this perovskite family. The key aspect for real structure-property-relation was stated to be the so-called morphotropic phase boundary (MPB), with 'morphotropic' describing phase transitions of a system as a result of compositional changes [154, 155]. Particularly for PZT (and later adopted for other ferroelectrics), Jaffe et al. [156] introduced the term MPB as separation between a tetragonal and rhombohedral phase. Both phases represent a specific distortion of the cubic $Pm\bar{3}m$ unit cell, in accordance with the perovskite group-subgroup relation, respectively, and causes a net dipole moment per unit volume or polarization [157, 158]. At the MPB, an instability of the polarization state is present which facilitates a polarization rotation under an external electric field [159]. This is considered as potential reason for an anomalously sharp maximum for the piezoelectric coefficients and the dielectric constant at the MPB [159]. Further, the tetragonal and rhombohedral phases are mediated at the MPB by monoclinic phases [160, 161, 162], representing an overall lowering of the symmetry and thus promoting the polarization rotation [162]. Even triclinic symmetries were postulated by theoretical stud-

ies [163]. However, in fields of biological applications and for the environment the usage of lead is a delicate subject due to its toxicity. An promising alternative is $(Ba_{0.7}Ca_{0.3}TiO_3)$ 0.5-$[Ba(Zr_{0.2}Ti_0.8)O_3]$0.5 (BCZT) with a piezoelectric coefficient of 620 pm/V at the MPB, as stated by Liu and Ren [164]. The structural details of the material still appear puzzling: In a first study three distinct phases (rhombohedral, tetragonal, cubic) were described with the coincidence of all those at a triple point in the corresponding phase diagram [164, 153], see Figure 4.13a. The latter was adjusted by an orthorhombic phase, which separates the rhombohedral and tetragonal phases [165], cf. Figure 4.13b. Consequently, the triple point would turn out to be a quadruple point, which is in contradiction to Gibbs phase rule. Keeble et al. [165] suggested for this case a phase convergence region instead of a point, where the orthorhombic phase is accompined with a high instability gradient. Both, presence and instability gradient of the orthorombic phase are considered as beneficial for the piezoelectric properties of the material [165]. The transitions (cubic-to-tetragonal, cubic-to-rhombohedral, and tetragonal-to-orthorhombic symmetry) can all be rationalized by a group-subgroup relation for perovskites. A direct relation between the rhombohedral (trigonal space group: $R\bar{3}m$ [165]) and the orthorhombic (space group: Amm2 [165]) phase is not existing. Monoclinic phases could serve as intermediate phases similar to PZT and other lead-based perovskites [160, 166] although no experimental evidence was stated until now.

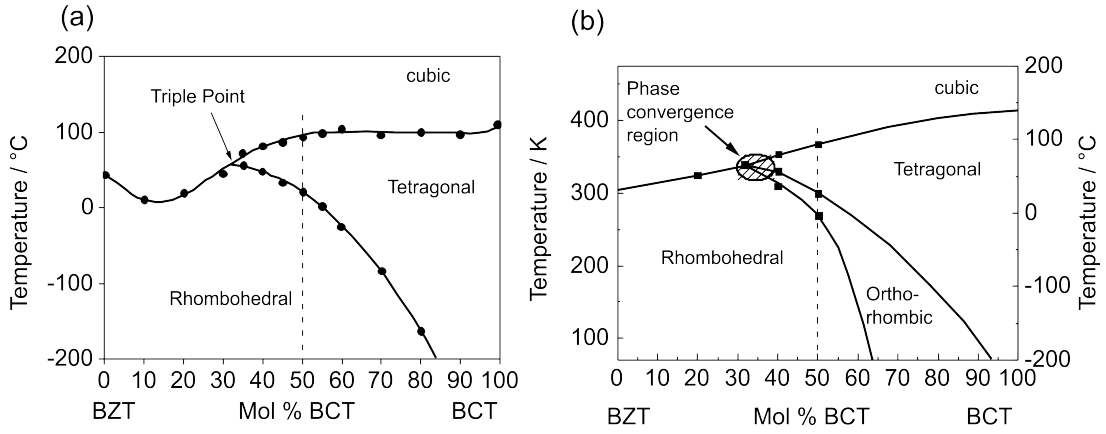

Figure 4.13: Phase diagram for the pseudo-binaries $Ba(Zr_{0.2}Ti_{0.8})O_3$ and $Ba_{0.7}Ca_{0.3}TiO_3$ stated by (a) Liu and Ren [164] and (b) Keeble et al. [165]. Taken from [167].

Although the structural characteristics of BCZT are apparently not fully understood yet and, particularly, a lack of substantial real structure investigations must be notified, encouraging properties were determined. In the following, first comprehensive TEM measurements are provided on bulk and thin film samples for BCZT. Also an interpretation of these data will be given in the context with the macroscopic properties[14] of both specimens.

[14]The synthesis and property measurements of BCZT were performed by Andre Piorra and can be found in [167].

4.2.1 Bulk Specimen

The phase diagram of BCZT is set up by the pseudo-binaries $Ba(Zr_{0.2}Ti_{0.8})O_3$ (BZT) and $Ba_{0.7}Ca_{0.3}TiO_3$ (BCT) [102, 164, 153]. At room temperature the pure Zr-rich BZT and the Ca-rich BCT phases exhibit a rhombohedral (trigonal)[15] (space group: $R\bar{3}m$) and a tetragonal (space group: $P4mm$) symmetry [165], respectively. First in-situ XRD investigations performed by Liu and Ren [164] showed that the distortions of the corresponding unit cells are marginal regarding an ideal cubic (space group: $Pm\bar{3}m$) symmetry. The determined lattice parameters of BCZT for the tetragonal phase were found to be a = 4.007 Å, c = 4.025 Å, c/a = 1.005 at 32 °C and a = 4.00 Å, $\alpha = 89.88°$ for the rhombohedral phase at -63 °C[164]. At 14 °C the presence of the MPB and, hence, the coexistence of tetragonal and rhombohedral phase was stated [164]. The latter finding is in agreement with the XRD results obtained for the BCZT bulk systems presented by Piorra et al. [102].

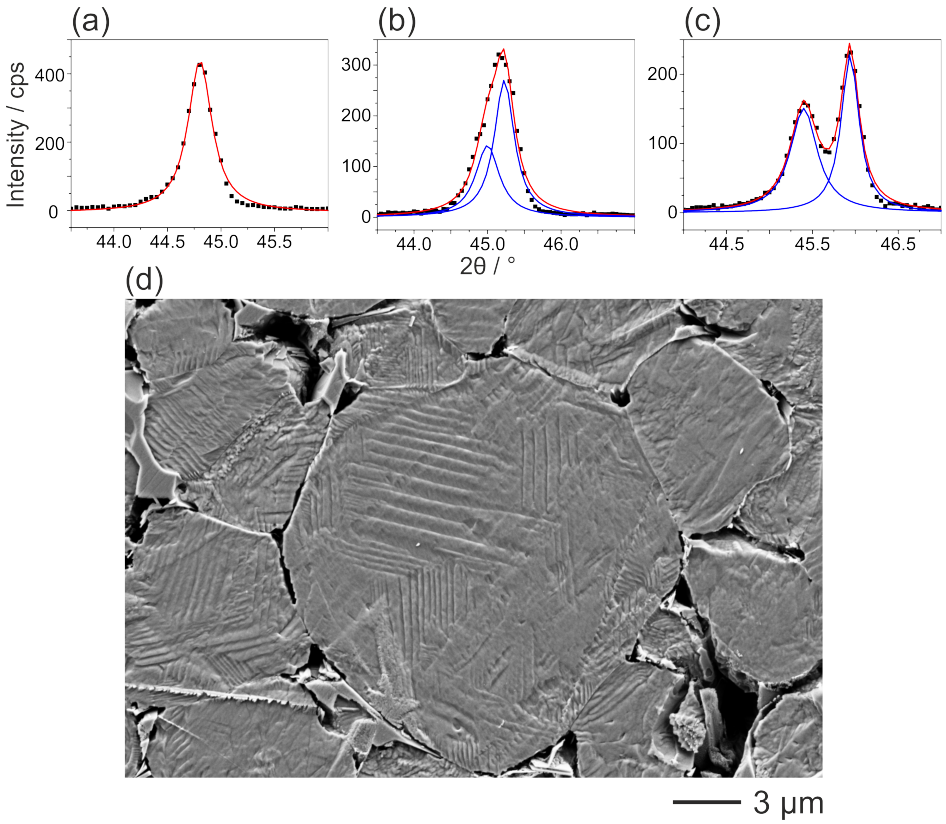

Figure 4.14: XRD data set for selected range around 45° within the respective (a) BZT, (b) BCZT, and (c) BCT pattern: Black dots - experimental data, red - fit of the experimental data, blue - computational obtained identification of single peaks. (d) SEM micrograph of a BCZT bulk sample with lamella as characteristic features at a compositional ratio of 0.5BZT-0.5BCT. Partially excerpted from [167].

[15] Note that the term 'rhombohedral' describes a lattice system, the corresponding crystal system is *trigonal*.

To illustrate the structural nature of the assumed MPB, a comparision of the XRD data of BCZT with BZT and BCZT is provided for the peaks around 45° in Figure 4.14a, b, c[16]. The single peak of the rhombohedral BZT phase (Figure 4.14a) can be assigned to (0 0 2), while the peaks of the tetragonal BCT phase (Figure 4.14c) were identified as (0 0 2) and (2 0 0), respectively. With a 0.5BZT-0.5BCT compositional ratio at about room temperature, the structural characteristics within XRD pattern differ with respect to the former pure phases. In this intermediate case, a coexistence of the tetragonal and rhombohedral phase was claimed, which is expressed by superposition of the characteristic peaks of the pure components [164]. Indeed, with a closer inspection of the {2 0 0} peak (Figure 4.14b) such a behavior seems to be present.
Another argument for the coexistence of multiple phases is the presence of lamellar shaped domains in a microscale regime, see Figure 4.14d. TEM studies performed by Gao et al. [153] showed two important results in this context. First, a tendency of miniaturization into nanodomains is observable within the lamellas as part of a so-called domain hierarchy, which is known to occur in lead consisting perovskites [148, 168]. Second, the formation of different symmetries for adjacent domains was proven with suggested rhombohedral and tetragonal phases. Although such an interpretation is crystallographically plausible, the presented data did not exclude orthorhombic nor monoclinic symmetry, which must be considered particularly concerning the findings of Keeble et al. [165] on an orthorhombic phase directly at the 0.5BZT-0.5BCT composition.

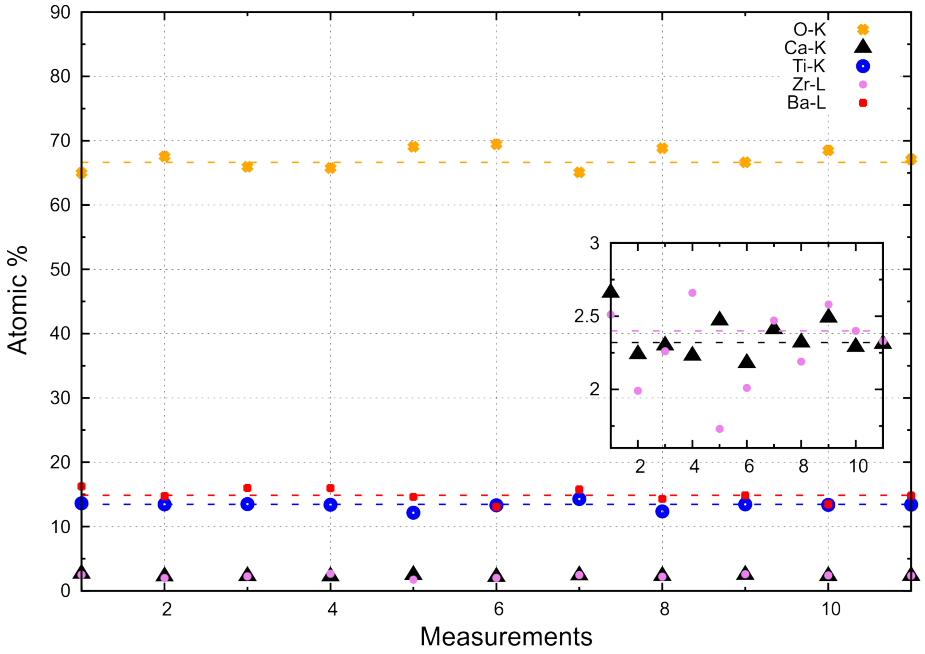

Figure 4.15: Nanoprobe EDX measurements for the chemical composition of different positions within the bulk specimen. The dashed lines represent the respective medians for the single elements. Inset: Detailed view on Ca-K and Zr-L.

The structural investigations of this study start at this point and adress the possi-

[16]The data presented in Figure 4.14 was recorded and processed by Andre Piorra [167].

bilites and issues of TEM investigations on the BCZT systems. As preliminary result, chemical observation are presented in Figure 4.15 via STEM-EDX nanoprobe, demonstrating an almost consistent composition for all examined areas. For the bulk specimen chemical measurements were performed via EDX nanoprobe. The experimental data is in good agreement with the assumed stoichiometry.

Evaluating the Influence of Ca and Zr in PED and HRTEM

For a determination of the symmetry of the bulk specimens a combined approach of electron diffraction and HRTEM was applied to a grinded bulk specimen. A representative PED tilting series on comparable grains is depicted in Figure 4.16 with the first three patterns (zone axis [1 1 1], [2 1 0], [1 1 0][17]) recorded from the same area.

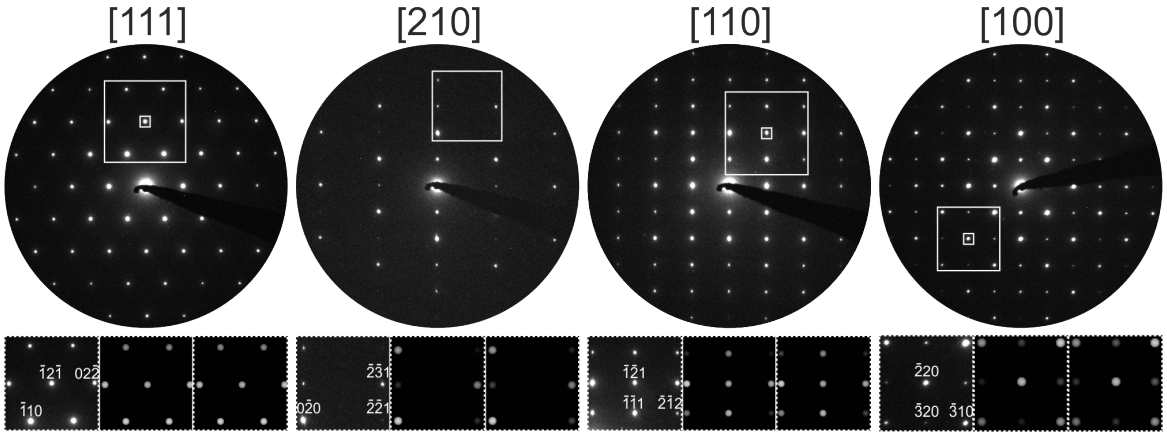

Figure 4.16: PED tilting series of a BCZT bulk specimen. Rows below a respective pattern: (light) Magnified view of the marked area in the pattern, compared with simulations of (center) BCZT and (right) $BaTiO_3$. The patterns for the [1 1 1], [2 1 0], [1 1 0] zone axes were recorded from the same grain. The pattern along [1 0 0] belongs to another comparable grain.

The evaluation of the different orientations of the BCZT structure shows a cubic system with no compelling indication for distortion of the main structure within the patterns. Calculation using the software *Crisp* and *Endeavour*[18] confirmed a cubic system with the space group $Pm\bar{3}m$. However, the simulation was based on the formula type ABX_3 with A = Ba, B = Ti and X = O. In order to improve the quantification of the experimental results Ca and Zr were introduced into the model. The occupancy factor for the atoms was determined by the ratio $(Ba_{0.7}Ca_{0.3})(Ti_{0.8}Zr_{0.2})O_3$. The different experimental patterns were compared with the two cubic models: BCZT model including Ca and Zr and a $BaTiO_3$ [169] model. The marks in Figure 4.16 demonstrate the investigated areas. For each area quantitative intensity ratios were calculated and compared to the corresponding ratios of both models. To enhance

[17]The zone axis refer to a pseudocubic notation.
[18]These programs allow an *ab inito* structure calculation from electron diffraction pattern.

the significance of the results additional patterns with the same orientation were investigated, respectively. Thus, statistical fluctuations in the measurements could be reduced. In all cases, the BCZT model was verified to be in a better agreement with the experiments than the pure $BaTiO_3$ model, with the restriction that the differences between both models were relatively low.
For a further evaluation of the cubic BCZT model, a high resolution tilting and defocus series was performed, cf. Figure 4.17. As demonstrated an excellent agreement between the experiments and the simulations can be observed.

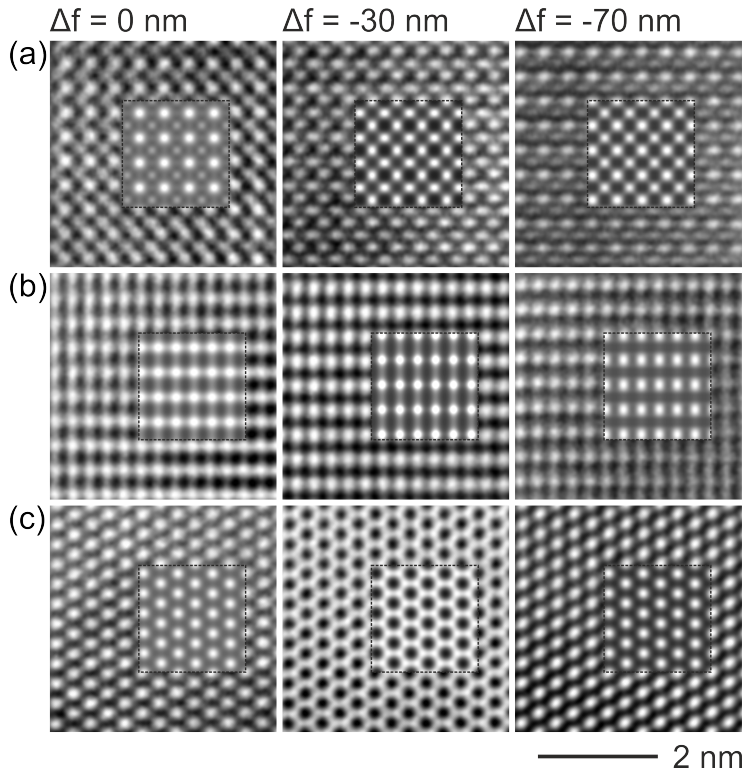

Figure 4.17: HRTEM tilting and defocus series of a BCZT bulk specimen. The experimentally obtained micrographs were filtered and compared with BCZT (space group: $Pm\bar{3}m$) simulations (insets). Rows: zone axis (a) [1 0 0], (b) [1 1 0], (c) [1 1 1]; specimen thickness (a) 5.23 nm, (b) 5.69 nm, (c) 4.87 mn. Columns objective lens defocus 0 nm, 30 nm, 70 nm, respectively.

A phase transitions is expected for BCZT at ca. 20 °C for a rhombohedral-to-tetragonal transition, and at ca. 90 °C for a tetragonal-cubic transition [164]. As no clear tetragonal or rhombohedral structure was observed, a potential heating induced by beam irriadiation must be considered which exceeds the temperature at the specimen over the transition temperature [170, 171]. Cryo experiments were performed using PED for the same grains at room temperature and at -171 °C for the zone axes [1 0 0] and [1 1 1]. At both temperatures the PED patterns showed no significant difference. According to these results it must be assumed that the lattice distorion of the tetragonal and rhombohedral structures are too marginal to be detected by PED and HRTEM causing the observation of cubic or pseudocubic symmetry. In other studies CBED was used to provide reliable symmetry informa-

tion about perovskite and particularly BCZT system [153, 166]. Thus, this technique was also applied to the bulk specimen.

CBED Studies on BCZT thin film specimens

With the suggested centrosymmetric space group of $Pm\bar{3}m$ a corresponding point group of $m\bar{3}m$ must be present for a cubic systems demanding a $4mm$ symmetry along [1 0 0]. For the determination of the point group CBED was performed additionally to the other ED techniques, cf. Figure 4.18a.

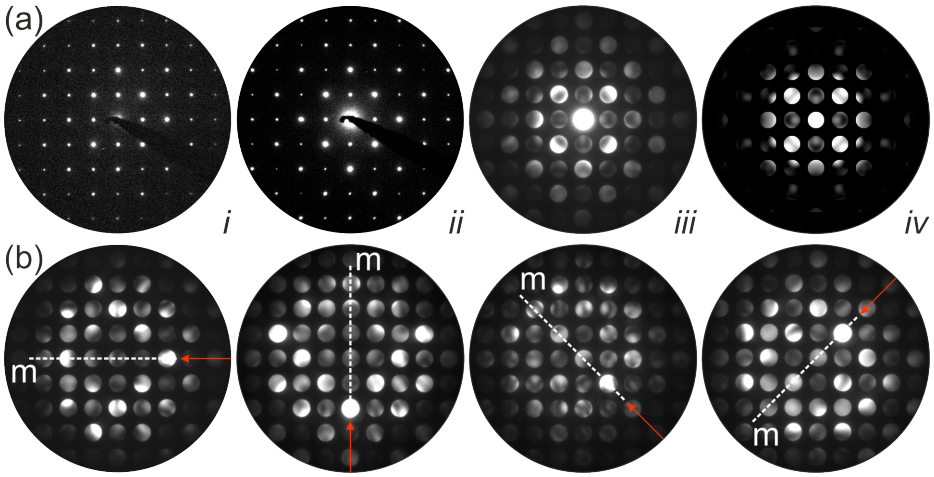

Figure 4.18: (a) Bulk: Comparision of three different ED techniques for the [1 0 0] direction (cubic symmetry). experimentally obtained (i) SAED, (ii) PED, (iii) CBED, (iv) simulated CBED pattern. The investigated area for the CBED pattern was within the illuminated area of SAED and PED. (b) Symmetry investigations of the CBED pattern. CBED pattern of (a) recorded in off-axis condition, preserving only one respective symmetry plane (marked by red arrow). The dashed lines mark the position of a mirror plane.

Tilting the CBED pattern of Figure 4.18a into an off-axis condition along the <0 1 0> and <0 1 1> directions, respectively, the presence of the symmetry elements (namely mirror planes) can be investigated separately, as demonstrated in Figure 4.18b. The horizontal and vertical arrows mark tilts along <0 1 0> and the vertical arrows along <0 1 1>. In all cases a mirror plane can be assumed (dashed lines in Figure 4.18b), indicating the presence of the cubic structure. Comparing the experimentally obtained CBED of Figure 4.18a - (iii) with a simulated CBED pattern based on the cubic BCZT model (Figure 4.18a - (iv)), a good agreement seems to be achieved. However, a closer inspection of the experimental data exhibits slight variations in the intensities of mirrored discs in many instances, which could be more expressed in areas with higher specimen thickness. For the simulation of the CBED pattern a thickness of 80 nm was used. Additionally, a tetragonal BCZT model[19] was used for the simulation of further CBED pattern[20]. The latter exhibited only a considerable

[19] Based on a tetragonal $BaTiO_3$ structure with a $P4mm$ space group [172].
[20] A simulation of a CBED pattern with tetragonal symmetry is depicted in Figure 4.22.

deviation to the cubic pattern after setting the specimen thickness >> 100 nm. It must be assumed that the investigated areas were rather thin with respect to other studies: [173, 174, 153], section 4.2.2 - *CBED Studies on BCZT Thin Films.*
According to the domain structure observed in SEM, the XRD measruements as well as the observed ferroelectric properties of the bulk specimen, the presence of a cubic phase is a negligible phenomenon, which is most probably introdcuded due to the preparation and the selection of grains for TEM investigations.

Local Defect Phenomenon

In some high resolution studies the presence of a superlattice phenomenon was detected within the bulk sample, as depicted in the HRTEM micrograph and the corresponding FFT pattern of Figure 4.19a. Approaches to investigate this superstructure by PED were not successful, as these structural variations are too small compared to the illuminated area (aperture size 100 nm) to be detected. This effect is expressed in the HRTEM contrast by alternating intensities of the bright spots as demonstraded in Figure 4.19b.

EDX nanoprobe measurements excluded a substantial deviation of the chemical composition, as depicted in measurement 2 of Figure 4.15. In order to obtain three dimensional information of the structure and the symmetry, a tilting series was performed, see Figure 4.19c. The indexing of the (h k l) and [u v w] indices are based on a pseudocubic symmetry. The additional Bragg intensities of the FFT pattern along [1 0 0] are commensurable and placed at the 1/2{h k 0} positions, which indicates a doubling of the unit cell. The two other patterns exhibit also commensurable superlattice spots, however, less pronounced and with faint intensities. In the FFT pattern along [1 1 0] a modulation vector of 1/2{h k l} was determined and along the viewing direction [1 1 1] intensities were oberseved at the commensurable n/4{1 1 1} positions (with n as natural number). For the latter case a quadrupling of was indicated. Moreover, spots at 1/2(0 k 0) were also found after evaluating a defocus series of the FFT patterns along [1 1 1] for the same region. The presence of 1/2{h 0 l} spots was not detected. According to generally low intensities of the superlattice spots their existence cannot be excluded. The presence of commensurable superlattice reflections can originate from ordering processes of A- and B-site cations or octahedron rotation [175, 158]. For complex perovskites, such as BCZT, the order-disorder behavior was reported to appear in nanosized regions [176, 177]. In that case, additional spots, at the <1 1 1> positions, were found in an ordering process of B-site cations during conversion of $Pm\bar{3}m$ to its type IIb subgroup $Fm\bar{3}m$ [176, 178, 179]. The symmetry reduction is a k2-type (klassensgleiche) and causes the basis transformation 2a, 2b, 2c of the unit cell.
By using this doubled and face centered unit cell, a simulation of all intensities within the experimental FFT patterns cannot be calculated along the zone axes [1 0 0] and [1 1 1]. Also the quadrupling of the <1 1 1> direction is not explainable by the unit cell. Further symmetry reductions were performed: First the $Fm\bar{3}m$ symmetry is

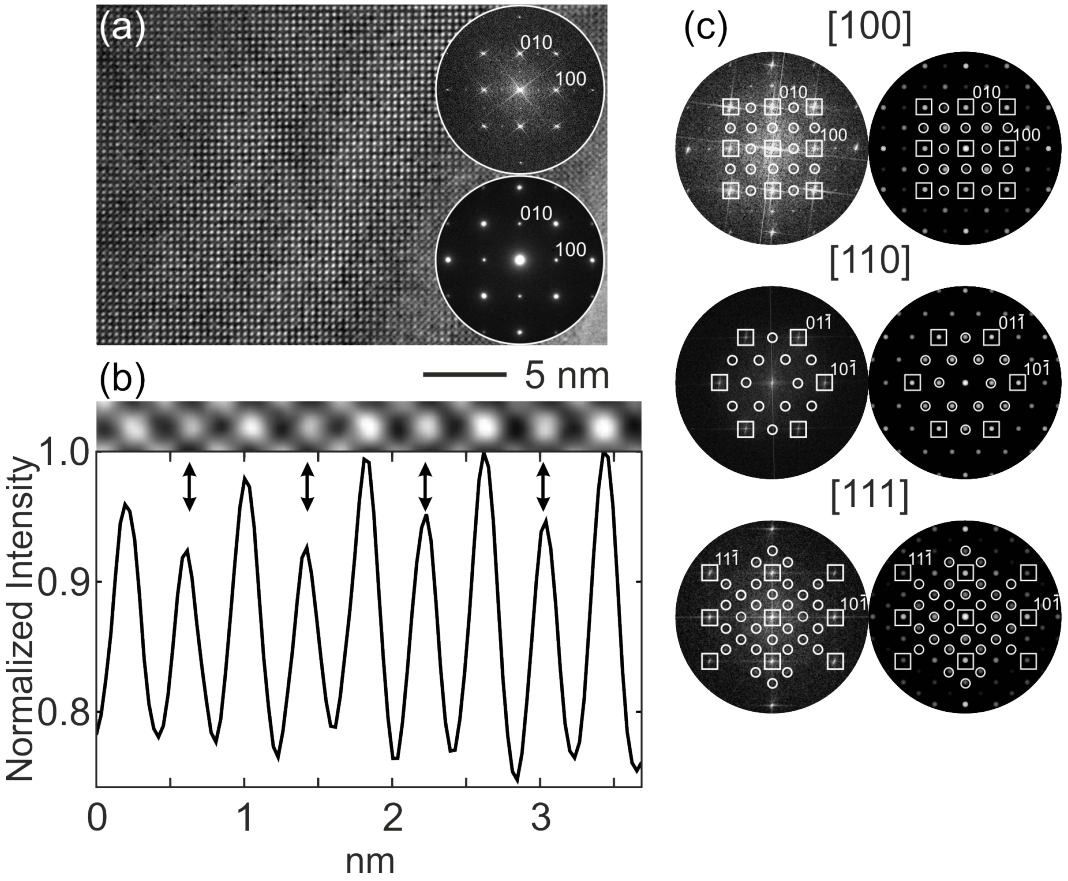

Figure 4.19: Locally restricted superlattice phenomena in the bulk system. (A) HRTEM micrograph along the pseudocubic [1 0 0] zone axis, insets: (top) correlated FFT pattern with additional Bragg intensities, not present in the PED pattern (which includes the area of high resolution investigation). (b) Magnified view of the real structure exhibiting an alternating contrast of the bright spots, emphasized by an intensity scan of the area. (c) (left) FFT tilting series: squares indicate fundamental Bragg intensities of a pseudocubic structure, circles mark superlattice Bragg intensities. (right) Tilting series of simulated diffraction pattern based on a cubic $Fd\bar{3}m$ symmetry.

transformed into the k4-subgroup $Pn\bar{3}m$ (a, b, c, type IIa), followed by the transformation into the type IIb subgroup $Fd\bar{3}m$ (2a, 2b 2c). The lattice parameter of the obtained unit cell is a = 16.08 Å. Corresponding simulations of electron diffraction patterns showed a good agreement with the experimental results, see Figure 4.19c. Thus, all patterns show a good agreement with the simulations under considering ordering of the cations. A similar case was described for $Ca_{1-x}Sr_xNbO_3$ systems by Istomin et al. [180]. As the superlattice phenomena were found at thin areas close to the edges of BCZT grains, also oxygen vacancies must be considered as reasonable origin of quadrupled unit cells.

4.2.2 Investigations on a Thin Film Specimen

A thin film BCZT layer was fabricated on a Pt (1 1 1) substrate, as shown in Figure 4.20. A columnar growth of BCZT grains perpendicular to the substrate interface can be observed with a more or less pronounced wedge shaped character of these columns. In following the most prominent structural features will be discussed.

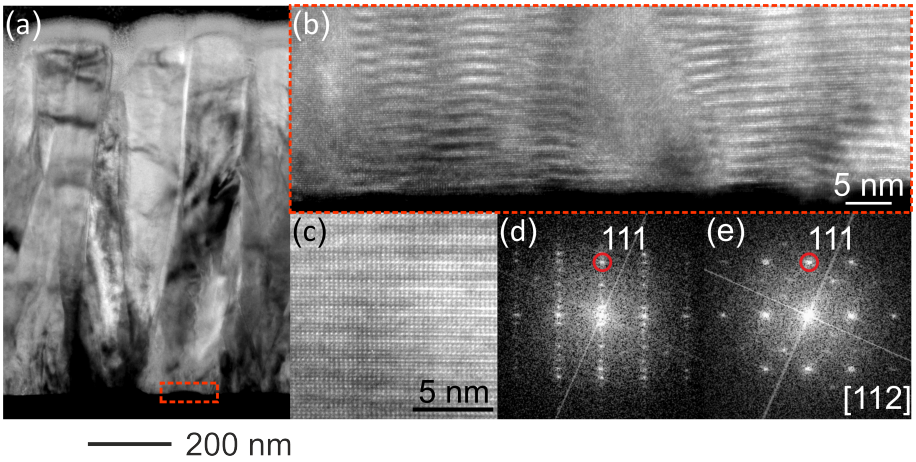

Figure 4.20: (a) TEM bright field image of a BCZT layer sample deposited on Pt. (b) Magnified view of the marked area in (a) show the presence of a modulation. (c) HRTEM microgah of a stripes. (d, e) Comparision of FFT patterns with additional Bragg intensities due to the modulation vs. the fundamental pseudocubic structure along the [1 1 2] zone axis.

Modulation Along the Pseudocubic [1 1 1] Direction

In some instances the presence of lamellar fringes was observed propagating parallel to the Pt surface, which is expressed by an alternating bright-dark contrast, as shown in Figure 4.20b. Chemical investigations excluded a diffusion of Pt into the fringe dominated areas and also variations of the composition on a larger scale. Calculating the FFT of a HRTEM micrograph from such an area (see Figure 4.20c, d), the presence of satellite intensities were identified along the fundamental {1 1 1} Bragg intensities of the perovskite structure, additionally illustrated with another FFT calculated form a defect-free region (Figure 4.20e) along the same [1 1 2] zone axis.

A detailed inspection of the fringe area exhibits a periodic arrangement of a seven layer (7L) sequence, as demonstrated in the HRTEM micrograph of Figure 4.21a. Evaluating the corresponding FFT and a correlated SAED pattern, the satellites can be interpreted as modulation [181] of the ideal pseduocubic structure with a modulation vector of $1/7 <1\,1\,1>$ along different viewing directions, cf. Figure 4.21b. Further, the enlarged views of the diffraction patterns reveal an incommensurable behaviour of the satellite reflections, which is particularly visible in the SAED pattern. The incommensurability indicates high order satellites. In annular dark field

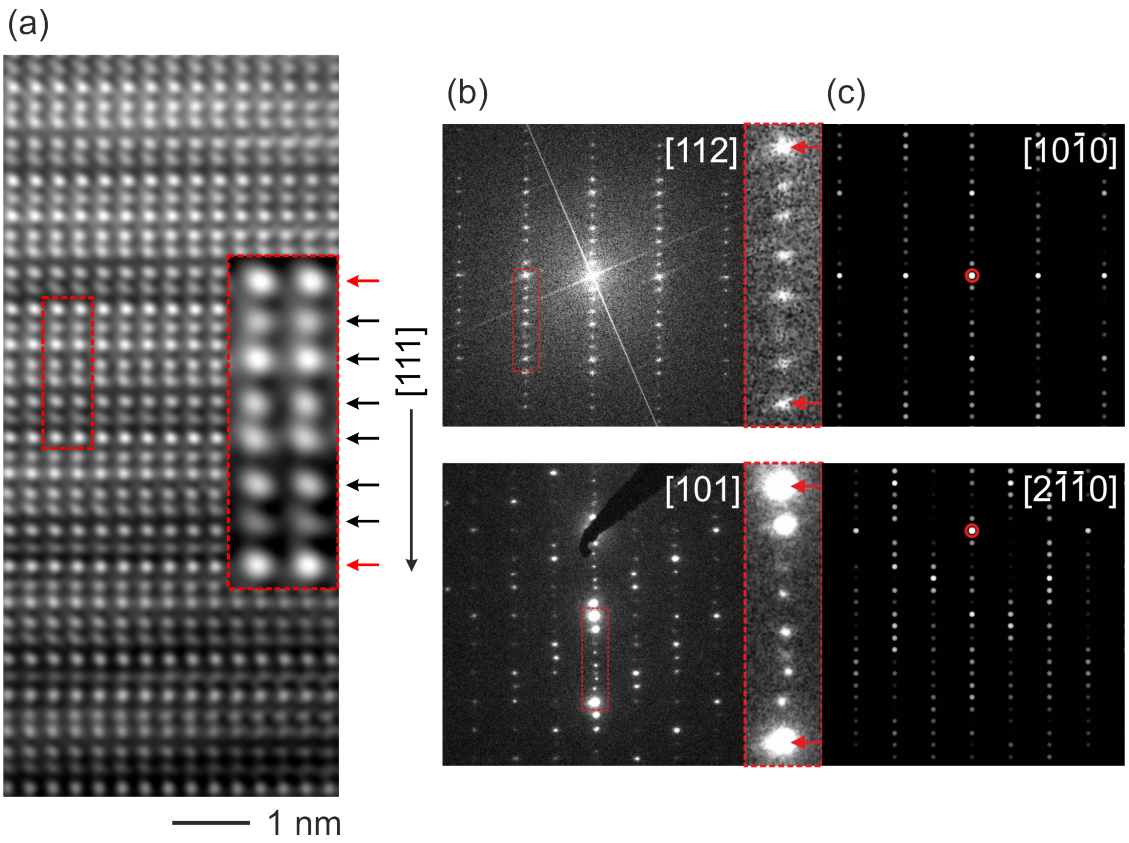

Figure 4.21: BCZT thin film: (a) HRTEM micrograph of a potential polytype structure, the read box exhibits a 7L periodicity along the zone axis [1 1 2]. The red arrows mark repeating layers, the further black arrows emphasize the other single layers. (b) Observation of the modulated BCZT structure along (top) [1 1 2] in a FFT pattern and (bottom) [1 1 0] in a SAED pattern. The modulation vector is identified as $1/7<1\,1\,1>$ using pseudocubic notation. The red arrows mark the fundamental {1 1 1} Bragg intensities in the respective pattern. (c) For rationalization of the modulation, a comparison is provided with simulated electron diffraction pattern of a 7H-$Ba_7Nb_4MoO_{20}$ polytype. The structure is set in the trigonal $P\bar{3}m1$ space group; the zone axis [1 0 $\bar{1}$ 0] corresponds to the pseudocubic [1 1 2] direction and [2 $\bar{1}$ $\bar{1}$ 0] to [1 0 1]. The red rings mark the center of the simulated patterns.

(ADF) STEM Z-contrast images an alternating contrast similar to the fringes of Figure 4.20c were detected. This result may serve as indication for a compositional segragation or ordering. However, in ADF-STEM images structural contributions due to Bragg reflections is not completely excluded. To verify the STEM data chemical investigations on an atomic level are mandatory calling for methods as aberration corrected HRSTEM-EELS [182]. A possible interpretation of the experimental findings can be provided by assuming polytypism. The definition of the international union of crystallography reads [183]: "An element or compound is polytypic if it occurs in several different structural modifications, each of which may be regarded as built up by stacking layers of (nearly) identical structure and composition, and if the modifications differ only in their stacking sequence.[...]"

In the literature polytypes were discussed for several pervoskites or perovskite-related oxides, e. g. [184, 185, 186]. In those cases, the stacking sequences were alternating between cubic (c) and hexagonal (h) layers or, expressed in terms of polyhedra, corner sharing (c) and face sharing (h) octahedrons along a certain direction. The study of Garcia-Gonzalez et al. [184] described a 7H-$Ba_7Nb_4MoO_{20}$ polytype, in which the number (7) is declaring the sequence size and the capital letter (H - hexagonal) the crystal system[21] of the polytpe. The stacking sequence was given by (hhchhcc) along the crystallographic c-axis ([0 0 0 1] direction) for the trigonal $P\bar{3}m1$ space group (lattice parameters a = 5.8644(2) Å and c = 16.5272(4) Å). Particularly, the c parameter shows similarities with the experimentally found length of the modified 1/7 <1 1 1> vector in the BCZT thin film (calculated distance ca. 16.1Å). In order to rationalize the further similarites between the experimentally obtained 7L-structure with the 7H-polytype model, electron diffraction pattern were simulated based on the 7H model. The zone axes $[1\,0\,\bar{1}\,0]$ and $[2\,\bar{1}\,\bar{1}\,0]$ of the trigonal setting correspond with the (pseudo)cubic [1 1 2] and [1 0 1] directions, respectively, and were compared with the experimental data, see Figure 4.21c. Although a good match between the modulation vectors is observable, the intensities of the reflections show significant differences[22]. In the 7H model the Bragg reflections are commensurable. Apparently, the atomic species differ, but a variation of the modulated layer sequence must also be considered in the BCZT thin film system with respect to the 7H model. For a substantial prediction of the layer sequence for BCZT and the fully polytype further experimental investigations with aberration corrected high resolution and electron diffraction will be applied as part of future works.
In another context, perovskites with the stoichiometry of AA'BB'O_6 were reported with similar modulations as structural feature [175]. As stated by García-Martín et al. [187] the compositional modulation is related to the A-site cations. Interestingly, a twinning of the octahedral tilt system was always accompanied with the modulation in the same studies, which was only shown by neutron powder diffraction measurements [175, 187, 181]. The presence of twinning is assumed as reduction of strain, which is generated by the different compositional domains [175].

CBED Studies on BCZT Thin Films

Electron diffraction studies were performed on the BCZT thin film for the determination of symmetry. As the ED pattern series along the pseudocubic [1 0 0] direction demonstrates in Figure 4.22a, the SAED pattern was strongly influenced by thickness effects, resulting in almost uniform intensities for the Bragg reflections. Although a successful reduction of these dynamical effects was achieved by

[21] There are also polytypes descriptions using 'R' for rhombohedral. In this case a trigonal crystal system is present with the specification of a rhombohedral Bravais lattice. Further, a footnote in [183] should be noted:"The *Ad-Hoc* Committee is aware that this notation does not conform with that of *International Tables for Crystallography* (1983) or *Structure Reports* but recommends its retention since it is embedded in the literature. It is, however, recommended that use of these symbols be confined exclusively to polytype description terminology."

[22] A scientifically useful comparison of the intensities can only be considered by comparing the experimental and computational obtained SAED pattern.

PED, the corresponding pattern exhibited no concret evidence for a tetragonal nor trigonal (rhombohedral) symmetry. Applying CBED to an associated area, the corresponding pattern revealed a symmetry with the two dimensional space group *pm*. Keeping the pseudocubic notation the mirror plane in this pattern can be identified as (0 0 1) or (0 1 0). A further verification for the presence of only one mirror plane is provided in Figure 4.22b. The pattern was tilted along the [0 1 0] and [0 0 1] directions, respectively. While a mirror plane is still detectable after the tilting, the tilt along the perpendicular directions caused a clear breakdown of mirror symmetry, see marks in Figure 4.22b. Also potential {1 1 0} mirror planes were excluded in the same manner.The experimentally obtained CBED pattern of Figure 4.22a - (iii) was further compared with a simulated CBED pattern (specimen thickness was set to 160 nm), which is based on a tetragonal BCZT model with the space group $P4mm$ (Figure 4.22a - (iv)). The simulations rationalize the experimental findings. Hence, the tetragonal symmetry seems to be an adequate candidate for the interpretation of the CBED pattern.

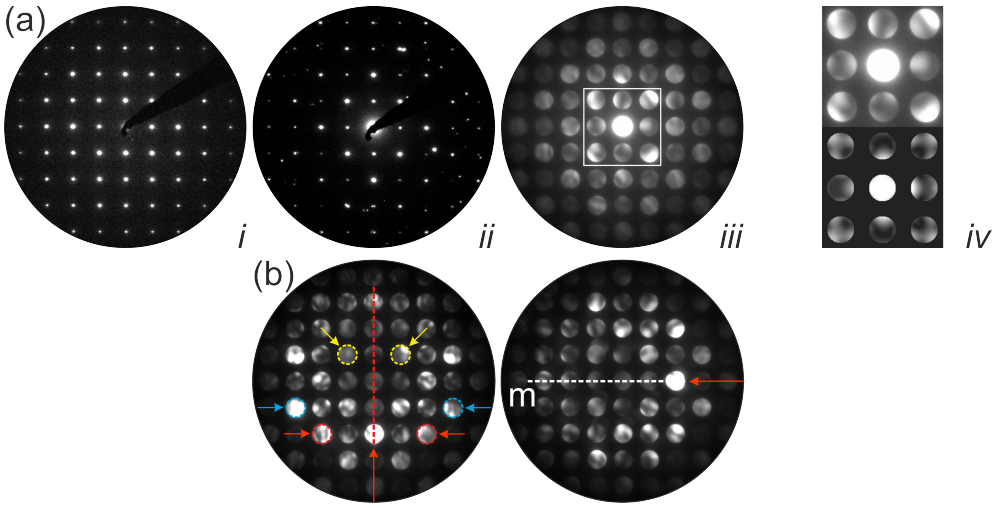

Figure 4.22: (a) BCZT thin film: Comparison of three different ED techniques for the [1 0 0] direction (assuming pseudocubic structure): experimentally obtained (i) SAED, (ii) PED, (iii) CBED, and (iv) Rationalization of the experimental CBED (top) with a simulation (bottom). The investigated area for the CBED pattern was within the illuminated area of SAED and PED. (b) Symmetry investigations of the CBED pattern. (b) CBED pattern of (a) recorded in off-axis condition, after deliberate tilting away from pattern center (red arrows). (left) No mirror plane observable: red dashed line demonstrats the expected position of the mirror plane; correlated discs (see circles and arrows) show considerable differences. (right) A (0 0 1) or (0 1 0) mirror plane (dashed line (m)) is obserable, indicating the two dimensional space group *pm*.

With a closer inspection, a non-perfect symmetry is present for the CBED pattern including the mirror plane. An interpretation for similar results was provided by Tsuda et al.[173]. In these studies, CBED measurements demonstrated an order-disorder character in phase transformations for $BaTiO_3$. The non-perfect symmetry

within the CBED pattern may results from local contributions of coexisting trigonal (rhombohedral) symmetry, which are restricted to a size of few nanometers [173]. It should be noted, that the experimental findings and the suggested presence of a morphotropic phase boundary (MPB) [166] allow the possibility of interpreting the CBED data with a monoclinic symmetry (space group Pm). The observed patterns, including mirror planes (0 0 1) or (0 1 0), would then be assigned to the monoclinic zone axis [h 0 l] or [0 h $\bar{\text{l}}$]. Minute studies of Wang et al. [166] were performed on hierarchical micro-/nanoscale domain structure confirming the existence of a monoclinic Pm phase in (1-x)Pb($Mg_{1/3}Nb_{2/3}$)O_3-x$PbTiO_3$ also by using CBED. However, in the present investigations clear evidence are missing for the monoclinic symmetry. Due to the relevance of monoclinic structures and hierarchical domains for the properties of perovskite materials at the MPB, comparable in-depth studies with respect to those of Wang [166] and Tsuda et al. [173] will be subject of future studies.

Twinning Defects

Investigations on the wedged shaped colums revealed the presence of domains separated by planar defects, as depicted in the HRTEM micrograph of Figure 4.23. Calculating the FFT pattern of the respective domains two mirrored areas (i, iii) can be identified. Both regions are oriented along the [1 1 0] zone axis and are mirrored along the {1 1 1} planes, see marks in Figure 4.23. These domains are not directly adjacent, but enclose another domain (area (ii) in Figure 4.23). In the latter, a superposition of the Bragg intensities from area (i) and (iii) was determinded, with area (iii) contributing as minority component. Similar to the satellite reflections descripted in section 3.3.1 - *Nanospike Morphology and Resulting TEM Features*, additional intensities appear as superposition introducd phenomena and are located on commensurable positions within the FFT pattern of area (ii) (see yellow marks). The two twin boundaries t, b (twin plane {1 1 1}, respectively) separate the pure single domains from the superposition domain, as the differences in the respective high resolution contrasts of region (ii) (left) and region (iii) (right) demonstrate within the HRTEM micrograph of Figure 4.23.

To analyse quantitatively the origin of the respective Bragg intensities from the calculated FFT (ii) of the defect area (Figure 4.23), a modified supercell/SPS approach (as introduced in section 3.3.1) was carried out. For the calculation of the supercell a pseudocubic symmetry was assumed.
Similar to the ZnO nanospike case the experimentally observed main viewing direction [1 1 0] for BCZT must coincide with a principle axis for the supercell. This can be established by a two-step symmetry reduction from $Pm\bar{3}m$ (a = 4.0191 Å) to the t (translationsgleiche)-subgroup $P4/mmm$ (c/a = 1) and afterwards to $C2/mmm$ (a-b, a+b, c) (also t-subgroup). In the orthorhombic $C2/mmm$ unit cell the {1 1 1} twin plane is transformed to {1 0 1}. A straightforward realization of the rectangular supercell can be achieved using the transformation matrix

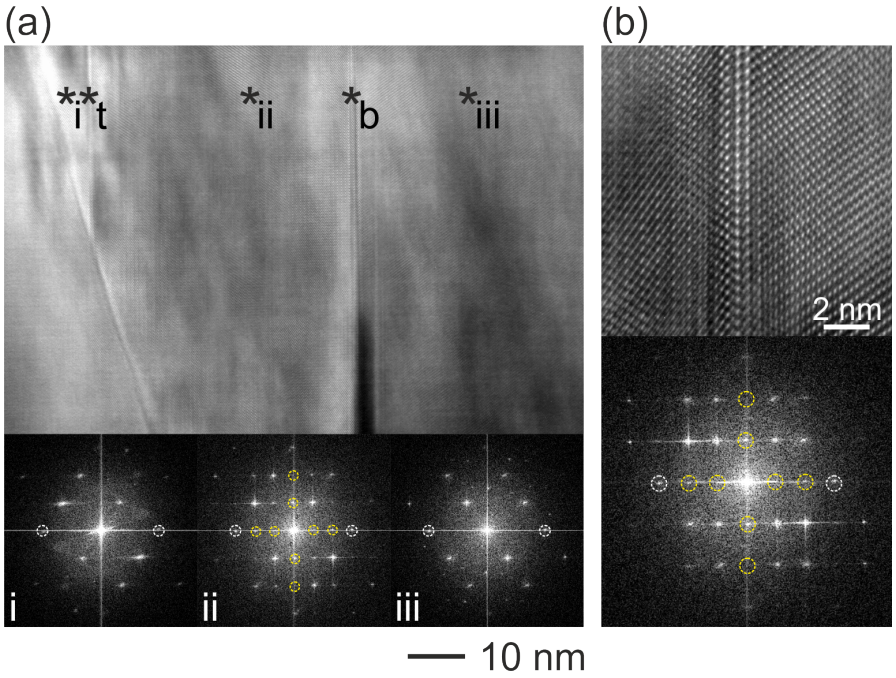

Figure 4.23: (a) BCZT thin film: HRTEM mircorgaph of BCZT domains separated by twin boundaries along [1 1 0]. Region (i, iii): single perovskite domains, Region (ii) superposition of domains oriented equivalent to region (i) and (iii). The twin boundaries t, b separate the domains with the twin planes {1 1 1} (white circles). Yellow circles: Bragg intensities appearing as superposition phenomena. (b, top) Magnified edge-on view at the twin boundary with (bottom) associated FFT pattern.

$$\mathbf{P} = \begin{pmatrix} 2 & 0 & -2 \\ 0 & 1 & 0 \\ 2 & 0 & 4 \end{pmatrix}$$

The lattice parameters for the supercell are a = 13.9226 Å, b = 5.6839 Å, c = 19.6895 Å with α, β, $\gamma = 90°$.The a-axis of the supercell coincides with the twin plane {1 1 1} of the pseudocubic structure. Generating a second supercell with inverted x-parameters and superimposing it with the former supercell a SPS is created with the experimentally observed twinning/ superposition phenomena as incorporated features. A separation step is omitted as the main emphasis lies on the investigations of the Bragg intensities.

Two respective ED pattern were simulated based on a kinematical and dynamical approach for the pseudocubic zone axis [1 1 0] and compared with the experimental findings, cf. Figure 4.24. The experimental obtained SAED patterns were recorded on an edge-on view of a twin boundary separating two single domains, see Figure 4.24a, c. The SAED pattern recorded directly at the interface region (Figure 4.24b) is in excellent agreement with the kinematical simulation (Figure 4.24d). The specimen thickness of experimental patterns can be considerd as relativly high as the primary beam shows a similar intensity with respect to the Bragg reflections. However, additional reflections were not observable like in the FFT pattern of Figure

4.23b. Assuming a superposition of two [1 1 0] oriented domains in a dynamical simulation, the additional Bragg reflections appeared on the commensurable lattice positions of the twin pattern (see yellow marks in Figure 4.24d). Thus, the initial assumption as superposition phenomena was confirmed for these reflections.

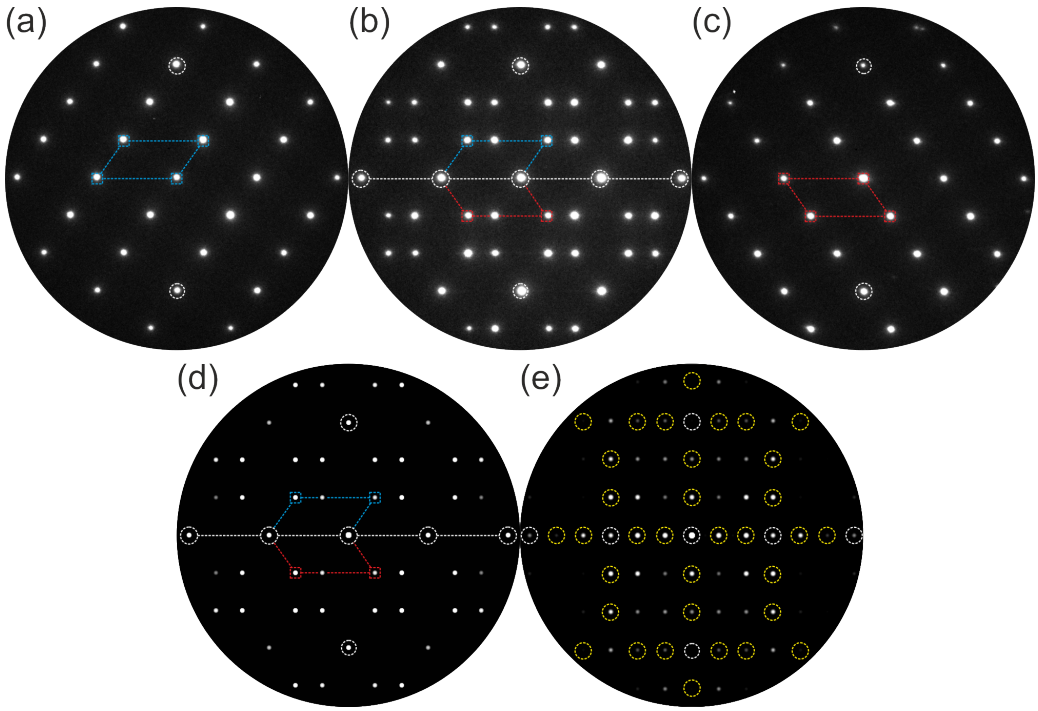

Figure 4.24: (a, b, c) Experimental SAED studies of twinned domains with the twin boundary at a {1 1 1} along the [1 1 0] zone axis: (a, c) single domains of BCZT and (b) twinned region. Blue and red marks depict the perodicity of the respective domain, white circles emphasize coinciding Bragg reflections of both domains with {1 1 1} as twin plane (also marked by dashed line) and {1 1 2} planes perpendicular. (d, e) Simulated diffraction pattern based on a SPS (see text for details): (d) kinematical simulation, (e) Dynamical approach (specimen thickness 22.7 nm) with additional reflections originating from superpositioning (yellow marks), comparable with experimental observations from Figure 4.23.

The experimentally observations predict a complicated three dimensional domain structure. However, an unambiguous interpretation of the superimposed contrast cannot be provided. A possible explanation is multiple twinning of the {1 1 1} planes in terms of triplets.
The formation of (polysynthetic) {1 1 1} growth twins is a well-known characteristic for $BaTiO_3$ bulk and thin films with cubic and tetragonal symmetry [188, 189, 190]. In particular, extensive research was carried out for a crystallographic interpretation of the twin structure as well as a detailed interpretation of high resolution contrasts [188, 191, 192, 193, 190]. According to these studies, the defect structure can be described as $\Sigma = 3$ twin boundary with coinciding 1 1 1 and 1 1 2 reflections in ED diffraction patterns along the zone axis $[1\,\bar{1}\,0]$ [188], see also Figure 4.23c.

Further, it was shown, that Ti-O octahedra share common faces when twinning involves a BaO_3 layer for cubic and tetragonal structure [188, 192]. Minute aberration corrected analysis provided information of the atomic configuration directly at the twin interface [192, 193, 190] for $BaTiO_3$.
These results can be transferred in many instances analogue to BCZT. However, to obtain in-depth information about the atomic configuration directly at the interface region, further aberration corrected HRTEM investigations are essential.

Properties Differences between Bulk and Thin Film

The main difference[23] between the bulk and the thin film sample manifests in the change of dielectric permittivity with respect to the temperature and frequency, as demonstrated in Figure 4.25.

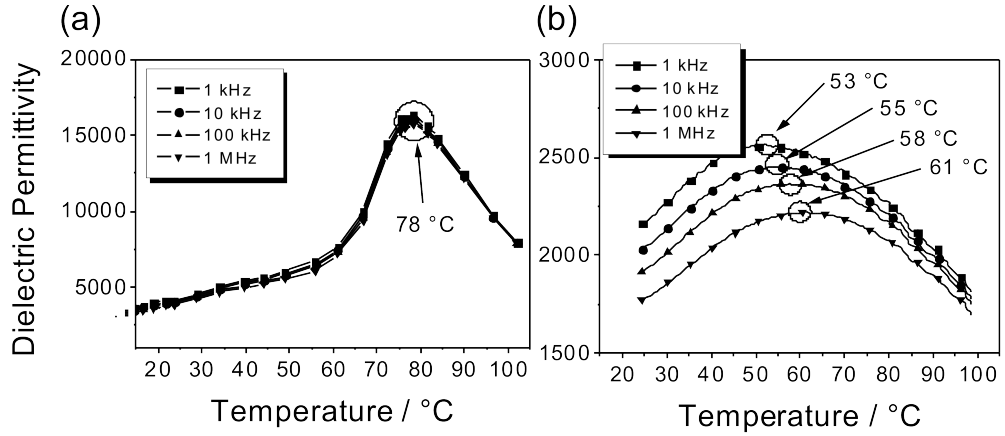

Figure 4.25: Dielectric permittivity in dependence of the temperature and recorded for different frequencies. (a) Bulk and (b) thin film system.

In the case of the bulk specimen (Figure 4.25a), a frequency independent maximum for the permittivity is observed at 78 °C which represents the Curie temperature and, hence, the transition from ferroelectric to paraelectric behavior. For the thin films (Figure 4.25b), a frequency dependency for the Curie temperature is observable, further, accompanied with a general decrease of this transition temperature. Also a considerable peak broadening and lower values for the maxima were detected with respect to the bulk samples. The characteristics of the dielectric permittivity indicate a relaxor ferroelectric for the BCZT thin film. The broadening of the peaks in Figure 4.25b can be related to the presence of grain/domain boundaries [194].
In the work of Bokov [176] two interesting aspects were provided regarding the crystal structure of relaxors with comparable stoichiometry. The first expression states: "[In the real complex perovskite crystals and ceramics the quenched compositional disorder is often inhomogeneous, e. g. small regions of the ordered state are embedded in a disordered matrix.]". This is strongly reminiscent of the sporadically

[23] The investigations on macroscopic properties were perfomred by A. Piorra and are detailed described in [167].

and spatially limited appearing of the found modulation. However, as the nature of the modulation is not yet fully understood, this structure-property relation must be considered as highly speculative at this point in time.
The second extracted aspect of Bokov is an example:"[In $Pb(B'_{1/2}B''_{1/2}O_3$ perovskites the ordering of B-site ions converts the disordered [paraelectric] $Pm\bar{3}m$ structure into the ordered $Fm\bar{3}m$ structure in which B' ions alternate with B" ions along the <1 0 0> directions (1:1 ordering). [...] These chemical nanoregions [several nanometers] give rise to weak superlattice reflections (the so-called F-spots).]". Again, a comparable case was observed in the structural experiments on BCZT with the transition of $Pm\bar{3}m$ to $Fd\bar{3}m$ symmetry (with the lattice parameter a = 16.08 Å). The suprise is the appearing of the effect in the bulk system, which is not showing the discussed relaxor behavior. The verification of this observation and a possible interpretation by relaxor behavior must be part of dedicated studies in future works.

4.2.3 Outlook - Future Studies on BCZT

For future investigations two strategies should be pursued for BCZT. In the first one, a focus must be placed on aberration corrected microscopy, as this technique allows a more precise determination of the atomic configuration at the nanoscale:
An aberration corrected HRTEM micrograph of the BCZT is depicted in Figure 4.26a. To illustrate the increase in information within this experimental data, a series of high resolution simulations were carried out, which were both based on the same tetragonal[24] structure model (Figure 4.26b - (i)). Via the calculation of the same projected potential (Figure 4.26b - (ii), two different high resolution micrographs were obtained, see Figure (Figure 4.26b - (iii) and (iv). For the latter, only blurry high resolution contrasts is observable, failing to picture the details of the structure model. Particularly, the position of light atoms (namely oxygen) cannot be detected. This changes with the use of aberration corrected microscopy. The contrast of the micrograph in Figure 4.26b - (iii) exhibits great similarities with the structure model and improves, therefore, the interpretation of experimental data. Apparently, studies on structural features, such as defects (e. g. twin boundaries, modulations), greatly benefit. In Figure 4.27 two investigations on ferroelectric materials are presented from Urban et al. [28], demonstrating the enormous capabilities of this method[25]. It should be noted, that the effect of spontaneous polarization is less express for BCZT (or $BaTiO_3$) with respect to PZT (Figure 4.27a). Thus, performing such type of investigation will become challenging for BCZT.
The second strategy should be the structure and symmetry investigations on different length scales:
Particularly, for the thin film samples a strong variation of the piezoelectric coefficient was observed from 80 pm/V to 200 pm/V [167]. In all these investigated specimens, the previously discussed features were traced. A possible difference within the

[24] The space group is $P4mm$
[25] "[However, understanding the results is generally not straightforward and only possible with extensive quantum-mechanical computer calculations.]" [28].

thin films may be found in the grain structure and/or in the alternating presence of defect structures. For a proper evaluation, a statistical analysis is indispensable. Using the ACOM device, a large-scale data acquisition is enabled with the advantageous of a TEM-specific resolution. Thus, the detection of prominent features is simplified, which can be part of further investiagtions.

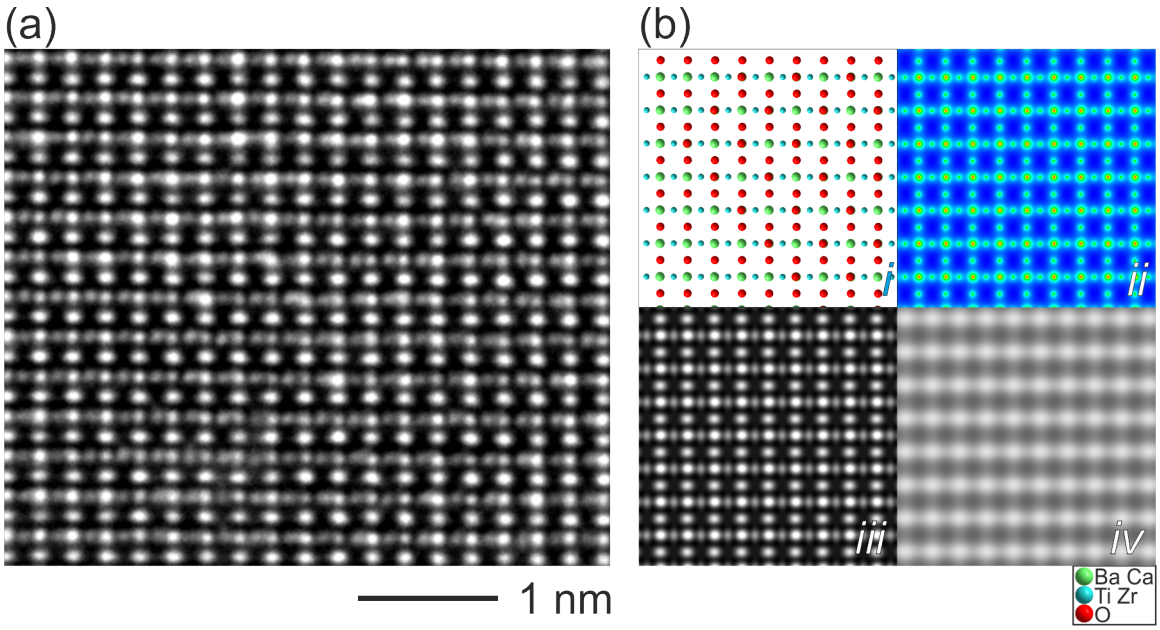

Figure 4.26: (a) Experimental data of BCZT: aberration corrected HRTEM micrograph of a thin film specimen along the pseudocubic zone axis [1 1 2]. (b) Simulated data of BCZT: (i) Structural model, (ii) corresponding projected potential, (iii) aberration corrected HRTEM contrast (Δf = 9 nm | specimen thickness ca. 4 nm), (iv) HRTEM contrast (C_S = 1.15) (Δf = –58 nm (Scherzer focus)| specimen thickness ca. 4 nm). For all panels the viewing direction is along the pseudocubic [1 1 2] direction.

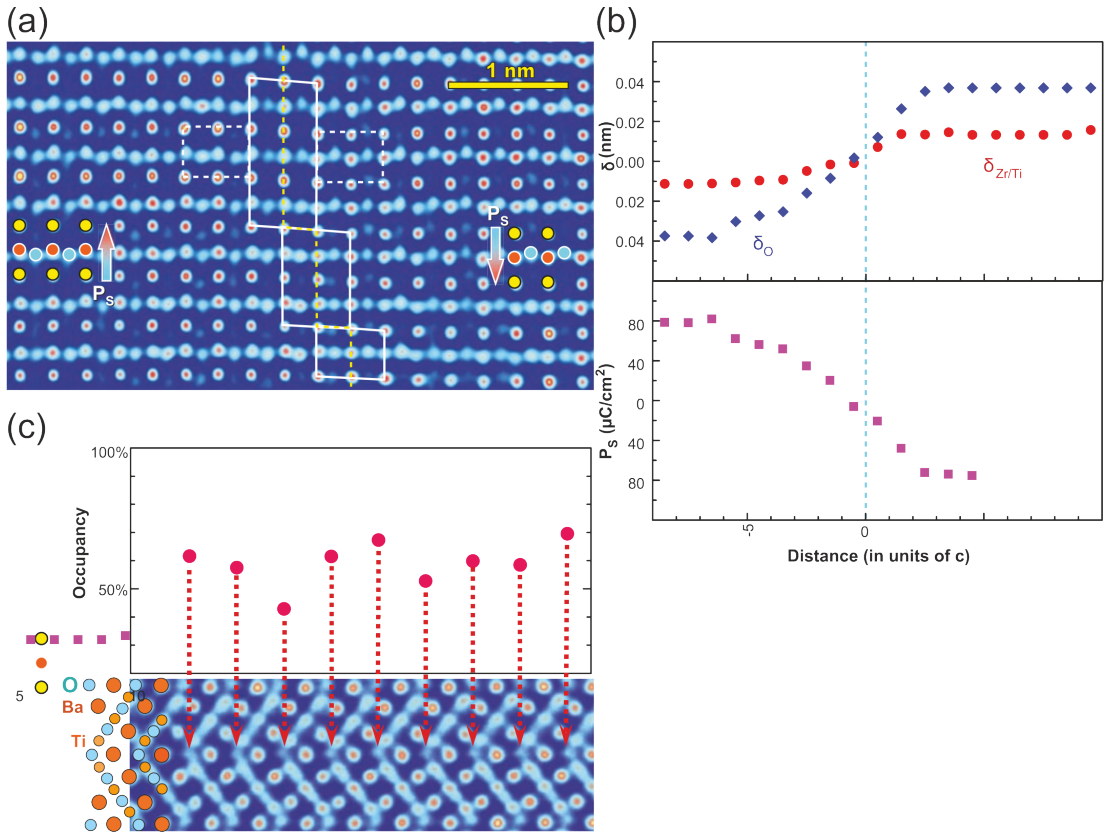

Figure 4.27: "[(a) Transversal inversion polarization-domain wall in ferroelectric PZT. Arrows give the direction of the spontaneous polarization, which can be directly inferred from the local atom displacements. The shifts of the oxygen atoms (blue circles) out of the Ti/Zr-atom rows (red circles) can be seen directly, as well as the change of the Ti/Zr-to-Pb (yellow circles) separation. (b) Atomic resolution measurements of the shifts of oxygen (δ_0), and titanium/zirconium ($\delta_{\mathrm{Ti/Zr}}$) atoms in a longitudinal-inversion domain wall and the value of the local polarization P that can be calculated from these data. (c) $\Sigma 3\{1\,1\,1\}$ twin boundary in $BaTiO_3$. All atomic species, including oxygen, can be identified. The atomic resolution is confirmed by image simulations. These indicate that, because of negligible point spread, neighboring atoms have no effect on the intensity measured in a given atomic position. This provides the basis for the quantitative site-occupation measurements. The local intensity values indicate that, in the individual oxygen-atom columns seen end-on, only between about 40 and 70% of the sites are occupied. This provides evidence for oxygen deficiency, which is presumed to have a detrimental influence on electronic properties.]" [Excerpted from [28].]

4.3 Summary: Piezoelectric Thin Films

Two possible candidates were investigated for the role of the piezoelectric component in the ME sensors. In the case of the hexagonal AlN, the crucial parameter for achieving relevant piezoelectric properties is the deliberate adjustment of a strict c-axis ([0 0 0 1] direction) oriented growth. This crystallographic characteristic was investigated on thin films composed by columnar grains via methods of electron diffraction. Representative and comparable samples were prepared along two perpendicular perspectivs: A cross-sectional view enabled a vertical investigation of the growth behaviour from the common substrate/ AlN interface to the surface of the AlN thin film. Conventional (SAED) and advanaced (PED) diffraction methods revealed in the corresponding patterns a pronounced (0 0 0 1) texture along the growing direction, evidencing the c-axis growth. Further, these PED patterns exhibited a superposition for the zone axes of the domains $[u\ v\ t\ 0]$ with the joined rotation axis of [0 0 0 1]. Hence, for the columnar grains a high degree of freedom was detected for the azimuthal directions.
In a basal view the crystallographic information was obtained by ACOM measurements. In principle, the cross-sectional observations were confirmed. Additionally, grains were visualized with a non c-axis oriented growth, which was explained by the formation of subgrains as part of partial coalescence of AlN islands during the growth procedure.
With piezresponse measurements exhibiting areas with low piezoelectric signals for the same thin films, it appears plausible to associate this property result with grains tilted apart from a deliberate [0 0 0 1] growth.
Processing the ACOM data, high angle misorientations of grains to each other can be assigned in several instances with Σ values from the CSL theory. GPA analysis of grain boundries showed the presence of strain exclusively at the common boundary of the grains.
In HRTEM analyses defect structures were frequently observed features. A quantitative study of stacking mismatch boundaries (SMB) was carried out using the description of Xin et al. [123] and implementing it into a supercell approach. The resulting idealized model exhibited a connection of distored Al-N tetrahedrons by one common edge directly at the SMB. In comparision, the bulk tetrahedrons reveal corner-connection to each other. An influence of the SMB to the piezoelectric properties can be excluded.
By incorporating Co nanoparticles into an AlN thin film a first 0-3 demonstrator was established. Electron diffraction studies demonstrated a significant deterioration of the c-axis texture of AlN already for low Co filling factors, which is synonymous with bad piezoelectric properties. As one of the fundamental results, these TEM findings served as an essential evidence[26] for declaring the 0-3 approach as unsuitable for the production of highly sensitive ME sensors.
Structural investigations on the perovskite-type BCZT were performed on bulk and thin film specimens. The XRD results and macroscopic properties of the bulk sam-

[26] For more information on the critical evaluation of the 0-3 approach for magnetoelectric nanocomposites with metallic nanoparticles the reader is referred to [12, 117].

ples showed a good agreement with previous studies [164, 153] revealing an axial ratio of c/a = 1.005 for the BCZT composition of $(Ba_{0.7}Ca_{0.3}TiO_3)0.5$-(Ba $Zr_{0.2}Ti_{0.8})0.5$.
A seemingly contradiction was found using TEM methods. For all the acquired data, the presence of a paraelectric cubic phase appeared as possible interpretation due to the good agreement of experiments and simulations. For a more critical discussion of the results, several aspects must be considered: As the specimens were grinded in terms of the TEM preparation, the relative small size of the investigated grains and the simultaneously irradiation of the beam might heat the grain over the (tetragonal-cubic) transition temperature, causing a loss of the tetragonality. Due to the limited resolution of conventional HRTEM, the tetragonal distortion (c/a = 1.005) is not detectable. Also it is debatable whether the use of aberration corrected HRTEM can be a substantial improvement for such a small distortion. The method of choice for symmetry investigations, particularly in this case, is CBED. However, it must be considered, that the thickness of the grains was probably not sufficient enough to exclude unambiguously a cubic symmetry within the CBED patterns.
Only in a minority of cases defects were observed in the bulk specimen. A local symmetry reduction was analyzed via a HRTEM tilting series. The experimentally observations were rationalized using a structural model with a $Fd\bar{3}m$ symmetry and a lattice parameter of a = 16.08 Å.
The BCZT thin films exhibited a considerable difference with respect to the bulk samples. These thin films are setup by columnar grains with a preferred $[1\,1\,1]$[27] growth.
The presence of a 7L modulation was an often observed feature along the $[1\,1\,1]$ direction. A polytype was provided as potential interpretation, which was indicated also by comparing electron diffraction data with simulations of a structure model from [184]. However, the quality of the experimental data does not allow a clear assignment of the layer sequence.
Twin boundaries were found in the thin films. In a particular case, an arrangement of connected edge-on and superposition $\{1\,1\,1\}$ twin domains was detected. The presence of superposition was verified by the comparison of experimentally obtained FFT and SAED patterns with dynamical simulations: The experiments revealed for the edge-on $\{1\,1\,1\}$ twin interface two superimposed single domain pattern along $[1\,1\,0]$, while the superposition area exhibited additional commensurable reflections in the corresponding data. Simulations based on the supercell approach, clearly proved the origin of the additional reflections as an superposition effect due to dynamical scattering.
CBED studies on the FIB prepared thin films provided an indication for the presence of a tetragonal $P4mm$ symmetry. However, an interpretaion of the same data with a monoclinic Pm symmetry cannot be excluded. The presence of rhombohedral phases could not be confirmed.
The structural peculiarities of the different samples (bulk and thin films) are reflected in the variation of the properties as demonstrated for the dielectric permittivity. Only the thin film exhibited a macroscopic ferroelectric relaxor behavior. Further, a structural indication for the relaxor was suggested with the modulation

[27] Using a pseudo-cubic symmetry as notation.

phenomenon. As part of future work, aberration corrected microscopy must be applied to elaborate more precisely the atomic configuration of the defect structures for BCZT. For a significant statement on the symmetry and the orientation of the grains in the BCZT thin films, large and low scale measurements should be combined. The two TEM techniques, ACOM and CBED, could provide a good statistical analyze of the grain structure and, thus, an improved correlation regarding the macroscopic properties.

5 Exchange Biased Magnetostrictive Materials

The development and characterization of suitable magnetostrictive components for ME nanocomposites will be discussed in this chapter. In the first part, a multilayer design is introduced which is capable of exchange biasing individual magnetostrictive layers[1]. In the second and third part structural investigations of these multilayers will be discussed and related to the magnetic properties of the material. The structural investigations include a comparison of in-situ/ex-situ annealing procedures[2] and a three dimensional study on an optimized ME demonstrator system.

5.1 Exchange Biasing of Magnetoelectric Composites

The main requirements for magnetic sensing and imaging for biological (particularly neurological and cardiological) signals is to attain a high sensitivity to a.c. magnetic fields and a high spatial resolution. Taking into account that in many instances an external magnetic bias field must be applied for a sufficient magnetoelectric effect [196, 197, 198], undesired restrictions to the functionality of a biomagnetic sensor may occur: First, the applied magnetic field increases the space needed for the corresponding sensor which, in turn, decreases the possible spatial resolution. In a second aspect, it serves as further noise source influencing negatively the signal-to-noise ratio of a single sensor and others in its vicinity (when considering a sensor network for a vector-field approach.)
By using an internal magnetic exchange biasing for the magnetostrictive component such limitations can be avoided. Magnetic bilayers, which are set up by a common interface of a ferromagnet with a large exchange parameter and an antiferromagnet with large magnetic anisotropy, constitute the fundament for the exchange bias effect. The latter causes a pinning of the interfacial magnetic spins of the ferromagnet and a uni-directional behavior of the structure [199, 200, 201, 202]. As consequence, a magnetic hysteresis loop associated with the bilayer exhibits a shift apart from a zero centered magnetic field by the bias field H_{EB}, as demonstrated in Figure 5.1a.

[1] Section 5.1 is based on studies from [18].
[2] Section 5.2 is based on studies from [195].

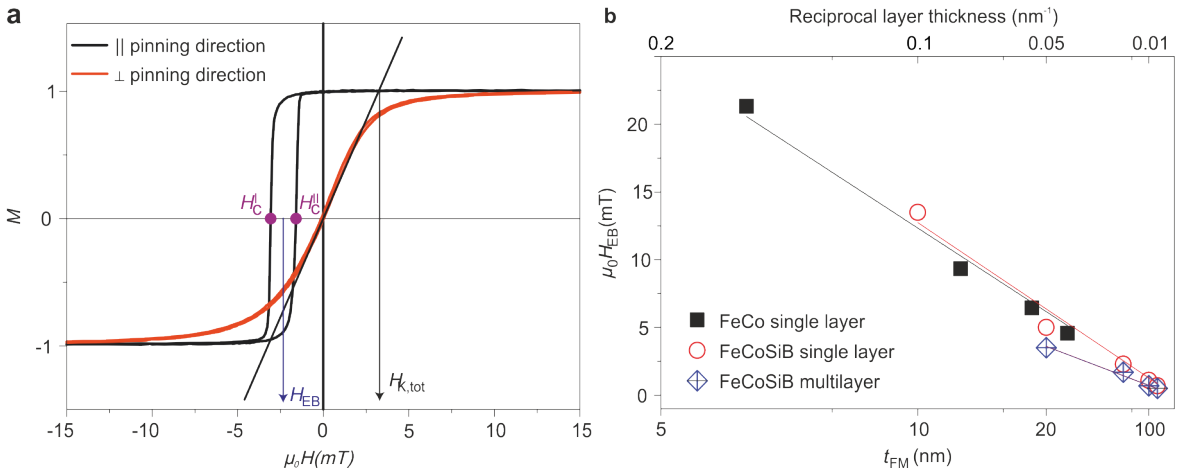

Figure 5.1: Exchange biasing of ferromagnetic single-layer and multilayer systems. (a) Typical normalized magnetization curves of an exchange-biased ferromagnet (here $Fe_{70.2}Co_{7.8}Si_{12}B_{10}$) measured along (black) and perpendicular to (red) the induced pinning direction. The exchange bias field H_{EB} is defined as the midpoint of both coercive fields $H_C^{\perp}$ and $H_C^{\parallel}$ recorded along the pinning direction. The total anisotropy field $H_{K,tot}$ is determined by the extrapolation of the linear magnetization regime obtained along the hard axis to the value of the saturation magnetization. (b) Thickness dependency of exchange bias for $Fe_{50}Co_{50}$ (squares) and $Fe_{70.2}Co_{7.8}Si_{12}B_{10}$ (circles). A reciprocal illustration was used to confirm the $1/t_{FM}$ dependency of the exchange bias. For the multilayer case, t_{FM} represents the thickness of the magnetostrictive layer incorporated in a single sequence. By repetition of the sequence the total magnetostrictive layer thickness was adjusted to roughly 1 μm. (Graphic and caption excerpted from [18].)

Moreover, the bias field has a maximum for the directions along the antiferromagnet easy axis (induced pinning direction) and vanishes for the corresponding perpendicular directions. In the perpendicular direction it contributes to an enhanced total anisotropy field $H_{k,tot}$, see Figure 5.1a [18].
Studies performed by Greve et al. [198] for mangetoelectric composites demonstrated the necessity of a moderate and precise biasing for magnetostrictive layers with thickness in the range of several micrometers. Concerning the dependency of thickness for both, antiferromagnet and ferromagnet, layer in the exchange material a roughly proportional relation between exchange bias and the reciprocal thickness of the ferromagnet (t_{FM}) layer can be found

$$H_{EB} \propto \frac{1}{t_{FM}} \text{ [203].}$$

In Figure 5.1b a plot shows the relation of the exchange bias field of the highly magnetostrictive materials $Fe_{50}Co_{50}$ and $Fe_{70.2}Co_{7.8}Si_{12}B_{10}$ coupled to $Mn_{70}Ir_{30}$ as a natural antiferromagnet with respect to different t_{FM} ranging from 6 to 200 nm."An upper limit for the ferromagnetic layer thickness is set by the domain-wall width" [[18]].

These investigations suggested that only repeating sequences of individual magnetostrictive layers within a multistack design provide a sufficiently exchanged biasing system in the micrometer regime.

The Antiferromagnetic Mn_xIr_{1-x} Layer

Former studies on Mn_xIr_{1-x} stated a relatively strong exchange-biasing interaction (interfacial exchange energy up to J_{eb} = 0.4 mJ/m[23] depending on the antiferromagnetic/ ferromagnetic bilayer) with a high thermal stability (blocking temperature of approximately 560 K) [205, 206]. These studies showed that the best results for the H_{EB} were achieved with a crystallographic <1 1 1> texture for Mn_xIr_{1-x} along the growing direction. In the presented study the <1 1 1> texture for a $Mn_{70}Ir_{30}$ composition was promoted for a single antiferromagnetic layer by the introduction of an annealed Ta/Cu bilayer as substrate, cf. the HRTEM micrograph of Figure 5.2 and the correlated FFT patterns (i) and (ii).

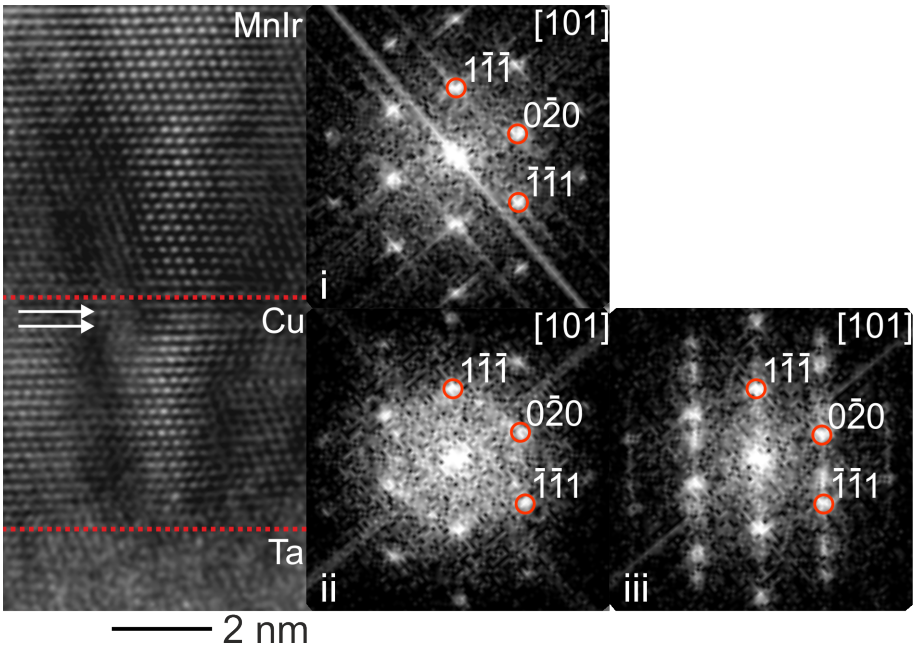

Figure 5.2: Filtered HRTEM micrograph of representative stacking sequence of $Mn_{70}Ir_{30}$ Cu and Ta used for all multistack systems discussed in the thesis. The orientation relationship was investigated by FFT: Both $Mn_{70}Ir_{30}$ (i) and Cu (ii) structures have a cubic symmetry (space group: $Fm\bar{3}m$) and are oriented along the [1 0 1] zone axis. The growth direction of both layers is along the <1 1 1> direction corresponding to the marked {1 1 1} planes. Moreover, the presence of stacking faults was observed in the Cu layer close to the interface of $Mn_{70}Ir_{30}$ and Cu (marked with white arrows). The structural influence is emphasized by calculating the FFT pattern without (ii) and with (iii) the defect planes within the Cu layer.

[3]Comparative values: ϵ-Mn_3Ga with CoFe - 0.09mJ/m^2 [204],

The formation of structural defects was a frequently observed feature within these layers. An example is provided in Figure 5.2 with the presence of stacking faults, as marked with white arrows. A FFT analysis which excludes (Figure 5.2 (ii)) and includes (Figure 5.2 (iii)) these stacking faults, respectively, exhibits the presence of additional intensities for the defect structure. However, the <1 1 1> texture and thus the exchange coupling are not noticeable influenced by such kind of defects.

Morphology of Exchange Coupled Multilayer Systems and Magnetoelectric Composites

The principle morphology of an exchange coupled multilayer system will be discussed using $Fe_{50}Co_{50}$ as ferrmagnetic component. A first specimens was prepared directly on a columnar grown AlN substrate, as depicted in the HAADF-STEM Z-contrast image of Figure 5.3a. The high degree of roughness from the AlN surface[4] was transmitted into the multilayer next to their common interface, however, with a notable decrease of the roughness effect through the entire cross-section up to the surface region. As a result, individual adjacent layers seems to superimpose in the projected view provided by (S)TEM images (see Figure 5.3). A focused study on the potential influence of the roughness to the functionality of the material is provided in section 5.3.
Another intrinsic feature of the specimen was the presence coarsening of the smooth stacking sequence, with increasing relevance from interface to surface contrary to the roughness (discussion see below). To validate the strict periodicity of the respective sequences, chemical nanoprobe analyses were carried out on different areas of the specimen. A representative measurement with absence of the roughness is demonstrated in Figure 5.3b. The data from the profile of Figure 5.3b (position mark in Figure 5.3a inset) indicates separated layers and thus predicts a chemical integrity of the material [18]. In the case of the Ir plot the presence of artifacts must be considered. The spatial overlap with the Cu and Ta peaks stem from the narrow energy differences of the Ir-L lines (α 9.137 keV) and Ta-L lines (β 9.34 keV) [18]. From the profile measurement varying sequence thicknesses were determined in the range of 36.5 to 37.8 nm. An average value of 36.6 nm was calculated for a high number of sequences.
The inset of Figure 5.3a shows also a magnified view of multilayer sequences which were strongly influenced by the roughness effect. Conventional (2D) chemical investigations are incapable of an unambiguous detection of the compositional integrity of such layers. Using tomography (data discussed in section 5.3) chemically separated layers were found with complex 3D-bended shapes.
A second specimen was fabricated on a silicon substrate, ensuring a planar stacking of the multilayer sequences and, thus, allowing a minute investigation of the orientation relationship between respective layers, cf. Figure 5.3c. Studies performed by SAED (aperture size 250 nm corresponding to approximately six multilayer sequences) exhibited a highly textured structure directly at the substrate/multilayer

[4]Discussed in the structural study of AlN in section 4.1.2

interface region (see blue marked SAED in Figure 5.3c). The Bragg reflections of the texture can be related to pairs of partially superimposing reflections along the growing direction. Moreover, a slight elongation of these reflections was observed.

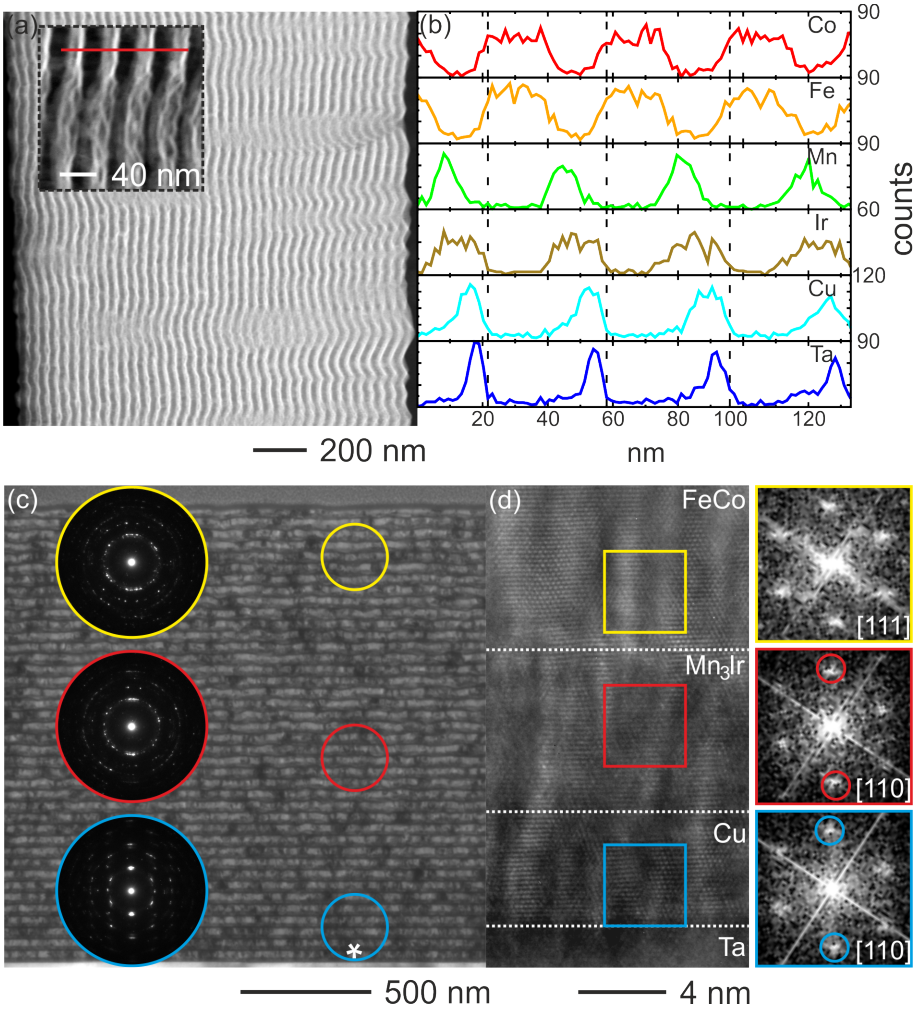

Figure 5.3: Cross sectional TEM images of an exchange-biased magnetostrictive multilayer system. (a) Z-contrast image of the $Fe_{50}Co_{50}$ multilayer system on a AlN substrate (right-hand side of the image, columnar grown) and a magnified view (inset) with a line indicating the selected area for chemical analysis. (b) Associated energy-dispersive X-ray spectra for several multilayer sequences. The single sequences (dashed lines) vary from 36.5 to 37.8 nm. (c) Bright-field image of the $Fe_{50}Co_{50}$ multilayer system on a silicon substrate with SAED patterns of different specimen areas. Asterisk: area next to multilayer/substrate interface. (d) Associated HRTEM micrograph (left) and corresponding FFT patterns (right) of the multilayer sequence next to the multilayer/substrate interface. The marked spots correspond to (1 1 1) planes for $Mn_{70}Ir_{30}$ and Cu layers, respectively. Partially excerpted from [18].

Using a HRTEM micrograph recorded directly at the multilayer next to the substrate (Figure 5.3d) a well-defined orientation relationship between the (1 1 1) planes of

the $Mn_{70}Ir_{30}$ and the (1 1 0) planes of the $Fe_{50}Co_{50}$ layers was observed, causing the formation of the partially superimposed reflections in the SAED pattern. In all analyzed FFTs (cf. Figure 5.3d) an orientation of the seed layers (Ta, Cu) and the $Mn_{70}Ir_{30}$ layer were identified along the zone axes [1 1 0]. The $Fe_{50}Co_{50}$ layers were polycrystalline with preferred orientation of the grains along [1 1 1] and [1 0 0]. Furthermore, with increasing distance to the interface an enhancement of coarsening was detected within the layer sequences, as the different degrees of the texture in the SAED patterns showed by a series of concentric diffraction rings (5.3c) instead of the well-aligned Bragg intensities along [1 1 1] [18].

Concept of Exchange-Biased Magnetoelectric Composites for Magnetic-Field-Sensor Applications

In this section[5] the capabilities and requirements of a biomagnetic field sensor based on an exchanged biased multistack are demonstrated and discussed. A detailed description is provided in [18]. The main findings are briefly addressed.
For the production of a fully exchange biased multilayer stack a collinear alignment of the unidirectional anisotropy due to the exchange-bias effect and the uniaxial anisotropy of the ferromagnetic magnetostrictive phase is unavoidable. This leads to the formation of an antagonism:

- "[The exchange bias is always observed along the pinning direction of the material whereas magnetostriction is maximum perpendicular to it (Figure 5.4a, b). Accordingly, an adjustment of the exchange bias of the ferromagnetic layers parallel to the direction of the measurement direction would result in an almost complete extinction of the magnetostrictive response of the sensors.]" [Excerpted from [18].]

A solution provided by Lage et al. [18] was the inducement of the exchange bias under a certain inclination angle. The selection of the parameters depends on the present sample conditions. Functional measurements were performed with the magnetoelectric cantilevers based on the $Fe_{50}Co_{50}$/AlN setup. The magnetoelectric voltage coeffcient was determined with a value of $21.2\,\mathrm{V\,cm^{-1}\ Oe^{-1}}$ (at zero external field and at mechanical resonance $f = 1{,}011.5\,\mathrm{Hz}$). An improvement to $96.7\,\mathrm{V\,cm^{-1}\ Oe^{-1}}$ was achieved by modifying the magnetostrictive multilayer using the sequence $7\,\mathrm{nm\,Ta}$/ $3\,\mathrm{nm\,Cu}$/ $7\,\mathrm{nm}\,Mn_{70}Ir_{30}$ / $130\,\mathrm{nm}\,Fe_{70.2}Co_{7.8}Si_{12}B_{10}$ and fabricating it on a 2-μm-thick piezoelectric AlN layer. The functionality of the sensor combined with a low-noise charge amplifier is presented in the following:

- "[A responsivity of $5.7\,\mathrm{V\,mT^{-1}}$, a noise level of $66\,\mathrm{pT}/\sqrt{\mathrm{Hz}}$ and a resulting limit of detection of 10 $\mathrm{pT}/\sqrt{\mathrm{Hz}}$ at resonant frequency were achvied]" [excerpted from [18]]. The performance of the sensor is presented in Figure 5.4c.

[5] The magnetic and electric measurements were performed by Enno Lage and Robert Jahns respectivley. The results and parts of the section were partially excerpted from [18].

- The respective effectiveness of different sensor systems is presented in Figure 5.4d. The high capability of the exchange-biased sensor is proven by the fact that the response at zero bias field is reduced only by a factor of 2.4 when compared with the sensor without exchange bias at its optimum bias field [18]. As reference a sensor without any bias field was also measured. Such a sensor is established by using Tantalum for decoupling the antiferromagnetic and magnetostrictive layer.

In the work of Jahns et al. [9] a further particularity of the exchanged biased ME sensors was discussed, which should be mentioned here:"[Application of an AC magnetic field perpendicular to theanisotropy in this geometry now immediately causes an alternating elongation and contraction of the magnetostrictive phase. These result in a corresponding voltage response at the same frequency of the magnetic field at zero bias field.[...] Due to the integrated magnetic bias field, the maximum response was obtained at zero field and corresponds to a magnetoelectric coefficient of 800 V/cm Oe.]"

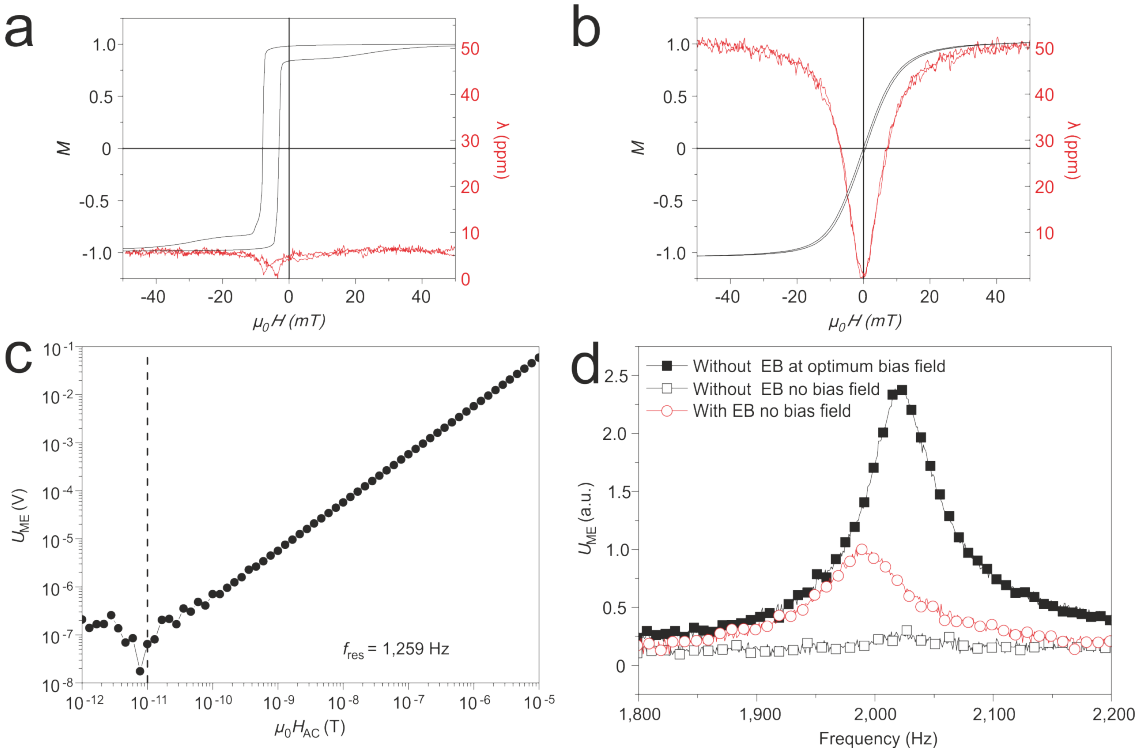

Figure 5.4: (a, b) The antagonism between exchange bias and magnetostriction. Normalized magnetization curves (black) and magnetostriction curves (red) of $Fe_{50}Co_{50}$ multilayers deposited on cantilevers. The pinning direction is induced either parallel (a) or perpendicular (b) to the longitudinal cantilever axis. Whereas the exchange bias shows a maximum value when measured parallel to the pinning direction, the magnetostrictive response almost vanishes. In the case of the measurement perpendicular to the pinning direction, the projection of the exchange bias vanishes; however, the magnetostrictive response is maximal. (c) Performance of the $Fe_{70.2}Co_{7.8}Si_{12}B_{10}$-based magnetoelectric sensor operated with a charge amplifier. Sensitivity curve at mechanical resonance $f_{res} = 1.259\,\mathrm{Hz}$. For several orders of magnitude the sensors voltage response U_{ME} is linear and yields a responsivity of $5.7\,\mathrm{V\,mT^{-1}}$ at the output of the charge amplifier. Data scattering starts at about 100 pT. Below the limit of detection of about 10 pT, the signal is covered by noise. (d) Comparison of magnetoelectric sensors with and without exchange bias. The graph shows the frequency-dependent magnetoelectric voltage response U_{ME} of a non-internally-biased sensor for absent (open squares) and optimum external magnetic bias field (filled squares). The response of a sensor holding exchange bias is also plotted (circles). For clarification the signals are normalized to the maximum response of the exchange-biased sensor. (Graphic and caption excerpted from [18].)

5.2 Annealing of Amorphous Exchanged Biased Multistack Systems

With the usage of amorphous $Fe_{70.2}Co_{7.8}Si_{12}B_{10}$ (FeCoSiB) an improvement was achieved with respect to $Fe_{50}Co_{50}$ for the effectiveness of exchanged biased ME sensors. However, detailed (structural) studies of biasing amorphous alloys are less often discussed until the present state [207, 208].
In order to establish the unidirectional anisotropies a field annealing procedure with subsequent cooling of the temperature is required. For this purpose two aspects must be considered for appropriate temperature settings. The cooling through the Neel temperature of the material is demanded to promote a coupling between the antiferromagnetic and the ferromagnetic layer, in the presence of an applied magnetic field [209, 210]. For $Mn_{70}Ir_{30}$ the temperature limit is about 250 °C. Additionally, the applied temperature should not cause any crystallization processes within the amorphous layer, as a deterioration of the (soft) magnetic properties is expected[6]. Structural in-situ and ex-situ annealing procedures are carried out investigating the influence of $Mn_{70}Ir_{30}$ at the interface to the FeCoSiB layer. These results are then discussed with corresponding magnetic properties.

5.2.1 As-Deposited Condition: Morphology and Texture

The morphology of the as-deposited magnetostrictive multilayer is provided in the bright field image of Figure 5.5a. The thickness of the specimen is about 1.2 μm and it consists of a ten time repeating individual layer sequence of Ta; Cu; $Mn_{70}Ir_{30}$; FeCoSiB. Thereby, the dark stripes in the bright field image represents the Ta, Cu, $Mn_{70}Ir_{30}$ layers and the grey contrasts can be assigned to FeCoSiB. The multilayer was fabricated on a Si substrate, thus, roughness effects were excluded. A noticeable feature within the multilayer specimen was filaments appearing in the FeCoSiB layers as faint darker contrast, see Figure 5.5a. In order to clarify the cause of filaments an additional multilayer system was prepared expanding a single stacking sequence by an additional Ta layer and decoupling the interface of $Mn_{70}Ir_{30}$ and FeCoSiB layers. For this specimen no filaments could be traced, cf. bright field image of Figure 5.5b. As consequence, the filaments are not an artifact related phenomenon introduced by TEM preparation, but must originate from interactions of the common interface of $Mn_{70}Ir_{30}$ with FeCoSiB. The structural influence and characteristic of the filaments to the entire morphology of the multilayer system was first studied by SAED. For large scale investigation of the structure a diffraction aperture was applied limiting the illuminated area of specimen to a diameter of 850 nm (including ca. 7 layer sequences) for the recording of the patterns.

[6] The complete production of this functional thin films is discussed in the PhD thesis of Enno Lage [199]

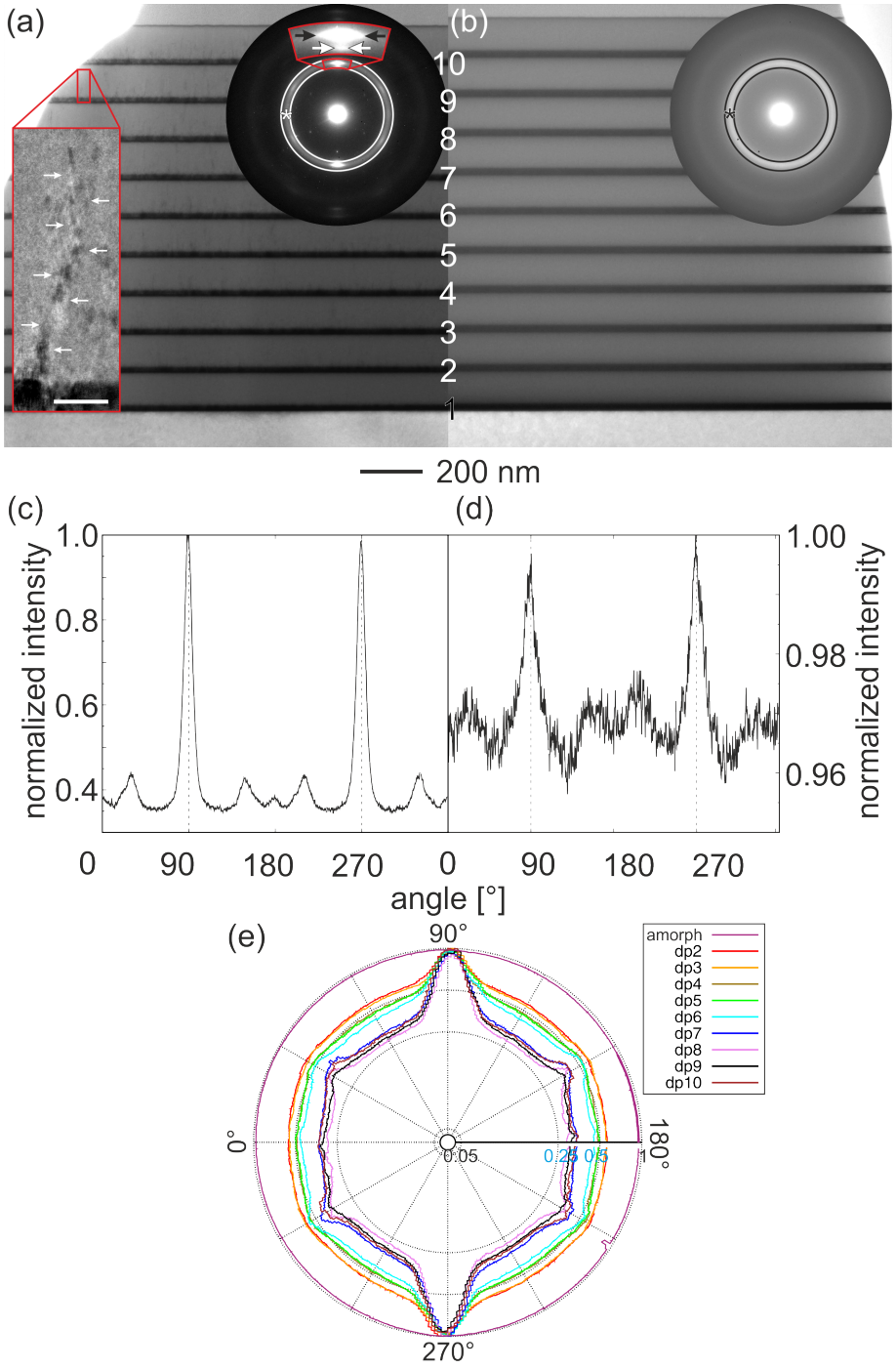

Figure 5.5: TEM bright field images of multi-stack systems (a) coupled, (b) decoupled. Magnified area in (a, left) crystalline filament (marked by white arrows) in an amorphous FeCoSiB layer, the white bar express 20 nm. Insets: Associated SAED patterns. Enlarged view in SAED (a): Two partially superimposed Bragg reflections, from the filaments (elongated Bragg reflections (black arrows)) and $Mn_{70}Ir_{30}$ (white arrows). (c, d) Normalized intensity distribution of the marked arc segments of the SAED patterns. The asterisk in (a, b) mark the starting point (angle = 0°) of the measurements. The strongest peaks represent the texture along the growing direction. The minor peaks can be used for the determination of preferred crystal orientations. (e) Normalized radial plots of SAED series recorded at the numbered single sequences for the coupled system (dp x). As reference for an (almost) amorphous specimen (d) was reploted (labelled by *'amorph'*).

In both, coupled and decoupled, multilayers, the presence of diffuse intensities on concentric rings was observed representing the amorphous character of FeCoSiB, see the insets in Figure 5.5. As additional feature, the coupled system shows a texture along the growing direction similar to the findings in Figure 5.3c (blue marked SAED pattern). Indeed, the intensities of the texture can be related to pairs of partially superimposing reflections with d-spacings of ca. 2.18 Å stemming from {1 1 1} planes of $Mn_{70}Ir_{30}$ and ca. 2.01 Å from the crystalline filaments showing a preferred growing direction along [1 1 0] assuimg a cubic structure (verification by HRTEM see below). Evaluating the radial intensity distribution for the first order diffuse ring of the SAED patterns (see Figure 5.5c), a polycrystalline character of these filaments was detected with a prefered orientaion of the filaments. Two distinct periodicities for the angle distances of the intensity peaks were detected: (i) a 60° interval (starting at ca. 30°) and (ii) a 90° interval (starting at ca. 0°) corresponding to the crystal orientations (i) [1 0 0] and (ii) [1 1 1] for a cubic structure. As it can be seen from the SAED pattern of Figure 5.5 the reflections from the filaments exhibit a slight elongation, which indicates a non-strict growth perpendicular to the surface interface.
Performing the same investigation on the decoupled system, only a weakly pronounced texture was observed from the (1 1 1) planes of $Mn_{70}Ir_{30}$ and Cu with a crystal orientations along [1 0 1]. The weak peak-to-base signal results from a dominating volume of amorphous FeCoSiB with respect to the crystalline layers.
With a further decrease of the aperture size (resulting in an illuminated area with a diameter of 250 nm) a series of SAED pattern were recored along the growing direction on each layer sequence. The radial intensity distributions, calculated for the first diffuse ring are depicted as radial plot in Figure 5.5e. The elongation of the filament reflections is expressed by broad peaks especially accentuated at 90° and 270°. However, these peaks exhibited only minor variations through the entire cross-section and, thus, excluded also the presence of coarsening. A tendency of increasing crystallinity was determinded from substrate interface to the surface of the specimen, which is expressed by a decreasing diameter of the radial plots[7] of sequences with high numbering. This effect originates by an increasing substrate temperature during the deposition process. The higher thermal energy leads to an enhanced mobility of the surface adatoms and, thus, supports the formation of the thermodynamically more stable i. e. crystalline structure [211].

As Deposited Condition: Nanostructure Observations

A comparative analysis of represenative interfaces within an individual layer sequence for the coupled and decoupled systems are provided in the HRTEM micrograph of Figure 5.6a, b. The stacking sequences of FeCoSiB; Ta; Cu; $Mn_{70}Ir_{30}$[8] and their structural features can be regarded as highly related. A significant difference is

[7] This correlates with the reduction of diffuse background intensity in the evaluated SAED patterns.

[8] The orientation relationship of the bilayer system and the antiferromagnetic layer follow the description provided in section 5.1

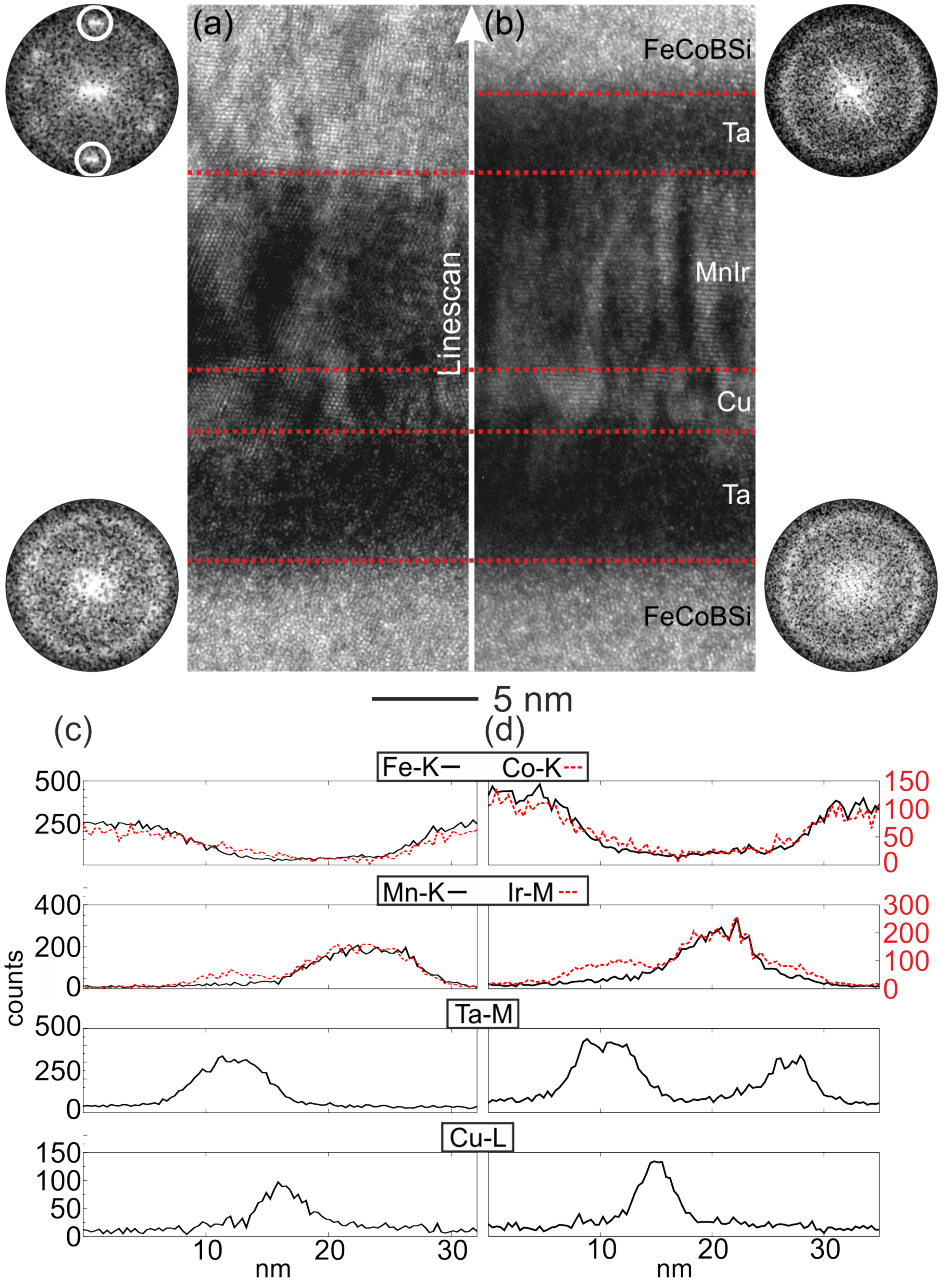

Figure 5.6: Interface study via HRTEM for represenative sequences of (a) a coupled and (b) a decoupled system with the (c, d) correlated chemical investigations of the single layers. $Mn_{70}Ir_{30}$ serves as seed layer for crystallitzation of FeCoSiB when coupled to the layer. The FFT patterns in (a) and (b) correspond to the respective FeCoSiB layers. Only in the top FeCoSiB layer of the coupled system a crystalline behavior with a texture along a cubic [1 1 0] direction is detectable. All other patterns exhibit diffuse intensities representing an amorphous character.

provided by the introduction of Ta: In the coupled system the presence of a thin and continuous crystalline layer is observed directly at the interface to the $Mn_{70}Ir_{30}$ (cf. Figure 5.6a), while in the decoupled system the FeCoSiB layer remains amorphous

(cf. Figure 5.6b). As a result, the (1 1 1) grown $Mn_{70}Ir_{30}$ acts as seed layer for crystallization and textured growth within the FeCoSiB layer, similar to the findings for the $Mn_{70}Ir_{30}$/ FeCo interface. The chemical separation and integrity for the layers within a single sequence are demonstrated in Figure 5.6c, d with the measured layer thickness of ca. 7 nm Ta, 3 nm Cu, 9 nm $Mn_{70}Ir_{30}$, 100 nm FeCoSiB, and 4 nm for the Ta-buffer layer.

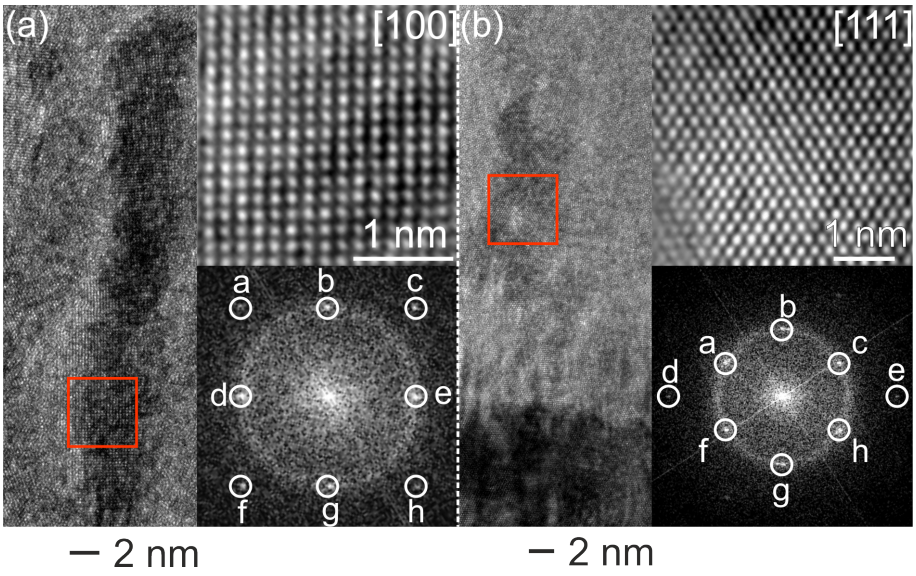

Figure 5.7: HRTEM micrograph of the filaments within the FeCoSiB layer exhibiting a cubic symmetry. (a) Filament along the [1 0 0] zone axis: (top) magnified view (filtered) of the marked area; (bottom) associated FFT (b) Filament along the [1 1 1] zone axis: (top) magnified view (filtered) of the marked area; (bottom) associated FFT. The FFTs of the respective regions show the single crystalline filament (marked intensities) along with a superimposing amorphous ring from FeCoSiB. The indexing for the labelled Bragg intensities are listed in Table 5.1.

All analyzed filaments originated directly from the thin crystalline layer at the interface to $Mn_{70}Ir_{30}$ and show dimensions up to 50 nm in length and 10 nm in width, as demonstrated in the (HR)TEM micrographs of Figure 5.5 and 5.7. Analysing the local FFT patterns a cubic symmetry was evident. Although, long-term chemical investigations were carried out under STEM Z-contrast conditions with nanoprobe measurements, an unambiguous assignment of the composition was not achievable. The nanocrystalline filaments were embedded in the amorphous matrix of the FeCoSiB layers, see the superimposing of single crystalline patterns with diffuse rings in the FFTs of Figure 5.7. According to previous studies based on Mössbauer spectroscopy on amorphous magnetic alloys with similar compositions [212, 213] nanocrystalline phases of FeSi, FeCo and FeCoSi must be considered. In Table 5.1[9] a comparison of the experimental results with literature values of the possible phases are provided.

[9]The d-spacings are obtained from [214, 215, 216, 217]

Table 5.1: Comparison of the experimentally obtained d-values from the FFT patterns of Figure 5.7 with literature d-spacings and miller indices (hkl) from different compositions.

	Experiment		Fe [Im$\bar{3}$m]		Fe_3Si [Fm$\bar{3}$m]		FeCo [Pm$\bar{3}$m]		Co_2FeSi [Fm$\bar{3}$m]	
	Pos	d-value [nm]	d-value [nm]	hkl	d-value [nm]	hkl	d-value [nm]	hkl	d-value [nm]	hkl
[010]	a	0.140	0.141	$00\bar{2}$	0.140	$00\bar{4}$	0.143	$00\bar{2}$	0.141	$00\bar{4}$
	b	0.204	0.199	$10\bar{1}$	0.198	$20\bar{2}$	0.202	$10\bar{1}$	0.200	$20\bar{2}$
	c	0.143	0.141	200	0.140	400	0.143	200	0.141	400
	d	0.203	0.199	$\bar{1}0\bar{1}$	0.198	$\bar{2}0\bar{2}$	0.202	$\bar{1}0\bar{1}$	0.200	$\bar{2}0\bar{2}$
	e	0.203	0.199	$10\bar{1}$	0.198	202	0.202	101	0.200	202
	f	0.143	0.141	$\bar{2}00$	0.140	$\bar{4}00$	0.143	$\bar{2}00$	0.141	$\bar{4}00$
	g	0.204	0.199	$\bar{1}01$	0.198	$\bar{2}02$	0.202	$\bar{1}01$	0.200	$\bar{2}02$
	h	0.140	0.141	002	0.140	004	0.143	002	0.141	004
[111]	a	0.196	0.199	$01\bar{1}$	0.198	$02\bar{2}$	0.202	$01\bar{1}$	0.200	$02\bar{2}$
	b	0.196	0.199	$10\bar{1}$	0.198	$20\bar{2}$	0.202	$10\bar{1}$	0.200	$20\bar{2}$
	c	0.193	0.199	$1\bar{1}0$	0.198	$2\bar{2}0$	0.202	$1\bar{1}0$	0.200	$2\bar{2}0$
	d	0.114	0.115	$\bar{1}2\bar{1}$	0.114	$\bar{2}4\bar{2}$	0.116	$\bar{1}2\bar{1}$	0.115	$\bar{2}4\bar{2}$
	e	0.114	0.115	$1\bar{2}1$	0.114	$2\bar{4}2$	0.116	$1\bar{2}1$	0.115	$2\bar{4}2$
	f	0.193	0.199	$\bar{1}10$	0.198	$\bar{2}20$	0.202	$\bar{1}10$	0.200	$\bar{2}20$
	g	0.196	0.199	$\bar{1}01$	0.198	$\bar{2}02$	0.202	$\bar{1}01$	0.200	$\bar{2}02$
	h	0.196	0.199	$0\bar{1}1$	0.198	$0\bar{2}2$	0.202	$0\bar{1}1$	0.200	$0\bar{2}2$

5.2.2 In-Situ and Ex-Situ Annealing Procedure

The heating procedure was applied to the multilayer systems following a heating rate of 15 °C/min up to 250 °C. The specimens were maintained at this temperature for 30 min and subsequently cooled down. Afterwards the specimens were heated again with the same heating rate (15 °C/min) up to 350 °C and kept on this temperature for 30 min. For both multilayer systems heating experiments were performed in-situ in the TEM. Additionally, for the exchanged coupled sample also ex-situ heating was analyzed using the same heating parameters and additional application of a magnetic field of 2000 Oe during dwell time and cooling. The annealing stage of 350 °C was selected as significant changes in the structural nature were expected. A comparison of the different heating condition enables conclusions regarding the potential influence of atmosphere or volume-to-surface ratio.
An SAED series was recorded using the aperture to restrict the illumination to a circular area of 850 nm for the decoupled (in-situ annealing) and the coupled system (in/ex-situ heating), respectively. The patterns and the correlated bright field images for the final temperatures are depicted in Figure 5.8.

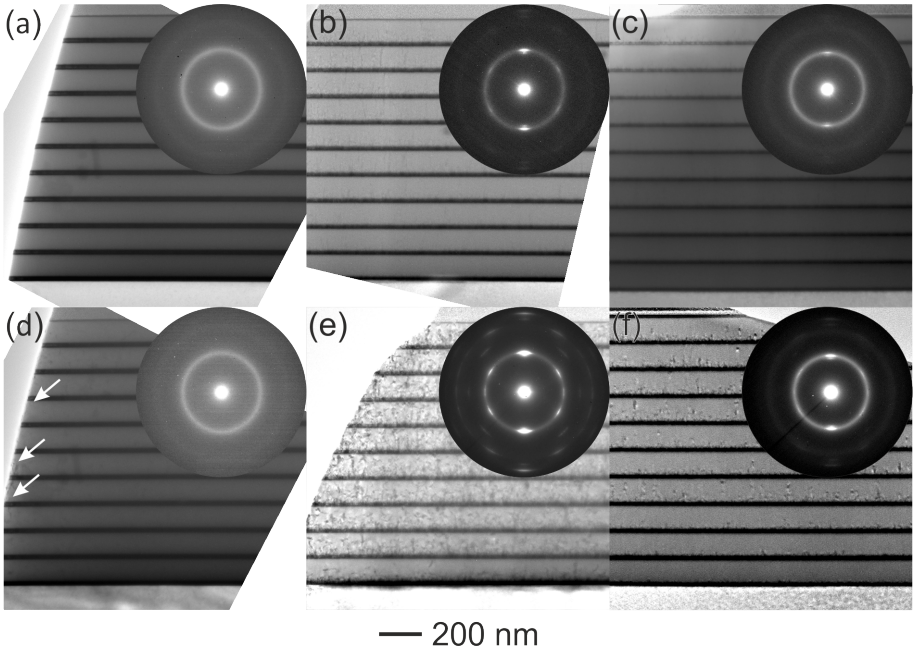

Figure 5.8: Bright field images and associated SAED patterns recorded after annealing at (a, b, c) 250 °C and duration of 30 min, (d, e, f) 350 °C and duration of 30 min. (a, d) In-situ annealing of the decoupled system. In (d) minor crystallization effects are observable at the edges of the specimen (arrows). (b, d) In-situ and (e, f) ex-situ annealing of the coupled system

The decoupled system (Figure 5.8a, d) is mainly unaffected by the thermal treatment, as no substantial changes were traced for the diffuse rings in the diffraction patterns. Only for 350 °C minor structural changes appeared in terms of crystallization phenomena, which occur directly at the edges of the specimen, see arrows in Figure (Figure 5.8d). A similar behavior was observed for the coupled system

during the annealing up to 250 °C (Figure 5.8b, c). Independent of choosing the in-situ or ex-situ heat treatment, no significant changes were observed with respect to the as-deposited condition. At a temperature of 350 °C the FeCoSiB layers, which already contained filaments, exhibited an increased volume of coherently scattering areas, as expressed by enhanced Bragg intensities in the SAED patterns and the corresponding bright field images of Figure 5.8e, f (and 5.9a, b). A considerable difference in the degree of crystallinity was detected between in-situ and ex-situ experiments. It can be suggested, that the lower volume-to-surface ratios favor the crystallization kinetic within the FeCoSiB layer for the in-situ heated TEM lamella. This behavior is emphasized by an enhanced peak to base-signal ratio for the radial intensity distributions collected from the diffraction patterns of the respective systems (Figure 5.9a, b), as shown in Figure 5.8c and 5.8d.
Restricting the area of interest to 250 nm for SAED and collecting a series of patterns along the growing direction of each layer sequence, radial intensity distribution can be calculated analogues to Figure 5.5e. The results for in-situ and ex-situ annealing are depicted in Figure 5.9e, f, respectively. After annealing an enhanced variation of single sequences apart from the strict textured growth were found for the crystallites in the FeCoSiB layers. The tendency of increasing crystallinity from substrate interface to specimen surface is maintained.

5.2.3 Influence of Heat Treatment to the Magnetic Behavior

In the magnetic characterization[10] only the coupled system was considered as no exchange biasing is present for the decoupled stack.
At first, magnetization curves were recorded along the easy axis (induced pinning direction) for different temperatures as depicted in Figure 5.10a. In the as-deposited condition a H_{EB} of ca. 9 Oe was observed. The hysteresis shows the presence of kinks and steps indicating randomized pinning directions. An annealing to 250 °C and 350 °C increased the H_{EB} to ca. 13 Oe and caused a vanishing of kinks and steps.
For the investigation of the hard axis (perpendicular to the easy axis) the determination of $H_{K,tot}$ becomes essential as it provides direct information about the steepness around zero magnetic field of the magnetization curve and the piezomagnetic coefficient. In the as-deposited condition $H_{K,tot}$ was found to be ca. 15.6 Oe and after annealing values of 19.2 Oe (250 °C) and 18.6 Oe (350 °C) were obtained, see magnetization curves along the hard axis in Figure 5.10b.
The most noticeable changes in the magnetic propeties after the first annealing step are the strong increase of $H_{K,tot}$ paired with a pronounced rounding of the hysteresis along the hard axis and an enhanced rectangular character along the easy axis. Such a behaviour originates from the change of random to ordered pinning and the resulting change of the magnetization reversal process as discussed by [218].

[10] Experiments were performed by Enno Lage. A detailed discussion on magnetic properties of ex-change biased systems can be found in [199].

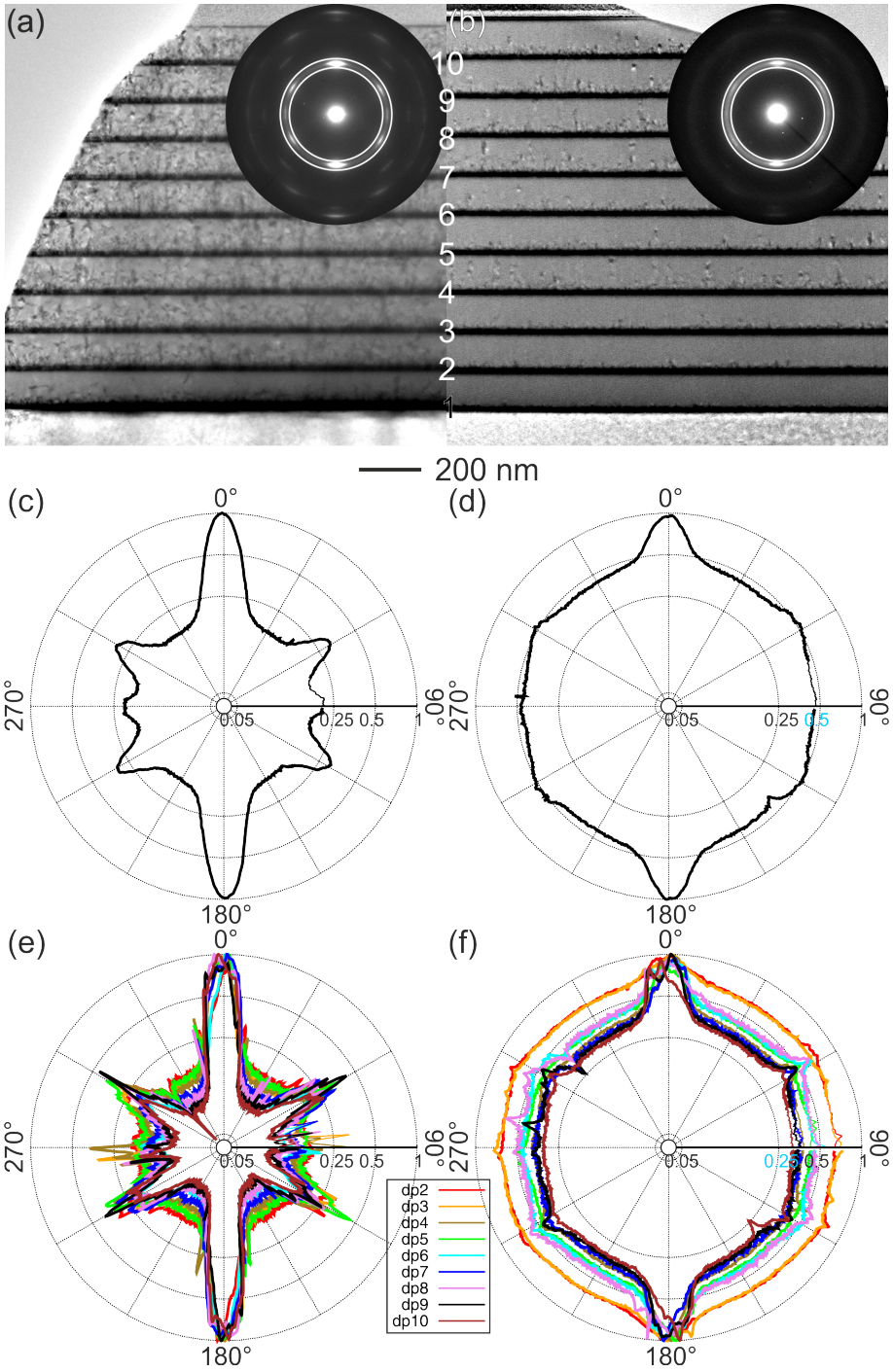

Figure 5.9: Coupled system: Bright field image and associated SAED pattern after (a) in-situ and (b) ex-situ annealing. Normalized radial intensity distribution for the marked regions in the SAED pattern (c) in-situ and (d) ex-situ. Normalized radial plots of SAED series recorded at the numbered single sequences for the coupled system (dp x)(collecting area for SAED: 250 nm) (e) in-situ and (f) ex-situ.

The same annealing procedure was repeated for a modified coupled system. The thickness of the FeCoSiB layer was extended to 200 nm with a reduced sequence

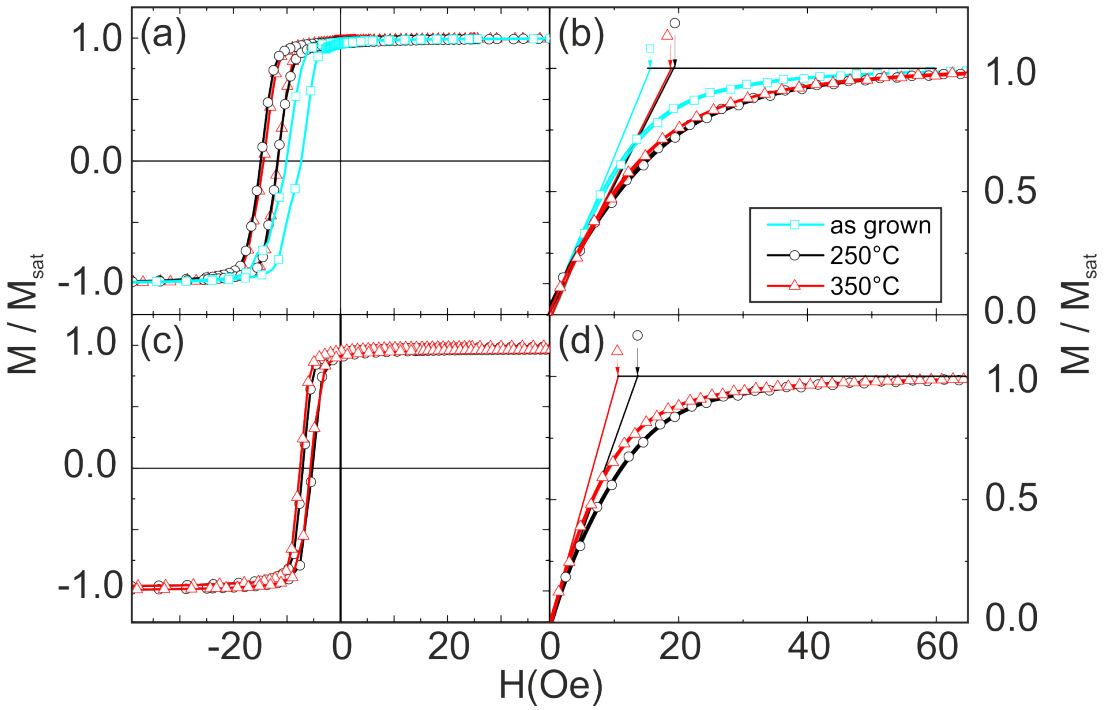

Figure 5.10: Hysteresis loops of exchange coupled multilayer systems for different stages of annealing. Multilayer stack with 100 nm thick FeCoSiB layers: (a) Easy axis and (b) hard axis. Multilayer stack with 200 nm thick FeCoSiB layers: (c) Easy axis and (d) hard axis. The total anisotropy field $H_{K,tot}$ indicated by arrows and symbols in the hard axis loops corresponding to the stages of heat treatmen.

number of 5. Thus, the total dimensions of the system maintained with respect to the original coupled system, but with a higher relevance of the bulk properties of the ferromagnet to the exchange bias.

For the easy axis a H_{EB} of ca. 6.3 Oe was obtained after annealing, cf. Figure 5.10c. Along the hard axis $H_{K,tot}$ was measured to be 13.2 Oe (250 °C) and 10.8 Oe (350 °C), cf. Figure 5.10d. The values of $H_{K,tot}$ show an enhanced difference compared to the corresponding values from the original coupled system. This behavior is based on the dependency of $H_{K,tot}$ to H_{EB} and anisotropy field H_K. The latter is determined by the bulk properties while the exchange bias is an interfacial effect. As conseqeunce, only a slightly increase can be generated for H_{EB}, but an enhanced effect to the anisotropy field is achived due to annealing effects. All measurements excluded a substantial increase of $H_{K,tot}$. The hard axis permeability and thus the piezomagnetic coefficient is not diminished for small fields. Due to the defined unidirectional anisotropy a configuration allowing application of an excitation field perpendicular to the easy axis is achieved. This is favourable in order to optimize the magnetostrictive response for small magnetic fields at zero external bias.

5.3 Tomography on an Optimized ME Demonstrator System

In a varity of previous studies it was pointed out that a crucial relation between the morphology and the magnetic properties of different functional thin film materials (including Co, CoPt, CoNi [219, 220, 221]) is existing. A dominating factor in this context is the quality of the substrate surface for the deposited film. As explicitly stated by Chang and Kryder [222] and Shaw et al. [219], a surface roughness of the substrate influences not only the thin film structure directly at the common interface but also following layer structures, which, in turn, causes a deterioration of the magnetic properties. The roughness within magnetic layers is described in many instances with a unfirom sinusoidal function [223], however, Schrag et al. [224] raised concerns to this assumption as a discrepancy was found between their experimentally obtained TEM data and the ideal model.
Although the sinusoidal model seems to be not accurate enough for the roughness describtion, conventional TEM investigation methods are also not useful for investigation and interpretation of such real structure feature. In this section, the limiations of normal two-dimensional (2D) TEM projection-view modes are demonstrated. Further the electron tomography [225] is introduced, allowing to achieve and to evaluate a complete data set of the structural roughness.

First Investigations on 3D Roughness Evolution in Magnetostrictive Multilayers

In the section 4.1.2 a topography recording of AlN (Figure 4.6) exhibited the high surface roughness of the thin film. The exchange biased multilayer (introduced in section 5.1) was deposited directly on the rough surface of AlN, as depicted in Figure 5.3a. From this STEM Z-contrast image it became apparent, that the AlN roughness is transferred into the magnetostrictive component. However, a single two-dimensional (S)TEM projection of the structure fails to provide an accurate prediction of the layer morphology. As can be seen from the inset of Figure 5.3a, the strong variation in the contrast (and also in the corresponding chemical analysis) may lead to ambiguous or to incorrect interpretations: The origin of this effect can be explained plausibly as projection phenomenon of a 3D roughness. Also a disturbance of a proper layer sequence, in terms of chemically not separated layers, must be considered which may result from problems in the deposition process. Only by applying electron tomography, a full understanding of the 3D morphology can be obtained within the multilayer system and its incremental variation of the topology from a single layer sequence to next following. The tomography results of the ME system (the magnetostrictive multilayer $Fe_{50}Co_{50})/Mn_{70}Ir_{30}$ system on AlN) are depicted in Figure 5.11. Starting directly from the ME interface, the first four layer sequences of the multilayer stack were investigated. To emphasize the evolution of layer deformation, which arises from the initial AlN roughness, only the Ta layers are presented.

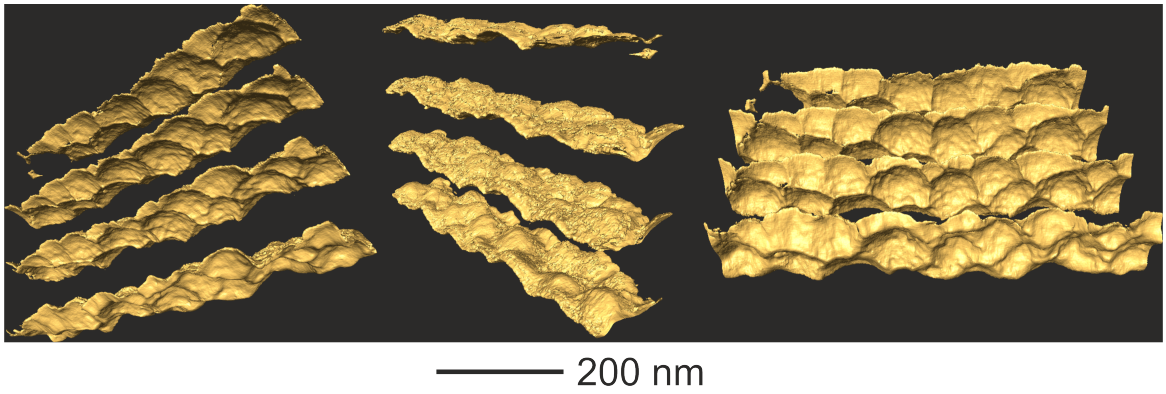

Figure 5.11: (S)TEM electron tomography on exchanged biased ME demonstrator specimen introduced in section 5.1 and Figure 5.3a: Exclusive view on a set of consecutive Ta-layers in different perspectives. The bottom layer is directly adjacent to the rough surface of the AlN substrate. The influence and the propagation of this initial three-dimensional roughness are visualized for the set of Ta-layers.

As can be seen, the Ta layers exhibit a complicated wave-like character and the amplitudes of these wave extremums decrease with increasing distance to the multilayer-AlN interface. Further, the reduced amplitude is combined with a broadening of the wave length, causing a merging of the maxima in the Ta layers with higher distance to the interface. Using for instance the marked maxima of the enlarged view depicted in Figure 5.12a, a geometrical model (Figure 5.12b) can be deduced to describe the surface of single and intersecting maxima.

In the first Ta layer (case (i): adjacent to the AlN surface) the separated maxima exhibited an approximately circular base area (distortion of the circular area $<2\%$) with peak heights of 56 nm and 44 nm, respectively. The shapes of these maxima can be described in a general treatment as ellipsoidal caps, where the decisive parameters are the semi-axes of the cap base (r_a, r_b) and the height of the cap (h). For case (i), the geometrical shape can be simplified into a spherical cap, allowing the calculation of the lateral surface area M_{spc} [226]:

$$M_{spc} = \pi(r^2 + h^2)$$

with r as the radius of the base of the cap. In case (ii), the maxima transfer into oblate ellipsoidal caps with a difference in the length of the semi-axes of ca. 20% and 10% and a simultaneous reduction of the height by 40% and 30% with respect to case (i). For the determination the lateral surface area M_{oec}, Erbil and Meric [227] provided a solution for a so-called three-parameter ellipsoidal cap model:

$$M_{oec} = \frac{\pi}{b^2 \cdot e}\{b^2[ea^2 + b^2\ln(eab + ab)] - y_0 ea\sqrt{(eay_0)^2 + b^4} - b^4\ln(y_0 ea + \sqrt{(eay_0)^2 + b^4})\}$$

with e as the eccentricity, here set as

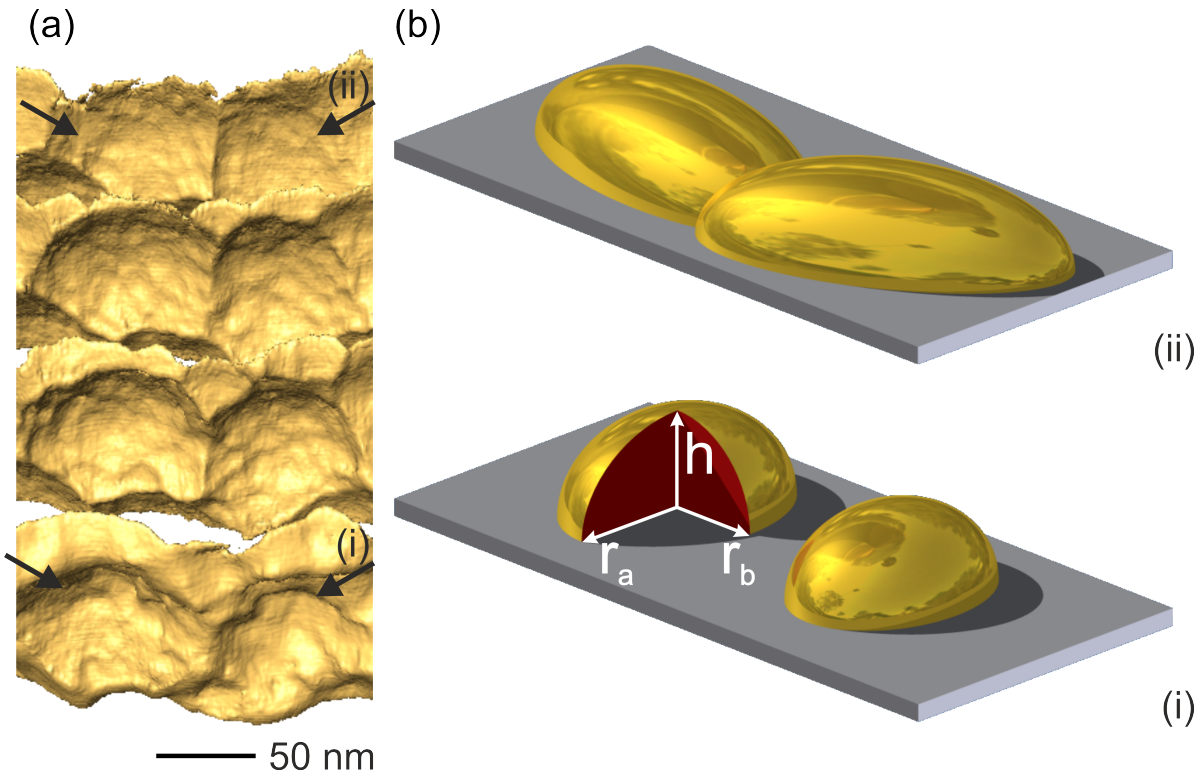

Figure 5.12: (a) Focussed view on the Ta layer sequences form Figure 5.11. The arrows mark the variation of two roughness induced structure-maxima within the different layer sequences. (b) Simplified model illustrating the structural evolution of the distortion within the magnetostrictive sequences. The three-dimensional distortion can be rationalized by ellipsoidal caps with the semi-axes of the base of the cap r_a, r_b and the height h. In case (i) a spherical cap can be assumed for the two maxima, while in case (ii) the maxima tranfer into oblate ellipsoidal caps.

$$e \equiv \sqrt{1 - \left(\frac{b}{a}\right)^2}$$

the parameters a, b are the semi-axis lengths of a 2-D ellipse, which corresponds to ellipsoidal cap, and $y_0 = b - h$. A general calculation of the surface area and intersections of ellipsoids were provided by Tee [228]. As prognosis for future works, this may serve a basis for computational calculation of experimental determined surface real-structures.

It is worth to note, that an assummption of smooth surfaces for the ellipsoidal cap model holds for the regime of tens of nanometers. As the experimental data exhibits, additional deformation of the layer structures are visible for even lower scales. To study this nanoscale behavior more precise tomography investigations become essential. Scott et al. [229] demonstrated the possibilty of gaining full surface-morphology information with a 2.4 Å resolution of 10 nm gold particles using the capabilites of state-of-the-art TEM equipment. With such resolution, an enhanced understand-

ing between structural nano-phenomena and resulting property effects should be achievable.

5.4 Summary: Exchange-Biased Magnetostrictive Materials

In this chapter, a magnetostrictive material was introduced suitable for biomagnetic sensing. It is based on the exchange coupling of the {1 1 1} textured antiferromagnet $Mn_{70}Ir_{30}$ with magnetostrictive components such as $Fe_{50}Co_{50}$ or the amorphous FeCoSiB. The texture of $Mn_{70}Ir_{30}$ was established by using the bilayer Ta/ {1 1 1} Cu as seed layer. Superior magnetic properties of the material were achieved with a multilayer stacking using the repeating sequence of Ta, Cu, $Mn_{70}Ir_{30}$, and a magnetostrictive component. Transmission electron microscopy was applied to evaluate the necessary strutucal integrity and to verify the orientation relationship on different length scales.
Further, the structural behavior during heat treatment and its influence on the magnetic properties were analyzed for a multilayer system using FeCoSiB as magnetostrictive component. The investigations include exchange coupled (direct interface $Mn_{70}Ir_{30}$/ FeCoSiB) and decoupled samples ($Mn_{70}Ir_{30}$/ Ta/ FeCoSiB) on different length scales. Same annealing procedures were performed and compared in- and ex-situ. Two main aspects can be deduced from these studies: First, multilayer specimens, particularly the FeCoSiB layers, maintained almost unaffected during the heating process up to 250 °C. Second, the presence of crystal nuclei within the amorphous layers (observed only in the ex-changed coupled systems) crucially influences the formation of crystalline grains after increasing the annealing temperature over 250 °C.
Also a considerable higher degree of crystallization was observed for in-situ annealing with regard to the ex-situ one, as explicitly demonstrated for temperature of 350 °C.
For corresponding magnetic properties of the exchange coupled systems, it was found[11], that the total anisotropy field $H_{k,tot}$ (achieved after annealing at 250 °C) decreases for a further annealing step at 350 °C. Although the presence and the growth of crystalline filaments was observed before and during the annealing procedure, the entire annealing procedure causes no decrease of the permeability recorded along the magnetic hard axis. This indicates a conservation of the soft magnetic properties.
In order to produce ME sensors based on the exchange coupled multilayers, those magnetostrictive samples were deposited on the rough surface of piezoelectric AlN. With electron tomography the initial roughness at the common multilayer/ AlN interface and the evolution of the roughness within the multilayer was detectable with a full three-dimensional model. A first geometric model was proposed to describe quantitatively the respective surfaces within the multilayer and to rationalize the roughness evolution.

[11] Measurements perforemd by Enno Lage [199]

6 Conclusion and Outlook

In this work, structural characterizations on single components and demonstrators for ME devices[1] were presented. These TEM based results were accompanied in majority with quantitative analysis and were associated subsequently with the macroscopic properties[2] of the respective material.
For 0-3 and 2-2 ME nanocomposites, thin films of AlN were used as piezoelectric component. The piezoelectric functionality of AlN depends on the quality of the [0 0 0 1] texture. The morphology was determined by electron diffraction methods and HRTEM, offering precise information on size, shape, texture, and orientation relationship for the entire thin films as well as for single AlN columnar grains. Particularly, by using the advanced ACOM method a comprehensive collection of such information was enabled for lager length scales ($>>100\,\mathrm{nm}$) with lateral resolution in the range of a few nanometers. In the studied case of the AlN thin films, multiple grains exhibited the optimal growth along [0 0 0 1] direction, however, also a minority of grains were observed which were strongly tilted apart from this direction. Such structural features were related with distortions of piezoelectric signals by using a methodical combination with PFM measurements.
A 0-3 ME demonstrator system was established by incorporating metallic Co nanoparticles into AlN. The influence of the Co particles to the AlN matrix was worked out by electron diffraction, showing a considerable decrease of the [0 0 0 1] texture and, thus, correlating with a poor functionality of the material. Also according to this fundamental result, the design of 0-3 ME nanocomposites was critical evaluated and considered as not suitable for high-performance ME sensors [12, 117].
A 2-2 demonstrator system was obtained with the combination of AlN thin films and a specially developed magnetostrictive multilayer. The latter is set up by a repetition of the layer sequence $\mathrm{Ta/\,Cu/\,Mn_{70}Ir_{30}/\,Fe_{50}Co_{50}}$ (or FeCoSiB) with an exchange coupled interface between the antiferromagnet $\mathrm{Mn_{70}Ir_{30}}$ and ferromagnet $\mathrm{Fe_{50}Co_{50}}$ (or FeCoSiB). While exposing the multilayer to an external magnetic field, a heat treatment on the sample allows a deliberate adjustment of a defined exchange bias. By applying TEM in-situ annealing experiments on FeCoSiB containing multilayers, such a heat treatment was simulated and structural changes were studied. Although crystallization processes were observed within the amorphous FeCoSiB before and during the annealing procedure, strong indications were found for a conservation of the soft magnetic properties after the entire annealing procedure.
Interface studies were performed for a 2-2 demonstrator system using electron tomography. Thus, a three dimensional reconstruction was enabled for the morphology

[1] Synthesis and fabrication of all materials were performed by other SFB members.
[2] Property measurements were always performed by other SFB members.

of adjacent layers within the multilayer phase. The propagation and variation of a roughness, introduced by the AlN surface, was visualized and rationalized by a basic ellipsoidal cap model. Investigating this 2-2 demonstrator system with a state-of-the-art TEM, capable of electron tomography, a better spatial resolution is achievable. In this manner, a better understanding between structural nano-phenomena and magnetic property effects could be elaborated.
As another candidate for the piezo- (and ferro-)electric component, lead-free BCZT ($Ba_{0.8}Ca_{0.2}Ti_{0.8}Zr_{0.2}O_3$) was investigated. The crystal structure and the presence of sophisticated defect phenomena depend on synthesis conditions. Bulk material, prepared by the sol-gel process, exhibited in the majority a pseudocubic structure. The minimal distortions within the specimen could be addressed to a coexistence of orthorhombic and tetragonal phase as indicated by XRD data. Only in few cases defect structures could be observed. Thin films, prepared by pulsed laser deposition, contained a variety of defects, including twin-defects and modulations. The latter was interpreted as 7L polytype, with a corresponding modulation vector along the [1 1 1] direction[3]. The properties of the thin film show a relaxor behavior. In order to contribute to an enhanced property-real structure relation and to provide more validation on the stated structural features, additional characterization processes are mandatory. Similar to the presented AlN analyses, ACOM measurements should be performed on cross-section and basal view specimens. This allows the precise study of the morphology on a larger scale with nanometer resolution. In this manner, a localization and statistical evaluations of features are simplified or enabled. Using the combined approach of CBED and aberration corrected HRTEM on these features, a precise structure characterizations can be performed. It should be noted that for aberration corrected microscopy a dedicated specimen preparation becomes demanding to ensure excellent framework conditions for structural interpretation and model design.
Particularly, for the modulation within the BCZT thin films, the aim in future works must be a comprehensive understanding. A suitable approach for the analysis of defect structure was demonstrated by using supercells. The discussed examples in this work were the stacking mismatch boundary in AlN thin films and twin defects for flame transport synthetized (FTS) materials (hierarchical structures based on SnO_2 and ZnO sea-urchin nanospikes). Apart from the latter materials, the FTS provides one dimensional ZnO nanostructures suitable for 1-1 demonstrators. Preliminary studies on ZnO nanorods exhibited the possibility of obtaining mechanical and electric information using an in-situ push-to-pull (PTP) device[4]. In future works, the combination of the PTP device measurements with aberration corrected high resolution microscopy (and thus the usage of GPA) must be evaluated particular for fundamental research. Such measurements would allow the analysis of deformation processes directly on an atomic scale. Already stated by Kobler et al. [39] PTP measurements can be successfully combined with ACOM measurements. Independently form the design of the ME nanocomposite, this type of investigation offers an interesting approach for in-situ process simulation.

[3]Using a pseudocubiuc notation.
[4]Measurements performed by Hysitron.

In this work the properties and the functionality of ME demonstrator systems or single piezoelectric/ magnetostrictive components were related to their respective structural characteristics. Based on these findings, an evaluation of the suitability for high sensitive ME devices was executed for different composite designs, excluding less promising variants as the 0-3 nanocomposites[5]. In other words, a stringent focusing can be placed on the high potential designs, including 2-2 and 1-1 composites, for a future development within the framework of the SFB.
In-situ studies and quantitative data analysis created impulses for further optimization processes of materials produced within the SFB and exhibited fundamental limitations and opportunities of the newly established FTS method with respect to application development.

[5]In this thesis the structural aspects of 0-3 nanocomposites (based on AlN/Co) were discussed, other critical aspects of on the functionality of the nanocomposites are presented in [117].

Bibliography

[1] S. Groppa, M. Muthuraman, B. Otto, and H. S. J. Raethjen G. Deuschl. Subcortical substrates of tms induced modulation of the cortico-cortical connectivity. *Brain Stimulation*, 6:138 – 146, 2013.

[2] A. Fasano and G. Deuschl. Patients and {DBS} targets: Is there any rationale for selecting them? *Basal Ganglia*, 2(4):211 – 219, 2012.

[3] M. Muthuraman, K. Arning, R.B. Govindan, U. Heute, G. Deuschl, and J. Raethjen. Cortical representation of different motor rhythms during bimanual movements. *Experimental Brain Research*, 223(4):489 – 504, 2012.

[4] N. Japaridze, M. Muthuraman, F. Moeller, R. Boor, A. R. Anwar, G. Deuschl, U. Stephani, J. Raethjen, and M. Siniatchkin. Neuronal networks in west syndrome as revealed by source analysis and renormalized partial directed coherence. *Brain Topography*, 26(1):157 – 170, 2013.

[5] R. C. Helmich, M. Hallett, G. Deuschl, I. Toni, and B. R. Bloem. Cerebral causes and consequences of parkinsonian resting tremor: a tale of two circuits? *Brain*, 2012.

[6] D. Cohen. Magnetoencephalography: Detection of the brain's electrical activity with a superconducting magnetometer. *Science*, 175(4022):664 – 666, 1972.

[7] E. Quandt. *Geplanter Sonderforschungsbereich 855 Magnetoelektrische Verbundwerkstoffe - biomagnetische Schnittstellen der Zukunft, Finanzierungsantrag 2010 - 2013.* Christtian Albrechts Universität, e. quandt edition.

[8] C.-W. Nan, M. I. Bichurin, S. Dong, D. Viehland, and G. Srinivasan. Multiferroic magnetoelectric composites: Historical perspective, status, and future directions. *Journal of Applied Physics*, 103(3):031101, 2008.

[9] R. Jahns, A. Piorra, E. Lage, C. Kirchhof, D. Meyners, J. L. Gugat, M. Krantz, M. Gerken, R. Knöchel, and E. Quandt. Giant magnetoelectric effect in thin-film composites. *Journal of the American Ceramic Society*, 96(6):1673 – 1681, 2013.

[10] W. Eerenstein, N. D. Mathur, and J. F. Scott. Multiferroic and magnetoelectric materials. *Nature*, 442(7104):759 – 765, August 2006.

[11] M. Fiebig. Revival of the magnetoelectric effect. *Journal of Physics D: Applied Physics*, 38(8):R123, 2005.

[12] B. Gojdka, V. Hrkac, J. Xiong, M. Gerken, L. Kienle, T. Strunskus, V. Zaporojtchenko, and F. Faupel. A critical evaluation of the 0-3 approach for magnetoelectric nanocomposites with metallic nanoparticles. *Journal of Applied Physics*, 112(4):044303, 2012.

[13] S. Marauska, R. Jahns, H. Greve, E. Quandt, R. Knöchel, and B. Wagner. Mems magnetic field sensor based on magnetoelectric composites. *Journal of Micromechanics and Microengineering*, 22(6):065024, 2012.

[14] H. Greve, E. Woltermann, R. Jahns, S. Marauska, B. Wagner, R. Knöchel, M. Wuttig, and E. Quandt. Low damping resonant magnetoelectric sensors. *Applied Physics Letters*, 97(15):152503, 2010.

[15] G. Srinivasan, E. T. Rasmussen, B. J. Levin, and R. Hayes. Magnetoelectric effects in bilayers and multilayers of magnetostrictive and piezoelectric perovskite oxides. *Physical Review B*, 65:134402, Mar 2002.

[16] E. Quandt, Simon Stein, and Manfred Wuttig. Magnetic vector field sensor using magnetoelectric thin-film composites. *Magnetics, IEEE Transactions on*, 41(10):3667 – 3669, 2005.

[17] R. Jahns, R. Knöchel, H. Greve, E. Woltermann, E. Lage, and E. Quandt. *IEEE International Symposium on Medical Measurements and Applications*, pages 107 – 110, 2011.

[18] E. Lage, C. Kirchhof, V. Hrkac, L. Kienle, R. Jahns, R. Knöchel, E: Quandt, and D. Meyners. Exchange biasing of magnetoelectric composites. *Nature Materierals*, 11(6):523 – 529, 2012.

[19] F. Argin, H. Ahrens, and L. Klinkenbusch. Improved measurement surface for meg using magnetic-dipole sources and a spherical-multipole expansion. *Advances in Radio Science*, 10:93 – 97, 2012.

[20] J. H. Park, H. M. Jang, H. S. Kim, C. G. Park, and S. G. Lee. Strain-mediated magnetoelectric coupling in batio$_3$-co nanocomposite thin films. *Applied Physics Letters*, 92(6):062908, 2008.

[21] J. Ma, J. Hu, Z. Li, and C. W. Nan. Recent Progress in Multiferroic Magnetoelectric Composites: from Bulk to Thin Films. *Advanced Materials*, 23(9):1062 – 1087, 2011.

[22] Matthias C. Krantz and Martina Gerken. Theory of magnetoelectric effect in multilayer nanocomposites on a substrate: Static bending-mode response. *AIP Advances*, 3(2):022103, 2013.

[23] E. Lage, F. Woltering, E. Quandt, and D. Meyners. Exchange biased magnetoelectric composites for vector field magnetometers. *Journal of Applied Physics*, 113(17):17C725, 2013.

[24] B. Gojdka, R. Jahns, K. Meurisch, H. Greve, R. Adelung, E. Quandt, R. Knochel, and F. Faupel. Fully integrable magnetic field sensor based on delta-e effect. *Applied Physics Letters*, 99(22):223502, 2011.

[25] D. G. Stroppa, L. F. Zagonel, L. A. Montoro, E. R. Leite, and A. J. Ramirez. High-resolution scanning transmission electron microscopy (hrstem) techniques: High-resolution imaging and spectroscopy side by side. *ChemPhysChem*, 13(2):437 – 443, 2012.

[26] X. H. Liu and J. Y: Huang. In situ tem electrochemistry of anode materials in lithium ion batteries. *Energy Environ. Sci.*, 4:3844 – 3860, 2011.

[27] K. W. Urban. Is science prepared for atomic-resolution electron microscopy? *Nat Mater*, 8(4):260 – 262, 2009.

[28] K. W. Urban. Studying atomic structures by aberration-corrected transmission electron microscopy. *Science*, 321(5888):506 – 510, 2008.

[29] Z. L. Wang. Picoscale science and nanoscale engineering by electron microscopy. *Journal of Electron Microscopy*, 60:S269 – S278, 2011.

[30] D. B. Williams and C. B. Carter. *Transmission Electron Microscopy: a Textbook for Materials Science.* (Springer, New York), 2009.

[31] J. B. Le Poole. *Philips Technical Review*, 9:33, 1947.

[32] W. Kossel and G. Möllenstadt. *Annals of Physics*, 36, 1939.

[33] J. W. Steeds and R. Vincent. Use of high-symmetry zone axes in electron diffraction in determining crystal point and space groups. *Journal of Applied Crystallography*, 16(3):317–324, Jun 1983.

[34] P. A. Midgley, M. E. Sleight, M. Saunders, and R. Vincent. Measurement of Debye-Waller factors by electron precession. *Ultramicroscopy*, 75(2):61 – 67, 1998.

[35] U. Schürmann, V. Duppel, S. Buller, W. Bensch, and L. Kienle. Precession Electron Diffraction - a versatile tool for the characterization of Phase Change Materials. *Crystal Research and Technology*, 46(6):561–568, 2011.

[36] P. Oleynikov, S. Hovmöller, and X. D. Zou. Precession electron diffraction: Observed and calculated intensities. *Ultramicroscopy*, 107(7):523 – 533, 2007.

[37] E. F. Rauch, M Veron, J. Portillo, D. Bultreys, Y. Maniette, and S. Nicolopoulos. Automatic crystal orientation and phase mapping in TEM by precession diffraction. *Microscopy and Analysis*, 5, 2008.

[38] M. Watanabe and D. B. Williams. Development of diffraction imaging for orientation analysis of grains in scanning transmission electron microscopy. *Microsc. Microanal.*, 13:962–963, 2007.

[39] A. Kobler, A. Kashiwar, H. Hahn, and C. Kübel. Combination of in situ straining and acom tem: A novel method for analysis of plastic deformation of nanocrystalline metals. *Ultramicroscopy*, 128:68 – 81, 2013.

[40] M. J. Hÿtch, E. Snoeck, and R. Kilaas. Quantitative measurement of displacement and strain fields from HREM micrographs. *Ultramicroscopy*, 74(3):131 – 146, 1998.

[41] M. J. Hÿtch and F. Houdellier. Mapping stress and strain in nanostructures by high-resolution transmission electron microscopy. *Microelectronic Engineering*, 84(3):460 – 463, 2007.

[42] P. B. Hirsch, A. Howie, and M. J Whelan. A kinematical theory of diffraction contrast of electron transmission microscope images of dislocations and other defects. *Philosophical Transactions of the Royal Society of London. Series A, Mathematical and Physical Sciences*, 252(1017):499–529, 1960.

[43] J. F. Nye. *Physical Properties of Crystals: Their Representation by Tensors and MatricesClarendon.* (Clarendon Press, Oxford), 1957.

[44] W. O. Saxton. *Scanning Microscopy Supplement*, 6:53, 1992.

[45] E. Sarigiannidou, E. Monroy, N. Gogneau, G. Radtke, P. Bayle-Guillemaud, E. Bellet-Amalric, B. Daudin, and J. L. Rouvière. Comparison of the structural quality in Ga-face and N-face polarity GaN/AlN multiple-quantum-well structures. *Semiconductor Science and Technology*, 21(5):612, 2006.

[46] P.A. Stadelmann. EMS - A software package for electron diffraction analysis and HREM image simulation in material science. *Ultramicroscopy*, 21(2):131–145, 1987.

[47] K. Ishizuka and N. Uyeda. A new theoretical and practical approach to the multislice method. *Acta Crystallographica Section A*, 33(5):740–749, Sep 1977.

[48] R. Kilaas. Optimal and near-optimal filters in high-resolution electron microscopy. *Journal of Microscopy*, 190(1-2):45 – 51, 1998.

[49] R. Adelung, S. Kaps, Y. K. Mishra, M. Claus, T. Preusse, and C. Wolpert. Resilient material for use as heat-resistant, thermal cyclability adhesive between materials with different thermal expansion coefficients, has particles concatenated by connecting nano-bridges to macroscopic resilient material, 2011.

[50] Y. K. Mishra, S. Kaps, A. Schuchardt, I. Paulowicz, X. Jin, D. Gedamu, S. Freitag, M. Claus, S. Wille, A. Kovalev, S. N. Gorb, and R. Adelung. Fabrication of macroscopically flexible and highly porous 3D semiconductor networks from interpenetrating nanostructures by a simple flame transport approach. *Particle & Particle Systems Characterization*, 2013.

[51] S. Kaps. PhD thesis, Christian-Albrechts-University, Kiel, *(to be published).*

[52] V. Hrkac, L. Kienle, S. Kaps, A. Lotnyk, Y. K. Mishra, U. Schürmann, V. Duppel, B. V. Lotsch, and R. Adelung. Superposition twinning supported by texture in ZnO nanospikes. *Journal of Applied Crystallography*, 46(2):396–403, 2013.

[53] S. Kaps, Y. K. Mishra, V. Hrkac, H. Greve, L. Kienle, E. Quandt, and R. Adelung. High aspect ratio free standing ZnO-magnetostrictive mesoscale cylindrical magnetoelectric core shell composite. *MRS Online Proceedings Library*, 1398, 2012.

[54] I. Paulowicz, V. Hrkac, Y. K. Mishra, E. Quiroga-González, H. Föll, R. Adelung, and L. Kienle. *in preparation.*

[55] G. R. Grinton and J. M. Cowley. Phase and amplitude contrast in electron micrographs of biological-material. *Optik*, 34(3):221–&, 1971.

[56] L. Kienle and A. Simon. Polysynthetic twinning in $RbIn_3S_5$. *Journal of Solid State Chemistry*, 167(1):214 – 225, 2002.

[57] H. J. Deiseroth, C. Reiner, K. Xhaxhiu, M. Schlosser, and L. Kienle. X-ray and transmission electron microscopy investigations of the new solids In5S5Cl, In5Se5Cl, In5S5Br, and In5Se5Br. *Zeitschrift für Anorganische und Allgemeine Chemie*, 630(13-14):2319–2328, 2004.

[58] T. Hahn. *International Tables for Crystallography, Volume A: Space Group Symmetry*, volume Volume A. Springer, 5th edition edition, 2005.

[59] I. Paulowicz. Synthesis and characterization of SnO_2 micro- and nanostructures. Master's thesis, Christian-Albrechts-University, Kiel, 2010.

[60] L. Zhang, G. Zhang, H. B. Wu, L. Yu, and X. W. Lou. Hierarchical tubular structures constructed by carbon-coated SnO_2 nanoplates for highly reversible lithium storage. *Advanced Materials*, 25(18):2589 – 2593, 2013.

[61] J. G. Zheng, X. Pan, M. Schweizer, F. Zhou, U. Weimar, W. Göpel, and M. Ruhle. Growth twins in nanocrystalline SnO_2 thin films by high-resolution transmission electron microscopy. *Journal of Applied Physics*, 79(10):7688–7694, 1996.

[62] J. E. Dominguez, L. Fu, and X. Q. Pan. Effect of crystal defects on the electrical properties in epitaxial tin dioxide thin films. *Applied Physics Letters*, 81(27):5168–5170, 2002.

[63] Z. Zhu, J. Ma, C. Luan, W. Mi, and Y. Lv. Twin structures of epitaxial SnO_2 films grown on a-cut sapphire by metalorganic chemical vapor deposition. *Journal of Vacuum Science & Technology A: Vacuum, Surfaces, and Films*, 30(2):021503, 2012.

[64] W.-Y. Lee, P. D. Bristowe, Y. Gao, and K. L. Merkle. The atomic structure of twin boundaries in rutile. *Philosophical Magazine Letters*, 68(5):309–314, 1993.

[65] M. Nagasawa, S. Shionoya, and S. Makishima. Vapor reaction growth of sno_2 single crystals and their properties. *Japanese Journal of Applied Physics*, 4(3):195–202, 1965.

[66] U. Özgür, Y. I. Alivov, C. Liu, A. Teke, M. A. Reshchikov, S. Dogan, V. Avrutin, S. J. Cho, and H. Morkoc. A comprehensive review of ZnO materials and devices. *Journal of Applied Physics*, 98(4):041301, 2005.

[67] A. Dal Corso, M. Posternak, R. Resta, and A. Balderschi. Ab initio study of piezoelectricity and spontaneous polarization in ZnO. *Physical Review B*, 50(15):10715–10721, 1994.

[68] A. Ashrafi and C. Jagadish. Review of zincblende ZnO: Stability of metastable ZnO phases. *Journal of Applied Physics*, 102(7), 2007.

[69] Z. L. Wang. Zinc oxide nanostructures: growth, properties and applications. *Journal of Physics: Condensed Matter*, 16:R829–R858, 2004.

[70] Z. L. Wang. ZnO nanowire and nanobelt platform for nanotechnology. *Materials Science & Engineering: R*, 64:3–4, 2009.

[71] S. B. Hrkac, M. Abes, C. T. Koops, C. Krywka, M. Müller, S. Kap, R. Adelung, J. McCord, E. Lage, E. Quandt, O. M. Magnussen, and B. Murphy. Local magnetization and strain in single magnetoelectric microrod composites. *Journal of Applied Physics*, (Accepted).

[72] C. Borchers, S. Muller, D. Stichtenoth, D. Schwen, and C. Ronning. Catalyst-nanostructure interaction in the growth of 1-D ZnO nanostructures. *Journal of Physical Chemistry B*, 110(4):1656–1660, 2006.

[73] Z. L. Wang. Nanostructures of zinc oxide. *Materials Today*, 7(6):26–33, 2004.

[74] Z. L. Wang. Piezotronic and Piezophototronic Effects. *Journal of Physical Chemistry Letters*, 1(9):1388–1393, 2010.

[75] J. Molarius, J. Kaitila, T. Pensala, and M. Ylilammi. Piezoelectric ZnO films by r.f. sputtering. *Journal of Materials Science: Materials in Electronics*, 14(5-7):431 – 435, 2003.

[76] S. J. Pearton, D. P. Norton, K. Ip, Y. W. Heo, and T. Steiner. Recent progress in processing and properties of ZnO. *Progress in Materials Science*, 50(3):293 – 340, 2005.

[77] J. Liu, Z. Guo, F. Meng, Y. Jia, T. Luo, M. Li, and J. Liu. Novel single-crystalline hierarchical structured zno nanorods fabricated via a wet-chemical route: Combined high gas sensing performance with enhanced optical properties. *Crystal Growth & Design*, 9(4):1716 – 1722, 2009.

[78] E. Comini, G. Faglia, G. Sberveglieri, Z. W. Pan, and Z. L. Wang. Stable and highly sensitive gas sensors based on semiconducting oxide nanobelts. *Applied Physics Letters*, 81(10):1869–1871, 2002.

[79] Y. F. Yan, M. M. Al-Jassim, M. F. Chisholm, L. A. Boatner, S. J. Pennycook, and M. Oxley. $[1\,\bar{1}\,0\,0](1\,1\,0\,2)$ twin boundaries in wurtzite ZnO and group-III-nitrides. *Physical Review B*, 71(4), 2005.

[80] A. Bere and A. Serra. Atomic structures of twin boundaries in GaN. *Physical Review B*, 68(3), 2003.

[81] Y. Dai, Y. Zhang, Y. Q. Bai, and Z. L. Wang. Bicrystalline zinc oxide nanowires. *Chemical Physics Letters*, 375:96–101, 2003.

[82] Y. Ding and L. Wang. Structures of planar defects in ZnO nanobelts and nanowires. *Micron*, 40:335 – 342, 2009.

[83] B. H. Huang, S. Y. Chen, and P. Shen. $1\,0\,\bar{1}\,1$ and $1\,1\,\bar{2}\,1$-specific growth and twinning of ZnO whiskers. *Journal of Physical Chemistry C*, 112:1064–1071, 2008.

[84] B. H. Huang, P. Y. Shen, and S. Y. Chen. Tapered zno whiskers: {hkil}-specific mosaic twinning VLS growth from a partially molten bottom source. *Nanoscale Research Letters*, 4:503–512, 2009.

[85] H. Sowa and H. Ahsbahs. High-pressure X-ray investigation of zincite ZnO single crystals using diamond anvils with an improved shape. *Journal of Applied Crystallography*, 39(2):169 – 175, 2006.

[86] H. M. Otte and A. G. Crocker. Crystallographic formulae for hexagonal lattices. *Physica Status Solidi (b)*, 9(2):441 – 450, 1965.

[87] U. Kaiser, A. Chuvilin, P. D. Brown, and W. Richter. Origin of threefold periodicity in high-resolution transmission electron microscopy images of thin film cubic SiC. *Microscopy and Microanalysis*, 5(6):420 – 427, 1999.

[88] E. Müller and F. Krumeich. A simple and fast TEM preparation method utilizing the pre-orientation in plate-like, needle-shaped and tubular materials. *Ultramicroscopy*, 84(84):143 – 147, 2000.

[89] H. Chen, Y. Gao, H. Yu, H. Zhang, L. Liu, Y. Shi, H. Tian, S. Xie, and J. Li. Structural properties of silver nanorods with fivefold symmetry. *Micron*, 35(6):469 – 474, 2004.

[90] B. F. Vieweg, B. Butz, W. Peukert, R. N. Klupp-Taylor, and E. Spiecker. TEM preparation method for site- and orientation-specific sectioning of individual anisotropic nanoparticles based on shadow-FIB geometry. *Ultramicroscopy*, 113:165 – 170, 2012.

[91] R. M. Langford. Focused ion beams techniques for nanomaterials characterization. *Microscopy Research and Technique*, 69(7):538 – 549, 2006.

[92] L. Kienle, V. Duppel, B. Mogwitz, J. Janek, and M. von Kreutzbruck. Synthesis-real structure-property: The showcase of silver-rich Ag2Se. *Crystal Growth & Design*, 11(6):2412–2421, 2011.

[93] Y. K. Mishra, V. S. K. Chakravadhanula, V. Hrkac, S. Jebril, D. C. Agarwal, S. Mohapatra, D. K. Avasthi, L. Kienle, and R. Adelung. Crystal growth behaviour in Au-ZnO nanocomposite under different annealing environments and photoswitchability. *Journal of Applied Physics*, 112(6):064308, 2012.

[94] S. Jebril, H. Kuhlmann, S. Müller, C. Ronning, L. Kienle, V. Duppel, Y. K. Mishra, and R. Adelung. Epitactically interpenetrated high quality zno nanostructured junctions on microchips grown by the Vapor-Liquid-Solid method. *Crystal Growth & Design*, 10(7):2842–2846, 2010.

[95] M. Abes, C. T. Koops, S. B. Hrkac, H. Greve, E. Quandt, S. P. Collins, B. M. Murphy, and O. M. Magnussen. Direct measurements of field-induced strain at magnetoelectric interfaces by grazing incidence x-ray diffraction. *Applied Physics Letters*, 102(1):011601, 2013.

[96] S. Bhowmick, D. Stauffer, H. Guo, S. Kaps, Y.K. Mishra, V. Hrkac, O. Warren, R. Adelung, A. Minor, and L. Kienle. In Situ Electromechanical Study of ZnO Nanowires. *Microscopy and Microanalysis*, 19:434–435, 8 2013.

[97] S. Marauska, V. Hrkac, T. Dankwort, R. Jahns, H. J. Quenzer, R. Knöchel, L. Kienle, and B. Wagner. Sputtered thin film piezoelectric aluminum nitride as a functional MEMS material. *Microsystem Technologies*, 18(6):787–795, 2012.

[98] B. Gojdka, V. Hrkac, T. Strunskus, V. Zaporojtchenko, L. Kienle, and F. Faupel. Study of cobalt clusters with very narrow size distribution deposited by high-rate cluster source. *Nanotechnology*, 22(46):465704, 2011.

[99] B. Gojdka, V. Zaporojtchenko, V. Hrkac, J. Xiong, L. Kienle, T. Strunskus, and F. Faupel. Highly versatile concept for precise tailoring of nanogranular composites with a gas aggregation cluster source. *Applied Physics Letters*, 100(13):133104, 2012.

[100] V. Hrkac, U. Schürmann, S. Marauska, B. Wagner, A. Petraru, H. Kohlstedt, V. Duppel, B. V. Lotsch, V. S. K. Chakravadhanula, A. Kobler, C. Kübel, and L. Kienle. Combined structural TEM observations on different length scales for characterization of AlN texture and columnar growth. *in preparation.*

[101] V. Hrkac, A. Piorra, V. Duppel, E. Quandt, and L. Kienle. Investigations on BCZT. *in preparation.*

[102] A. Piorra, A. Petraru, H. Kohlstedt, M. Wuttig, and E. Quandt. Piezoelectric properties of $0.5(Ba_{0.7}Ca_{0.3}TiO_3) - 0.5[Ba(Zr_{0.2}Ti_{0.8}])O_3]$ ferroelectric lead-free laser deposited thin films. *Journal of Applied Physics*, 109(10):104101, 2011.

[103] F. Bernardini, V. Fiorentini, and D. Vanderbilt. Spontaneous polarization and piezoelectric constants of III-V nitrides. *Phys. Rev. B*, 56:R10024 – R10027, Oct 1997.

[104] I. Vurgaftman, J. R. Meyer, and L. R. Ram-Mohan. Band parameters for III-V compound semiconductors and their alloys. *Journal of Applied Physics*, 89(11):5815 – 5875, 2001.

[105] V. Fuflyigin, E. Salley, A. Osinsky, and P. Norris. Pyroelectric properties of AlN. *Applied Physics Letters*, 77(19):3075 – 3077, 2000.

[106] P. Muralt. Recent progress in materials issues for piezoelectric MEMS. *Journal of the American Ceramic Society*, 91(5):1385 – 1396, 2008.

[107] A. Andrei, K. Krupa, M. Jozwik, P. Delobelle, L. Hirsinger, C. Gorecki, L. Nieradko, and C. Meunier. Aln as an actuation material for MEMS applications: The case of aln driven multilayered cantilevers. *Sensors and Actuators A: Physical*, 141(2):565 – 576, 2008.

[108] P. Muralt, J. Antifakos, M. Cantoni, R. Lanz, and F. Martin. Is there a better material for thin film baw applications than AlN? *Proceedings of the IEEE Ultrasonics Symposium*, pages 315 – 320, 2005.

[109] I. L. Guy, S. Muensit, and E. M. Goldys. Extensional piezoelectric coefficients of gallium nitride and aluminum nitride. *Applied Physics Letters*, 75(26):4133 – 4135, 1999.

[110] S.-H. Lee, J.-K. Lee, and K. H. Yoon. Growth of highly c-axis textured AlN films on Mo electrodes for film bulk acoustic wave resonators. *Journal of Vacuum Science & Technology A: Vacuum, Surfaces, and Films*, 21(1):1 – 5, 2003.

[111] F. Martin, P. Muralt, and M.-A. Dubois. Process optimization for the sputter deposition of molybdenum thin films as electrode for AlN thin films. *Journal of Vacuum Science & Technology A: Vacuum, Surfaces, and Films*, 24(4):946 – 952, 2006.

[112] A. Rodriguez-Navarro, W. Otano-Rivera, J. M. Garcia-Ruiz, R. Messier, and L. J. Pilione. Development of preferred orientation in polycrystalline AlN thin films deposited by rf sputtering system at low temperature. *Journal of Materials Research*, 12:1850 – 1855, 1997.

[113] M.-A. Dubois and P. Muralt. Stress and piezoelectric properties of aluminum nitride thin films deposited onto metal electrodes by pulsed direct current reactive sputtering. *Journal of Applied Physics*, 89(11):6389 – 6395, 2001.

[114] S. Trolier-McKinstry and P. Muralt. Thin Film Piezoelectrics for MEMS. *Journal of Electroceramics*, 12(1-2):7–17, 2004.

[115] S. Tadigadapa and K. Mateti. Piezoelectric MEMS sensors: state-of-the-art and perspectives. *Measurement Science and Technology*, 20(9):092001, 2009.

[116] R. Lanz, C. Lambert, L. Senn, L. Babathiler, and G. J. Reynolds. *Ultrasonics Symposium IEEE*, 1:1481–1485, 2006.

[117] B. Gojdka. *New Concepts for Functional 0-3 nnanocomposite and Magnetic Field Sensors*. PhD thesis, Christian-Albrechts-University of Kiel, 2012.

[118] S. Marauska. PhD thesis, Christian-Albrechts-University of Kiel, 2013.

[119] A. Artieda, M. Barbieri, C. S. Sandu, and P. Muralt. Effect of substrate roughness on c-oriented AlN thin films. *Journal of Applied Physics*, 105(2):024504, 2009.

[120] L. Sagalowicz, G. R. Fox, M. A. Dubois, C. A. P. Muller, P. Muralt, and N. Setter. Microstructure and defects of wurtzite structure thin films. *Journal of the European Ceramic Society*, 19(6-7):1427 – 1430, 1999.

[121] F. Engelmark, G. F. Iriarte, I. V. Katardjiev, M. Ottosson, P. Muralt, and S. Berg. Structural and electroacoustic studies of AlN thin films during low temperature radio frequency sputter deposition. *Journal of Vacuum Science & Technology A: Vacuum, Surfaces, and Films*, 19(5):2664–2669, 2001.

[122] J. L. Rouviere, M. Arlery, B. Daudin, G. Feuillet, and O. Briot. Transmission electron microscopy structural characterisation of GaN layers grown on (0001) sapphire. *Materials Science and Engineering: B*, 50:61 – 71, 1997.

[123] Y. Xin, P. D. Brown, C. J. Humphreys, T. S. Cheng, and C. T. Foxon. Domain boundaries in epitaxial wurtzite gan. *Applied Physics Letters*, 70(10):1308–1310, 1997.

[124] V. Lebedev, K. Tonisch, F. Niebelschutz, V. Cimalla, D. Cengher, I. Cimalla, C. Mauder, S. Hauguth, O. Ambacher, F. M. Morales, J. G. Lozano, and D. Gonzalez. Coalescence aspects of IIi-nitride epitaxy. *Journal of Applied Physics*, 101(5):054906, 2007.

[125] C. M. Drum. Intersecting faults on basal and prismatic planes in aluminium nitride. *Philosophical Magazine*, 11(110):313 – 334, 1965.

[126] J. E. Northrup. Structure of the $11\bar{2}0$ inversion domain boundary in GaN. *Physica B: Condensed Matter*, 273 - 274(0):130 – 133, 1999.

[127] Y. Yan, M. Terauchi, and M. Tanaka. The structures of inversion domain boundaries in AlN ceramics. *Philosophical Magazine A*, 75(4):1005 – 1022, 1997.

[128] J. Jasinski, Z. Liliental-Weber, Q. S. Paduano, and D. W. Weyburne. Inversion domains in AlN grown on (0001) sapphire. *Applied Physics Letters*, 83(14):2811–2813, 2003.

[129] N.-E. Lee, R. C. Powell, Y.-W. Kim, and J. E. Greene. Molecular beam epitaxy of GaN(0001) utilizingNH_3 and/or NH_x^+ ions: Growth kinetics and defect structure. *Journal of Vacuum Science & Technology A: Vacuum, Surfaces, and Films*, 13(5):2293–2302, 1995.

[130] P. Vermaut, P. Ruterana, G. Nouet, and H. Morkoc. Structural defects due to interface steps and polytypism in III-V semiconducting materials: A case study using high-resolution electron microscopy of the 2H-AlN/6H-SiC interface. *Philosophical Magazine A*, 75(1):239–259, 1997.

[131] E. F. Rauch and M. Veron. Coupled microstructural observations and local texture measurements with an automated crystallographic orientation mapping tool attached to a tem. *Materialwissenschaft und Werkstofftechnik*, 36(10):552 – 556, 2005.

[132] B. J. Rodriguez, A. Gruverman, A. I. Kingon, and R. J. Nemanich. Piezoresponse force microscopy for piezoelectric measurements of III-nitride materials. *Journal of Crystal Growth*, 246(3-4):252 – 258, 2002.

[133] W. Qian, M. Skowronski, M. De Graef, K. Doverspike, L. B. Rowland, and D. K. Gaskill. Microstructural characterization of alpha-GaN films grown on sapphire by organometallic vapor phase epitaxy. *Applied Physics Letters*, 66(10):1252 – 1254, 1995.

[134] P. Lejcek. Grain boundaries: Description, structure and thermodynamics. In *Grain Boundary Segregation in Metals*, volume 136 of *Springer Series in Materials Science*, pages 5 – 24. Springer Berlin Heidelberg, 2010.

[135] M. L. Kronberg and F. H. Wilson. Secondary recrystallization in copper. *Transactions of the American Institute of Mining and Metallurgical Engineers*, 185:501 – 514, 1949.

[136] D. H. Warrington. The coincidence site lattuce (CSL) and grain boundary (DSC) dislocations for the hexagonal lattice. *J. Phys. Colloques*, 36:C4–87–C4–95, 1975.

[137] A. Ostapovets, P. Molnar, A. Jäger, and P. Lejcek. Analysis of near-coincidnear site lattice boudnary frequencey in az31 magnesium alloy. In *Metal 2012*, 2012.

[138] G. L. Bleris, G. Nouet, S. Hagège, and P. Delavignette. Characterization of grain boundaries in the hexagonal system based on tables of coincidence site lattices (CSL's). *Acta Crystallographica Section A*, 38(4):550–557, Jul 1982.

[139] R. Bonnet, E. Cousineau, and D. H. Warrington. Determination of near-coincident cells for hexagonal crystals. Related DSC lattices. *Acta Crystallographica Section A*, 37(2):184 – 189, 1981.

[140] D.G Brandon. The structure of high-angle grain boundaries. *Acta Metallurgica*, 14(11):1479 – 1484, 1966.

[141] G. Wilde, J. Ribbe, G. Reglitz, M. Wegner, H. Rösner, Y. Estrin, M. Zehetbauer, D. Setman, and S. V. Divinski. Plasticity and grain boundary diffusion at small grain sizes. *Advanced Engineering Materials*, 12(8):758 – 764, 2010.

[142] H. Rösner, C. Kübel, Y. Ivanisenko, L. Kurmanaeva, S. V. Divinski, M. Peterlechner, and G. Wilde. Strain mapping of a triple junction in nanocrystalline Pd. *Acta Materialia*, 59(19):7380 – 7387, 2011.

[143] F. Bodker, S. Morup, S.W. Charles, and S. Linderoth. Surface oxidation of cobalt nanoparticles studied by Mössbauer spectroscopy. *Journal of Magnetism and Magnetic Materials*, 196 - 197:18 – 19, 1999.

[144] M. Li, J. Shi, Y. Nakamura, and R. Yu. Magnetoresistance of nanocrystalline Co-AlN films. *Applied Physics A*, 89(3):807 – 812, 2007.

[145] L. Maya, M. Paranthaman, J. R. Thompson, T. Thundat, and R. J. Stevenson. Ferromagnetic nanocomposite films from thermally labile nitride precursors. *MRS Online Proceedings Library*, 457, 1996.

[146] A. A. Bokov and Z.-G. Ye. Domain structure in the monoclinic Pm phase of $Pb(Mg_{1/3}Nb_{2/3}O_3$-$PbTiO_3$ single crystals. *Journal of Applied Physics*, 95(11):6347 – 6359, 2004.

[147] U. Belegundu, X. H. Du, A. Bhalla, and K. Uchino. Effect of electric field on domain formation in relaxor based Pb(Zn1/3Nb2/3)O3 - PbTiO3 single crystals. *Ferroelectrics Letters Section*, 26(5-6):107–116, 1999.

[148] F. Bai, J. F. Li, and D. Viehland. Domain hierarchy in annealed (001)-oriented $Pb(Mg_{1/3}Nb_{2/3}O_3$-$xPbTiO_3$ single crystals. *Applied Physics Letters*, 85(12):2313 – 2315, 2004.

[149] Y. Saito, H. Takao, T. Tani, T. Nonoyama, K. Takatori, T. Homma, T. Nagaya, and M. Nakamura. Lead-free piezoceramics. *Nature*, 432(7013):84 – 87, 2004.

[150] T. Yamamoto. Ferroelectric properties of the $PbZrO_3$-$PbTiO_3$ system. *Japanese Journal of Applied Physics*, 35(Part 1, No. 9B):5104 – 5108, 1996.

[151] T. Takenaka and H. Nagata. Current status and prospects of lead-free piezoelectric ceramics. *Journal of the European Ceramic Society*, 25(12):2693 – 2700, 2005.

[152] X. Ren. Large electric-field-induced strain in ferroelectric crystals by point-defect-mediated reversible domain switching. *Nature Materials*, 3(2):91 – 94, 2004.

[153] J. Gao, D. Xue, Y. Wang, D. Wang, L. Zhang, H. Wu, S. Guo, H. Bao, C. Zhou, W. Liu, S. Hou, G. Xiao, and X. Ren. Microstructure basis for strong piezoelectricity in Pb-free $Ba(Zr_{0.2}Ti_0.8)O_3$-$(Ba_{0.7}Ca_0.3)TiO_3$ ceramics. *Applied Physics Letters*, 99(9):092901, 2011.

[154] P. Groth. Ueber beziehungen zwischen krystallform und chemische constitution bei einigen organischen verbindungen. *Annalen der Physik*, 217(9):31 – 43, 1870.

[155] V. M. Goldschmidt. Crystal structure and chemical constitution. *Transactions of the Faraday Society*, 25:253 – 283, 1929.

[156] B. Jaffe, R. S. Roth, and S. Marzullo. Piezoelectric properties of lead zirconate-lead titanate solid-solution ceramics. *Journal of Applied Physics*, 25(6):809 – 810, 1954.

[157] R. E. Cohen. Origin of ferroelectricity in perovskite oxides. *Nature*, 358(6382):136 – 138, July 1992.

[158] O. Bock and U. Müller. Symmetrieverwandtschaften bei Varianten des Perowskit-Typs. *Acta Crystallographica Section B*, 58(4):594 – 606, 2002.

[159] H. Fu and R. E. Cohen. Polarization rotation mechanism for ultrahigh electromechanical response in single-crystal piezoelectrics. *Nature*, 403(6767):281 – 283, 2000.

[160] B. Noheda, D. E. Cox, G. Shirane, J. A. Gonzalo, L. E. Cross, and S.-E. Park. A monoclinic ferroelectric phase in the $Pb(Zr_{1-x}Ti_x)O_3$ solid solution. *Applied Physics Letters*, 74(14):2059 – 2061, 1999.

[161] B. Noheda, D. E. Cox, G. Shirane, R. Guo, B. Jones, and L. E. Cross. Stability of the monoclinic phase in the ferroelectric perovskite $PbZr_{1-x}Ti_xO_3$. *Physical Review B*, 63:014103, 2000.

[162] B. Noheda, D. E. Cox, G. Shirane, S.-E. Park, L. E. Cross, and Z. Zhong. Polarization rotation via a monoclinic phase in the piezoelectric 0.92 $PbZn_{1/3}Nb_{2/3}O_3$ - 0.08 $PbTiO_3$. *Physical Review Letters*, 86:3891 – 3894, 2001.

[163] D. Vanderbilt and M. H. Cohen. Monoclinic and triclinic phases in higher-order Devonshire theory. *Physical Review B*, 63(9):094108, 2001.

[164] W. Liu and X. Ren. Large piezoelectric effect in pb-free ceramics. *Physical Review B*, 103:257602, 2009.

[165] D. S. Keeble, F. Benabdallah, P. A. Thomas, M. Maglione, and J. Kreisel. Revised structural phase diagram of $(Ba_{0.7}Ca_{0.3}TiO_3)$-$(BaZr_{0.2}Ti_{0.8}O_3)$. *Applied Physics Letters*, 102(9):092903, 2013.

[166] H. Wang, J. Zhu, N. Lu, A. A. Bokov, Z.-G. Ye, and X. W. Zhang. Hierarchical micro-/nanoscale domain structure in M_C phase of (1 - x)$Pb(Mg_{1/3}Nb_{2/3})O_3$ - x$PbTiO_3$ single crystal. *Applied Physics Letters*, 89(4):042908, 2006.

[167] A. Piorra. *Ferroelektrische Schichten für agnetoelektrische Komposite*. PhD thesis, Christian-Albrechts-University of Kiel, *to be published*.

[168] Y. M. Jin, Y. U. Wang, A. G. Khachaturyan, L. F. Li, and D. Viehland. Conformal miniaturization of domains with low domain-wall energy: Monoclinic ferroelectric states near the morphotropic phase boundaries. *Physical Review Letters*, 91:197601, 2003.

[169] N. Inoue, T. Okamatsu, A. Ando, H. Takagi, T. Hashimoto, C. Moriyoshi, and Y. Kuroiwa. Structural characteristics of (ba0.94 gd0.06) (ti0.97 mg0.03) o3 in cubic structure determined by high-energy synchrotron-radiation powder diffraction. *Japanese Journal of Applied Physics*, 48:1–4, 2009.

[170] B. G. Demczyk, R. S. Rai, and G. Thomas. Ferroelectric domain structure of lanthanum-modified lead titanate ceramics. *Journal of the American Ceramic Society*, 73(3):615 – 620, 1990.

[171] D. I. Woodward, J. Knudsen, and I. M. Reaney. Review of crystal and domain structures in the $PbZr_xTi_{1-x}O_3$ solid solution. *Physical Review B (Condensed Matter and Materials Physics)*, 72(10):104110, 2005.

[172] C.J. Xiao, C.Q. Jin, and X.H. Wang. Crystal structure of dense nanocrystalline BaTiO3 ceramics. *Materials Chemistry and Physics*, 111:209 – 212, 2008.

[173] K. Tsuda, R. Sano, and M. Tanaka. Nanoscale local structures of rhombohedral symmetry in the orthorhombic and tetragonal phases of $BaTiO_3$ studied by convergent-beam electron diffraction. *Physical Review B*, 86:214106, 2012.

[174] K. Tsuda, R. Sano, and M. Tanaka. Observation of rhombohedral nanostructures in the orthorhombic phase of $knbo_3$ using convergent-beam electron diffraction. *Applied Physics Letters*, 102(5):051913, 2013.

[175] S. Garcia-Martin, E. Urones-Garrote, M. C. Knapp, G. King, and P. M. Woodward. Transmission electron microscopy studies of NaLaMgWO6: Spontaneous formation of compositionally modulated stripes. *Journal of the American Chemical Society*, 130(45):15028 – 15037, 2008.

[176] A. A. Bokov and Z.-G. Ye. Recent progress in relaxor ferroelectrics with perovskite structure. *Journal of Materials Science*, 41(1):31 – 52, 2006.

[177] A. S. Bhalla, R. Guo, and R. Roy. The perovskite structure - a review of its role in ceramic science and technology. *Material Research Innovations*, 4(1):3 – 26, 2000.

[178] Q. Hang, Z. Xing, X. Zhu, M. Yu, Y. Song, J. Zhu, and Z. Liu. Dielectric properties and related ferroelectric domain configurations in multiferroic $BiFeO_3$-$BaTiO_3$ solid solutions. *Ceramics International*, 38, Supplement 1(0):S411 – S414, 2012.

[179] M. E. Akbas and P. K. Davies. Structure and dielectric properties of the Ba(Mg1/3Nb2/3)O3-La(Mg2/3Nb1/3)O3 System. *Journal of the American Ceramic Society*, 81(8):2205 – 2208, 1998.

[180] S. Ya. Istomin, G. Svensson, O. G. D'yachenko, W. Holm, and E. V. Antipov. Perovskite-type $ca_{1-x}sr_xnbo_3$ $(0 \leq x \leq 1)$ phases: A synthesis, structure, and electron microscopy study. *Journal of Solid State Chemistry*, 141(2):514 – 521, 1998.

[181] G. King, S. Garcia-Martin, and P. M. Woodward. Octahedral tilt twinning and compositional modulation in $NaLaMgWO_6$. *Acta Crystallographica Section B*, 65(6):676 – 683, Dec 2009.

[182] S. Van Aert, J. Verbeeck, R. Erni, S. Bals, M. Luysberg, D. Van Dyck, and G. Van Tendeloo. Quantitative atomic resolution mapping using high-angle annular dark field scanning transmission electron microscopy. *Ultramicroscopy*, 109(10):1236 – 1244, 2009.

[183] A. Guinier, G. B. Bokij, K. Boll-Dornberger, J. M. Cowley, S. Ďurovič, H. Jagodzinski, P. Krishna, P. M. de Wolff, B. B. Zvyagin, D. E. Cox, P. Goodman, Th. Hahn, K. Kuchitsu, and S. C. Abrahams. Nomenclature of polytype structures. Report of the International Union of Crystallography *Ad hoc* Committee on the Nomenclature of Disordered, Modulated and Polytype Structures. *Acta Crystallographica Section A*, 40(4):399 – 404, 1984.

[184] E. Garcia-Gonzalez, M. Parras, and J. M. Gonzalez-Calbet. Crystal structure of an unusual polytype:7H-$Ba_7Nb_4MoO_{20}$. *Chemistry of Materials*, 11(2):433 – 437, 1999.

[185] H. Yang, Y. K. Tang, L. D. Yao, W. Zhang, Q. A. Li, F.Y. Li, C. Q. Jin, and R. C. Yu. Synthesis, structure and phase separation of a new 12R-type perovskite-related oxide Ba3NdMn2O9. *Journal of Alloys and Compounds*, 432(1-2):283 – 288, 2007.

[186] J.-G Cheng, J. A. Alonso, E. Suard, J.-S. Zhou, and J. B. Goodenough. A new perovskite polytype in the high-pressure sequence of BaIrO3. *Journal of the American Chemical Society*, 131(21):7461 – 7469, 2009.

[187] S. Garcia-Martin, G. King, G. Nenert, C. Ritter, and P. M. Woodward. The incommensurately modulated structures of the perovskites NaCeMnWO6 and NaPrMnWO6. *Inorganic Chemistry*, 51(7):4007 – 4014, 2012.

[188] O. Eibl, P. Pongratz, and P. Skalicky. Crystallography of (111) twins in $batio_3$. *Philosophical Magazine Part B*, 57(4):521 – 534, 1988.

[189] A. Recnik, J. Bruley, W. Mader, D. Kolar, and M. Rühle. Structural and spectroscopic investigation of (111) twins in barium titanate. *Philosophical Magazine Part B*, 70(5):1021 – 1034, 1994.

[190] C. L. Jia. Atomic structure of a sigma=3, {111} twin-boundary junction in a $batio_3$ thin film. *Philosophical Magazine Letters*, 79(3):99 – 106, 1999.

[191] M. Fujimoto. Defects in epitaxially grown perovskite thin films. *Journal of Crystal Growth*, 237 - 239(0):430 – 437, 2002.

[192] C. L. Jia, K. Urban, M. Mertin, S. Hoffmann, and R. Waser. The structure and formation of nanotwins in $BaTiO_3$ thin films. *Philosophical Magazine A*, 77(4):923 – 939, 1998.

[193] C. L. Jia and A. Thust. Investigation of atomic displacements at a $\Sigma = 3\{111\}$ twin boundary in $BaTiO_3$ by means of phase-retrieval electron microscopy. *Physical Review Letters*, 82:5052 – 5055, 1999.

[194] P. Bao, F. Yan, W. Li, Y. R. Dai, H. M. Shen, J. S. Zhu, Y. N. Wang, H. L. W. Chan, and Chung-Loong Choy. Mechanical properties related to the relaxor-ferroelectric phase transition of titanium-doped lead magnesium niobate. *Applied Physics Letters*, 81(11):2059 – 2061, 2002.

[195] V. Hrkac, E. Lage, G. Köppel, J. Strobel, J. McCord, E. Quandt, D. Meyners, and L. Kienle. Amorphous FeCoSiB for exchange bias coupled and decoupled magnetoelectric multilayer systems: Real-structure and magnetic properties. *in preparation.*

[196] V. M. Laletin, N. Paddubnaya, G. Srinivasan, C. P. De Vreugd, M. I. Bichurin, V. M. Petrov, and D. A. Filippov. Frequency and field dependence of magnetoelectric interactions in layered ferromagnetic transition metal-piezoelectric lead zirconate titanate. *Applied Physics Letters*, 87(22):222507, 2005.

[197] G. Srinivasan, E. T. Rasmussen, J. Gallegos, R. Srinivasan, Yu. I. Bokhan, and V. M. Laletin. Magnetoelectric bilayer and multilayer structures of magnetostrictive and piezoelectric oxides. *Physical Review B*, 64:214408, 2001.

[198] H. Greve, E. Woltermann, H.-J. Quenzer, B. Wagner, and E. Quandt. Giant magnetoelectric coefficients in $(Fe_{90}Co_{10})_{78}Si_{12}B_{10}$-AlN thin film composites. *Applied Physics Letters*, 96(18):182501, 2010.

[199] Lage. PhD thesis, Christian-Albrechts-University of Kiel, *(to be published).*

[200] R. L. Stamps. Mechanisms for exchange bias. *Journal of Physics D: Applied Physics*, 33(23):R247, 2000.

[201] W. H. Meiklejohn and C. P Bean. New magnetic anisotropy. *Phys. Rev.*, 102:1413 – 1414, 1956.

[202] W. H. Meiklejohn and C. P. Bean. New magnetic anisotropy. *Phys. Rev.*, 105:904 – 913, 1957.

[203] J. Nogues and I. K. Schuller. Exchange bias. *Journal of Magnetism and Magnetic Materials*, 192(2):203 – 232, 1999.

[204] H. Kurt, K. Rode, H. Tokuc, P. Stamenov, M. Venkatesan, and J. M. D. Coey. Exchange-biased magnetic tunnel junctions with antiferromagnetic ϵ-Mn3Ga. *Applied Physics Letters*, 101(23):–, 2012.

[205] J. van Driel, F. R. de Boer, K.-M. H. Lenssen, and R. Coehoorn. Exchange biasing by $ir_{19}mn_{81}$: Dependence on temperature, microstructure and antiferromagnetic layer thickness. *Journal of Applied Physics*, 88(2):975 – 982, 2000.

[206] H. Li, P. P. Freitas, Z. Wang, J. B. Sousa, P. Gogol, and J. Chapman. Exchange enhancement and thermal anneal in $mn_{76}ir_{24}$ bottom-pinned spin valves. *Journal of Applied Physics*, 89(11):6904 – 6906, 2001.

[207] M. Fecioru-Morariu, G. Guntherodt, M. Ruhrig, A. Lamperti, and B. Tanner. Exchange coupling between an amorphous ferromagnet and a crystalline antiferromagnet. *Journal of Applied Physics*, 102(5):053911, 2007.

[208] A. Kohn, J. Dean, A. Kovacs, A. Zeltser, M. J. Carey, D. Geiger, G. Hrkac, T. Schrefl, and D. Allwood. Exchange-bias in amorphous ferromagnetic and polycrystalline antiferromagnetic bilayers: Structural study and micromagnetic modeling. *Journal of Applied Physics*, 109(8):083924, 2011.

[209] K. O'Grady, L.E. Fernandez-Outon, and G. Vallejo-Fernandez. A new paradigm for exchange bias in polycrystalline thin films. *Journal of Magnetism and Magnetic Materials*, 322(8):883 – 899, 2010.

[210] H. N. Fuke, K. Saito, Y. Kamiguchi, H. Iwasaki, and M. Sahashi. Spin-valve giant magnetoresistive films with antiferromagnetic ir-mn layers. *Journal of Applied Physics*, 81(8):4004 – 4006, 1997.

[211] D. L. Smith. *Thin Film Deposition: Principles and Practice*. McGraw-Hill, 1994.

[212] K. Lu. Nanocrystalline metals crystallized from amorphous solids: nanocrystallization, structure, and properties. *Materials Science and Engineering: R: Reports*, 16(4):161 – 221, 1996.

[213] J. M. Grenche. Soft magnetic nanocrystalline alloys. *Journal of Optoelectronics and Advanced Materials*, 5:133 – 138, 2003.

[214] D. R. Wilburn and W. A. Bassett. Hydrostatic compression of iron and related compounds: an overview. *American Mineralogist*, 63:591 – 596, 1978.

[215] J. Hafner and D. Spisak. Structure and stability of the low-index surfaces of Fe_3Si: An initio density functional investiagtions. *Physical Review B*, 75:195411, 2007.

[216] W. C. Ellis and E. S. Greiner. Equilibrium relations in the solid state of the iron cobalt system. *Trans. Am. Soc. Metals*, 29:415 – 432, 1941.

[217] K. H. J. Buschow, P. G. van Engen, and R. Jongebreur. Magneto-optical properties of metallic ferromagnetic materials. *Journal of Magnetism and Magnetic Materials*, 38(1):1 – 22, 1983.

[218] A. Berger, D. T. Margulies, and H. Do. Magnetic hysteresis loop tuning in antiferromagnetically coupled bilayer structures. *Applied Physics Letters*, 85(9):1571 – 1573, 2004.

[219] J. M. Shaw, R. Geiss, and S. Russek. Dynamic lorentz microscopy of micromagnetic structure in magnetic tunnel junctions. *Applied Physics Letters*, 89(21):212503, 2006.

[220] J. M. Shaw, H. T. Nembach, and T. J. Silva. Roughness induced magnetic inhomogeneity in Co/Ni multilayers: Ferromagnetic resonance and switching properties in nanostructures. *Journal of Applied Physics*, 108(9):093922, 2010.

[221] G. Choe and M. Steinback. Surface roughness effects on magnetoresistive and magnetic properties of NiFe thin films. *Journal of Applied Physics*, 85(8):5777 – 5779, 1999.

[222] C.-H. Chang and Mark H. Kryder. Effect of substrate roughness on microstructure, uniaxial anisotropy, and coercivity of Co/Pt multilayer thin films. *Journal of Applied Physics*, 75(10):6864 – 6866, 1994.

[223] J. C. S. Kools, W. Kula, D: Mauri, and T. Lin. Effect of finite magnetic film thickness on neel coupling in spin valves. *Journal of Applied Physics*, 85(8):4466 – 4468, 1999.

[224] B. D. Schrag, A. Anguelouch, S. Ingvarsson, Gang Xiao, Yu Lu, P. L. Trouilloud, A. Gupta, R. A. Wanner, W. J. Gallagher, P. M. Rice, and S. S. P. Parkin. Néel "orange-peel" coupling in magnetic tunneling junction devices. *Applied Physics Letters*, 77(15):2373 – 2375, 2000.

[225] V. S. K. Chakravadhanula, C. Kübel, T. Hrkac, V. Zaporojtchenko, T. Strunskus, F. Faupel, and L. Kienle. Surface segregation in tio_2 -based nanocomposite thin films. *Nanotechnology*, 23(49):495701, 2012.

[226] I. N. Bronstein, K. A. Semendjajew, G. Musiol, and H. Mühilg. *Taschenbuch der Mathematik*. Harri Deutsch, 2008.

[227] H. Y. Erbil and R. A. Meric. Evaporation of sessile drops on polymer surfaces: Ellipsoidal cap geometry. *The Journal of Physical Chemistry B*, 101(35):6867 – 6873, 1997.

[228] G. J. Tee. *Surface area of ellipsoid segment*. Report series / Department of Mathematics, School of Mathematical and Information Sciences, University of Auckland, 539; Report series, 539. Auckland Univ., Department of Mathematics, School of Mathematical and Information Sciences, 2005.

[229] M. C. Scott, C.-C. Chen, M. Mecklenburg, C. Zhu, R. Xu, P Ercius, U. Dahmen, B. C. Regan, and J. Miao. Electron tomography at 2.4-angstrom resolution. *Nature*, 483(7390):444 – 447, March 2012.

[230] C. Drews, L. Berger, R. F. Wimmer-Schweingruber, A. B. Galvin, B. Klecker, and E. Möbius. Observations of interstellar neon in the helium focusing cone. *Journal of Geophysical Research: Space Physics*, 115(A10), 2010.

[231] C. Drews, L. Berger, R. F. Wimmer-Schweingruber, P. Bochsler, A. B. Galvin, B. Klecker, and E. Möbius. Inflow direction of interstellar neutrals deduced from pickup ion measurements at 1 au. *Journal of Geophysical Research: Space Physics*, 117(A9), 2012.

[232] C. Drews, Lars Berger, Robert F. Wimmer-Schweingruber, and Antoinette B. Galvin. Interstellar He+ ring-beam distributions: Observations and implications. *Geophysical Research Letters*, 40(8):1468–1473, 2013.

List of Publications

In reverse chronological order

1. V. Hrkac, L. Kienle, S. Kaps, A. Lotnyk, Y. K. Mishra, U. Schürmann, V. Duppel, B. V. Lotsch and R. Adelung. Superposition twinning supported by texture in ZnO nanospikes. *Journal of Applied Crystallography*, 46(2):434 - 435, 2013.

2. S Bhowmick, D. Stauffer, H. Guo, S. Kaps, Y. K. Mishra, V. Hrkac, O. Warren, R. Adelung, A. Minor, and L. Kienle. In Situ Electromechanical Study of ZnO Nanowires. *Microscopy and Microanalysis*, 19:396 - 403, 2013.

3. B. Gojdka, V. Hrkac, J. Xiong, M. Gerken, L. Kienle, T. Strunskus, V. Zaporojtchenko, and F. Faupel. A critical evaluation of the 0-3 approach for magnetoelectric nanocomposites with metallic nanoparticles. *Journal of Applied Physics*, 112(4):044303, 2012.

4. B. Gojdka, V. Zaporojtchenko, V. Hrkac, J. Xiong, L. Kienle, T. Strunskus, and F. Faupel. Highly versatile concept for precise tailoring of nanogranular composites with a gas aggregation cluster source. *Applied Physics Letters*, 100(13):133104, 2012.

5. S. Kaps, Y. K. Mishra, V. Hrkac, H. Greve, L. Kienle, E. Quandt, and R. Adelung. High aspect ratio free standing ZnO-magnetostrictive mesoscale cylindrical magnetoelectric core shell composite. *MRS Online Proceedings Library*, 1398, 2012.

6. E. Lage, C. Kirchhof, V. Hrkac, L. Kienle, R. Jahns., R. Knöchel, E. Quandt, and D. Meyners. Exchange biasing of magnetoelectric composites. *Nature Materierals*, 11(6):523 - 529, 2012.

7. S. Marauska, V. Hrkac, T. Dankwort, R. Jahns, H. J. Quenzer, R. Knöchel, L. Kienle, and B. Wagner. Sputtered thin film piezoelectric aluminum nitride as a functional MEMS material. *Microsystem Technologies*, 18(6):787 - 795, 2012.

8. Y. K. Mishra, V. S. K. Chakravadhanula, V. Hrkac, S. Jebril, D. C. Agarwal, S. Mohapatra, D. K. Avasthi, L. Kienle, and R. Adelung. Crystal growth behaviour in Au-ZnO nanocomposite under different annealing environments and photoswitchability. *Journal of Applied Physics*, 112(6):064308, 2012.

9. B. Gojdka, V. Hrkac, T. Strunskus, V. Zaporojtchenko, L. Kienle, and F. Faupel. Study of cobalt clusters with very narrow size distribution deposited by high-rate cluster source. *Nanotechnology*, 22(46):465704, 2011.

10. V. Hrkac, Y. K. Mishra, V. S. K. Chakravadhanula, S. Jebril, D. K. Avasthi, R. Adelung, and L. Kienle. Au-ZnO Nanocomposites for Functional Devices. *Zeitschrift für anorganische und allgemeine Chemie*, 636(11):2081 - 2081, 2010.

Acknowledgements

Die ganz persönlichen, subjektiven Wahrnehmungen des Verfassers und der Leser zur Dissertation können unterschiedlicher kaum sein. Betrachtet man zunächst die letztere Gruppe, so ergibt sich grob die folgende Einteilung: Während das Fachpublikum sich ausschließlich mit der wissenschaftlichen Präzision der Texte sowie dem übermittelnden Informationsgehalt der Abbildungen befasst, reduzieren diese Inhalte bei dem wohlgesonnen Außenstehenden zu farbenfrohen Bildchen, deren Bedeutung er bestenfalls mit dadaistischer oder surrealistischer Kunst assoziiert. Es gereicht dem Außenstehenden die aufbereiteten Daten (in Gegenwart des Verfassers) mit einem Wertschätzung ausdrückenden Zungenschnalzer zu loben[6]. Gleich welcher Gruppe man angehört, gemein bleibt allen Lesern jedoch nur die Konfrontation mit einem vollendeten Werk.
Der Autor hingegen erlebt aktiv die gesamte Entwicklung vom ersten Schreckensgedanken an eine kaum zu bewältigende Aufgabe bis hin zu einer im Zusammenspiel von Blatt und Druckertinte, gerahmt von festen Buchdeckeln, erstellten Endfassung. Das ein breites emotionales Spektrum, beginnend bei optimistischem Frohsinn über Wahnwitz bis zu einer demoralisierten Kapitulation gegenüber allem Guten und Schönen, während des Schreibprozesses durchlaufen wird, resultiert fast schon automatisch[7].
Obschon das Schreiben der Doktorarbeit eine eigenständige und gesonderte Einzelleistung darstellt, gibt es dennoch eine Viezahl von Unterstützungen. Im Promotionszeitraum, dessen Höhepunkt durch die Dissertation gekennzeichnet ist, bedarf es an Inspiration, Diskussionen und sozialem Ausgleich nicht nur als Grundbasis sondern auch als Triebkraft für ein erfolgreiches Vorgehen in der wissenschaftlichen Arbeit. Da es mir vergönnt war durch mein Arbeits- und Freundesumfeld dies alles zu bekommen, möchte ich mich an dieser Stelle aus vollem Herzen bei den entsprechenden Menschen individuell bedanken.
Ich möchte mich bei Prof. Dr. Lorenz Kienle für das Vertrauen bedanken, mich in seine Arbeitsgruppe aufzunehmen und mir die Möglichkeit zu geben eine eigenständige Forschung zu betreiben. Die warmherzige und offene Atmosphäre, die sich auch auf alle Mitarbeiter übertrug, sowie zahlreiche intensive Diskussionen erlaubten es mir, mich sowohl wissenschaftlich als auch menschlich zu entfalten. Es war mir eine enorme Freude ein Bestandteil dieser Arbeitsgruppe, besonders mit diesen Kollegen, zu sein.
Einen großen Dank gebührt Dr. Ulrich Schürmann, der mir mit vielen fruchtbaren

[6] In Abwesenheit des Verfassers wandeln sich die Beurteilungen in verwundertes Seufzen und Stöhnen.

[7] Dies darf natürlich zum Verständnis über Besonderheiten, u. a. des Stils oder der Orthographie, herangeführt werden.

Diskussionen, Einwänden und Ideen stets eine unvergleichliche Hilfe in meiner Forschung war. Durch sein fröhliches Naturell und seine offene Art war er mir ein guter Kollege und ein wichtiger Freund.
Rasit Burak Erkartals Promotionszeit überschnitt sich mit der meinen. Gemeinschaftlich haben wir so manche größere und kleinere Probleme gemeistert, ganz gleich, ob sie mit wissenschaftlichem Bezug waren oder sie sich im universitären Alltag befanden. Sein Esprit und seine Eloquenz konnten jeden noch so drögen Moment erhellen. Içten teşekkürler!
Einen großen Dank möchte ich besonders Christin Szillus aussprechen, deren handwerkliches Geschick die Grundlage all meiner wissenschaftlichen Arbeiten darstellte. Auch ohne Berücksichtigung dieser Qualitäten war ihre Persönlichkeit eine wunderbare Bereicherung in meinem Arbeitsumfeld.
Ich möchte mich bei allen Mitgliedern der Arbeitsgruppe Synthese und Realstruktur bedanken, da deren Herzlichkeit und Humor, mir sehr viel Freude während meiner gesamten Promotionszeit brachten. Ich bedanke mich bei Katrin Brandenburg, Dr. Venkata Sai Kiran Chakravadhanula, Dr. Andriy Lotnyk, Mao Deng, Torben Dankwort, Grit Köppel, Gero Neubüser, Julian Strobel, Niklas Wolff, Moritz Schultes, Rene Millies, Mathias Frank, Ekin Simsek, Marisa Hernandez Pavon, Michael Ciszewski und Irmak Kocabas.
Die Arbeit wäre ohne den SFB 855 (*Magnetoelectric Composites - Future Biomagnetic Interfaces*) nicht möglich gewesen. Ich bedanke mich bei der Organisation des SFBs und bei der deutschen Forschungsgemeinschaft (DFG) für die Förderung dieses Projektes.
Da die Tätigkeiten innerhalb des SFBs durch eine hohe Wechselwirkung zwischen den einzelnen Teilprojekten geprägt waren, war mein persönlicher Fortschritt immer auch von dem Engagement anderer abhängig. Ich möchte mich bei meinen Kollegen für die hervorragende und unkomplizierte Zusammenarbeit bedanken. Dies gilt vor allem für Dr. Björn Gojdka, Dr. Stephan Marauska, Enno Lage, Sören Kaps, Andre Piorra, Fabian Lohfink, Dr. Yogendra Kumar Mishra, Dr. Adrian Petraru, Erdem Yarar und Dr. Dirk Meyners.
Ich bin den Mitarbeitern der unterschiedlichen TEM Zentren (MPI, KIT, ER-C) für die zusätzlichen wissenschaftlichen TEM-Untersuchungen zu großem Dank verpflichtet. Besonders möchte ich mich bei Viola Duppel, Aaron Kobler, Dr. Venkata Sai Kiran Chakravadhanula und Dr. Martina Luysberg für ihre Mühe und kompetente Hilfe bedanken.
Ich möchte mich bei all meinen Thermodynamikstudenten für die gemeinsame Zeit bedanken. Es war mir eine Ehre junge motivierte Studenten in ihrer Ausbildung zu begleiten.
Das legendäre Ensemble des Büros F130 hat diesen Raum zu einer wahren Bühne gestaltet. Komödien und Tragödien spielten sich ab und großartige Charakterdarsteller konnten einem mit der kleinsten Gestik und Mimik den Atem rauben. Mein spezieller Dank gebührt Rasit Burak Erkartal, Dr. Venkata Sai Kiran Chakravadhanula, Dawit Gedamu, Iris Hölken, Mathias Hoppe, Grit Köppel und Stefan Freitag.

Betrachet man die vier Jahre an der Technischen Fakultät, so ist nicht die Beschäftigung der Aspekt, der diesen Zeitraum für mich definiert, sondern der menschliche Umgang von Kollegen und Freunden miteinander. Mein großer Dank gilt Dr. Ulrich Schürmann, Rasit Burak Erkartal, Christin Szillus, Dr. Venkata Sai Kiran Chakravadhanula, Grit Köppel, Torben Dankwort, Mao Deng, Iris Hölken, Mathias Hoppe, Stefan Freitag, Sören Kaps, Dr. Yogendra Kumar Mishra, Arnim Schuchardt, Ingo Paulowicz, Xin Jin, Dawit Menale Gedamu Mengesha Yohannes, Dr. Björn Gojdka, Kerstin Meurisch, Christian Ohrt, Christoph Ochmann, Marc-Daniel Berngroß, Enno Lage, Andre Piorra, Volker Röbisch, Patrick Hayes, Till Jurgeleit, Laith Kadem, Gero Neubüser, Julian Strobel, Niklas Wolff, Cai Müller und allen anderen Kollegen für die wundervolle Zeit am Institut für Materialwissenschaften.
Außerordentlicher Dank gebührt Animo Carlos Scucardo für die Entdeckung der Zeitverschränkung, der cerimalen Zonenverschiebung 7,9 und für die Neudefinition des Schürmannwinkels. Noch in den 1987er Jahren verspottet, avancierten seine postanachronistischen Sprachlinearitätstheorien zu einem semibarocken Existensmodell des Universums und der darin enthaltenen Dinge (unter Umständen).
Ich bedanke mich herzlich für die inspirierende Forschung von Dr. Christian Drews [230, 231, 232], die mich während meiner Promotionszeit anspornte.
Zum Schluss möchte ich meiner Familie einen speziellen Dank zukommen lassen. Ohne ihren uneingeschränkten Rückhalt, ihre bedingungslose Liebe und ihren aufopfernden Aufwand wäre mein bisheriger Werdegang nicht möglich gewesen.

So Long, and Thanks For All the Cake.

Eidesstattliche Erklärung

Ich erkläre, dass ich meine Abhandlung "*Nanocharacterization of Materials for Biomagnetic Sensing*", abgesehen von der Beratung durch den Betreuer, selbstständig und ohne Benutzung anderer als der angegebenen Hilfsmittel angefertigt habe. Alle Stellen, die ich wörtlich oder sinngemäß aus Veröffentlichungen entnommen habe, habe ich als solche kenntlich gemacht. Die Arbeit hat bisher in gleicher oder ähnlicher Form noch keiner Prüfungsbehörde vorgelegen. Auszüge der Arbeit wurden entsprechend der in Kapitel 6 *List of Publication* aufgeführten Referenzen bereits veröffentlicht. Die Dissertationsschrift entstand unter Einhaltung der Regeln guter wissenschaftlicher Praxis der Deutschen Forschungsgemeinschaft.

Kiel,

_____

(Viktor Hrkac)